ENVIRONMENTAL CONTROLS ON THE GENERATION OF SUBMARINE LANDSLIDES IN ARCTIC FIORDS: AN EXAMPLE FROM PANGNIRTUNG FIORD, EASTERN BAFFIN ISLAND, NUNAVUT

by

Philip R. G. Sedore

Submitted in partial fulfilment of the requirements
for the degree of Masters of Science

at

Dalhousie University
Halifax, Nova Scotia
March 2022

TABLE OF CONTENTS

LIST OF TABLES

LIST OF FIGURES

ABSTRACT

High-latitude fiords are susceptible to hazardous submarine and subaerial mass movements. Submarine landslides can damage seabed infrastructure and potentially trigger tsunami waves, which can damage low-lying coastal communities. Most surveyed Baffin Island fiords, including the deglaciated Pangnirtung Fiord, show evidence of submarine landslides, although their timing is relatively unknown. This study sought to generate a comprehensive understanding of the timing, as well as the distribution and the environmental controls of submarine landslides in Pangnirtung Fiord (Nunavut) to test the hypothesis that the submarine landslides are associated with subaerial features. Since the hamlet of Pangnirtung is situated along the coast of Pangnirtung Fiord, it is even more critical to understand the submarine-landslide hazard of the area. Acoustic data and sediment cores collected in 2019 were used to identify 180 near-surface submarine landslides. High-resolution multibeam bathymetry and sub-bottom profiler data enabled morphometric and geomorphological interpretations of the landslides, while gravity cores enabled the identification of lithofacies and determination of the landslide ages.

Morphometric analysis shows that most submarine landslides are relatively small (~0.13 km^2), with elongated depletion zones and wide deposits dispersed along the basin floor of the fiord. Landslide ages calculated from radiocarbon dating and $^{210}Pb/^{137}Cs$ activities indicate that 8 of the 11 dated landslides are younger than 500 years. Landslide-surface roughness was tested as a proxy for age, but the relationship was found to be weak, thus limiting the ability to accurately date all identified landslides. Four broad categories of submarine landslide environments were identified, and it was shown that at least 53% (96 of 180) of landslides are associated with subaerial sources and, at most, 31% (56 of 180) are shallow-water, non-subaerially influenced. These categories suggests that triggers of most submarine landslides within Pangnirtung Fiord include rapid flood-water input, subaerial debris flows and sea-ice loading during low tide. This research shows that landslides in a high-latitude fiord are affected by the interaction of numerous subaerial and submarine processes, leading to speculation that a potential increase in the frequency of subaerial debris flows and river floods due to climate change may increase the recurrence of submarine landslides. Future work is needed to evaluate the potential of submarine landslides in Pangnirtung Fiord to generate tsunami waves and assess the associated risk.

LIST OF ABBREVIATIONS AND SYMBOLS USED

3D	Three-dimensional
AMS	Accelerator Mass Spectrometry
BIO	Bedford Institute of Oceanography
BP	before present
BPI	Bathymetric position index
BPISD	Standard deviation of the bathymetric position index
bsl	metres below sea level
cal BP	calibrated years before present
CFCS	Constant Flux Constant Sedimentation
CTD	Conductivity-Temperature-Depth
GSC	Geological Survey of Canada
GSC-A	Geological Survey of Canada-Atlantic
m asl	metres above sea level
MSCL	Multi-Sensor Core Logger
ΔR	Reservoir correction
R/V	Research Vessel
SAR	Sediment Accumulation Rate
SIS	Seafloor Information System
SD	Standard deviation
UAV	Unmanned Aerial Vehicle
XCT	X-Ray computed tomography

ACKNOWLEDGEMENTS

I would like to offer sincere thanks to Dr. Alexandre Normandeau of the Geological Survey of Canada and Dr. Vittorio Maselli of Dalhousie University for their mentorship and guidance throughout this project. Thank you to my committee members Dr. Lawrence Plug and Dr. Owen Sherwood for their insight and constructive comments. I would also like to acknowledge the extremely helpful questions and comments from Dr. Calvin Campbell and Dr. Andrée Blais-Stevens as defence committee members. Colleagues of the Geological Survey of Canada-Atlantic also provided invaluable support and expertise throughout the project. Specifically, I would like to thank Angus Robertson, Emily Batt, Geneviève Philibert, Grace Nissen, Jenna Higgins, Kate Jarrett, Kimberley Jenner, Laura Broom, Owen Brown, and Parker Ingham of the Geological Survey of Canada-Atlantic. I also want to highlight the efforts of Kirk Regular of the Marine Institute in collecting acoustic data throughout the research cruise. Thank you to the crew of the R/V Nuliajuk (Captain Bob, Dez, Allen, Alf, Mary, and Evie) and the Hamlet of Pangnirtung for having us to their beautiful home. Finally, I would like to acknowledge the unwavering support of friends and family that have helped me through this project in countless ways.

Financial support for this study was provided by Crown-Indigenous Relations and Northern Affairs Canada (CIRNAC), the Government of Nunavut Fisheries and Sealing Division, the Public Safety Geoscience program of Natural Resources Canada (NRCan) and the Ocean Frontier Institute (OFI) through an award from the Canada First Research Excellence Fund.

Thank you all.

CHAPTER 1 INTRODUCTION

1.1 Statement of problem

Fiords are narrow submerged valleys carved by glaciers and flanked by high relief and steep sidewalls. The accumulation of sediments within fiords reflects both subaerial and submarine glacial and post-glacial depositional processes, which are in turn influenced by geological and climatic factors (Syvitski and Shaw, 1995). In this dynamic environment, subaerial and submarine landslides are one of the most active sedimentological processes and may represent a geological hazard for communities and infrastructure (Syvitski et al., 1987). Landslides may occur as a slow movement of rocks and sediments, also called creep, or as a sudden failure of material which is then deposited downslope of the depletion zone (Cruden and Varnes, 1996; Hampton et al., 1996). While active submarine landslides can be monitored using a combination of direct and remote sensing techniques, it is impractical, expensive, and time consuming (Clare et al., 2021). Morphological and sedimentological investigations of past landslides are consequently critical to understand the potential causes of such events and their associated risks (Talling et al. 2014).

Landslides in high-latitude fiords have the potential to damage land-based and seabed infrastructure and threaten coastal communities through the generation of displacement waves (i.e., tsunamis) (e.g., Brothers et al., 2016; Gauthier et al., 2017; Higman et al., 2018). In fact, over the last century, eight of the fourteen largest tsunamis recorded worldwide were caused by landslides in high-latitude fiords (Miller, 1960; Dahl-Jensen et al., 2004; Oppikofer et al., 2009; Gauthier et al., 2017; Higman et al., 2018; Waldmann et al., 2021), with one of the most recent events occurring in 2017, when a fiord flank

collapse generated a tsunami wave that flooded the village of Nuugaatsiaq in Karrat Fiord, Greenland, killing four people and destroying eleven buildings (Gauthier et al., 2017; Paris et al., 2019). In 1934, an estimated three million m^3 of rock and debris fell into Tafjorden, Norway, generating a tsunami with a run-up length of 300 m which killed 23 residents of Tafjord (Oppikofer et al., 2009). One further example is that of the subaerial Paaruut slide on the west coast of Greenland in November 2000, which generated a tsunami with maximum run-up heights of 50 m, destroying boats moored 40 km away in the village of Saqqaq, Greenland (Dahl-Jensen et al., 2004). The high relief topography, recent glaciation, and dynamic sedimentation in the fiords of Baffin Island present similarities to these high-latitude fiords of Alaska, Greenland, and Norway. Although there is no conclusive evidence that a landslide-triggered tsunami has occurred in a Baffin Island fiord, Reverend Edmund Peck documented an unexplained tsunami wave in 1903 along the coast of Blacklead Island, Cumberland Sound (Laugrand et al., 2006). In addition, Gosse et al. (2020) noted the presence of the Inuktut word "Ulinniq" that translates to "rapid inundation of land by seawater" or "rising tide", highlighting the presence of unexplained tsunami-like waves in the past. Clearly a better understanding of the distribution and timing of landslides in the region is required to integrate with these oral and written histories.

Several preconditioning and triggering mechanisms influence slope stability and cause slope failure. In recent years, various studies have proposed that climate change at millennial to centennial time scales may influence landslide generation. Anthropogenic climate warming, which is occurring at an amplified rate in the Canadian Arctic (Previdi et al., 2021), may alter the frequency and cause of landslides in fiords by increasing

precipitation and associated river runoff, frost-wedging, and permafrost thawing (Maslin et al., 2004; Tappin, 2010; McGuire and Maslin, 2013; Pope et al., 2015). However, to what extent climate influences the stability of submarine slopes is still poorly understood (see discussion in Urlaub et al., 2013).

Seafloor mapping initiatives reveal that submarine landslides occur within 86% of the mapped fiords of eastern Baffin Island (Bennett et al., 2021; e.g., Broom et al., 2017; Normandeau et al., 2019a; Brouard and Lajeunesse, 2019; Deering et al., 2019; Normandeau et al., 2021a), however, their timing and causes are generally poorly understood. To better constrain these aspects of submarine landslides within Pangnirtung Fiord, Baffin Island (Nunavut), multibeam echosounder and sub-bottom profiler data, along with gravity cores, and unmanned aerial vehicle (UAV) images were collected in September 2019, aboard the R/V Nuliajuk (Figure 1.1). This study investigates the distribution of submarine landslides, their morphology, and timing to identify the environmental controls that lead to the preconditioning and triggering of submarine landslides. Identifying these environmental controls will test the hypothesis that the distribution of submarine landslides in Pangnirtung Fiord coincide with subaerial physical features (e.g., rivers, and debris fans). The null hypothesis is that submarine landslide distribution is random. An understanding of this relationship may make it possible to predict the location of future submarine landslides. Finally, considerations of how climate may influence the environmental controls addresses how climate change may alter the frequency of landslide generation in a rapidly changing Arctic climate.

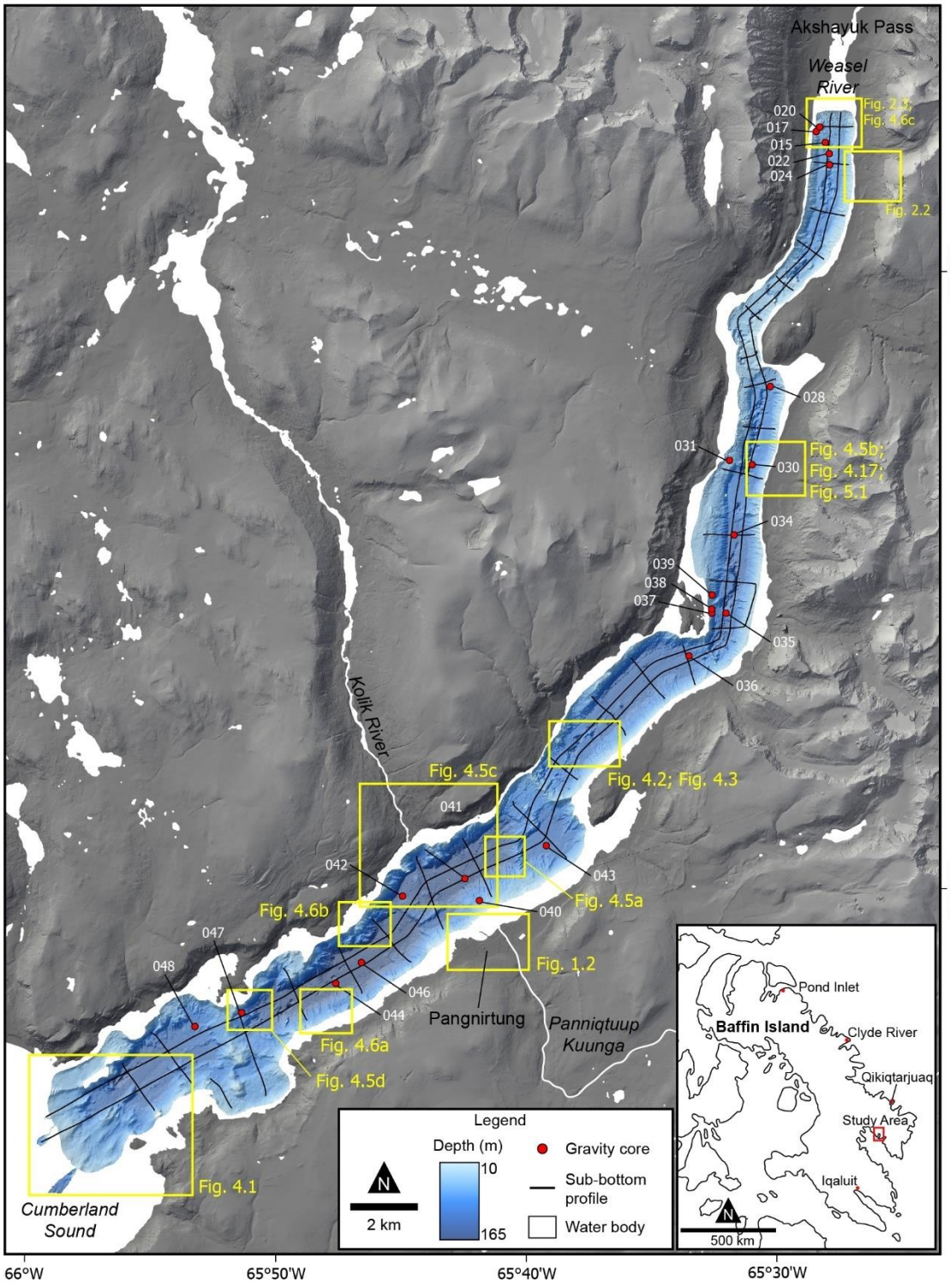

Figure 1.1: Study area: Multibeam bathymetry of Pangnirtung Fiord, Baffin Island, Nunavut, with the locations of gravity-core samples and sub-bottom profiles. Inset is the location of Pangnirtung Fiord. DEM created from DigitalGlobe, Inc. imagery.

An understanding of submarine geohazards in Baffin Island fiords can help increase the public safety for low-lying Arctic communities like the hamlet of Pangnirtung, Nunavut, located along the southeast coast of Pangnirtung Fiord (Figure 1.2). Pangnirtung has the third largest population on Baffin Island (population 1481). Here, all 467 dwellings lie below 60 metres above sea level (m asl) with most structures, including the airport, fuel storage, health centre, and schools, below 30 m asl. Additional infrastructure includes a small craft harbour, a fixed wharf, a breakwater, and proposed submarine telecommunication cables that will provide the community with access to a high-speed internet connection and are critical to the economic development of the community. Furthermore, Pangnirtung is an important hub for the increasing number of visitors to nearby Auyuittuq National Park. This essential infrastructure located in a dynamic fiord environment demonstrates the need to assess the submarine landslide hazard. Similar assessments throughout the fiords of Baffin Island will be imperative with future development and expansion of essential infrastructure in a rapidly changing Arctic climate.

Figure 1.2: a) North view of the hamlet of Pangnirtung (Nunavut). b) Aerial view of the hamlet with key infrastructure labelled. Base map from Maxar Technologies.

1.2 Objectives

The goal of this thesis is to improve the understanding of submarine landslides in the Canadian Arctic. The overall objective of this research is to gain new insight on the factors that affect landslide generation and influence the occurrence of submarine landslide generation in an Arctic Fiord. The specific objectives are to: (1) characterise the morphometric and sedimentological properties of submarine landslides in Pangnirtung Fiord; (2) establish the recurrence of submarine landslides; (3) determine the possible trigger mechanisms of submarine landslides within the study area; (4) identify the relationship of the submarine landslides to subaerial failures along the fiord sidewalls; (5) examine the possible influences of climate change on the timing and triggering of landslides within Pangnirtung Fiord.

CHAPTER 2 BACKGROUND

2.1 Geological and structural setting

Seafloor spreading associated with the rifting of Canada and Greenland in the Late Cretaceous is responsible for the opening of present-day Baffin Bay and Davis Strait (between Baffin Island and Greenland). Rifting resulted in the formation of horst (Cumberland Peninsula) and graben (Cumberland Sound) structures (Dyke et al., 1982). The orientation of tectonic structures throughout the Cumberland Peninsula controls the location of fiords and valleys, including glacial cirques, highlighting a distinct relationship between the structural trends and the geomorphic evolution of the area (Williams, 1972; Dyke et al., 1982). Cumberland Peninsula bedrock consists of two main rock types: Precambrian gneisses of amphibolite and granulite facies in the southeast, and Precambrian granites and quartz monzonites in the northwest (Dyke, 1982). The bedrock surrounding Pangnirtung Fiord is made of three rock types of the Paleoproterozoic Qikiqtarjuaq plutonic suite (ca. 1.88 – 1.9 Ga) (Jackson and Sanborn-Barrie, 2014). The northern portion of the fiord is flanked by two phases of granodiorite-monzogranites whereas the southwest section of the fiord is surrounded by a minor portion of the plutonic suite, a quartz-diorite-tonalite (Jackson and Sanborn-Barrie, 2014).

Seismic activity surrounding Pangnirtung is concentrated in the northern Labrador Sea, Davis Strait, and Baffin Bay, all of which are basins formed through seafloor spreading associated with the rifting of Canada and Greenland in the Upper Cretaceous (Basham et al., 1977; Figure 2.1; Figure 2.2). The northern Labrador Sea seismicity is attributed to differential uplift of either side of Baffin Island caused by a postglacial rebound to the west and minimal rebound along the west coast of Greenland (Basham et al., 1977).

Postglacial rebound is believed to be the cause of intraplate seismic events in Baffin Bay that occur during the reactivation of pre-existing faults from the original Cretaceous rifting (Stein et al., 1979). This rifted margin remains a seismically active region, yet the seismic influence on fiords of Cumberland Sound remains unknown. The largest recorded earthquake (7.3 M_s) in the Baffin Island region occurred in 1933 as a strike-slip intraplate earthquake in north-western Baffin Bay (Bent, 2002).

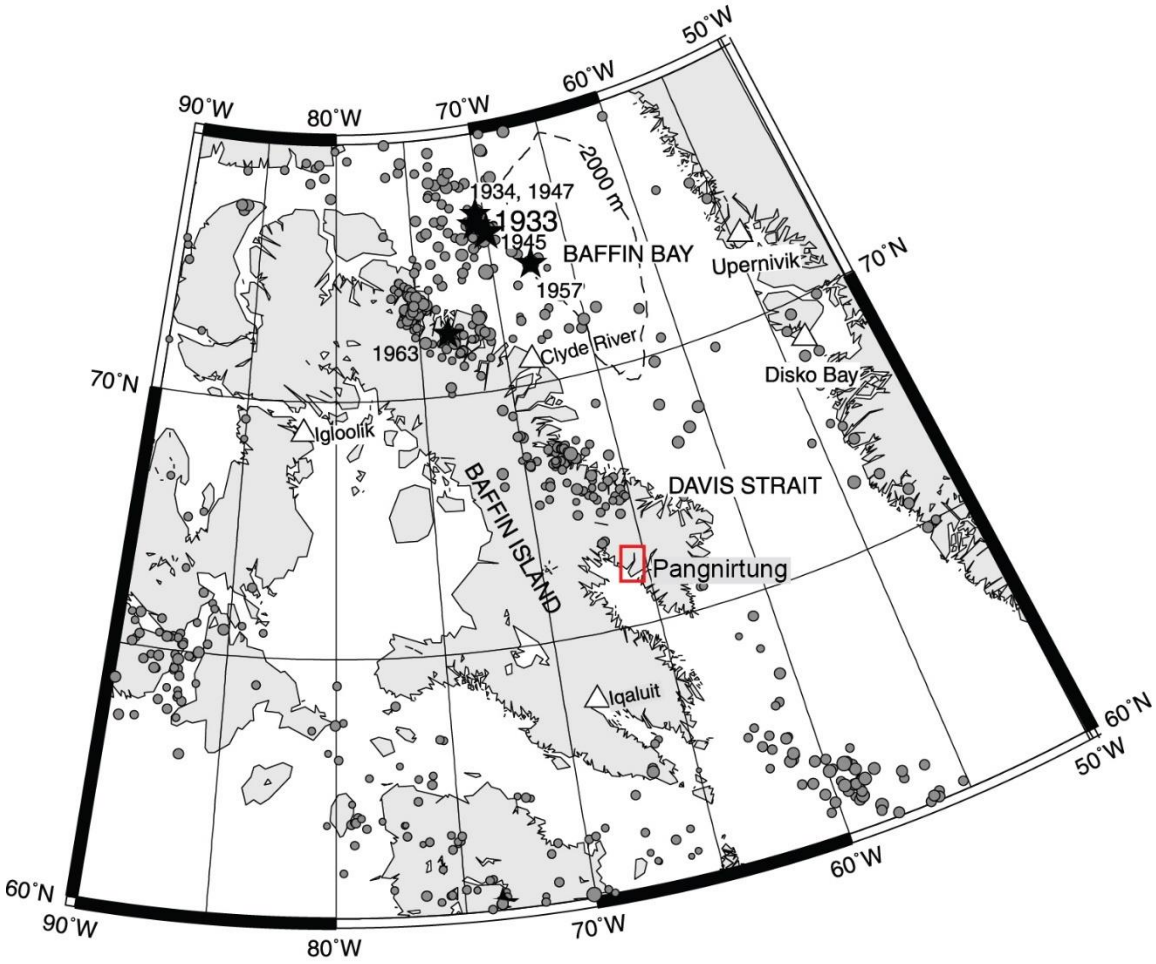

Figure 2.1: Seismicity map of Baffin Island, with highlighted magnitude 5.0 and greater earthquakes that occurred between 1900–1996, magnitudes 4.0–4.9 for 1960–1996, 3.0–3.9 for 1970–1996 and 2.0–2.9 for 1980–1996. Earthquakes with magnitudes greater than 6 are shown as stars and dated. Epicentres are from the Canadian Earthquake Epicentre File (CEEF). Modified from Bent (2002).

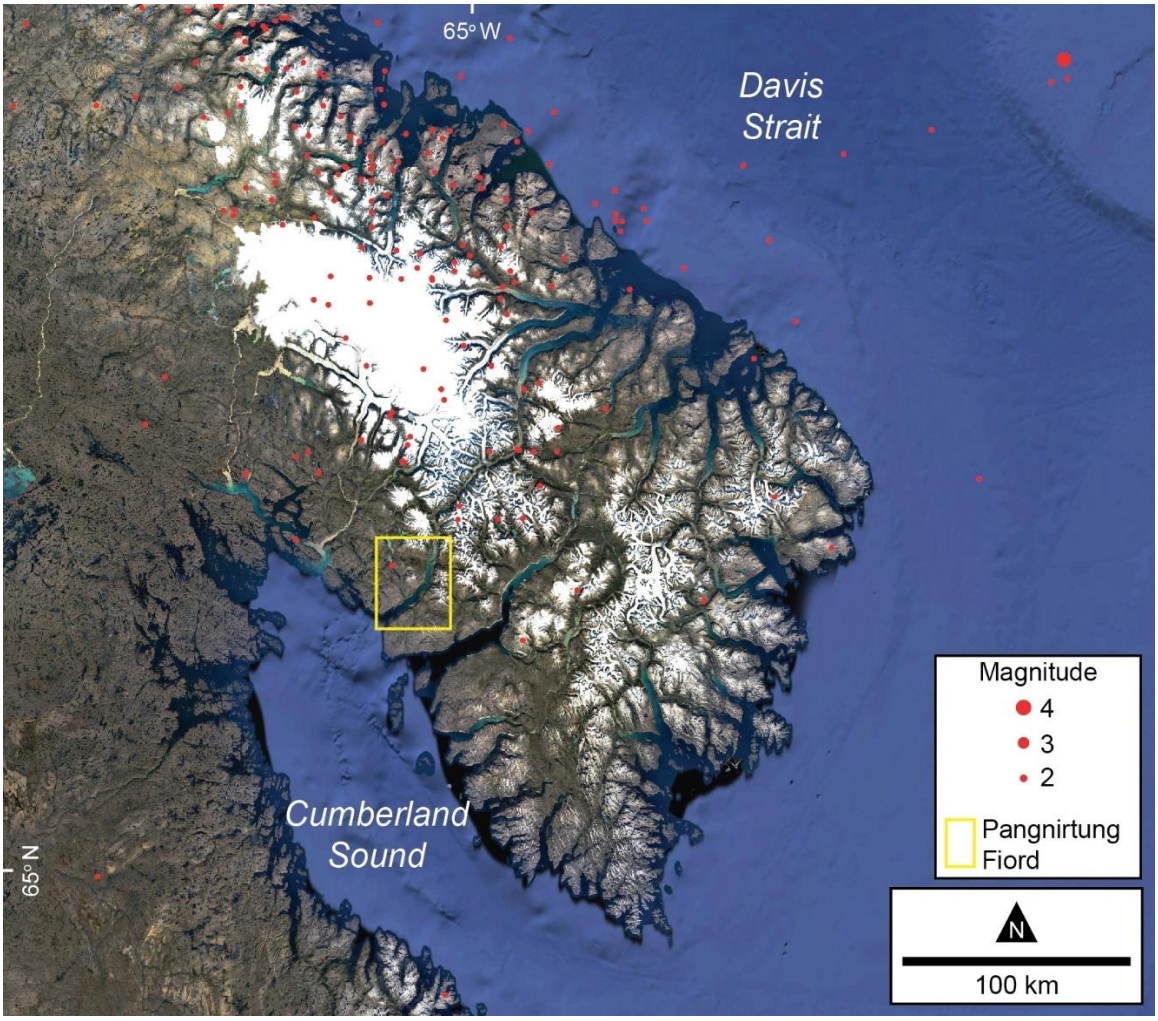

Figure 2.2: Seismicity map surrounding Pangnirtung Fiord. Seismicity data from International Seismological Centre representing data from 1985-2019. Satellite base map from Google Earth, 2021.

2.2 Physiography of Pangnirtung Fiord

Pangnirtung Fiord is located along the southwestern coast of the Cumberland Peninsula, Baffin Island, Nunavut (Canada) (Figure 1.1). The southwest coast is incised by several glacial troughs that connect the highlands of eastern Baffin Island with Cumberland Sound. Pangnirtung Fiord is oriented northeast-southwest with a length of 43 km and a width of 1 to 3 km. The fiord reaches a maximum water depth of 165 m, and the seafloor is divided into four basins by shallow sills, which lie at about 10 m below sea level and were formed during glacial erosion and retreat (Gilbert, 1978). In the southwest portion of the fiord, the surrounding subaerial landscape features low-relief terrain of glacial till overlying bedrock. The northeast section of the fiord is surrounded by high-relief terrain rising to 1500 m asl that is separated by glacial valleys and cirques. Erosion of the steep fiord side walls that surround the coast has produced talus slopes and debris cones that extend to the shallow intertidal zone (Figure 2.3). The tidal range is between 2.7 m and 6.7 m, and the tidal flats, strewn with boulders and cobbles deposited from the talus slopes and debris fans of the fiord sidewalls, extend up to 500 m wide during low tides.

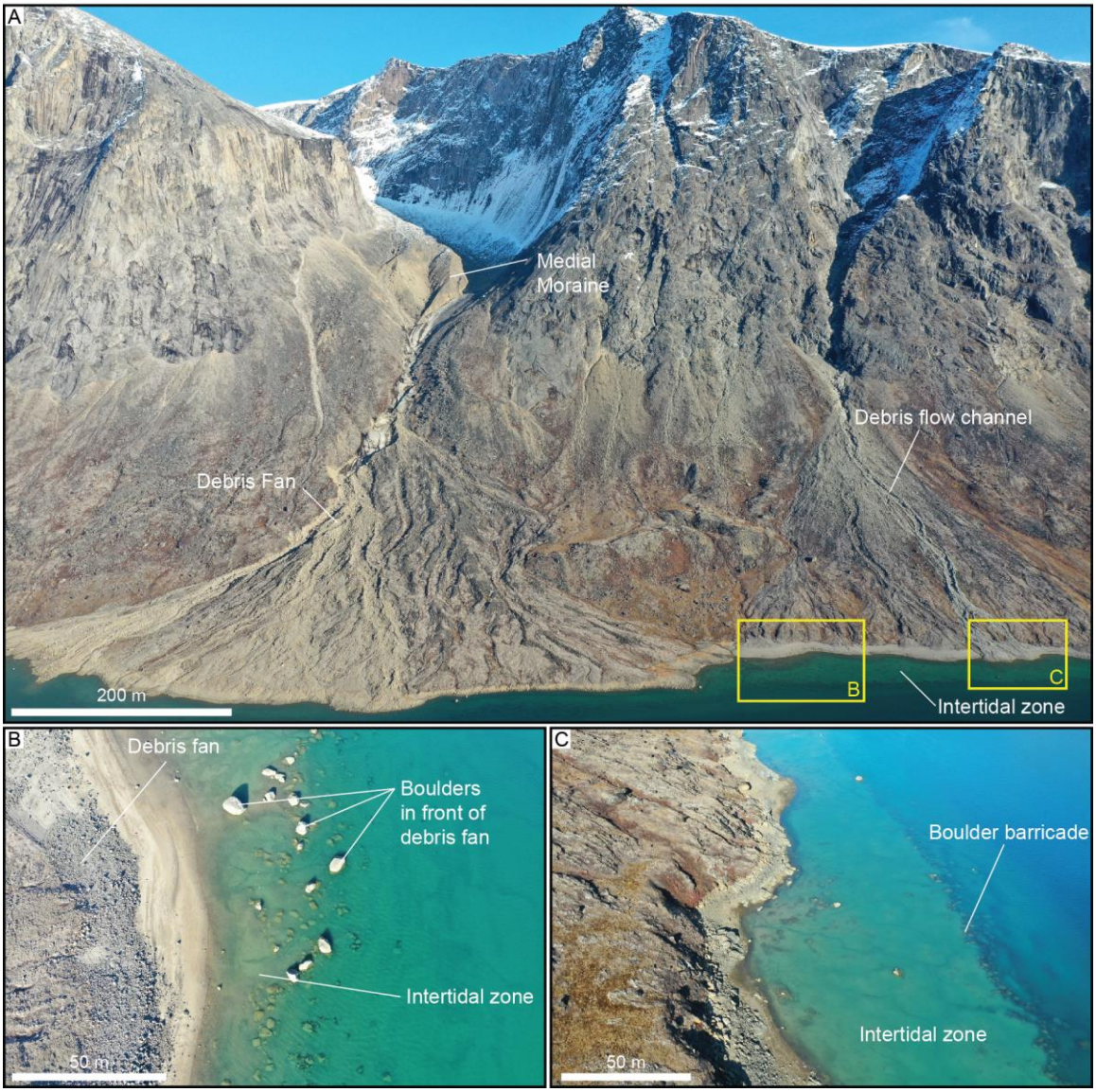

Figure 2.3: a) Debris fans with debris flow channels extending to the intertidal zone b) boulders identified in the intertidal zone in front of a debris fan. c) Boulder barricade identified at the edge of the intertidal zone.

2.3 Modern catchment basins and sedimentation

2.3.1 Sedimentation in Pangnirtung Fiord

Fiords are the deepest nearshore environments accumulating thick sequences of sediments from significant erosion of the surrounding high relief landscapes. In the case

of Pangnirtung Fiord, the partially glaciated drainage basin surrounding the fiord covers 1700 km^2, generating multiple sources of sediment from the surrounding environment (Gilbert, 1978).

Gilbert (1978) determined that large drop stones (Bennett et al., 1996) are not a large component of the Pangnirtung Fiord sedimentation, however they postulated that ice-rafted sediments may account for the silt, sand and pebbles found within hemipelagic sediments of deep fiord basins. These ice-rafted sediments originate from multiple processes recorded in the fiord. Gilbert (1978) recorded reports of Pangnirtung residents witnessing wind-blown sediments depositing onto the sea-ice, while Aitken (1982) recorded instances where wave transported sediment was deposited on top of the sea-ice. Finally, the incorporation of sediments into the sea-ice along the intertidal flats also results in transportation of coarse-grained sediments to the deep basins upon ice melt.

Sediments originating from inflowing fluvial sources are both deposited near the river mouths, developing deltas, and settling out of suspension. The suspended sediment is circulated throughout the fiord rapidly due to the large tidal range generating significant circulation of the entire water mass in the fiord (Gilbert, 1978). Although there is evidence of significant water mass circulation, seafloor sediment grain size analysis shows a coarser grain size closer to the mouth of the fiord (Gilbert, 1978). The proposed driver of this peculiar sediment dispersion is the large tidal range removing the suspended fine-grained sediments into Cumberland Sound, preventing deposition of suspended sediment near the mouth (Gilbert, 1978).

Finally, there is deposition of sediment originating from subaerial and submarine gravity-driven slope processes, including turbidity currents, debris flows, slumps, and subaerial landslides that extend to the water along talus and debris fans (Gilbert, 1982). These landslides were identified by Gilbert (1978) using echo-sounder profiles in which they were able to identify depletion zones along the side slopes from the sudden change in slope and landslide deposits from the undulating surfaces along the base of the fiord. Mass transport deposits are also identifiable in Huntec deep-towed high resolution seismic collected from the CSS Hudson 85-027 research cruise in September and October of 1985 (Figure 2.4). The seismic profile was positioned from the mouth of the fiord down the centre of the fiord and ended approximately 10 km past the Hamlet of Pangnirtung. They also collected two piston cores in the centre of one of the basins of the fiord.

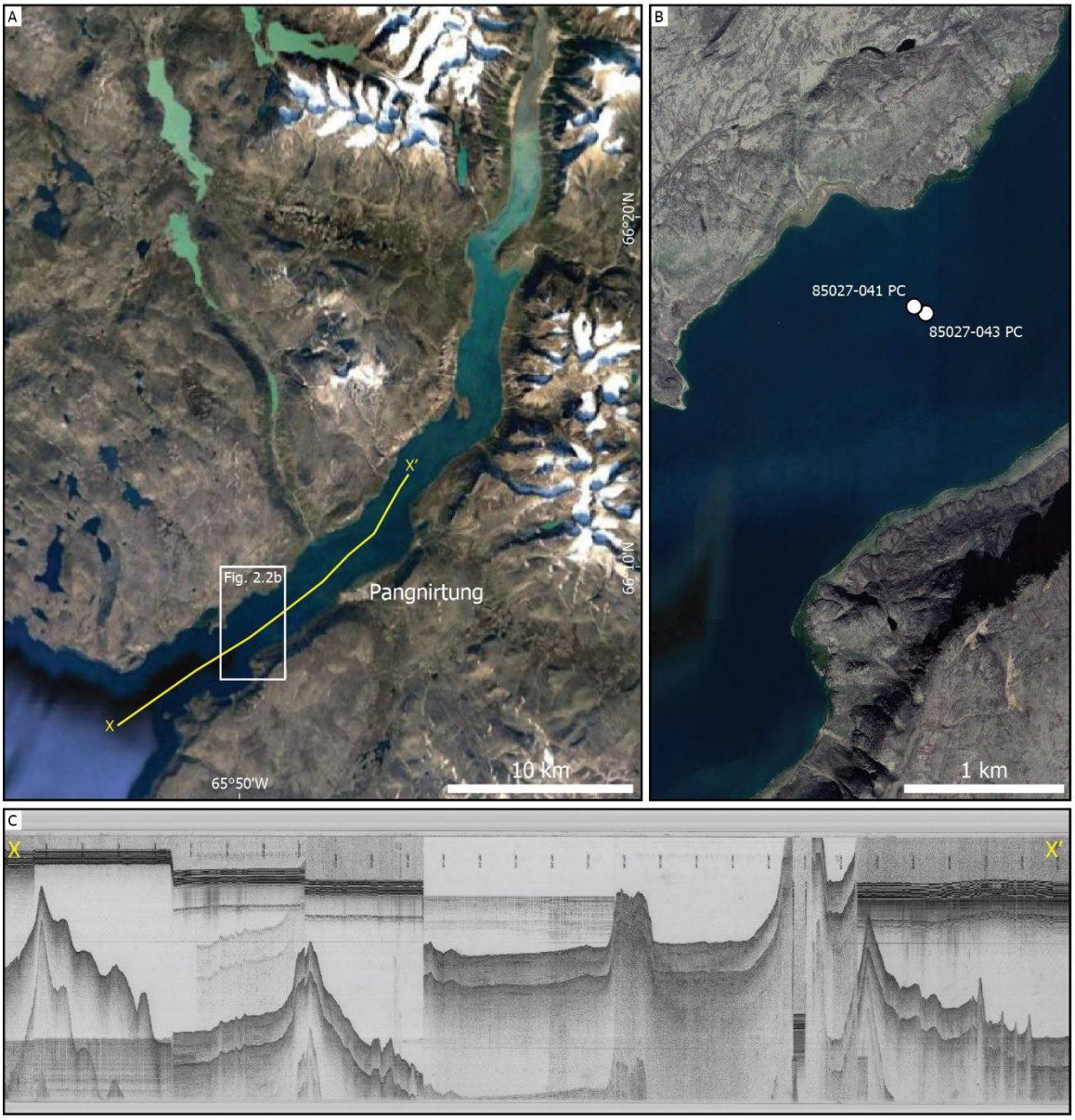

Figure 2.4: Overview of the Geological Survey of Canada cruise 85-027 data collection in Pangnirtung Fiord. A) Map of Pangnirtung Fiord with seismic reflection trace overlain. B) Location of piston cores 85027-41 and 85027-43. C) Seismic reflection profile 85027_H_279_1108 collected on 06/10/1985 in Pangnirtung Fiord. Sourced from NRCan Expedition Database (URL: https://ed.gdr.nrcan.gc.ca/).

2.3.2 Rivers

Pangnirtung Fiord is fed by numerous ephemeral streams and two main rivers: the Weasel River at the head of the fiord and the Kolik River across the fiord from the hamlet of Pangnirtung (Figure 1.1) which drain 67% of the catchment area (Gilbert, 1978). Other rivers include the Panniqtuup Kuunga (commonly referred as the Duval River in literature), which flows through the Hamlet of Pangnirtung, and the Puurusiq River, located to the northeast of the fiord.

The Weasel River is the largest river flowing into the fiord and transports sediment from a partially glaciated catchment basin and through Akshayuk Pass, formerly Pangnirtung Pass, creating an outwash plain before flowing into the head of the fiord, creating a fiord-head delta (Figure 2.5). Although flow rate measurements are sparse, the winter months generally see little to no flow. However, Gilbert and McKenna Neuman (1988) documented periods of warming (>0ºC) in Pangnirtung Fiord through the winter months in which melting of the uppermost layers of the snowpack, paired with the high relief and a frozen permafrost active layer in the winter can contribute to increased river runoff. Snowmelt and precipitation in the summer months lead to high and sporadic flow levels (Water Survey of Canada, 1983); the flow of the Weasel River reaches ~3 m^3/s in mid-June and more than 70 m^3/s in late July (Water Survey of Canada, 1977). During high flow and flooding periods, sediment loads have been measured at excess of 2 g/L (Gilbert, 1978). The Weasel River delta is not only a source of coarse-grained material at the head of the fiord, but residents report windblown sediment from the Pangnirtung Pass in the winter that may be incorporated into sea-ice and deposited throughout the fiord

upon sea-ice melt (Gilbert, 1978). The Puurusiq River has a similar discharge to the Weasel River, although it drains a third of the area (Gilbert, 1978).

Figure 2.5: Composite image of multibeam bathymetry overlain on a UAV photograph of the fiord-head Weasel River delta. Debris fans extending to the intertidal zone, sediment waves and sediment channels are identified.

The Kolik River flows into the fiord from the northwest through narrow valleys and forms a ~0.13 km^2 delta directly across from the Hamlet of Pangnirtung (Figure 1.2). The Kolik's outflow is estimated to be the same as the Weasel River (Gilbert, 1978). In contrast to the large catchment area of the Weasel River and the wide Pangnirtung Pass through which it flows, the Kolik River system is made up of a series of narrow valleys and glacially fed lakes that may trap sediment while moraines and plateaus also form barriers to flow.

The river called Panniqtuup Kuunga runs directly through the hamlet and flooded most recently in 2008 washing out the bridge and splitting the community for several days (Spinney and Pennesi, 2013). This flooding was caused by increased snow melt and runoff due to warm temperatures and rain in the region. The Panniqtuup Kuunga has an Arctic nival flow regime with peak flow in late June and early July of 25 m^3/s (Water Survey of Canada, 1983). The river flow decreases after this period except for high flows caused by high levels of precipitation. Even during flooding, the sediment discharge (<10 mg/L) is minor compared to the Weasel River, as the river flows over exposed bedrock (Gilbert, 1978).

2.3.3 Intertidal zone

The accumulation of an elongate ridge of boulders along the low-tide level of the intertidal zone represents a boulder barricade (Rosen, 1979; Dionne, 2002) (Figure 2.3) and indicates modern sea-level stability in the fiord (McCann, 1981; Cowan et al., 2021). These boulder barricades are formed by sea-ice rafting and transport of boulders (<0.5 m to >3.5 m), during sea-ice break-up of the intertidal ice, to the edge of persistent sea-ice (low-tide level) (Rosen, 1979; Forbes and Taylor, 1994). Aitken (1982) documents this process in Pangnirtung Fiord, showing the incorporation of sediment and boulders (>2 m) into the base of the sea ice within the intertidal zone. These sediment ice-rafting processes deposit sediment and boulders at the edge of the intertidal zone and throughout the fiord upon ice melt.

An 11.4 m percussion-drill core from the intertidal flat, located in-front of the hamlet of Pangnirtung, was obtained in 1984 (Aitken and Gilbert, 1989). This study revealed that

the upper 4 m of the intertidal zone is made up of intertidal flat deposits, closely resembling present day sediment accumulation. The remaining core sediments are interpreted as shoreface sediments. Two hammer seismic profiles of the intertidal zone in-front of the hamlet obtained in 1982 show that there is a bedrock ridge at 20-30 m depth at the mid-way point of the present-day tidal flat and that closer to the seaward edge of the intertidal flat, sediment accumulation exceeds 20 m in thickness (Aitken and Gilbert, 1989).

2.3.4 Modern climate

Between 1984 and 2014, the Canadian Arctic warmed by 1.6ºC, twice the global average over the same period, and has resulted in a loss of sea-ice, a reduction in the volume of glaciers, permafrost degradation, an increase in river runoff, and an increase in rain precipitation (Peterson et al., 2002; Zhang et al., 2006; Arctic Council 2016; Comiso et al., 2017; Noel et al., 2018). Galappaththi et al. (2019) documented qualitative examples of climate change in Pangnirtung through interviews with fishers who work in the area. The fishers spoke about these same climate change effects, with a relative consensus on sea-ice conditions changing drastically and warmer weather occurring earlier in the year and throughout winter.

Within Pangnirtung Fiord, high relief develops steep gradients in both temperature and precipitation. In the lowlands, this area sees an average of 400 mm of precipitation annually with 55-60% falling as snow. In the highlands of this area, there is an average of 500 mm of precipitation annually, with 80% being snowfall. In the winter (Mid-September to Mid-June) the temperature reaches -50ºC with windchill, and an average of

-25ºC. In the summer, the temperature averages between 5-15ºC (Maxwell, 1981). From 1996 to 2009, Environment Canada data reveal a warmer annual air temperature than pre-1990s and an increase in rain precipitation (Environment Canada, 2009). In fact, during the same period, 54% of the annual precipitation fell during the summer months, up from 44% pre-1990s.

2.4 Wisconsin glaciation and relative sea level in Pangnirtung Fiord

2.4.1 Wisconsin glaciation in Pangnirtung Fiord

In the late Wisconsin (ca. 25 – 11 ka), the Penny Ice Cap, presently situated north of Pangnirtung Fiord, merged with the northern expansion of the Laurentide Ice Sheet, and extended to the mouth of Cumberland Sound (Figure 2.6) (Marsella et al., 2000; Dyke et al., 2002; Margreth et al., 2017). The highlands of the Cumberland Peninsula have seen glacial advance and retreat throughout the Quaternary; however, studies suggest that limited erosion occurred during the glaciated periods due to cold-based ice (Bierman et al., 1999; Marsella et al., 2000; Margreth et al., 2016). During interglacial periods, these higher elevation landscapes were eroded by pro-glacial outwash and weathering. Branches of glaciers scoured the lower elevation areas of the landscape (Kaplan et al., 1999). Erratics at lower elevations were determined to have multiple ages of exposure which indicates several glacial and interglacial cycles (Marsella et al, 2000). These multiple glacial cycles have produced the glacial landforms seen in Pangnirtung Fiord.

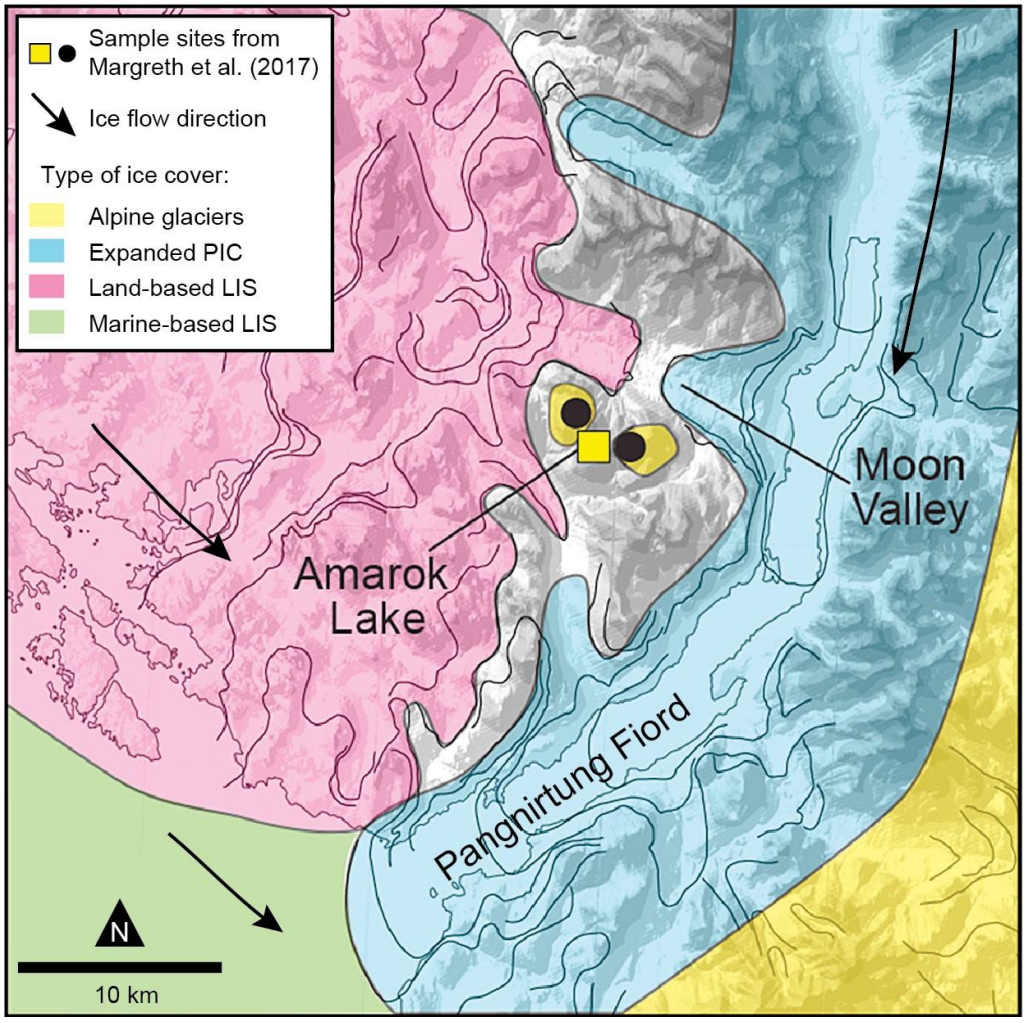

Figure 2.6: General location and the direction of ice flow during the most extensive glacier cover. The land-based Laurentide Ice Sheet (LIS) (pink shading), marine-based Laurentide Ice Sheet (LIS) (green shading), Penny Ice Cap (PIC) (blue shading), and alpine glaciers (yellow shading) were all present near Pangnirtung Fiord. Modified from Margreth et al. (2017).

Cosmogenic nuclide dating indicates that glacier retreat in Pangnirtung Fiord occurred at ca. 11 ka (Marsella et al., 2000; Corbett et al., 2016). In the Kolik River valley, dated ice-contact deltas formed in proglacial lakes suggest that the valley contained ice until ca. 11 ka (Marsella et al., 2000) and moraine emplacement ages of 10.1 ± 1.5 ka on the eastern side of the fiord reveal supporting evidence that glaciers began to retreat after these moraines were deposited (Marsella et al., 2000). Cosmogenic nuclide dating by Davis et

al. (1999) and Marsella (1998) indicates a complete deglaciation of Pangnirtung Fiord by ca. 7.5 ka. Margreth et al. (2017) found that the Penny Ice Cap lobe retreated at a rate of approximately 25 m/year, suggesting a slightly slower retreat rate than that of Corbett et al. (2016), who suggested the lobe retreated 75 km in a matter of hundreds to at most a thousand years. The remaining cirque and alpine glaciers make up ~ 25% of Pangnirtung Fiord's catchment area (Gilbert, 1978).

2.4.2 Relative sea level in Pangnirtung Fiord

Dyke (1979) used marine limits from the Last Glacial Maximum (LGM) mapped throughout various fiords to deduce the relative sea level (RSL) curves of Cumberland Peninsula (Figure 2.7). Radiocarbon dating of these marine limit features provided the basis for Holocene RSL curve reconstruction. The various fiords have differing RSL curves caused by differences in the rate of isostatic rebound, however, most show an intersection with present day sea level, deduced from the presence of submerged deltas along eastern Cumberland Peninsula (Miller and Dyke, 1974; Miller, 1975). Cowan et al. (2021) presented differing RSL curves for Cumberland Peninsula that were developed through glacial-isostatic modelling (Figure 2.8).

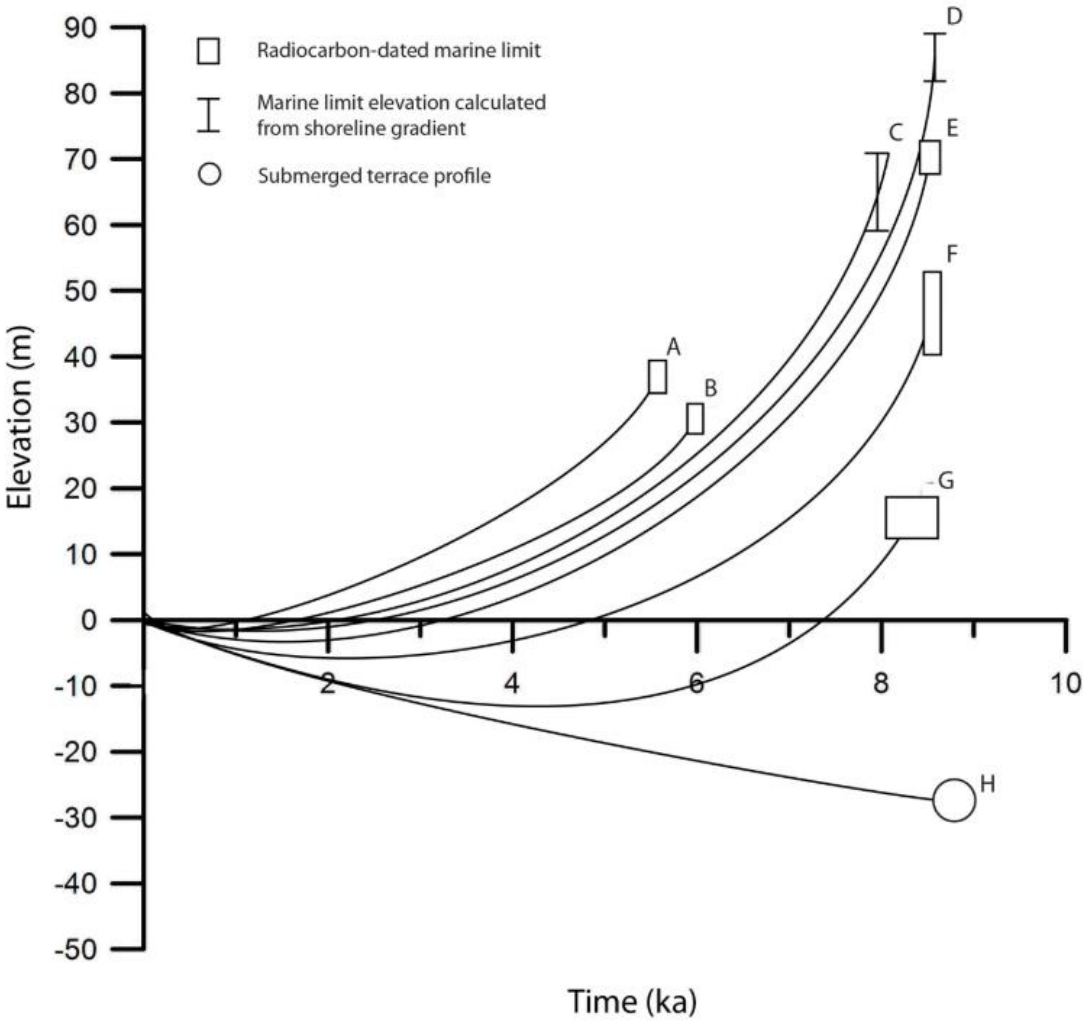

Figure 2.7: Marine limit elevations plotted against known or extrapolated ages and/or schematic RSL curves for southwestern Cumberland Peninsula and the submerged delta in Padle Fiord. Modified after Dyke (1979), with newly calibrated radiocarbon ages for marine limits (Table 2). See Fig. 1B for locations of sites: (A) Clearwater Fiord, (B) Middle Clearwater Fiord, (C) Shilmilik Bay, (D) Kangerk Fiord, (E) Usualuk Fiord, (F) Pangnirtung Fiord, (G) Kingnait Fiord, (H) Padle Fiord. Figure and caption sourced from Cowan et al. (2021); modified from Dyke (1979).

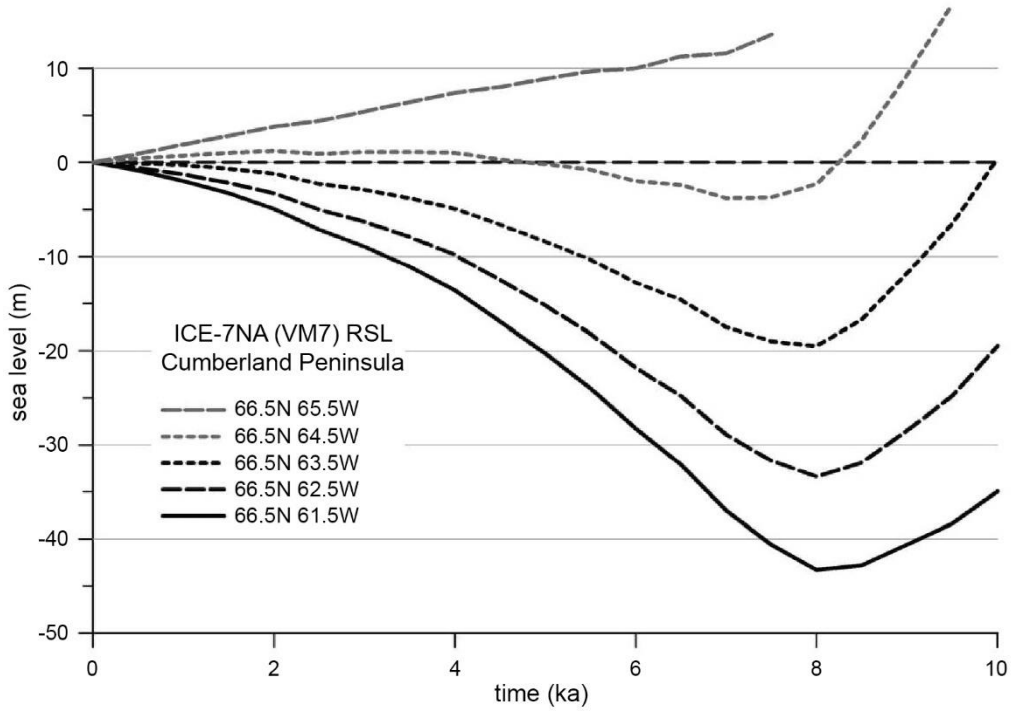

Figure 2.8: Simulated RSL histories for Cumberland Peninsula from Pangnirtung Fiord (65.5°W) to the mouth of Sunneshine Fiord (61.5°W) as output from the ICE-7G_NA (VM7) model (Peltier 2020). Figure and caption from Cowan et al. (2021).

In Pangnirtung Fiord (Figure 6, curve f), raised marine beach and deltaic sediments are documented at ~ 50 m asl on either side of the fiord (Gilbert, 1978; Dyke et al., 1979). Further work by Aitken and Gilbert (1989) found that these raised beach and deltaic sediments, from ca. 8.7 to 5.8 ka, unconformably overlie a shoreline facies, recording a Holocene marine regression from the marine limit. A lower RSL of about 10 metres through the mid-late Holocene is also confirmed by Aitken and Gilbert (1989), as they found that the intertidal deposits overlie buried shoreface deposits dated to 5830 ± 140 BP. They also propose that as sea-level dropped, the 10 m deep notch seen today along the southern edge of the sill at the mouth of the fiord was carved, representing a maximum drop in RSL of 10 m bsl.

2.4.3 Glacial landforms

Gilbert (1978) and Hughes Clarke et al. (2015) were able to survey Pangnirtung Fiord and identify glacial landforms, but were limited by time, in the case of Hughes Clarke et al. (2015), and rudimentary technology (Gilbert, 1978). Both surveys were able to identify irregularly shaped sills formed of bedrock and sills representing glacial moraines. The mouth of the fiord has a large sill interpreted as a terminal moraine, possibly emplaced in the Late Pleistocene (11.7-126 kya) approximately coeval with the Duval moraines found within the Duval River valley, east of Pangnirtung (Dyke, 1979).

2.5 Submarine landslides

Submarine landslides represent the underwater downslope movement of unlithified sediment and rock following failure along one or more surfaces (Eckel, 1958; Schuster, 1978). Equivalent terms used throughout the literature refer to the same processes, and involve the use of “marine”, “underwater”, “subaqueous”, or “submarine” combined with “landslide”, “slide”, “mass movement”, or “slope failure”. When a submarine slope fails, a mass of sediment and/or rock may slide downslope in cohesive blocks, however, as the landslide travels farther away from the failure scarp, the mass involved becomes less cohesive, and a dense sediment flow develops due to the progressive entrainment of water, potentially generating a turbidity current (Masson et al., 2006).

The two distinct elements that form submarine landslides are a rupture surface and a displaced mass (Figure 2.9). The rupture surface represents the plane on which the slope fails, and the head scarp marks the initial failure location (Hampton et al., 1996). Successive scarps can form along the sides of the depletion zone and further downslope

from the head scarp. The morphology of the rupture surface defines the initial failure type (Figure 2.9). A planar surface with translational movement of the displaced mass results in a “translational slide”. A curved surface results in a “rotational slide” and causes the failed material to slump. A “retrogressive slide” occurs when a rupture surface migrates progressively upslope (Hampton et al., 1996). The displaced mass represents the sediment or rock transported downslope. The area of the landslide closest to the head scarp is the head of the slide, whereas the most basinward portion of the landslide deposit represents the toe (Figure 2.9). Unsorted debris avalanches that have limited lateral constraints are identified as a submarine landsliding process. Debris flows forming in a confined depletion zone travel further distances than debris avalanche because of reduced grain-to-grain friction (Hampton et al., 1996; Tappin, 2010). If a landslide can entrain enough water during its downslope movement, it can develop into a turbidity current, which deposits a turbidite over a larger area, often indistinguishable on bathymetric data due to the minor relief produced (Figure 2.10). These submarine landslide processes have been identified globally with the most prevalent environments being deltas, submarine canyons, the open continental slope, oceanic volcanic islands, and fiords (Masson et al., 2006; Scarselli, 2020).

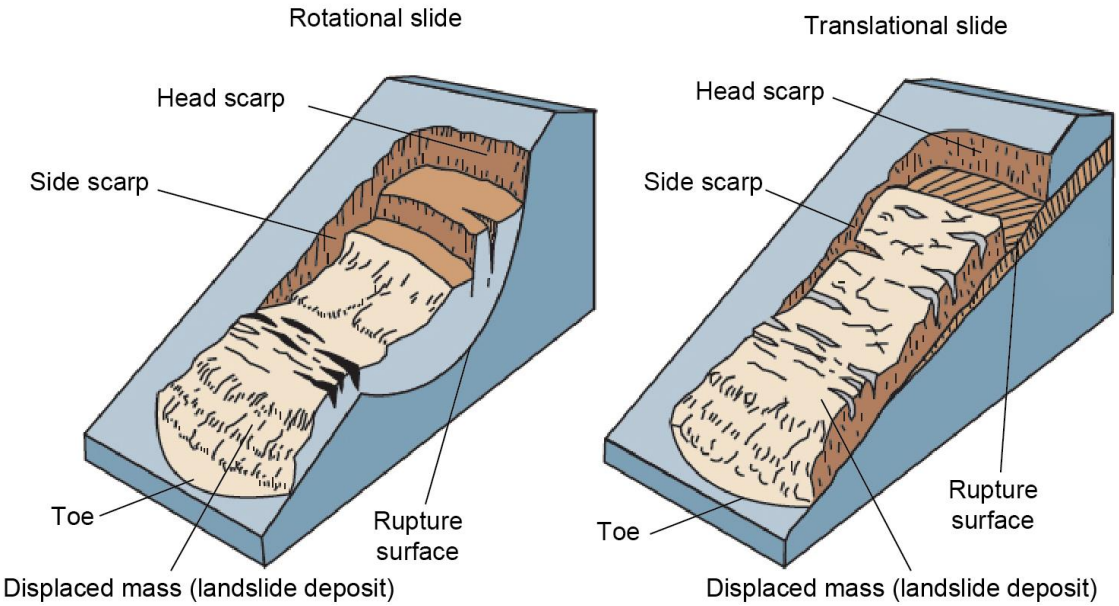

Figure 2.9: Conceptual diagram of a rotational landslide (left) and a translational landslide (right). Modified from Varnes (1978).

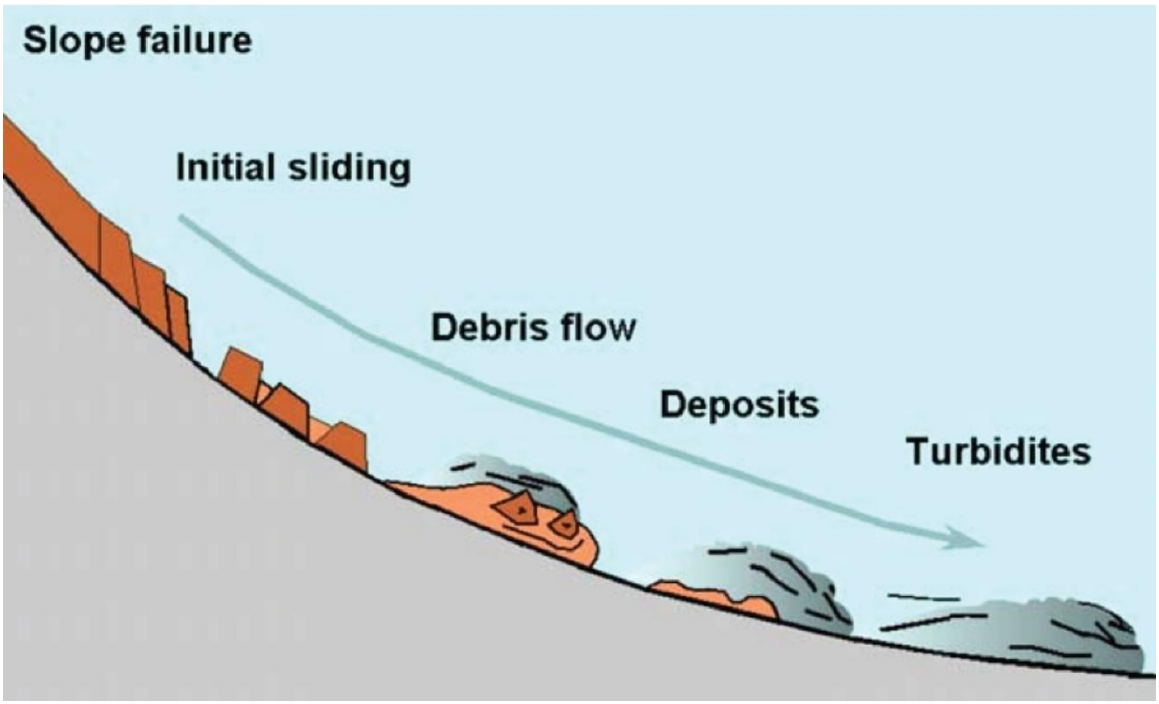

Figure 2.10: Schematic representation of the different stages of a landslide from slope failure to turbidite deposition. From Bryn et al. (2005).

Generally, submarine landslides are caused when the downslope forces acting on the sediment column exceed the sediment strength (Masson et al., 2006). The preconditioning factors influence the sediment properties and stability based on depositional and post-depositional alterations that can generate overpressure in shallow marine sediments as the amount of stress on the pore fluid between sediment grains increases (Clare et al., 2016). Examples of preconditioning of sediments include high sedimentation rates, weak sediment layers and gas-charged sediment (Bellwald et al., 2016). In fiords, variations in sedimentation rates and the supply of coarse-grained sediment from rivers, glaciers and the steep subaerial slopes create weak layers that can result in submarine landslides displacing large volumes of sediment (Canals et al., 2004; Tappin, 2010). The deposition of coarse-grained sediments, in contrast to the clay and silt accumulating from hemipelagic sedimentation, introduces permeability and shear strength contrasts through the sub-sea stratigraphy. These variabilities in lithological properties can cause increases in pore pressures, thereby developing weak layers (Gatter et al., 2021; e.g., L'Heureux et al., 2012). Gas-charged sediment results from the degradation of organic matter that is deposited within the sediment. High amounts of organic matter deposition may result in an accumulation of gas within the pore space of sediment and in doing so, destabilise the sediment (Talling et al., 2014).

An increase in shear stress or the further development of overpressure in the pore fluid between sediment grains can then provide the necessary triggering mechanism for slope failure (Tappin, 2010; Urlaub et al., 2013; Clare et al., 2016). Numerous processes can trigger submarine landslides, including earthquakes caused by tectonic plate movement (Kuenen, 1952) and isostatic adjustment (Brooks et al., 2016), wave action (Bea et al.,

1983; Prior et al., 1989), iceberg or sea-ice groundings (Normandeau et al., 2021a), tides (Johns et al., 1985; Chillarige et al., 1997) and increased river discharge which may promote rapid sediment accumulation and oversteepening of river delta fronts (Prior and Bornhold, 1989; Bornhold et al., 1994; Girardclos et al., 2007; Clare et al., 2016). Submarine landslides can also be triggered when a subaerial landslide extends to the water, destabilizing the seabed in shallow water. Subaerial landslides can be triggered by multiple processes, including permafrost thawing, increased precipitation, and frost-wedging (Gauthier et al., 2017; Higman et al., 2018).

CHAPTER 3 MATERIALS AND METHODS

This chapter provides a summary of the datasets used in this project, including details on how the data were acquired and processed, and the techniques and methods used to interpret them. This study used multibeam bathymetric data, sub-bottom profiler data, sediment gravity cores, and unmanned aerial vehicle (UAV) photos that were collected in Pangnirtung Fiord in September 2019 onboard the RV Nuliajuk during the 2019NULIAJUK research cruise (Normandeau et al., 2019b).

3.1 Multibeam bathymetric data

High-resolution multibeam bathymetric data were collected using a Kongsberg EM2040C in 10-164 metres of water depth (Figure 1.1). The EM2040C is a single head, hull-mounted system operated at 300 kHz, with 400 beams that were set equidistant from each other. This configuration provided a maximum swath angle of 120º, however, the total swath angle was often adjusted to less than 100º when mapping in water depths greater than 50 metres to reduce noise in the outer beams and artifacts in the dataset. During data acquisition, sound velocity variations in the water column were corrected directly through the Kongsberg Seafloor Information System (SIS) using sound velocity measurements from a Conductivity-Temperature-Depth (CTD) profiler. One to three CTD casts were taken each day using a Xchange CTD from AML Oceanographic to ensure survey accuracy. The multibeam bathymetric data were processed using Teledyne Caris HIPS and SIPS 10.4 software to correct for tide elevation and vessel movement (roll, pitch, heave, and yaw) during acquisition. The predicted tide elevations (Fisheries and Oceans Canada, 2019) and the vessel's movement, recorded from an Applanix

Marine-Vessel Position and Orientation System located near the ship's centre of gravity, were merged with the dataset. The final processing step involved significant manual cleaning of artifacts in the dataset that were a product of the concurrent acquisition of multibeam bathymetric and sub-bottom profiler data. The data were then gridded to 5 x 5 m horizontal resolution and exported to ESRI ArcGIS Pro 2.5 to create shaded relief maps intended for seafloor morphological interpretation.

3.2 Sub-bottom profiler data

Nine hundred and twenty-five kilometres of sub-bottom profiles were acquired, concurrently with multibeam bathymetry data, using a hull-mounted Knudsen 3260 3.5 kHz sub-bottom profiler collection. In addition, a grid of two profiles along the length of the fiord and 26 profiles perpendicular to the fiord's sidewalls, were collected following the complete mapping of the fiord (Figure 1.1). The maximum theoretical vertical resolution of the sub-bottom profiles is 11 cm, defined as a quarter of the wavelength (Knapp, 1990). The wavelength (λ) of the 3.5 kHz frequency system can be calculated using the average sound velocity in water (1500 m/s):

$$\lambda = \frac{\text{velocity}}{\text{frequency}} = \frac{1500 \text{ m/s}}{3500 \text{ Hz}} = 0.43 \text{ m} \qquad \text{Vertical resolution} = \frac{\lambda}{4} = \frac{0.43 \text{ m}}{4} = 11 \text{ cm}$$

The sub-bottom data were visualized and interpreted using SegyJp2Viewer developed by the GSC (Courtney, 2009). Low quality sub-bottom profile data makes interpretation difficult. A higher speed during acquisition may be a contributing factor as the grid of sub-bottom profiles was completed at a slower speed and without simultaneous multibeam echosounder acquisition, which resulted in slightly better quality. However,

the sub-bottom profile data are limited in their use for extensive sub-surface interpretation.

3.3 Morphological characterization of submarine landslide deposits

Submarine landslides were identified using ESRI ArcGIS Pro 2.5 and their surface extents were measured. The landslide deposit boundaries were identified in the bathymetry by their lobate shape and irregular surface topography (Mountjoy and Micallef, 2018). Head scarps and depletion zones were identified where possible; however, in instances where the head scarp is unidentifiable due to limited bathymetric coverage, the landslide's outline terminates at the edge of the mapped area. Where possible, landslides were also identified in the sub-bottom profiles based on the geometry, and amplitude of the reflections (Sangree and Widmier, 1979; DeMarco et al., 2017; Le Bouteiller et al., 2019). The geophysical datasets were used to measure the morphometric parameters of the submarine landslides following the standardised procedure outlined in Clare et al. (2019) (Figure 3.1; Table 3.1). The morphometric parameters were used to characterise the landslide deposits and investigate potential relationships between their extent, source area, and cause of the landslide. In this study, thirteen measured parameters and one calculated parameter were extracted from the geophysical imaging dataset**.**

Table 3.1: Descriptions of morphometric parameters used in this study.

Measured Parameters		Description
Area (km^2)	A	The total extent of the landslide deposit and associated scar and flow path.
Deposit length (m)	L_d	The total length of the landslide deposit that bisects the deposit. This is not necessarily a straight-line measurement.
Maximum deposit width (m)	W_d	The maximum width of the deposit measured perpendicular to the maximum deposit length.
Water depth minimum (m)	D_w	The minimum water depth of the mapped slope failure and associated deposit seen on bathymetric data.
Total length (m)	L_t	The total length of the landslide from the upper limit of the head scarp to the downslope extent of the landslide deposit.
Scar width (m)	W_s	The maximum width of the scar.
Slope gradient (º)	S	The measured slope of an adjacent slope outside of the slope failure scar and deposit.
Slope gradient at toe (º)	S_t	The slope of the seabed directly in front of the toe of the deposit.
Calculated Parameters		
Elongation	E	The ratio of the total length to the maximum width of the deposit. Dimensionless. A value less than 1 represents a longer width than length, and a value greater than 1, represents a longer length than width.

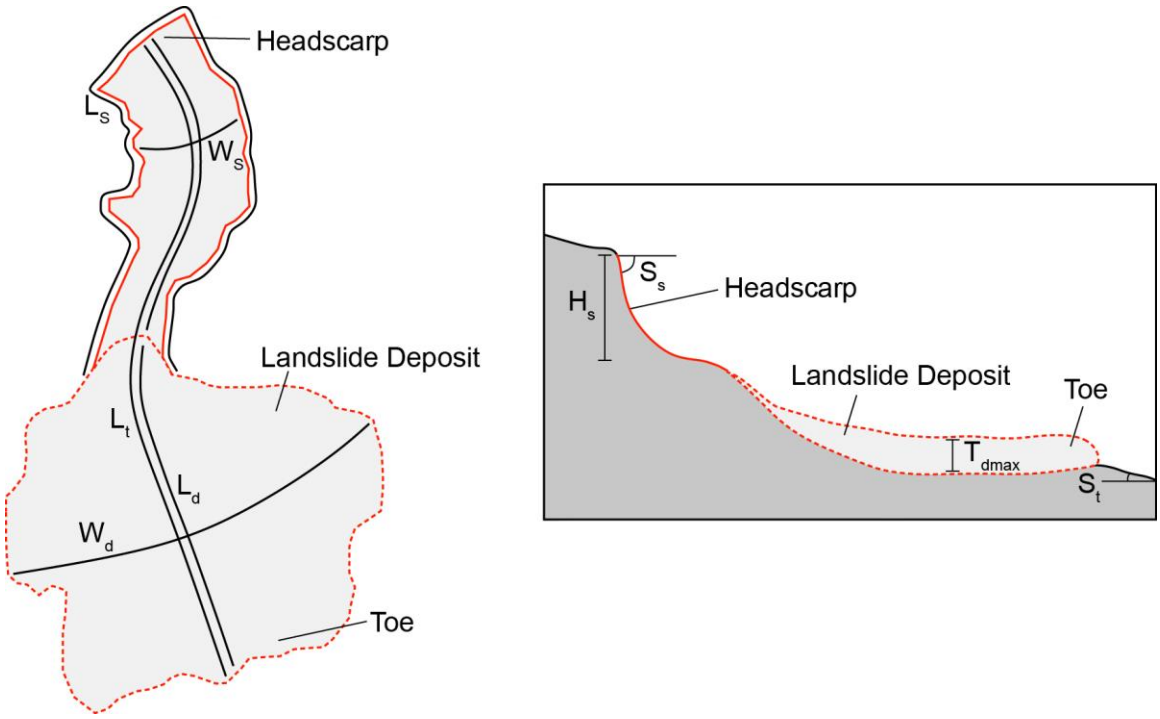

Figure 3.1: Plan view and profile of the morphometric parameters of submarine slope failures and associated deposits. Modified from Clare et al. (2019).

3.4 Surface roughness

The standard deviation (SD) of the bathymetric position index (BPI) was used to calculate the surface roughness for the delineated landslides using ArcGIS Pro 2.5. The BPI is a measurement of the relative position of a pixel compared to the surrounding neighbourhood of pixels (Lundblad et al., 2006; e.g., Strupler et al., 2019). A grid of 3 x 3 cell neighbourhoods of the minimum, maximum, and mean elevation were calculated from the bathymetric dataset using the focal statistics tool in ArcGIS Pro 2.5. From here, the BPI can be calculated based on the following equation (Strupler et al., 2019):

$$BPI = \frac{(meanDepth - minDepth)}{(maxDepth - minDepth)}$$

The resulting BPI grid includes values between 0 and 1. These values can then be used to calculate the standard deviation of BPI for the outlined landslide deposits using the 'Zonal Statistics' tool in ArcGIS Pro 2.5. The BPISD expresses the surface roughness for each landslide, as a highly variable topographic surface will have a larger standard deviation than a smoother topographic surface. Under the assumption that older, buried landslides will have a smoother surface than recently deposited landslides, this measurement can be used as a proxy for the landslide's relative age when compared to other landslides. The surface roughness of the landslides is also influenced by the type of landslide, the run-out distance, the slope, and the sediment type.

The BPISD for each deposit is a measurement of the surface roughness, as a highly variable surface will have a larger standard deviation than a smooth surface (Figure 3.2). The relationship between the absolute ages (from ^{14}C, ^{210}Pb and ^{137}Cs analysis) of the

deposits and the BPISD is determined to calculate the estimated age of each slope failure. A linear regression was used to test the validity of this method for Pangnirtung Fiord submarine landslides, comparing the BPISD value to the absolute ages of landslides determined from radiometric dating. From this, an age for each landslide was calculated based on the BPISD and then compared to the absolute age of the landslide.

This quantitative analysis of the surface roughness typically focuses on the depletion zone of the landslides (Strupler et al., 2019). The depletion zone is chosen because the type of landslide has little impact on the surface roughness of the depletion zone but can alter the deposit roughness substantially. For example, a debris flow with a relatively smooth lobe extending into a deep basin occurring at the same time as a blocky rockslide will have different initial surface roughness values. Additionally, variation in the surface roughness from proximal to distal portions of the deposits also presents a challenge when attempting to quantify the surface roughness. However, this study uses the landslide deposits, as the mapping limitations in shallow water prevent the accurate delineation of the total zone of depletion.

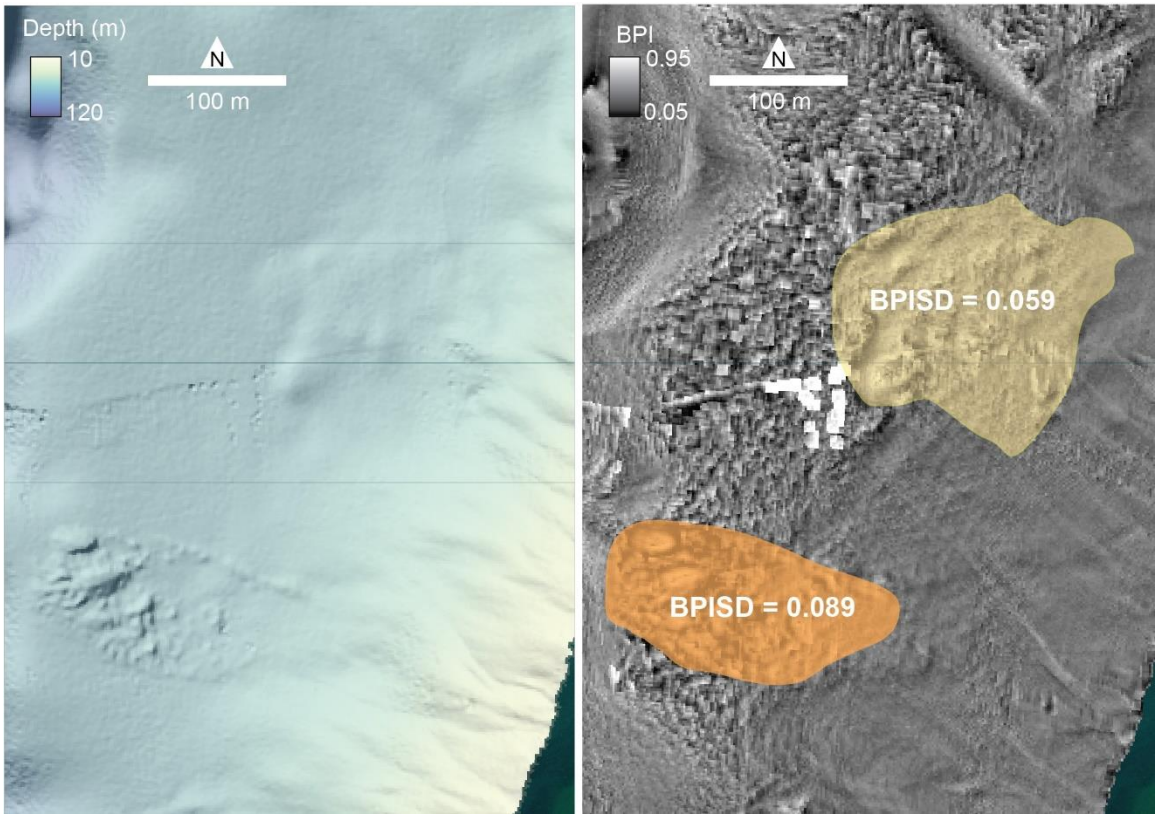

Figure 3.2: Example of BPISD values of a "low" surface roughness landslide (yellow) vs. a "high" surface roughness landslide (orange) shown in multibeam bathymetry and using the BPI overlain on the bathymetry.

3.5 Sedimentological investigations

Twenty-one sediment gravity cores (Figure 1.1; Table 3.2; Appendix A; Appendix B; Appendix C), ranging in lengths from 8 cm to 111 cm, were collected following standard GSC-A procedures outlined in Mudie et al. (1984). The gravity corer consisted of a 10 cm diameter aluminium core barrel at 172 cm or 228 cm lengths with either three, five, or six 22 kg weights in the core head. The various configurations of core barrels and core head weights were used to increase sediment recovery. The initial five cores were disturbed at the sediment-water interface whereas in the following 16 cores, the sediment-water interface was well preserved. The coring locations were based on an initial interpretation of the multibeam bathymetric data where landslides were identified. The depletion zones of landslides were targeted to understand the nature of the glide plane and capture any thin residual deposits. Coring locations downslope of the landslide deposit toe attempted to capture potential turbidites associated with the respective landslide and can be used for dating. Finally, to understand the background sedimentation rates in various sections of the fiord, the deepest portions of the basins were targeted.

The sediment cores were processed at the GSC-A facility located at the Bedford Institute of Oceanography (BIO) in Dartmouth (Nova Scotia, Canada). Whole cores were analysed for their physical properties using a Geotek Multi-Sensor Core Logger (MSCL) which includes magnetic susceptibility, bulk density, and compressional (P-wave) velocity measurements every 1 cm. The whole core magnetic susceptibility was measured via a Barrington loop sensor (MS2B) which applies a magnetic field to the core and measures the degree of magnetization in the material. Differences in the magnetic susceptibility may indicate a variation in sediment provenance, providing a potential distinction

between a landslide deposit and the surrounding sediment (St-Onge et al., 2007). The bulk density of the sediment is calculated based on Gamma Ray attenuation. A ^{137}Cesium source emits a gamma ray that is directed at the sediment core and a detector on the opposite side of the core measures how much energy is reduced by the sediment (Whitmarsh, 1971). Variations in the bulk density measurements throughout the core can aid in identifying changes in lithology (St-Onge et al., 2007).

The cores were then cut and split into a working half, and an archive half. A Geotek Geoscan camera was used to acquire a continuous digital image of the archive half of the split core immediately following core splitting, and prior to oxidation of the sediment. X-radiograph images were taken of both the archived and working half of the split cores using a Geotek X-Ray computed tomography (XCT) system. The X-radiograph images are useful for detecting features within the core that are not easily recognized from photos of the core surface like bioturbation, stratigraphic contacts, and shell fragments. The variations in x-ray travel time or attenuation through the sediment is mainly controlled by the bulk sediment density. The sediment density can be affected by lithology, grain size, and compaction (St-Onge, 2007). The Geotek MSCL was then used to analyse the archive half of the core for point-source magnetic susceptibility and colour reflectance every 1 cm. A Konica Minolta colour spectrophotometer was used to obtain reflectance measurements in L* (lightness), a* (green to red), and b* (blue to yellow) values. Each measurement can be used as a proxy for sediment characteristics, for example, L* can be attributed to the carbonate and organic carbon content within the core (St-Onge et al., 2007). The compressional wave velocity, or P-wave velocity, was measured along the working portion of the split core by inserting transducer probes into the sediment and

measuring velocity in the longitudinal and transverse directions every 10 cm. These velocity measurements, combined with density measurements, can be used to calculate the acoustic impedance (density multiplied by acoustic velocity). This calculation enables correlation of the sediment cores to the sub-bottom profiles (St-Onge et al., 2007). Shear strength measurements were also taken on the working half at a constant depth every 10 cm.

Grain size analyses were conducted at the GSC-Atlantic using a Beckman Coulter LS230 Laser Diffraction Analyser. Grain sizes of 4 to 2000 µm were distinguished by the analyser by measuring the angle and intensity of light scattered from the sediment particles when the sample passed through a laser. The smaller particles scatter light at larger angles, while the larger particles scatter light at smaller angles relative to the laser's path. Manual sieving of 22 coarse grained samples (>1000 microns) was used to account for larger grain sizes than could be measured using the Beckman Coulter analyser. Samples were weighed and then wet washed to remove the <63 µm portion. Everything above 1000 µm was manually sieved and weighed. These measurements were merged with the initial grain size measurements with a 10% correction factor.

The sub-sample depths for grain size analysis were determined based on the preliminary grain size and sedimentological characteristics revealed in the analysis of the physical properties. In coarse grained intervals, samples were taken every 1 cm to 2 cm, whereas fine grained sections were sampled every 5 to 10 cm (Table 3.2; Appendix C; Appendix D). Grain size analyses were used to determine the grain size distribution in the sample, helping to distinguish and characterise the lithology.

Ten thin sections were created from five of the cores (Table 3.2; Appendix E) for detailed interpretation of microfacies. The thin section preparation procedure followed Normandeau et al. (2019c) to extract the sediment from the core. To begin, 18 cm aluminium trays were pushed into the core to extract the sediment. Next, the sediments were freeze-dried to remove pore water without altering microstructures. The dehydrated sediments are then impregnated with a clear epoxy resin to fill the space once held by the pore water. After the epoxy resin dried in an oven at 60ºC over 48 hours, the sediments were cut using a rock saw into 6 cm and 7 cm lengths for thin-section preparation.

Table 3.2: Sediment gravity core location information, length of sediment core recovered, and the samples collected for additional analysis.

						Number of samples			
Expedition #	Core #	Latitude	Longitude	Water depth (m)	Core length (cm)	Grain size	Thin sections	^{210}Pb	^{14}C
2019NULIAJUK	15	66.3671	-65.4971	61	111	52	5	0	1
2019NULIAJUK	17	66.3699	-65.50354	27	89.5	16	0	0	1
2019NULIAJUK	20	66.3711	-65.50126	36.5	85	26	1	0	3
2019NULIAJUK	22	66.3641	-65.49412	80	25	0	0	0	0
2019NULIAJUK	24	66.3611	-65.49352	87	96	7	0	0	0
2019NULIAJUK	28	66.3006	-65.52752	67	31	0	0	0	0
2019NULIAJUK	30	66.2793	-65.53751	87	103	37	1	20	1
2019NULIAJUK	31	66.2802	-65.55283	44	29	0	0	13	0
2019NULIAJUK	34	66.2602	-65.54767	110	89	10	0	19	1
2019NULIAJUK	35	66.239	-65.551	101	23.5	0	0	0	0
2019NULIAJUK	36	66.227	-65.57465	113	11	0	0	0	0
2019NULIAJUK	37	66.2388	-65.56057	65	74	17	2	0	1
2019NULIAJUK	38	66.2399	-65.56075	57	8	0	0	0	0
2019NULIAJUK	39	66.2437	-65.56083	61	30	0	0	0	0
2019NULIAJUK	40	66.1586	-65.70787	70	20	0	0	0	0
2019NULIAJUK	41	66.1644	-65.71818	145	64	7	0	21	1
2019NULIAJUK	42	66.1589	-65.75927	140	30.5	14	0	0	0
2019NULIAJUK	43	66.1742	-65.66476	108	47	17	0	0	1
2019NULIAJUK	44	66.1346	-65.80121	156	11	0	0	0	0
2019NULIAJUK	47	66.1255	-65.86307	66	103	46	1	0	2
2019NULIAJUK	48	66.1212	-65.8938	98	25	11	0	0	1

3.6 Radiocarbon dating

Thirteen radiocarbon ages were obtained from shell fragments extracted from ten sediment cores. The samples were taken from above, below, and within identified landslide deposits. Radiocarbon analyses were performed at the Lalonde Accelerator

Mass Spectrometry (AMS) facility at the University of Ottawa. AMS analysis provided the necessary measurements of carbon ions to calculate a ratio ($F^{14}C$) of the $^{14}C/^{12}C$ in the sample to the $^{14}C/^{12}C$ in a standard. After the ratios are background-corrected, the half-life of ^{14}C (5568 years) is used to calculate the radiocarbon age in ^{14}C years before present (^{14}C yr BP), where BP represents before 1950 CE. The radiocarbon ages were calibrated to account for fluctuations in the atmospheric ^{14}C production rates through time (Bronk Ramsey, 2008). The ^{14}C ages were corrected using a local marine reservoir correction (ΔR) of –6 ±58 years, calculated as the average of the 10 nearest shell measurements (Appendix F; Coulthard et al., 2010) and calibrated using the Marine20 calibration curve in Calib 8.2 (Heaton et al., 2020). The average of the 10 measurements were used since the ΔR values are variable, even within Pangnirtung Fiord where three dates are available. This approach also agrees with Heaton et al. (2020) who suggested to not use this calibration curve for high latitudes (higher than 40–50°N) due to highly variable measurements and complicated ocean currents.

3.7 ^{210}Pb and ^{137}Cs activities

The ^{210}Pb and ^{137}Cs radioisotope activities for four sediment gravity cores were used to calculate sedimentation rates within the fiord (Pourchet and Pinglot, 1989; Bronk Ramsey, 2008). A total of seventy-three samples of about 8 grams each were collected within the top 30 cm of the cores at 1–2 cm intervals, and the isotope analyses were performed at the University of Ottawa LANSET Laboratory.

The ^{210}Pb isotope comes from the radioactive decay of ^{238}U present in the Earth's crust. Within the decay chain, ^{210}Pb is formed from both the decay of the solid ^{226}Ra found in

rock, sediments, and water and from the decay of ^{222}Rn in the atmosphere. The ^{210}Pb resulting from the decay of ^{226}Ra found in rock, sediments and water is in equilibrium and is referred to as supported ^{210}Pb. Unsupported ^{210}Pb is the result of ^{222}Rn decay which is removed from the atmosphere by wet and dry fallout and is integrated into sediment (Goldberg, 1963).

Lead-210 dating was completed using an Ortec High Purity Germanium Gamma Spectrometer (Oak Ridge, TN, USA). Efficiency corrections were completed using Certified Reference Materials obtained from International Atomic Energy Association (Vienna, Austria) and ScienTissiME (Barry's Bay, ON, Canada) was used to analyse the results. ^{137}Cs measurements were also made to validate the calculated ^{210}Pb ages. Unsupported ^{210}Pb is calculated by subtracting the supported ^{210}Pb that remains relatively constant from the total ^{210}Pb activity. Background sedimentation rates can be determined and used to infer the approximate age of landslide deposits (Pourchet and Pinglot, 1989).

Sedimentation rates were calculated using the 'serac' R package developed by Bruel and Sabatier (2020) and the Constant Flux Constant Sedimentation (CFCS) model (Krishnaswamy et al., 1971). This model assumes that the ^{210}Pb activity in the newly deposited sediment has been constant through time; however, bioturbation, which is a prevalent process occurring throughout the hemipelagic sediments within the fiord, will affect the measured ^{210}Pb and ^{137}Cs activities. The CFCS model is the simplest model, with other models requiring porosity measurements that were not recorded during sampling. The landslide deposits seen in the core can be dated using this age modelling package, providing further insight into the timing of slope failures in Pangnirtung Fiord.

3.8 Dating of submarine landslide deposits

The morphological and sedimentological characterizations of the submarine landslides were used to determine the intervals of interest. The ages of the submarine landslide deposits were constrained through a combination of radiocarbon ages and $^{210}Pb/^{137}Cs$ derived sedimentation rates. In cores with only radiocarbon ages available, the sedimentation rates in the sediment cores were calculated through manual age-depth modelling. For these calculations, the landslide deposits were excluded. Using these sedimentation rates, the ages of the instantaneous landslide deposits were calculated based on their depth in the cores and sub-bottom profiles using linear interpolation (e.g., Figure 3.3). Bayesian age-depth modelling was not completed for two reasons: 1) in the cores where there are multiple ^{14}C ages, they correspond to modern ages, nullifying any opportunity to model potential changes in sedimentation rate; and 2) where there is a combination of ^{14}C, ^{210}Pb, and ^{137}Cs radiometric ages in the same core, the landslide deposit lies within the ^{210}Pb sub-sample intervals, providing a more accurate age constraint.

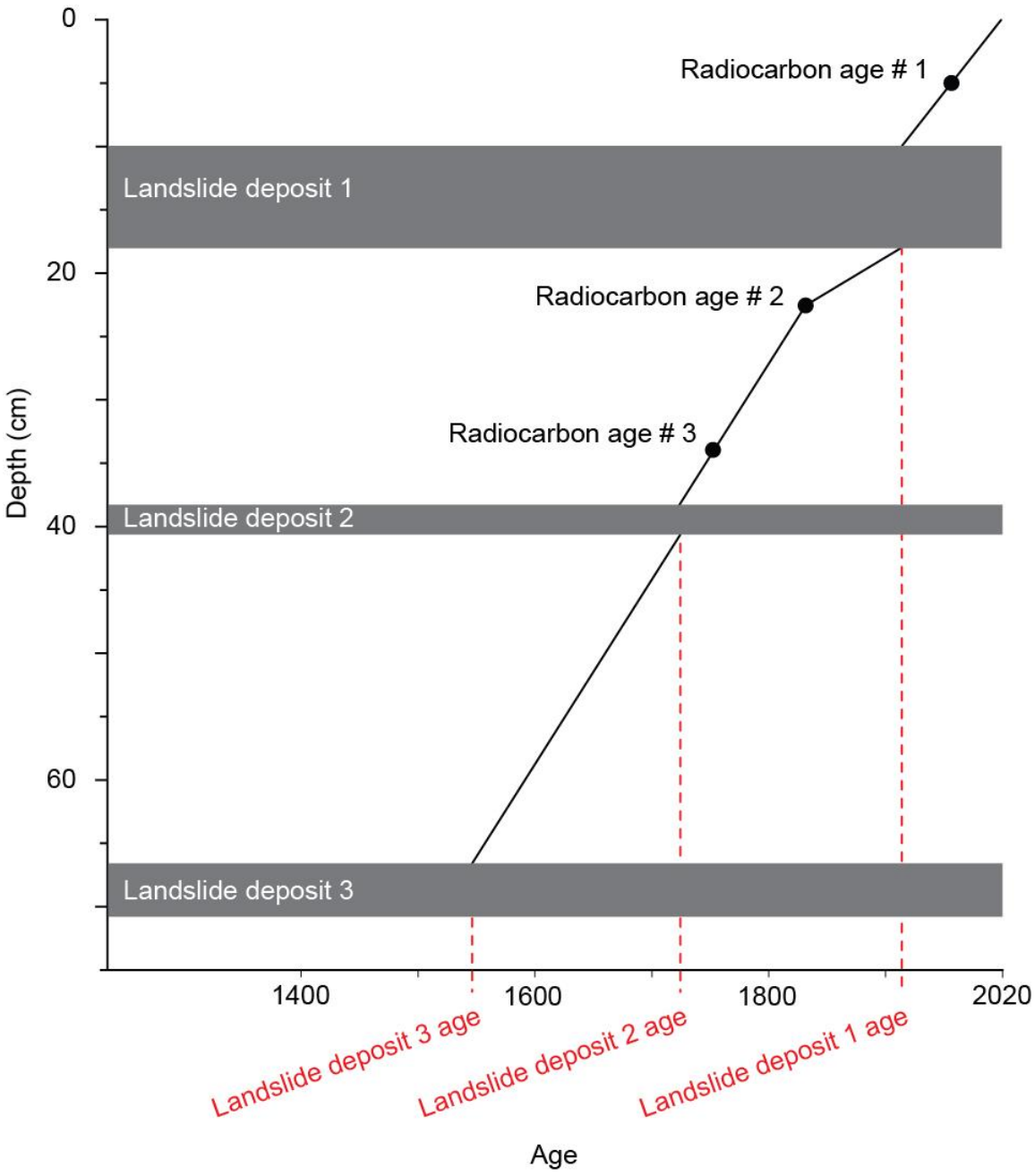

Figure 3.3: Conceptual example of an age-depth model.

3.9 Unmanned Aerial Vehicle (UAV) photogrammetry

Over 3800 photos from a DJI Mavic Pro 2 UAV were taken of the high-relief fiord sidewalls with a Hasselblad 1" CMOS sensor camera with an adjustable aperture (F2.8-F11) and mounted to a Gimbal stabiliser. The photos were taken at 100–500 m elevation, and 500 m – 1000 m away from the fiord sidewalls. The Pix4Dcapture application was used to capture photos while documenting the altitude, GPS location, pitch, and roll of the UAV for each photo. Using Photoscan software, these images were converted to 3-D point cloud renderings of the sub-aerial landscape, converted to a digital elevation model (DEM), and exported to ArcGIS Pro 2.5 for interpretation. The original photos were also used for interpretation.

CHAPTER 4 RESULTS

4.1 Geomorphology of Pangnirtung Fiord

4.1.1 Glacial landforms

High resolution multibeam bathymetric data and sub-bottom profiles reveal distinct glacial landforms throughout the fiord. Large sills spanning the width of the fiord (1–3 km in length and >40 m of relief), visible in the bathymetry as transverse narrow ridges, create topographic highs that divide the fiord into sub-basins with variable size, shape, and depth (Figure 1.1). These sills are interpreted as recessional moraines formed of glacial sediments. As noted in Gilbert (1978) and Hughes Clarke et al. (2015), the mouth of the fiord also consists of a terminal moraine that spans the entire width of the fiord (Figure 4.1). Shorter recessional moraines (<500 m in length and < 20 m of relief) occur throughout the fiord (Figure 4.2; Figure 4.3) and are often buried along their flanks by post-glacial basinal sediments. Circular depressions less than 220 m in diameter identified in the flattest and deepest portions of the basins are interpreted as kettles and are infilled with post-glacial sediments (Figure 4.2; Figure 4.3). Kettles are formed when ice left behind from a retreating glacier is surrounded by glacial sediment (Eyles and Lazorek, 2014). Clusters of two or more of these landforms are unevenly distributed throughout the fiord.

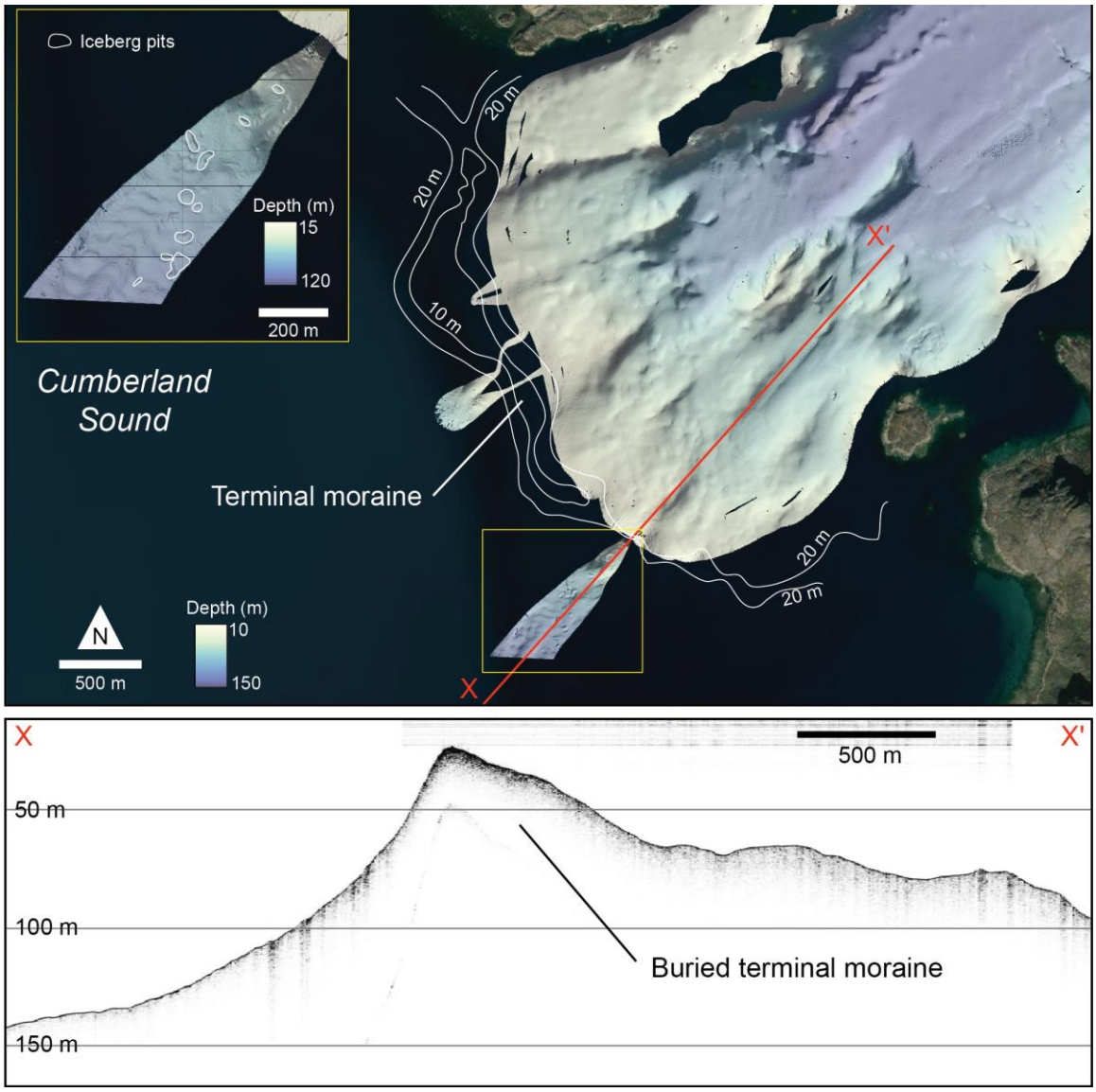

Figure 4.1: A buried terminal moraine identified at the mouth of Pangnirtung Fiord in bathymetric data and sub-bottom profile. Inset is a view of the Cumberland Sound side of the moraine featuring iceberg grounding pits. See Figure 1.1 for figure location.

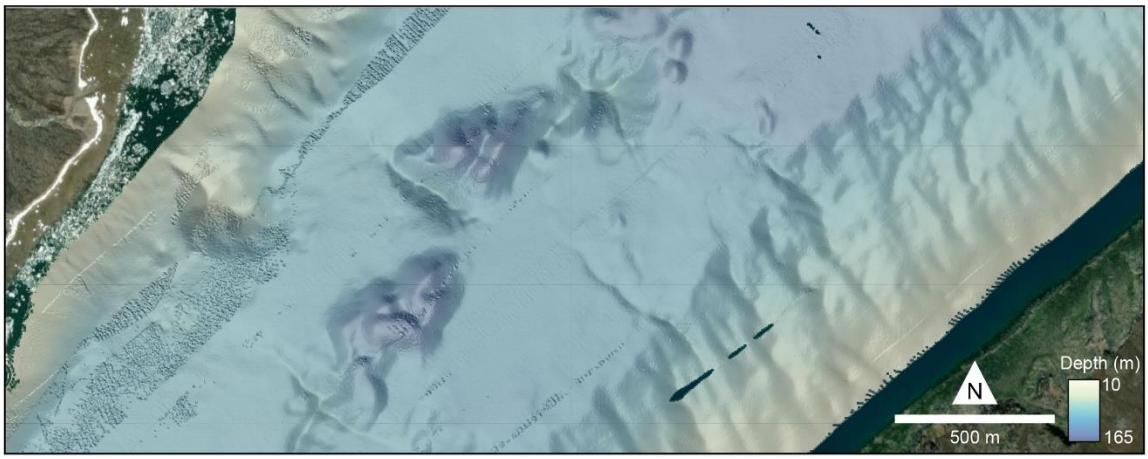

Figure 4.2: Examples of landforms identified in bathymetric and sub-bottom data. Refer to Figure 4.3 for interpretation. See Figure 1.1 for figure location.

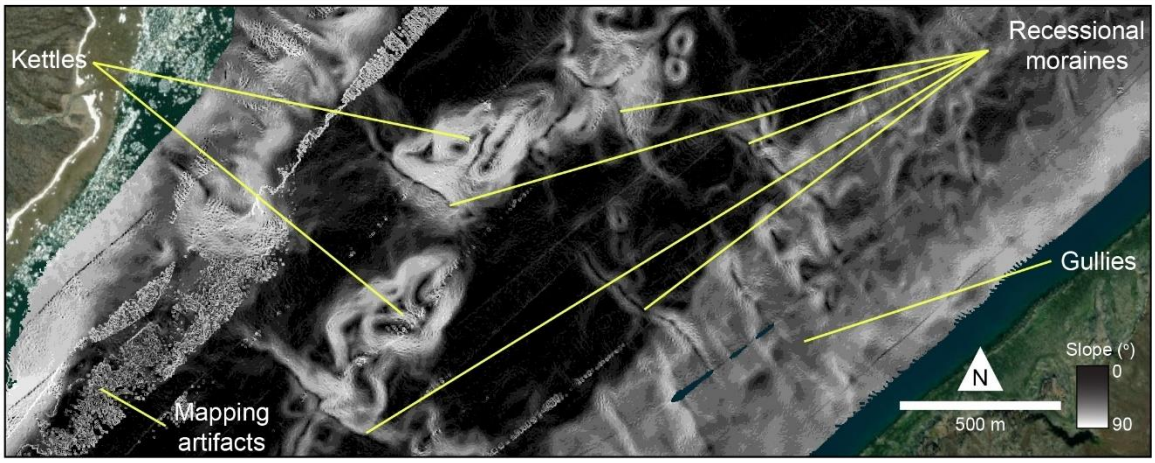

Figure 4.3: Interpretation of landforms identified in bathymetric and sub-bottom data. See Figure 1.1 for figure location.

4.1.2 Post-glacial landforms

Post-glacial processes have modified glacial landforms and are responsible for much of the modern and remanent morphologies visible on the seafloor. Submarine gullies form downslope of repeat small-scale sediment failures, where the seafloor gradient is 10–25°. In cross-section, they are characterised by V-shaped incisions with a maximum width of approximately 75 m. The submarine portion of the fiord head-delta features channels

(20–60 m wide) with sediment wave structures (5–30 m long and 2 m high) identified both in the incised channels and the channel flanks. A sub-bottom profile across the delta clearly images the progradation of the delta front over previous prodelta sediments (Figure 4.6).

Small, rounded depressions, often less than 50 m in width and organised in clusters, that occur on the Cumberland Sound side of the sill at the fiord's mouth are interpreted as ice pits. These are the results of iceberg groundings depressing the soft seafloor sediment (Barrie et al., 1992). The presence of these ice pits demonstrates how this topographic high formed by the terminal moraine prevents large icebergs with keel depths > 25 m from entering the fiord (Figure 4.1). Rounded depressions of smaller size (< 30 m) are identified in the shallowest areas of the fiord and represent groundings of smaller icebergs or sea-ice.

4.1.3 Submarine landslides

Lobate-shaped deposits that have an irregular topography and accumulate downslope of a depletion zone are identified as submarine landslide deposits. The upslope limit of the landslides, also called the head scarp, is not always visible due to mapping limitations in water shallower than 30 metres or reworking of slope sediments. A failure scarp with no associated deposit can indicate that the failed sediments are deeply buried, have dispersed over the seafloor creating features below the data resolution, or have been reworked and eroded.

The high-resolution bathymetric data reveal 180 partially or fully delineated submarine landslides and associated deposits throughout Pangnirtung Fiord, both in shallow and

deep water (Figure 4.4). The landslides initiated in shallow water (i.e., shallower than 40 m), represented by the green circles in Figure 4.4, account for 87% of all the mapped landslides. Generally, these shallow-water landslides originate along the submarine fiord sidewalls and are deposited on the basin floor. The geological and geomorphological characteristics of the subaerial part of the fiord immediately upslope of the shallow-water landslides are diverse (Dyke, 2011; Figure 4.5). In Figure 4.5a, a subaerial debris fan extends into the intertidal zone. Three submarine landslides are visible downslope of this debris fan; however, no head scarp is mapped in the bathymetry, only side scarps and a transition zone. The head scarps likely associated with the three landslides are visible in the satellite imagery just downslope of the debris fan and are characterised by a concave shape created at the cusp of the intertidal zone. Other shallow-water landslides appear to occur downslope of stable subaerial bedrock with no apparent active erosional processes (i.e., debris flow fans), however iceberg and sea-ice grounding pits are identified near the depletion zone (Figure 4.5b).

The largest landslide identified in the fiord, which covers an area of 2.1 km^2, is located downslope from the Kolik River delta (Figure 4.5c). Failure scarps are visible within the bathymetric coverage; however, the head scarp was not detected. This could be because it is located in shallower waters, outside of the mapping area, or it has been covered by deltaic sediments. A potential head scarp or portion of it is identified in satellite imagery (Figure 4.5c). The landslide deposit features large blocks (50–300 m wide) that create an undulating surface texture (Figure 4.5c).

Landslides originating in deeper water, marked by red circles in Figure 4.4, make up the remaining 13%. These landslides occur along topographic highs, such as sills and moraines, and have numerous scarps over a wide failure area (Figure 4.5d).

The morphologies and surface expressions of the mapped submarine landslides in the geophysical datasets represent distinct landslide types including individual and complex events (Figure 4.6). Individual events are made up of unsorted sediment and rock that move rapidly downslope and do not appear to have distinct lateral bathymetric constraints (Hungr et al., 2001). Within Pangnirtung Fiord, these individual events have distinct side scarps with both wide and narrow depletion zones. The associated deposits are blocky and rough with transverse compressional ridges identified.

Complex events have multiple failure locations and are relatively confined within the gullies developed along the submarine slope from repeated failures. Multiple deposits can be identified at the base of these channels or gullies. Side scarps are not as distinct, and the depletion zones are narrower creating an elongated landslide. Generally, the deposits have a smoother, lobate-shaped, appearance along the flat basin floor.

Turbidity currents are inferred from the distinct sediment wave structures at the head of the fiord (Normandeau et al., 2019a), as well as from the high-amplitude reflections interpreted as turbidites in the sub-bottom profiler data downslope of the fiord-head delta and the sediment cores collected downslope of the delta and submarine landslides (Figure 4.6). Building on these results, the landslide morphologies can be quantified by morphometric measurements, which provide a tool to compare landslides and can aid in the interpretation of the triggers.

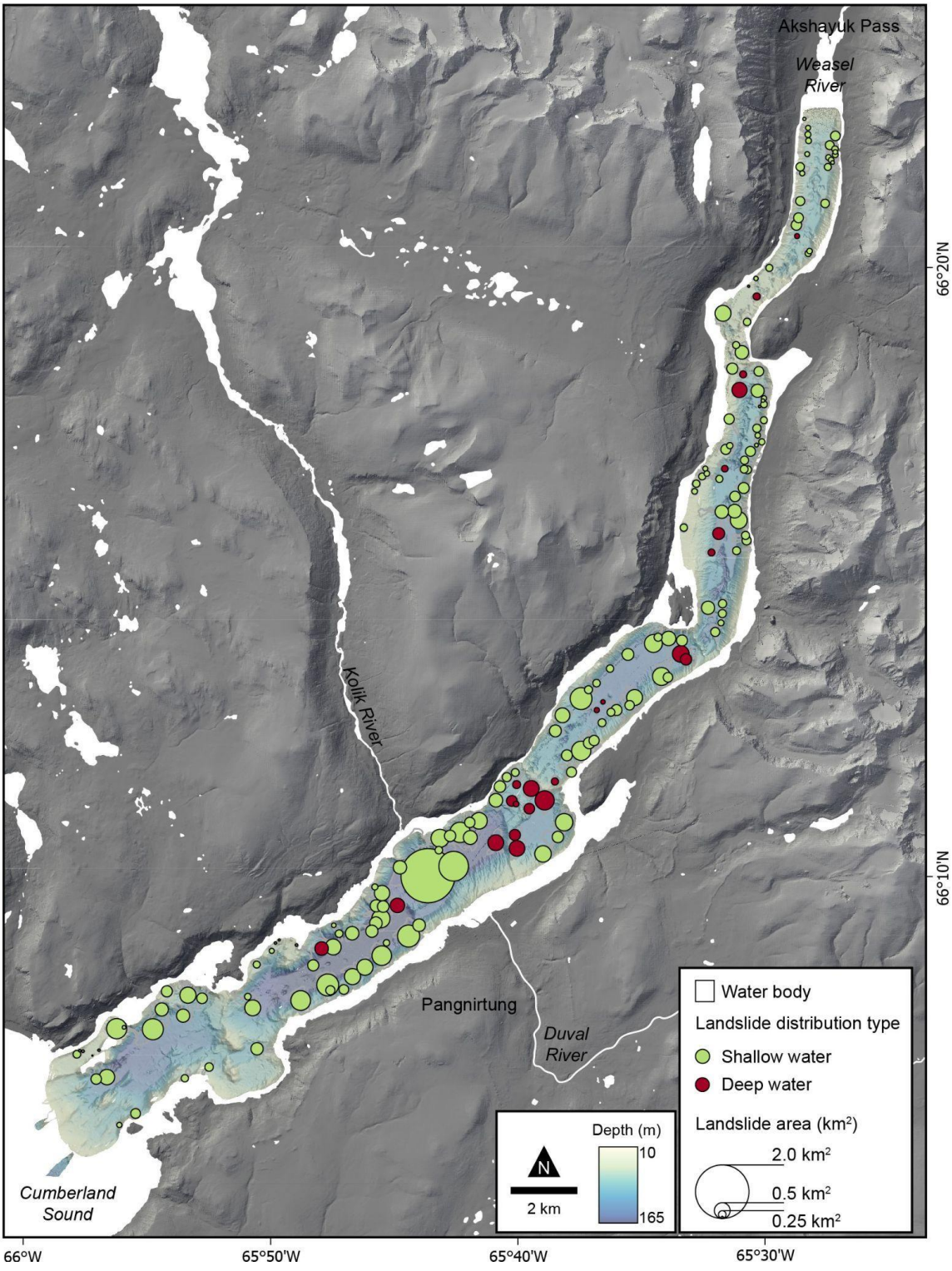

Figure 4.4: Mapped landslides within Pangnirtung Fiord depicted by their location and total area. In green, landslides initiated in shallow water (<40 m water depth) and in red, landslides initiated in deep water (>40 m water depth).

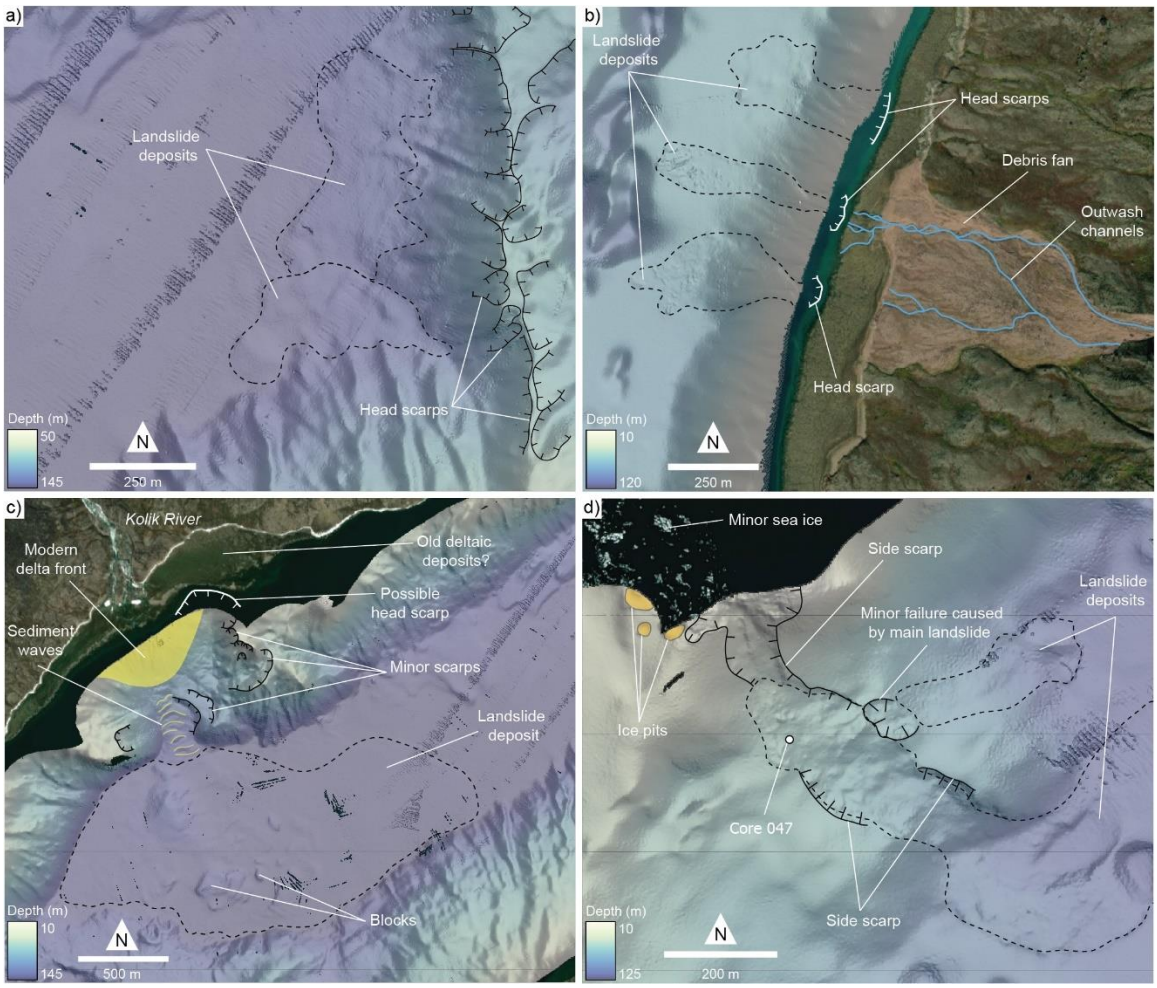

Figure 4.5: Examples of detailed mapping of submarine landslides: a) landslides occurring in deep water; b) shallow-water landslides occurring downslope of subaerial debris flows; c) shallow-water, fluvially influenced landslide at the mouth of the Kolik River; d) shallow-water, non-subaerially influenced landslides. See Figure 1.1 for locations. Base map from Maxar Technologies.

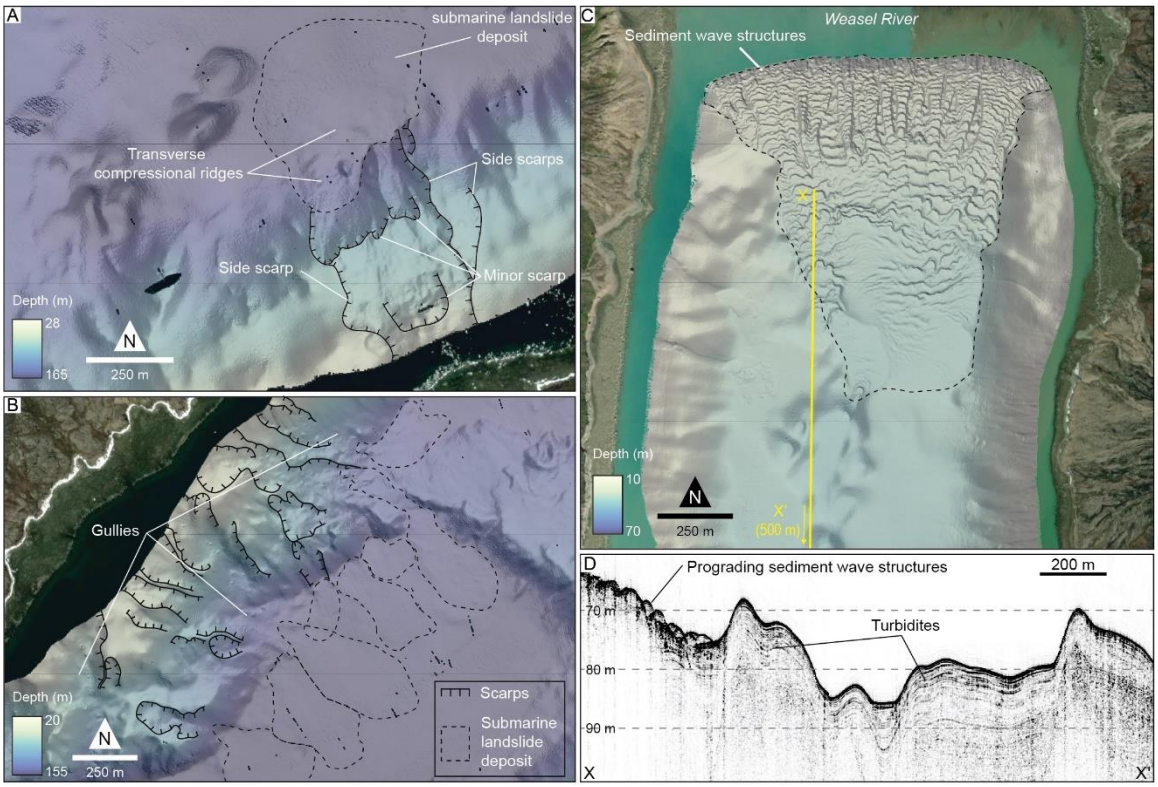

Figure 4.6: A) individual event, b) complex events, and c) turbidity currents identified in the multibeam bathymetry. See figure 1.1 for locations.

4.2 Morphometric analysis of submarine landslides

Morphometric parameters were measured for all submarine landslides (Figure 3.1; Table 3.1). Descriptive statistics, such as the interquartile range and mean, are used to provide the morphometrics of a typical submarine landslide in Pangnirtung Fiord (Figure 4.7; Table 4.1). Most depletion zones are identified in areas of high relative slope (lower quartile (Q1) = 9.5º), demonstrating an association between slope failure and high relief sections of the fiord, namely the subaqueous fiord sidewalls and glacial sills. Conversely, no distinct slope failure scarps are seen in areas of low slope (0–2º). Most landslide deposits are mapped along the relatively flat basin floors, and in some instances cross-cut other landslide deposits (Figure 4.6b). As previously mentioned, not every landslide

deposit can be linked to its head scarp mainly because of the lack of bathymetric data in the shallow water portions of the fiord. Because of this, measurements of the minimum water depth for the depletion zone are restricted to about 10–30 metres instead of extending to 0 m. Considering this mapping limitation, 65% of mapped landslides in Pangnirtung Fiord have a minimum water depth of the head scarp in less than 30 m.

Seventy-five percent of landslide deposits have an area less than 0.13 km^2 (Q1= 0.03 km^2 and upper quartile (Q3) = 0.13 km^2) while the minimum water depth of the landslides varies from 3-132 m (mean= 38 m). The ratio of the maximum deposit width (Q1= 130 m, Q3= 320 m) to the total length of deposit (Q1=310 m, Q3= 637 m) is used to calculate the dimensionless elongation parameter for each landslide deposit. The elongation value of most deposits is above 1 (Q1= 1.4, Q3= 3.4), indicating a long and narrow feature oriented toward the downslope gradient. The slope gradient measured adjacent to the slope depletion zone (Q1= 9.5º, Q3= 15º) is meant to provide insight into the unfailed slope angle, however slope measurements within the depletion zones show little deviation from the slope gradient parameter. The mean slope of less than 1º at the toe of the landslides demonstrates the landslide deposits coming to rest on the flat basin floor.

The largest landslide identified downslope from the Kolik River delta represents an outlier within the dataset (Figure 4.5c). The associated deposit extends across the basin and towards the opposite slope just offshore the Hamlet of Pangnirtung. Sub-bottom profile data reveal that the deposit is overlain by approximately 1 m of sediment.

Table 4.1: Summary statistics for morphometric parameters of submarine landslides.

Summary Statistics	Mean	Minimum	Q1	Q3	Maximum
Area (km^2)	0.10	0.001	0.03	0.13	2.14
Water depth minimum (m)	38	3	19	50	132
Scar Width (m)	203	26	98	260	1123
Total length (m)	501	26	310	637	1697
Maximum deposit length (m)	274	26	155	334	1130
Maximum deposit width (m)	254	40	130	320	2377
Slope Gradient (^{o})	12.1	2.0	9.5	15	25
Slope Gradient at Toe (^{o})	1	0	0	1	13
Elongation	2.5	0.2	1.4	3.4	9.3

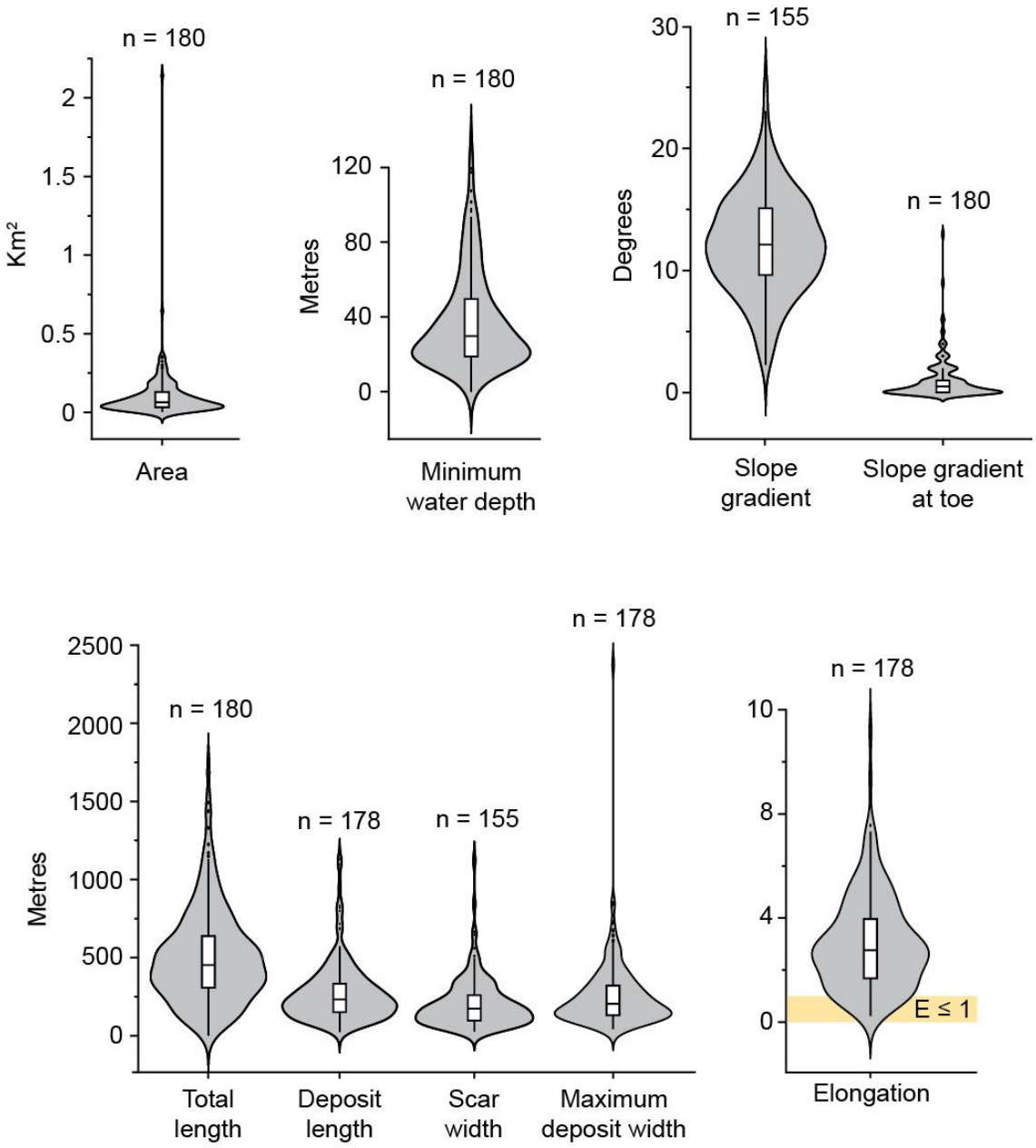

Figure 4.7: Violin plots of the morphometric parameters for the submarine landslides identified within Pangnirtung Fiord, including area, water depth minimum, slope gradient, slope gradient at toe, total length, deposit length, scar width, maximum deposit width, and elongation (parameters are defined in Table 4.1).

4.3 Lithostratigraphy

4.3.1 Lithofacies

Photographs, X-radiographs, and physical properties of 14 gravity cores (Appendix B; Appendix C) were used to describe the landslide deposits, as well as discern the dominant lithological facies found in the fiord (Figure 4.8).

Lithofacies 1 (L1) is formed of a dark grey clayey silt with intervals of very fine-grained sand and black mottling indicative of bioturbation. L1 makes up the bottom of cores 037 and 047 (Appendix B). Wavy parallel laminations are identified throughout with granules and pebbles identified in the x-radiograph images. Generally, this lithofacies has a higher (600–1200) magnetic susceptibility, and a variable bulk density (1.8–2.0 mg/mm^3). L1 is interpreted as glacimarine deposits or perhaps the reported shoreface deposits as described in Aitken and Gilbert (1989) as distinctly bedded, bioturbated, and pebbly muddy sand.

Lithofacies 2 (L2) consists of dark grey, highly bioturbated clay and silt with minor occurrences of very fine – fine sand and granules. L2 has a consistent p-wave velocity below 1600 m/s, and a variable bulk density (1.4–2.2 mg/mm^3). L2 occurs in cores 015, 017, 020, 024, and 030 (Appendix B), and consists of hemipelagic sedimentation within the fiord that also incorporates pebbles interpreted as ice-rafted debris.

Lithofacies 3 (L3) is composed of olive grey highly bioturbated clay and silt with minor fine to coarse sand and occurrences of irregularly distributed granules. Bedding and laminations are highly deformed by bioturbation. L3 occurs in cores 017, 020, 024, 034,

041, and 043 (Appendix B), and it is interpreted as hemipelagic sedimentation with pebbles interpreted as ice-rafted debris. The main characteristic differentiating L3 from L2 is the colour, possibly indicating a change in sediment provenance.

Lithofacies 4 (L4) consists of coarse-grained sands and gravel of various colours, which is interpreted as landslide deposits. This lithofacies has a variable magnetic susceptibility (100–600) and a higher bulk density than the hemipelagic sediments (>2 mg/mm^3). This lithofacies has an erosional lower contact with the underlying lithofacies, clearly identified in core 047, collected within the depletion zone of landslides. The pebbles and mud clasts are seen within a thin section taken in core 047 and the erosional contact with L1 is represented by a change in grain size and colour (Figure 4.9).

Lithofacies 5 (L5), found in cores 015, 017, 020, 030, and 043 (Appendix B), is characterised by fine to coarse grained sandy-silt laminations that are distinguished from the surrounding sedimentation based on the grain size. The sands are poorly to moderately sorted, with granules visible in the x-radiograph images. These intervals have a slightly higher bulk density than the surrounding hemipelagic sedimentation. Considering the location of the cores, downslope of the landslide toe, and the sedimentological characteristics, L5 is interpreted as turbidites representing the distal deposit of a submarine landslide (Talling et al., 2015).

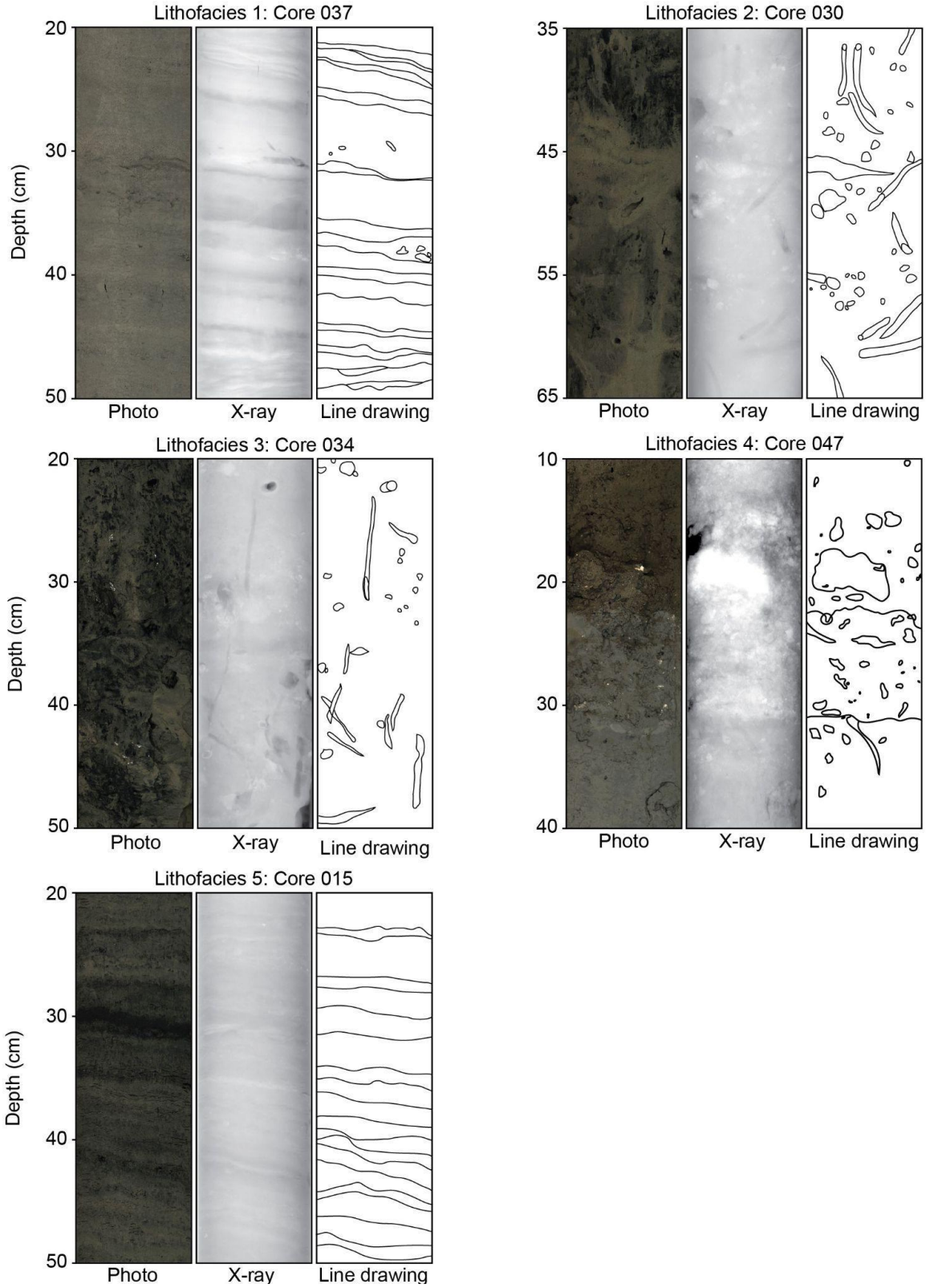

Figure 4.8: Examples of lithofacies identified in gravity cores throughout Pangnirtung Fiord.

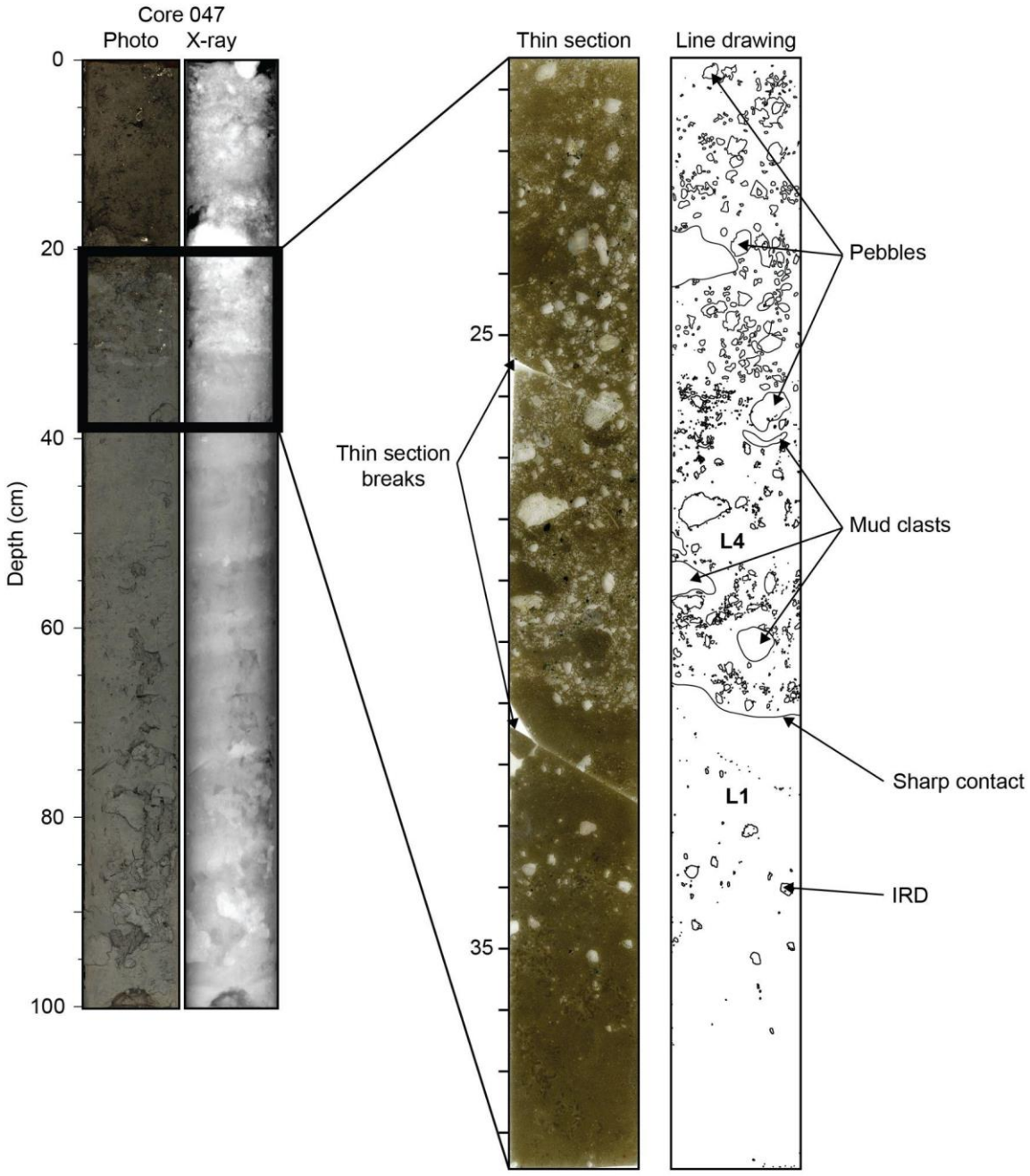

Figure 4.9: Thin section taken from core 047 (20.5 - 38.5 cm depth).

4.3.2 Absolute Dating

4.3.2.1 Radiocarbon dating

Radiocarbon dating of shell fragments collected from the sediment cores is used to determine sediment accumulation rates and approximate landslide ages. Thirteen shell samples were dated, and their depth in core, radiocarbon and calibrated ages are listed in Table 4.2 and depicted in Figure 4.10. Radiocarbon ages from cores 020, 034, 037, and 047 are all modern, i.e., younger than 1950. These samples with modern ages are either taken from within the upper 3 cm of the cores or are within a core located near the fiord head delta with a presumed higher sedimentation rate (core 020). Shell fragments in cores 015 and 017 have median calibrated ages of 184 (349-0) cal BP, and 162 (311-0) cal BP, respectively. These samples were also taken within cores near the fiord head delta which presents an active environment in which the sediments may have been reworked. These ages offer a greater uncertainty in the dating of landslides near the fiord head delta. Shell fragments collected from hemipelagic sediments come from cores 030, 041, and 043 where the deeper sample depths, paired with a calibrated radiocarbon age create an opportunity to date landslide deposits found within the cores, especially when these ages are used in conjunction with ^{210}Pb and ^{137}Cs activities. The samples taken from within intervals of L4 are considered maximum ages for the respective landslide deposit at the top of the core, as the landslide deposit is made up of reworked material. This explains why there are a wide range of ages for the same deposits. For example, the oldest median calibrated radiocarbon age of 4079 (4310–3847) cal BP at a depth of 22–25 cm in core 047 most likely represents the reworking of L1 sediments into a landslide deposit (L4) (Figure 4.9). However, a modern age at the top of the core indicates that this deposit has

been reworked recently. As a further example, core 048 has an interpreted landslide interval making up the entirety of the core, however the sample age is reported as 758 (929–603) cal BP, which represents the maximum age of the landslide. These examples highlight the importance of the lithological descriptions and using them as context when considering the landslide age.

Table 4.2: Radiocarbon dating analysis including the measured uncalibrated radiocarbon age and the calibrated age.

Core	Lab number	Sample depth (cm)	Radiocarbon age (yrs BP)	Uncertainty (yrs BP)	Median calibrated age (cal BP; ΔR = -6±58)	Associated Lithofacies
015	UOC-13995	38-39	722	26	184 (349–0)	L2
017	UOC-13996	68	697	24	162 (311–0)	L5
020	UOC-13997	20	Modern		>Modern	L3
020	UOC-13998	41-43	183	24	>Modern	L2
020	UOC-13999	49-51	Modern		>Modern	L2
030	UOC-14000	72	1129	25	559 (701–413)	L2
034	UOC-14001	2-3	Modern		>Modern	L3
037	UOC-14002	3-5	Modern		>Modern	L4
041	UOC-14003	49-51	899	25	364 (516–180)	L3
043	UOC-14004	40-41	1733	25	1135 (1292–952)	L2
047	UOC-14005	0-1	Modern		>Modern	L4
047	UOC-14006	22-25	4181	25	4079 (4310–3847)	L2
048	UOC-14007	2-3	1362	25	758 (929–603)	L4

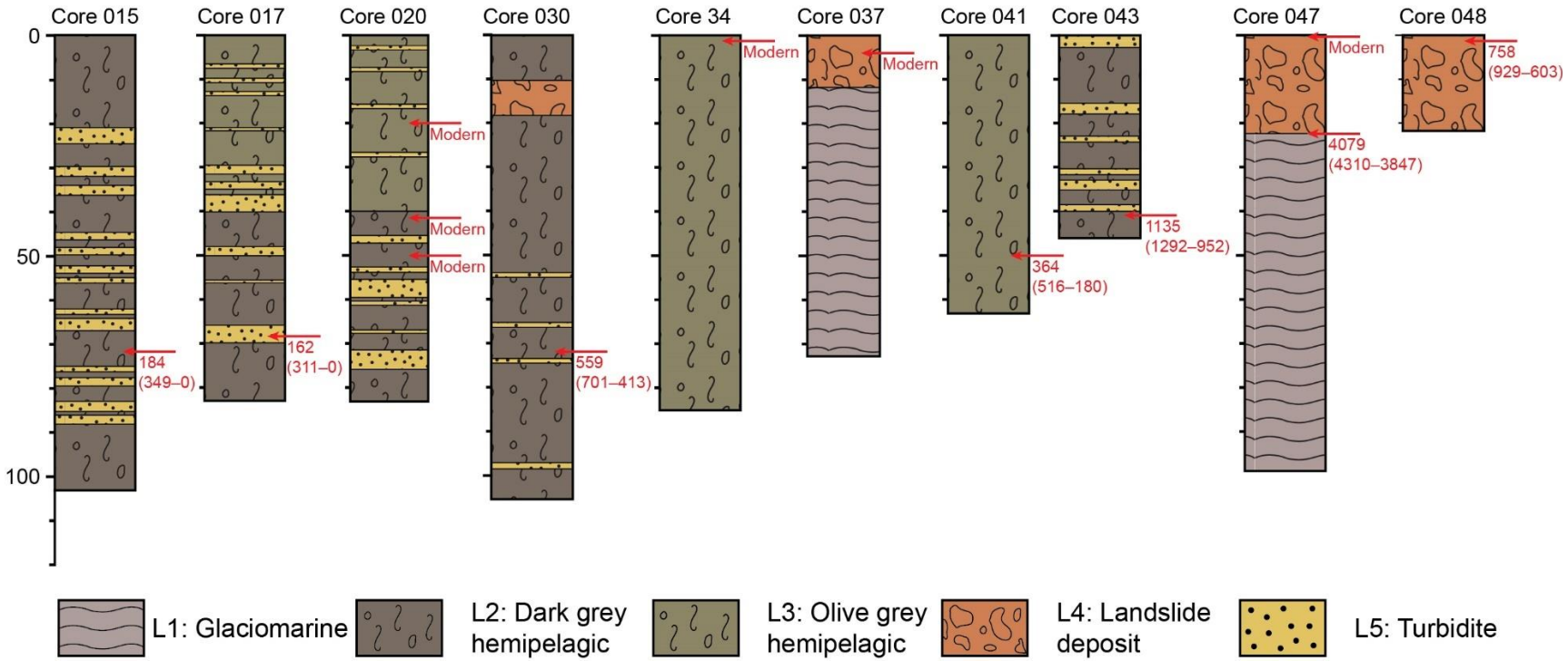

Figure 4.10: Interpreted core lithofacies and depth of median calibrated radiocarbon ages and the 2-sigma range (cal BP).

4.3.2.2 ^{210}Pb and ^{137}Cs activities

Age-depth modelling using 'serac' (Bruel and Sabatier, 2020) to model the $^{210}Pb_{ex}$ and ^{137}Cs activities for cores 0030, 0031, 0034, 0041 provide an estimate of sediment accumulation rates (SAR) for parts of Pangnirtung Fiord (Figure 4.11; Figure 4.12; Figure 4.13; Figure 4.14). In turn, the SAR can be used to calculate the ages of the landslides identified within the cores and in sub-bottom profiles. In cores 030 and 031, landslide intervals (L4) have a sudden decrease in ^{210}Pb activity, representing the reworking of older material. The supported ^{210}Pb was determined using ^{214}Pb in all cores. The $^{210}Pb_{ex}$ activity reaches the average supported ^{210}Pb background levels in all cores.

Activities of ^{137}Cs within the cores can be used to correct the modelled SAR as a peak in ^{137}Cs represents the 1963 peak due to nuclear bomb testing (Bruel and Sabatier, 2020). Core 030 has a distinct peak at 5-6 cm, correcting the SAR to better fit with the radiocarbon age of a sample down-core (Figure 4.11). Core 031, 034, and 041 all have less distinct peaks in ^{137}Cs. These gradual ^{137}Cs activity curves may be the result of bioturbation that dilutes the ^{137}Cs signal throughout the sample interval. The 'serac' modelled SARs are corrected with the peaks in ^{137}Cs to better fit the SARs found using radiocarbon ages in other cores. These SAR also fit with sedimentation rates calculated in Andrews et al. (1985) for other Baffin Island fiords.

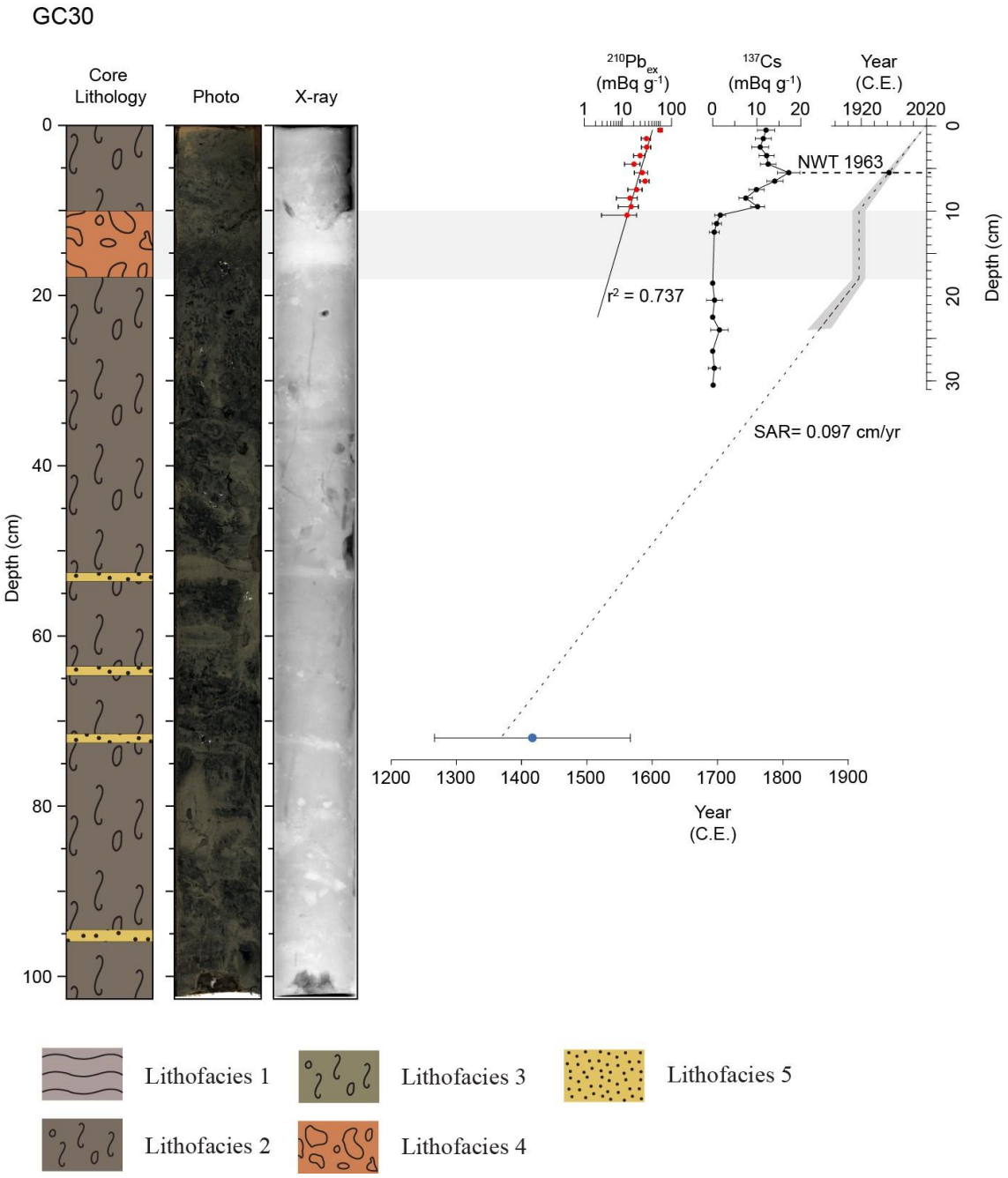

Figure 4.11: Core 030 lithofacies, photo and X-ray with a landslide deposit identified in core. ^{210}Pb and ^{137}Cs activities with the sediment accumulation rate (SAR) corrected using the nuclear weapons test (NWT) age of 1963. The radiocarbon age and 2-sigma range are shown by the blue dot.

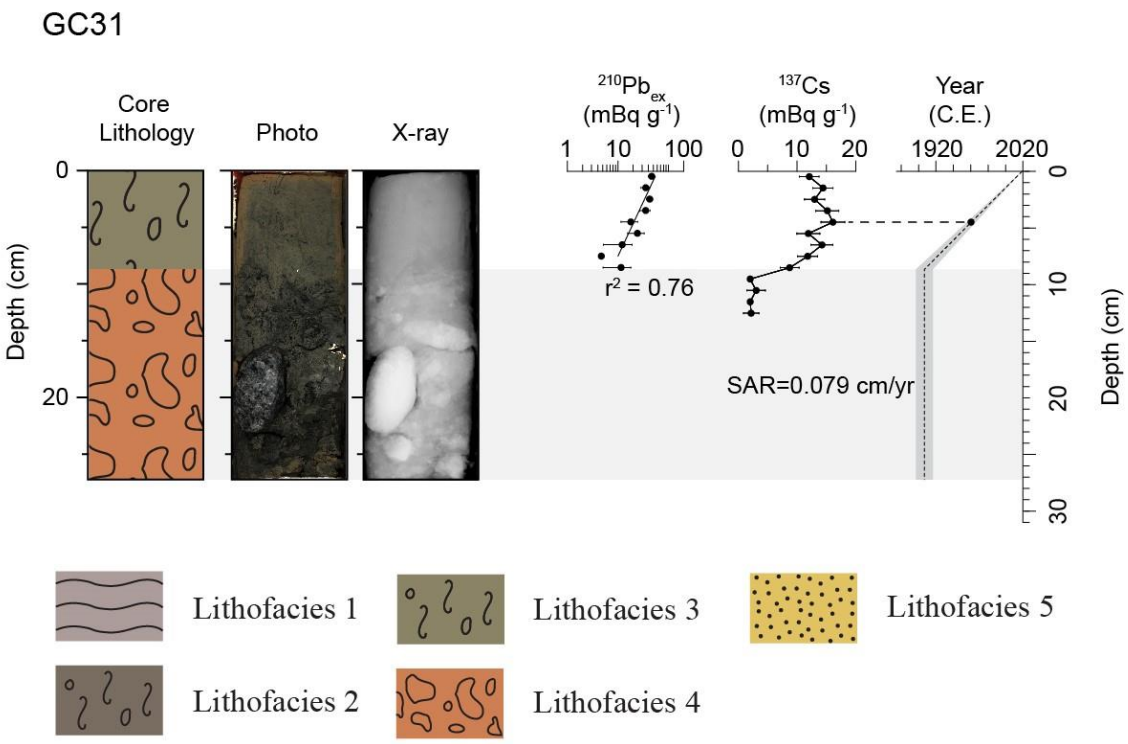

Figure 4.12: Core 031 lithofacies, photo and X-ray with a landslide deposit identified in core. ^{210}Pb and ^{137}Cs activities with the sediment accumulation rate (SAR) corrected using the nuclear weapons test (NWT) age of 1963.

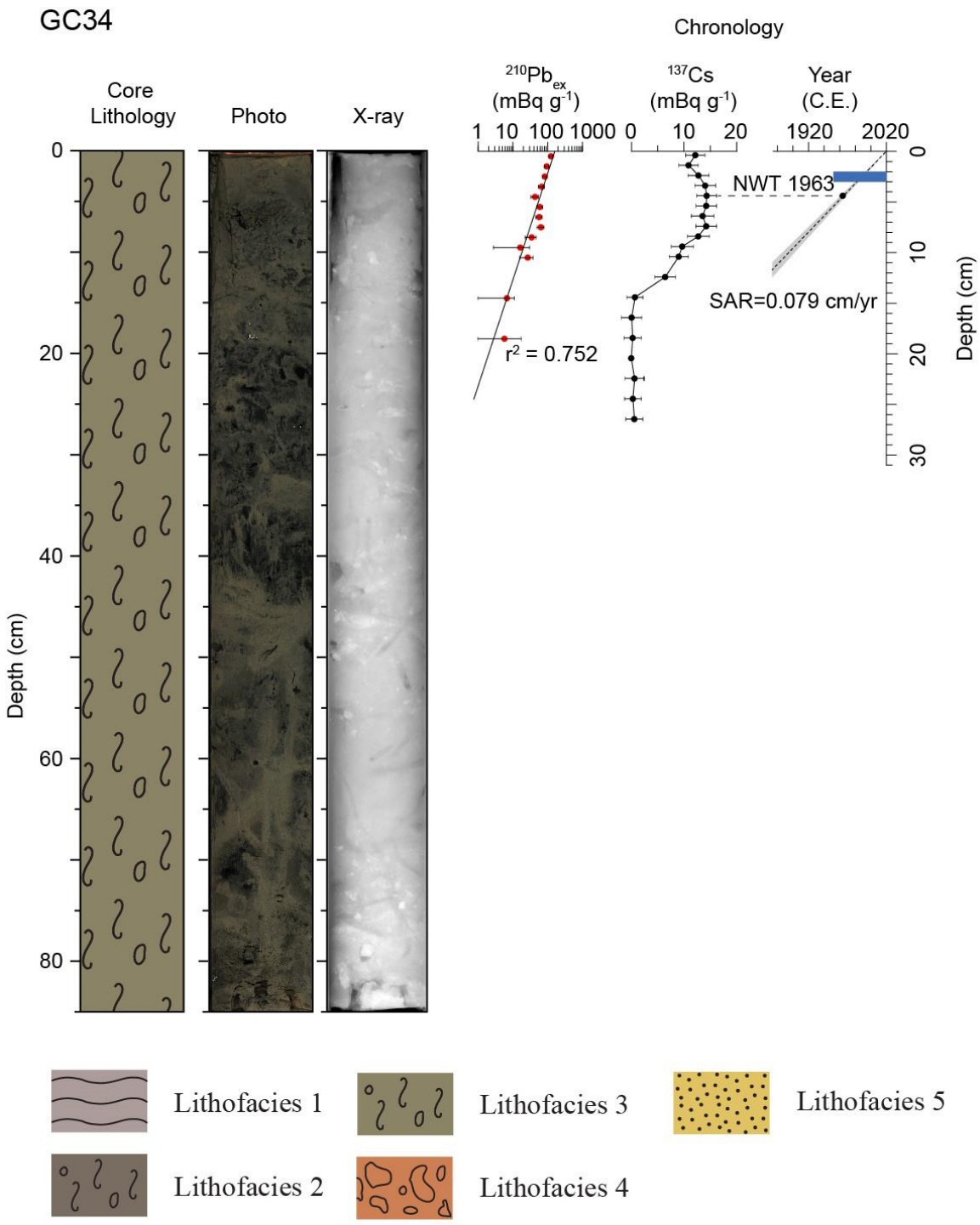

Figure 4.13: Core 034 lithofacies, photo and X-ray. ^{210}Pb and ^{137}Cs activities with the sediment accumulation rate (SAR) corrected using the nuclear weapons test (NWT) age of 1963. The modern radiocarbon age is shown by the blue line.

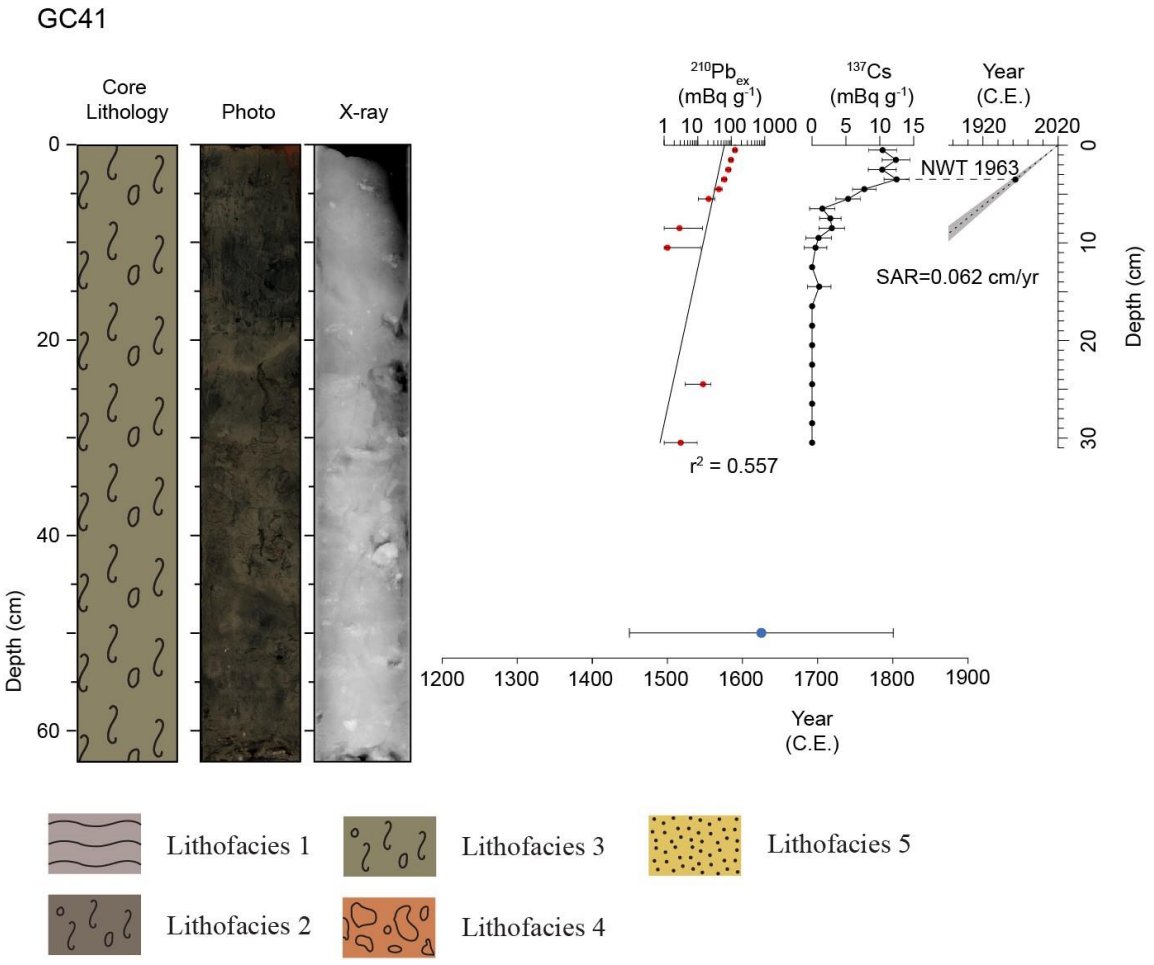

Figure 4.14: Core 041 lithofacies, photo and X-ray. ^{210}Pb and ^{137}Cs activities with the sediment accumulation rate (SAR) corrected using the nuclear weapons test (NWT) age of 1963. The radiocarbon age and 2-sigma range are shown by the blue dot.

4.3.3 Submarine landslide ages

Using sedimentation rates derived from ^{14}C dating, ^{210}Pb and ^{137}Cs activities, a total of 11 landslides could be dated throughout the fiord; eight of the 11 dated submarine landslides were calculated to have occurred within the last 500 years, with four landslides found to be modern events (post-1950) (Table 4.3).

Table 4.3: Landslide ages calculated from SARs determined through ^{210}Pb and ^{137}Cs activities and radiocarbon dating. Criteria for confidence levels: Low- located near fiord-head delta, identifiable in sub-bottom and multibeam bathymetry but not in core; medium- the age is misleading and most likely represents a modern landslide; and high- landslide deposit is identifiable in core as well as multibeam bathymetry.

Core	Method	Sample interval	Landslide interval depth (cm)	^{14}C age (cal BP)	SAR (cm/yr)	Landslide age (cal BP)	Confidence level
0015	^{14}C	38-39	20-24	184	0.183	109	Low
0017	^{14}C	68	36-39	162	0.432	83	Low
0020	^{14}C	49-51	51-60	Modern	-	0	Low
0030	$^{210}Pb/^{137}Cs$	0-30	10-18	-	0.097	43	High
0031	$^{210}Pb/^{137}Cs$	0-12	9-28	-	0.079	58	High
0034	$^{210}Pb/^{137}Cs$	0-26	300	-	0.079	3775	Low
0037	^{14}C	3-5	0-9	Modern	-	0	High
0041	$^{210}Pb/^{137}Cs$	0-30	100	-	0.062	1625	Low
0043	^{14}C	40-41	100	1135	0.035	2795	Low
0047	^{14}C	22-25	0-31	4079	-	0	High
0048	^{14}C	2-3	0-22	758	-	758	Medium

Included in these modern landslides is the landslide interval identified in core 048. The calibrated age of 758 cal BP is interpreted as a maximum age, however, with no overlying hemipelagic sedimentation, this landslide deposit is interpreted as a modern event. ^{210}Pb and ^{137}Cs modelling is used to calculate ages of landslides identified within cores 030 and 031. The oldest landslide deposit is covered by 3 m of sediment, as shown in sub-bottom data, and it is dated to approximately 4000 cal BP using the sedimentation rates determined from the sediment core 034 (Table 4.3; Figure 4.14). The thickness of the sediments overlying the largest landslide, called the Kolik River landslide, was also

estimated through sub-bottom data to one metre, and consequently the age of the landslide is tentatively dated to 1500-2000 cal BP. A new gravity core collected in August 2021 (Normandeau et al., 2022b) which penetrates through the overlying sediments and into the Kolik River landslide deposit will provide additional and potentially more precise dating.

For each of the eleven landslide ages, a confidence level (low, medium, and high confidence) was assigned (Table 4.3). The confidence level was introduced to account for factors that may influence the interpretation of landslide ages but can only be evaluated qualitatively, for example the clear identification of a landslide deposit in the sediment cores or in a sub-bottom profile, confusion between possible turbidites from the fiord-head delta, poor resolution of sub-bottom profiles, and uncertainty from the dating method.

4.4 BPISD of landslides

The standard deviation of the BPI (BPISD) of each landslide deposit is used to quantify the surface roughness of each deposit with a surface expression at the seafloor (Figure 4.15). Overall, the BPISD of all landslide deposits ranges from 0.037-0.17. In Figure 4.15, deposits with a high BPISD corresponding to a high surface roughness are shaded red, whereas deposits shaded yellow indicate a low BPISD, representing a low surface roughness (Figure 4.15). High roughness suggests a younger age whereas low roughness suggest an older age of landslides.

Each of the dated submarine landslide deposits have a corresponding BPISD value and can be used to determine the precision of BPISD as a proxy for landslide age (Figure

4.16). Of the landslide deposits dated in this study, recent landslides (cores 030, 037, 047, 048 in Table 4.4) have a wider range of BPISD values than older deposits (cores 034, 041, 043 in Table 4.4). The intervals tentatively interpreted as landslides in cores 015, 017, and 020 are not included in this BPISD analysis due to low confidence in the correct interpretation of the landslide interval as they are located near the fiord head delta. The landslide interval identified in core 031 is also not included as artefacts in the bathymetric data artificially increase the roughness analysis.

Plotting the absolute ages against their BPISD value enables a linear regression analysis which yields the equation in Figure 4.16, where BPISD refers to the BPISD of a landslide deposit and age refers to the calculated age of that same landslide ($R^2 = 0.364$; $p > 0.05$). From this equation, the age of the landslides can be calculated based on the associated BPISD value (Table 4.4). The difference, shown as a percentage, is determined between the calculated ages and the absolute ages to demonstrate the accuracy of the BPISD analysis. A smaller percentage represents a more accurate calculation of the landslide age.

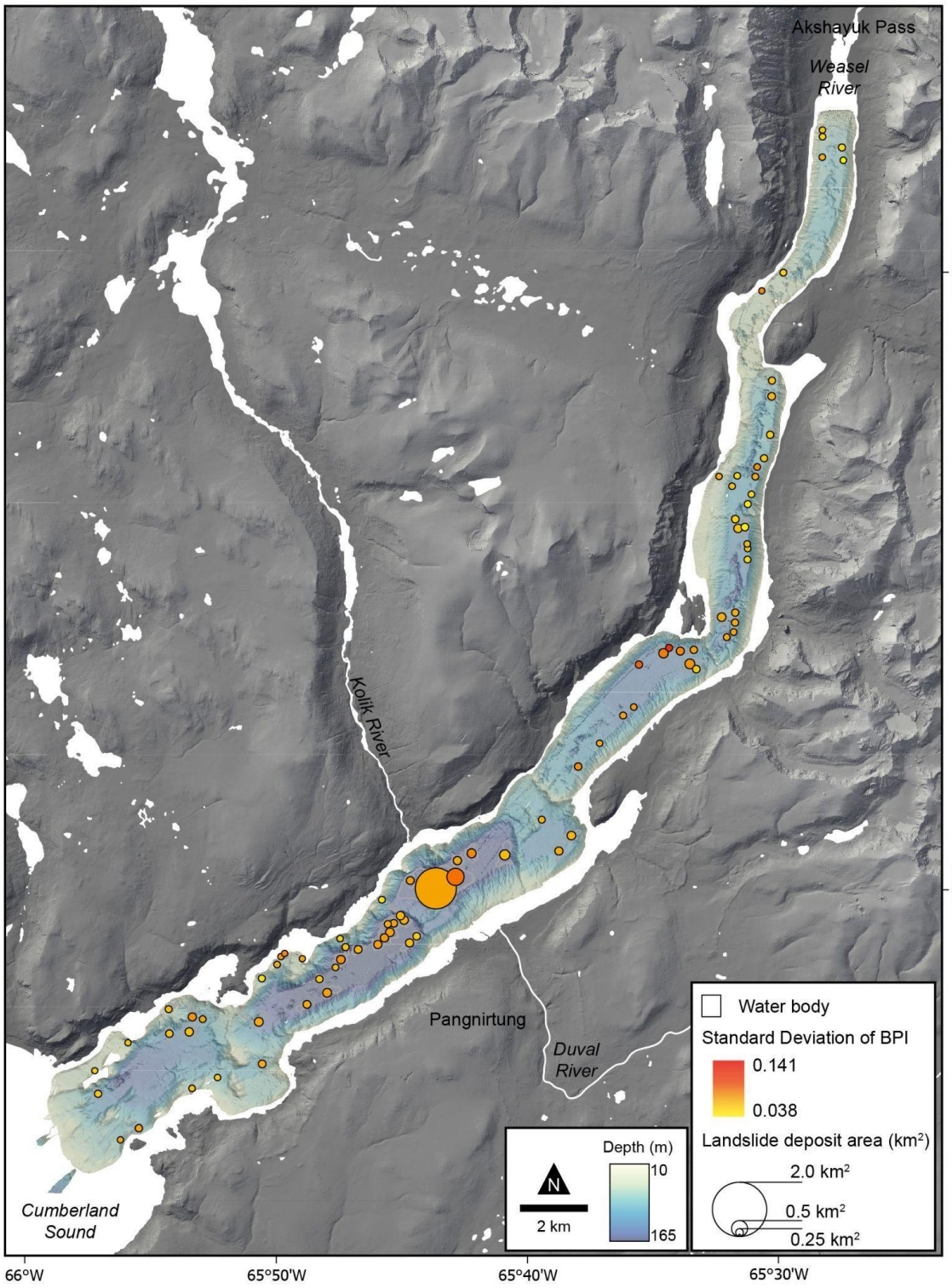

Figure 4.15: Standard deviation of the bathymetric position index (BPISD) for landslide deposits within Pangnirtung Fiord. A higher BPISD (red) represents a higher surface roughness and a lower BPISD (yellow) represents a lower surface roughness.

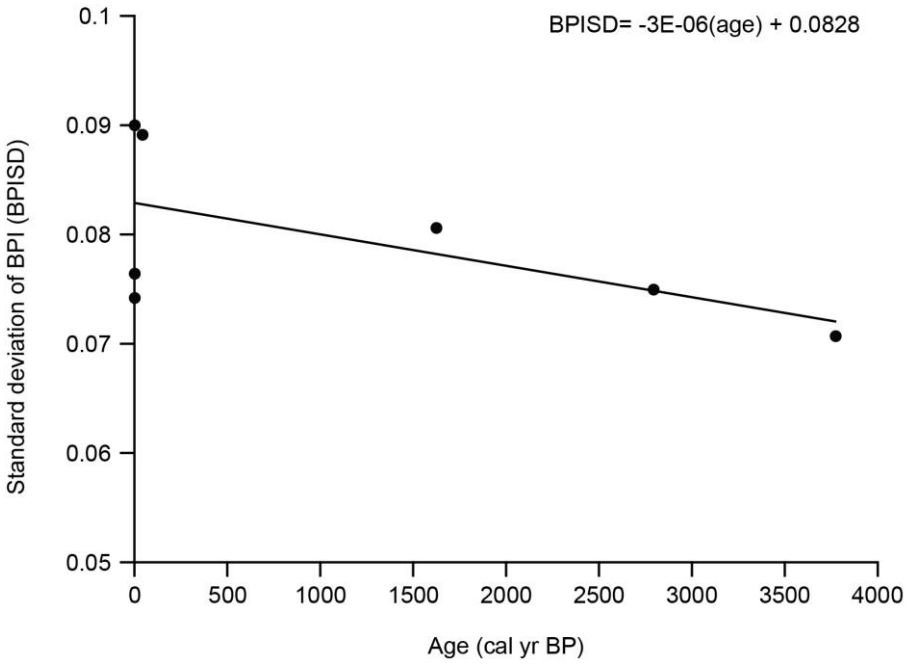

Figure 4.16: Standard deviation of the bathymetric position index (BPISD) plotted against the ages of the landslide deposits. Landslides are identified based on their respective core number (see Table 4.4). The trendline represents the calculated ages of the landslides.

Table 4.4: Landslide BPISD values, absolute ages, and calculated ages with the percentage difference between values.

Slide No.	Associated Core	BPISD	Absolute slide age BP (before 1950 AD)	Calculated slide age (BP)	Error between absolute age and calculated ages (%)
50	030	0.089135	43	-2112	-5011
64	034	0.070692	3775	4036	7
70	037	0.074186	0	2871	287000
115	043	0.074967	2795	2611	-7
127	041	0.080598	1625	734	145
159	047	0.076406	0	2131	213000
162	048	0.089996	0	-2399	-239900

CHAPTER 5 DISCUSSION

5.1 When did submarine landslides occur in Pangnirtung Fiord?

To date, studies of submarine landslides identified at the seafloor of the remote fiords of Baffin Island have mostly resulted in detailed geomorphological descriptions, with limited age constraints (Brouard and Lajeunesse, 2019; Deering et al., 2020; Bennett et al., 2021). This is mostly due to the difficulty of obtaining organic samples that can be dated using radiocarbon techniques and the logistics required to collect multiple cores on many landslides in remote locations. In Pangnirtung Fiord, previous studies have proposed the presence of submarine landslides from low resolution single-beam echosounder data (Gilbert, 1978). However, no chronological constraints exist for these landslides. The importance of the landslide ages calculated in this study is twofold: 1) they provide context for better evaluating triggering mechanisms and preconditioning factors based on the geological history of the area, and 2) given sufficient resolution, they allow estimation of landslide recurrence times.

5.1.1 Using radiometric dating to determine submarine landslide age

The timing of recent submarine landslides can be constrained through radiometric dating or repeat seafloor mapping. For example, in a recent study from nearby Southwind Fiord, Normandeau et al. (2021a) used repeat mapping to show how a new submarine landslide was triggered by an iceberg colliding at the seafloor. This study also showed that submarine failure events are recurrent hazards in Baffin Island fiords and that modern triggers are responsible for their presence. Prior to the 2019 survey, multibeam bathymetric data in Pangnirtung Fiord were available only for the deepest portions of the

fiord and at its mouth (Hughes Clarke et al., 2015), where no significant changes of the seafloor topography have been observed. Consequently, unlike Normandeau et al. (2021a) and other recent studies using repeat mapping to deduce both slope failure timing and triggering mechanisms (Clare et al., 2016; Mountjoy and Micallef, 2018), the landslide ages determined in this study using ^{14}C dating, and ^{210}Pb and ^{137}Cs activities (Table 4.3) are the only conclusive evidence of modern events occurring in Pangnirtung Fiord. This recent landslide activity not only indicates that underwater landslides are an ongoing geohazard but also that geological processes that are currently occurring in the fiord can be investigated to evaluate potential trigger mechanisms. Additionally, the landslides found to occur 2000–4000 years ago show that submarine landslides have likely periodically occurred since deglaciation. The three landslides dating back to the mid-late Holocene, which are also larger in size compared to the more recent ones, could be instead related to other processes which may relate to the deglaciation history of the fiord such as isostatic rebound induced seismic events and the pro-glacial geomorphology and sedimentation, as suggested in other studies (Stacey et al., 2020).

Landslide ages can also be used to determine the frequency of the landslides and evaluate possible controls posed by environmental factors. As discussed in Urlaub et al. (2013), localised studies, such as this study in Pangnirtung Fiord, are critical in determining the impact environmental changes have on the frequency of landslide events. These smaller scale studies allow more accurate examinations of climate-influenced processes and their influence on the frequency of landslides. However, to capture a complete understanding of the frequency of submarine landslides in Pangnirtung Fiord, integrating longer cores

with higher resolution sub-bottom profile data or legacy seismic reflection data (GSC expedition 85-027) is required.

5.1.2 Using the BPISD as a proxy for submarine landslide age

Without extensive radiometric dating of many submarine landslides, and a lack of subsurface resolution of multiple, vertically stacked, landslides, this study attempted to determine a proxy for age based on the surface roughness of each landslide. Strupler et al. (2019) found that, in a study of submarine landslides in Lake Zurich (Switzerland), dating based on BPISD can produce a first-order assessment of landslide ages, distinguishing between recent landslides that occurred within the last 150 years and sub-recent landslides. Of the landslide deposits dated in this study (Figure 4.16), recent landslides (cores 030, 037, 047 and 048 in Table 4.4) have a wider range of BPISD values than older deposits (cores 034, 041 and 043 in Table 4.4). The intervals tentatively interpreted as landslides in cores 015, 017 and 020 are not included in this BPISD analysis due to low confidence in the correct interpretation of the landslide interval, as they are located near the fiord-head delta. The landslide interval identified in core 031 is also not included, as artifacts in the bathymetric data prevent accurate surface-roughness analysis. The wide range of BPISD values in recent landslides is reflected by large differences between the absolute and calculated ages of the deposits. In older deposits, their calculated age is a more accurate representation of their absolute age. However, this does not result in a sufficient differentiation of BPISD values to enable the use of surface roughness of the landslides as a proxy for landslide age.

One key difference between the BPSID analysis in Pangnirtung and the one conducted by Strupler et al. (2019) is the location of the surface roughness analysis. In Strupler et al. 2019), the analysis is done on the glide plane. The glide plane should have a similar surface texture from one type of landslide to another. However, In Pangnirtung Fiord, many of the glide planes were not fully mapped, preventing the comprehensive use of this method. Therefore, the deposit was instead analysed. However, the large range of landslide surface-roughness values is most likely caused by the different types of landslides identified in the fiord, not their age, along with variations in slope and landslide run-out (total length). Additionally, possible variations in sedimentation rates of the overlying sediment, not captured in the dating results from this study, may cause less accurate age predictions of submarine landslides. Despite this, the surface roughness analysis suggests that landslide deposits near each other with different relative surface roughness values may be asynchronous, allowing for a semi-quantitative interpretation of the sequence of events. For example, Figure 4.5a highlights shallow water landslides occurring downslope of a subaerial debris fan. Examining these landslides in more detail, while considering the BPISD values in addition to the bathymetric and slope data, there is evidence of landslide reactivation causing a more recent slope failure (Figure 5.1).

The age constraints calculated in this study provide a general understanding of the submarine landslide timing in Pangnirtung Fiord. There is a bias toward modern landslides because only short sediment cores were collected; therefore, many buried landslide deposits identified in the multibeam data are excluded from this analysis. However, these results show that most of the fresh-looking landslides (BPISD >0.085) mapped on the multibeam bathymetry are likely to be younger than 500 years old. A lack

of submarine landslide recurrence highlights the need for a higher resolution subsurface dataset, paired with longer sediment cores. Additionally, repeat mapping, especially of the near shore submarine slopes, may provide evidence of present-day submarine landslides that can be used to determine active triggering mechanisms.

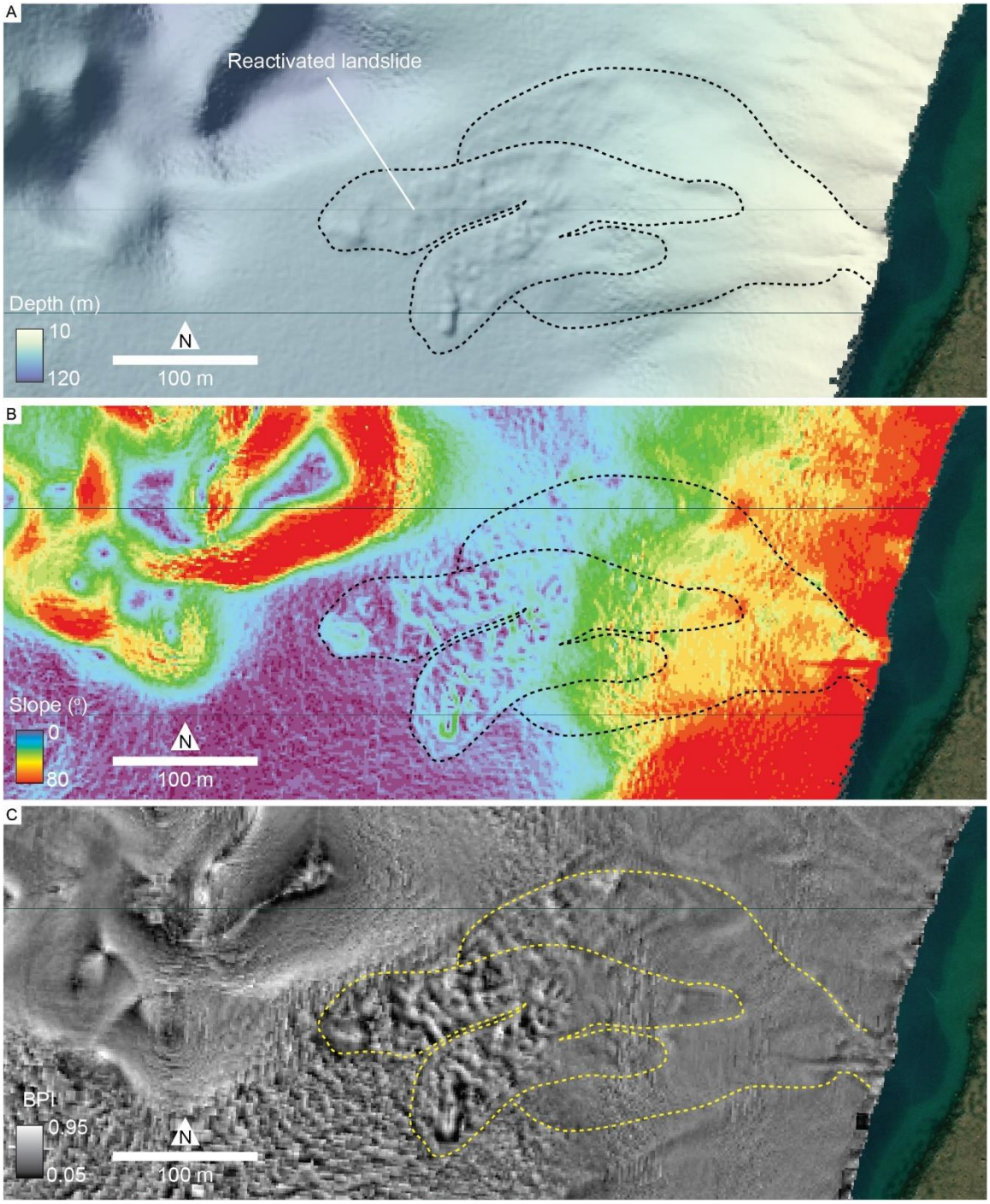

Figure 5.1: A reactivated submarine landslide overlain on a) multibeam bathymetric data; b) slope of the seafloor; and c) BPI of the seafloor.

5.2 What are the preconditioning and triggering mechanisms of submarine landslides in Pangnirtung Fiord?

To help evaluate potential preconditioning and triggering mechanisms, this study examined the morphometric parameters, spatial distribution, and age constraints of submarine landslides together with environmental and geological factors. Furthermore, additional factors considered include the proximity to fluvial sources, the slope, the tidal range, regional and local seismicity, and subaerial processes (e.g., L'Heureux et al., 2010; Clare et al., 2016; Broom et al., 2019; Deering et al., 2019).

As an initial discerning factor, the 'minimum water depth' measured parameter divides the mapped landslides into deep water and shallow water environments (Figure 4.4; Figure 4.5) as shallow water landslides occurring at less than 40 m water depth are likely triggered by different factors than deep-water ones occurring below 40 m water depth. The shallow water environments are then subdivided based on the submarine landslides relationship to the subaerial environment (Figure 4.5). Environmental factors in the nearshore may promote or trigger failures so understanding this relationship helps interpret trigger mechanisms. Based on this initial categorization of submarine landslide environments in Pangnirtung Fiord, four broad categories emerge that reflect their connection to trigger mechanisms and preconditioning factors (Figure 5.2). The four categories include: 1) deep-water; 2) shallow-water, connected to subaerial debris flow fan; 3) shallow-water, connected to fluvial source; and 4) shallow-water, non-subaerially influenced. These four categories serve to both highlight the most prominent triggers of submarine landslides in the fiord (Figure 5.3), as well as provide a basis for future research and mapping.

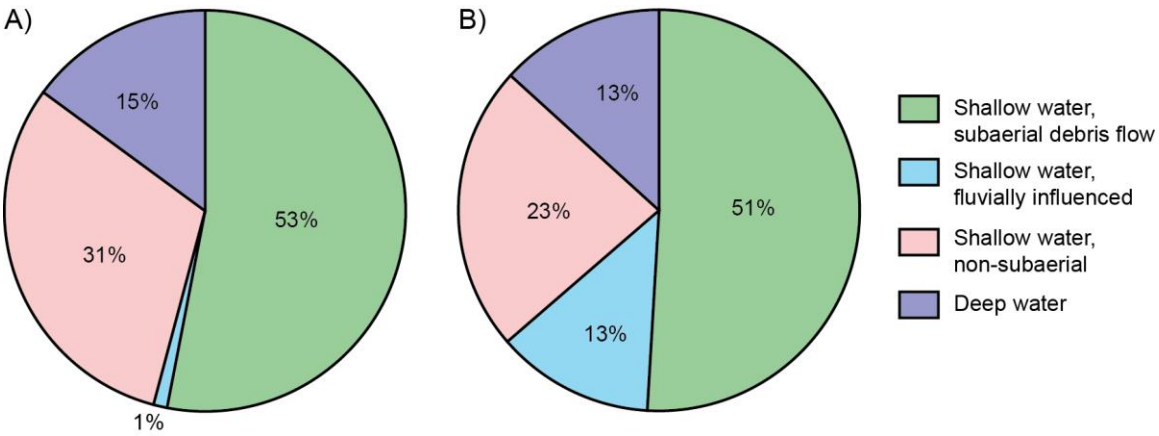

Figure 5.2: Proportion of interpreted triggering mechanisms of submarine landslides in Pangnirtung Fiord based on a) number of landslides, and b) total area of landslides in each trigger classification.

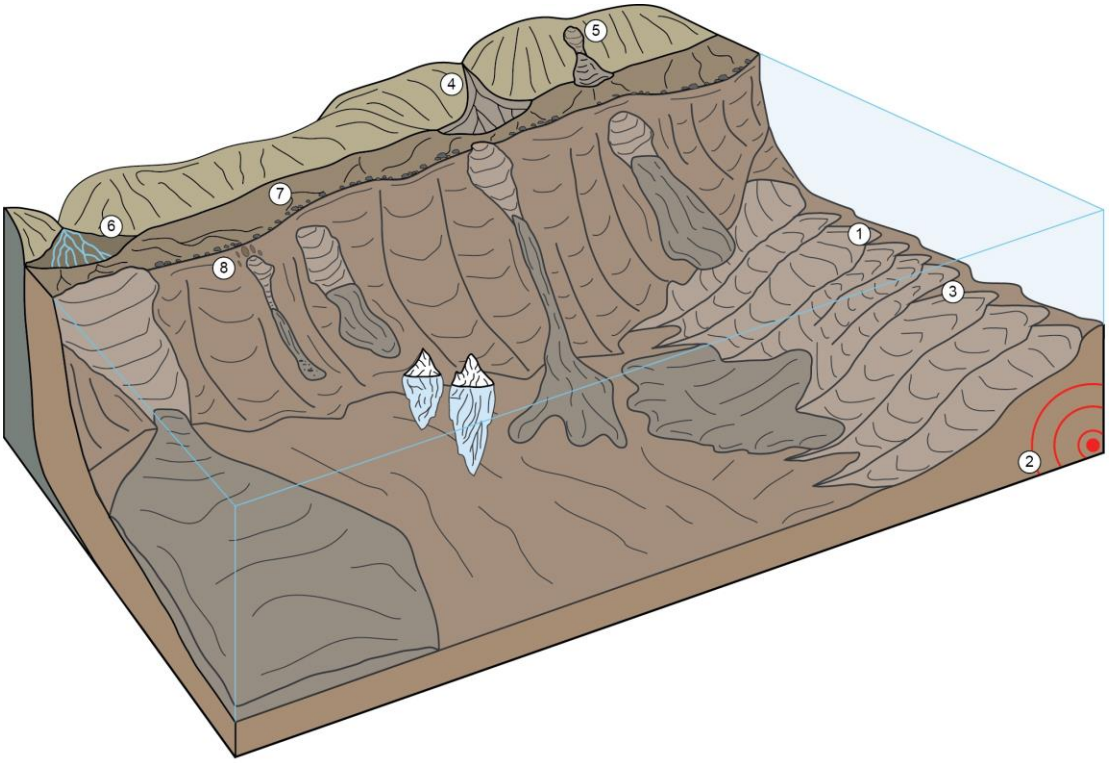

Figure 5.3: Conceptual model of preconditioning and triggering mechanisms of submarine landslides in Pangnirtung Fiord. 1) Oversteepening; 2) Earthquakes; 3) Ice-core melt; 4) Subaerial debris flows; 5) Subaerial rockslides; 6) River flooding; 7) Tidal loading; 8) Sea-ice and iceberg groundings.

5.2.1 Deep-water trigger mechanisms

Submarine landslides initiated in deep water (Figure 4.5a) constitute 15% of the mapped landslides and are not likely to have a shallow water or subaerial trigger (Figure 5.2). Subaerial and fluvial triggers likely have no influence because the depletion zones are identified along the middle of sills where the shallowest possible head scarp is far deeper (greater than 40 m) than wave or tidal influence, and far enough away from the fiord sidewalls and major sediment inputs. Many of these landslides appear to be the result of slope failures in sediments overlying glacial sediments that make up the sills and recessional moraines. The most probable triggers for these deeper water landslides are a combination of isostatic rebound induced seismicity during the retreat of the glaciers in Pangnirtung Fiord and the oversteepening of slopes during sill formation. For example, the largest landslides identified in the Douglas Channel (British Columbia) fiord were preconditioned by the oversteepening of glacial material, causing landslides during deglaciation (Stacey et al., 2020). Along with oversteepening of slopes, ice-core melt in the recessional moraines (Mattson and Gardner, 1991) may also promote instability in sediments leaving sediment susceptible to seismic triggers (e.g., Clare et al., 2016). Additional age constraints for these older landslides would provide the necessary evidence to point to a seismic trigger, as coeval landslides are indicative of a seismic trigger (e.g., Bellwald et al., 2016; Brooks et al., 2016).

5.2.2 Shallow-water, subaerial debris flow-influenced

Subaerial debris flows have been suggested as a potential trigger mechanism of shallow submarine landslides (Bellwald et al., 2016; Deering et al., 2019). Sudden rapid colluvial and alluvial outwash into the shallow water would increase the pore pressure and potentially increase shear stress in the shallow water sediments. Deering et al. (2019) suggested subaerial slope failures are a contributing triggering mechanism for most submarine landslides identified in Frobisher Bay, Baffin Island. In Pangnirtung Fiord, the shallow minimum water depth of most landslide depletion zones also suggests a possible subaerial influence. Conclusive evidence of a connection between the subaerial environment and submarine landslides in the fiord is shown in satellite imagery from 2019 overlain by the multibeam bathymetry (Figure 4.5b). The proximity of the submarine landslide head scarps to the subaerial debris fan demonstrates a clear connection between subaerial debris flows and submarine landslide occurrence. Based on ^{210}Pb geochronological data, the middle landslide in Figure 4.5b, with the highest surface roughness, occurred in the early 20th century (Core 30; Figure 4.11).

Building on these initial findings, subaerial susceptibility modelling of Pangnirtung Fiord (Normandeau et al., 2022a) can be used to understand which of the other submarine landslides were potentially triggered from subaerial debris flows. Normandeau et al. (2022a) employed subaerial landslide susceptibility modelling at the scale of the fiord to identify potential source and propagation areas for subaerial debris flow hazards following the steps of Horton et al. (2013). This subaerial landslide susceptibility modelling identifies the areal extent which may be affected by a debris flow if one were to occur upslope, and categorizes these areas based on the relative probability that it

could be affected. Figure 5.4 shows the results of subaerial susceptibility debris flow modelling for the subaerial debris flow example shown in Figure 4.5b. The area classified as a potential zone for ‘large torrents’, shaded black, is upslope of the submarine landslides with a clear subaerial connection. This example demonstrates that this subaerial debris flow susceptibility modelling can be used to quantify the number of submarine landslides potentially triggered by subaerial processes. Examining the entire fiord, Figure 5.4 presents the relative probability of the modelled subaerial landslides entering the fiord as well as the location of the submarine landslide deposits identified in the bathymetry. Those landslides located directly downslope of the modelled subaerial debris flows make up 53% of submarine landslides (Figure 5.2). Overall, this classification of submarine landslides presents a definitive relationship between submarine landslides and the subaerial environment and illustrates the impact subaerial debris flows have as a major triggering mechanism of submarine landslides in Pangnirtung Fiord.

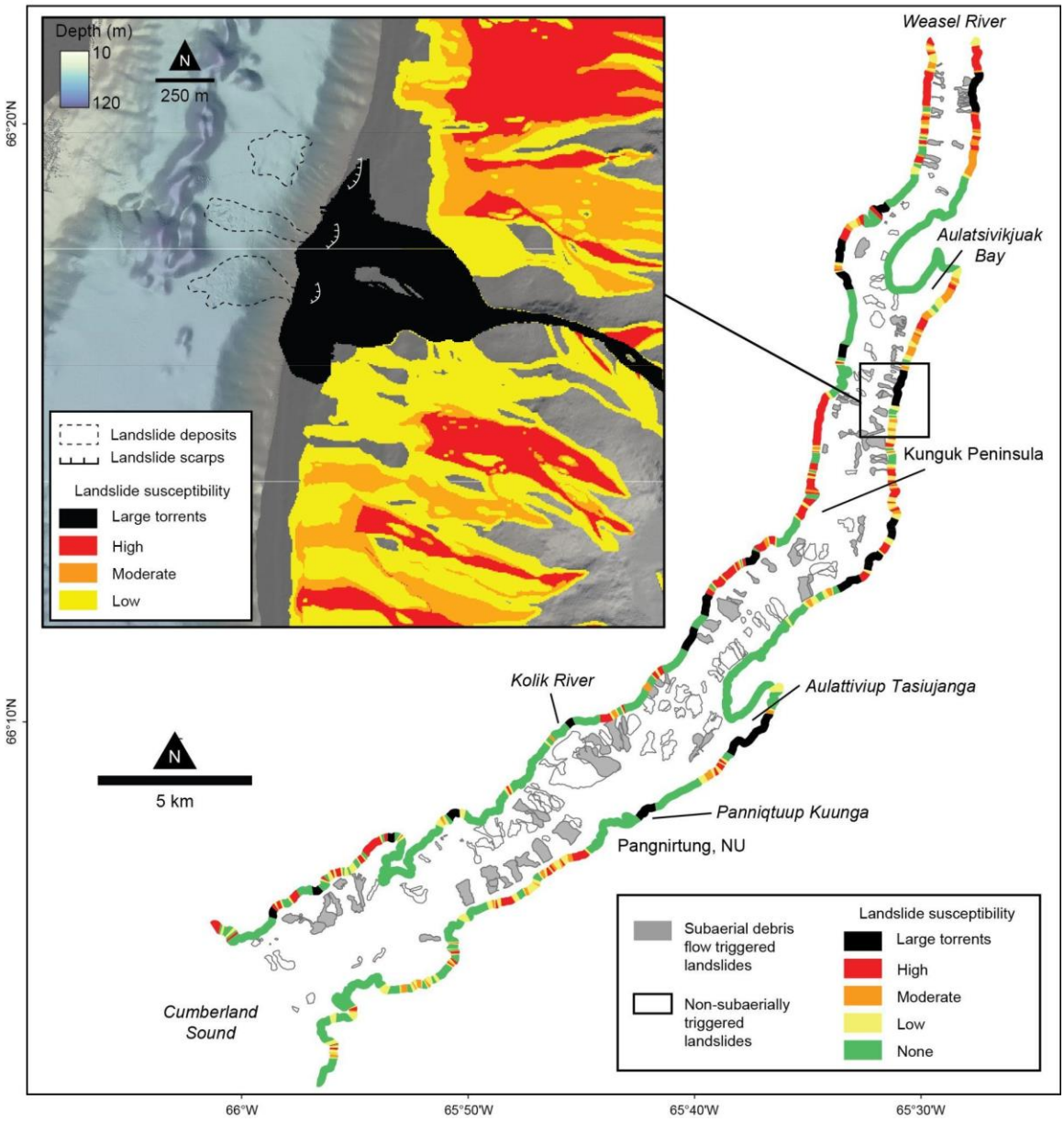

Figure 5.4: The relative probability of modelled subaerial debris flows (Normandeau et al., 2022a) extending to the coast and mapped submarine landslide deposits. Inset-Shallow-water, subaerially debris flow-influenced submarine landslides shown in Figure 4.5b, with subaerial debris flow susceptibility modelling results overlain. Digital elevation model was created from DigitalGlobe, Inc.

5.2.3 Shallow-water, fluvial trigger mechanisms

Landslides located downslope of fluvial sources account for 1% of the mapped landslides in the fiord, however they represent 13% of the total area of all submarine landslides in Pangnirtung Fiord (Figure 5.2). Delta collapse during a time of high discharge of the

Kolik River or an earthquake is the likely cause of the Kolik River landslide (Figure 4.5c). River discharge alone can precondition the sediments or trigger a landslide through rapid accumulation of sediment producing overpressure or by producing sufficient shear stress on the deltaic sediments (Clare et al., 2016). High levels of sediment laden fluvial discharge can both erode and increase the sediment load on the river delta, especially at periods of low tide (Prior and Bornhold 1989; Bornhold et al., 1994). The sediment concentration is unknown for the Kolik River at normal and peak flow, however, the lack of fluvial discharge in the winter months means that this trigger is more likely to occur during the spring freshet, or other periods of rapid rise in temperature. On the other end, an earthquake may be the ultimate trigger of slope failure in these preconditioned deltaic sediments. However, these external and singular triggers are not necessarily required to cause a delta collapse as identified for a similar landslide in Lake Brienz, Switzerland, which was triggered by normal sediment accumulation and resulted in a 0.5 m tsunami wave (Girardclos et al., 2007).

Elevated river discharge can also act as a sufficient preconditioning mechanism of submarine landslides due to higher rates of sediment supply which raise sediment pore pressures as observed in Bailey et al. (2021). In Pangnirtung Fiord, high sediment supply from rivers, alluvial fans and ephemeral rivers may provide the necessary sediment supply to elevate pore pressures in the near shore fiord sediments. Additionally, these sediment sources may provide sequences of coarse- and fine-grained layers with differences in porosity and permeability that can act as weak layers within fiords (Gatter et al., 2021). The short sediment cores collected in the study did not warrant detailed geotechnical analysis as the results would not provide an accurate representation of the

failed sediment. However, evidence of these grain size differences is highlighted by changes in bulk density and magnetic susceptibility, and identified in x-radiographs, and sedimentological descriptions (Appendix B).

5.2.4 Shallow-water, non-subaerial trigger mechanisms

Thirty-one percent of landslides (Figure 5.2) are initiated in shallow water but do not have an obvious relationship to a subaerial trigger (Figure 4.5d). Like the previous classification, the head scarps are identified in shallow water or the assumed head scarps are too shallow to map; however, these landslides do not occur downslope of an area modelled to be susceptible to subaerial landslides. In addition, there is often a wide intertidal zone upslope of the landslides. These landslides are also generally elongated, suggesting a point-source trigger. Likely point-source triggers for these landslides include sea-ice and iceberg groundings (Normandeau et al., 2021) and tides (Johns et al., 1985; Chillarige et al., 1997). The sill at the mouth of the fiord acting as a barrier to icebergs of a keel depth greater than 25 m (Figure 4.1) eliminates the possibility of icebergs triggering deep water landslides in Pangnirtung Fiord. However, sea-ice and smaller iceberg groundings, combined with low tide level are suggested as a viable preconditioning and triggering mechanism for these shallow-water landslides. Low tides can produce excess pore pressures in the sediment near the lip of the intertidal zone as Clare et al. (2016) suggested for the Squamish River Delta of Howe Sound, British Columbia. The comparably large tidal range of 2.7 - 6.7 m in Pangnirtung Fiord may be sufficient to precondition the shallow water fiord flanks for failure. At the Squamish Delta, Clare et al. (2016) found that the rupture surfaces occurred below approximately 10 metres of sediment, making tidal drawdown likely less effective, however, in

Pangnirtung Fiord, the relatively small size of most landslides (Table 4.1; Figure 4.7) may be the result of shallow rupture surfaces, meaning the tidal influence may be more effective at preconditioning. Paired with this change in pore pressure, sea-ice and iceberg groundings may ultimately increase the vertical load on sediment and trigger these landslides.

Earthquakes are a possible trigger mechanism, although they would likely cause a wider area of sediment to fail thus presenting lower elongation values, which is not supported by the morphometric measurements (Table 4.1; Figure 4.7). These trigger mechanisms may also trigger the previously described submarine landslides with perceived connections to fluvial and subaerial debris flows. These subaerial debris flows and rivers transport sediment to the marine environment, preconditioning the slopes for failure, with these shallow-water, non-subaerially influenced triggers ultimately triggering a landslide.

5.3 Can climate change increase landslide frequency?

As a result of climate change induced alterations to the Arctic hydrological and sedimentological cycles (i.e., Peterson et al., 2002; Zhang et al., 2006; Arctic Council 2016; Comiso et al., 2017; Noël et al., 2018; McCrystall et al., 2021; Syvitski et al., 2022), an increase in climate-influenced preconditioning and triggering mechanisms may cause more frequent submarine landslides in Pangnirtung Fiord in the future. An increase in rain precipitation, and rapid snowmelt events has been observed in the area surrounding Pangnirtung Fiord (Gilbert and McKenna Neuman, 1988; Environment Canada, 2009), while recent Arctic climate modelling suggest rain-dominated precipitation one to two decades earlier than previous models (McCrystall et al., 2021).

These elevated levels of precipitation may result in increased frequency of high fluvial outwash events and debris flows into the fiord. Based on the strong relationship between subaerial debris flows and river locations to submarine landslide distribution, this increase in subaerial debris flows may result in the preconditioning and triggering of more frequent submarine landslides in Pangnirtung Fiord. A potentially increasing occurrence of subaerial debris flows may also pose an additional risk of subaerial landslide generated tsunami waves, however; further investigation into this hazard is required. Warmer sea and air temperatures will drive a reduction in sea-ice thickness, as well as earlier and more frequent sea-ice break-up along the fiord margins (Comiso et al., 2017). Early break-up and more frequent break-up of sea-ice may also result in increased movement of sea-ice along the intertidal zone, transporting sediment to the edge of intertidal zone, possibly resulting in an unstable boulder barricade. More frequent break-ups may also result in a longer open water season at the mouth of the fiord, allowing icebergs to enter the fiord, potentially triggering shallow-water landslides. Furthermore, the rapid melting of the nearby Penny Ice cap (Zdanowicz et al., 2012; Schaffer et al., 2020) has potential to increase seismic activity in the area due to isostatic rebound, although more detailed isostatic rebound studies and seismic monitoring are required for a more complete understanding of the consequences. With evidence of submarine landslides occurring within 86% of Baffin Island fiords (Bennett et al., 2021) climate change may have a similar impact throughout Baffin Island, leading to potential increases in the hazard to low-lying communities.

Chapter 6 CONCLUSION

Landslides are proven geological hazards in high-latitude fiords. Landslide-generated tsunami waves of sufficient height can inundate coastal areas and damage low-lying infrastructure. Although there is no record of a landslide-generated tsunami occurring along the coast of Baffin Island to date, the existence of high-relief fiord sidewalls and mapped subaerial and submarine landslides in Pangnirtung Fiord provide the necessary elements seen in previous Arctic displacement-wave locations (e.g., Brothers et al., 2016; Gauthier et al., 2017; Higman et al., 2018). Without consideration of seafloor-sediment dynamics, submarine landslides can also damage seafloor infrastructure. This study of submarine landslides in Pangnirtung Fiord sought to provide an evaluation of the distribution, timing, and trigger mechanisms of these geohazards for the low-lying Arctic community of Pangnirtung, NU. Results of radiometric dating combined with an analysis of the surface roughness of the landslide deposits indicate that most landslides occurred within the last 500 years, and at least five have occurred since 1900. These age constraints guide preconditioning and triggering mechanism interpretations of submarine landslides. Dividing the submarine landslides into four environments helps discern the cause of these submarine landslides, producing four categories of triggers. The most abundant trigger mechanism is interpreted as subaerial debris flows entering the sea, causing a rapid influx of sediment and water, and triggering submarine landslides. An examination of subaerial debris flow susceptibility modelling shows that there is a clear relationship between the distribution of submarine landslides and the surrounding subaerial environment. This relationship demonstrates the need to integrate an evaluation of the subaerial environment when addressing geohazards in the high relief fiords of

Baffin Island. Although most submarine landslides do not appear to have the capacity to initiate a tsunami due to the reduced size, additional work is needed to determine the tsunamigenic potential of the larger submarine landslides observed in the fiord, such as the Kolik River landslide (Figure 4.5c). Considering that the majority of Baffin Island fiords have evidence of submarine landslides at the seafloor (Bennett et al., 2021), the categorized assessment of the potential triggering mechanisms provided through this study may be applicable to other Baffin Island fiords.

BIBLIOGRAPHY

Andrews, J.T., Jull, A.J.T., Donahue, D.J., Short, S.K., and Osterman, L.E. 1985. Sedimentation rates in Baffin Island fiord cores from comparative radiocarbon dates (Canada). Canadian Journal of Earth Sciences. 22, 1827–1834. https://doi.org/10.1139/e85-194

Aitken, A. E. 1982. Biophysical processes on the intertidal flats of Pangnirtung Fiord, Baffin Island, N.W.T. Kingston, Ontario, Queen's University. 223 pp.

Aitken, A.E., Gilbert, R. 1989. Holocene Nearshore Environments and Sea-Level History in Pangnirtung Fiord, Baffin Island, N.W.T., Canada, Arctic and Alpine Research. 21, 1, 34–44. https://doi.org/10.2307/1551515

Arctic Council 2016. Carson, M., Peterson, G. (Eds.), Arctic Resilience Report, Arctic Council. Stockholm Environment Institute and Stockholm Resilience Centre, Stockholm. https://oaarchive.arctic-council.org/handle/11374/1838 [July 2021]

Bailey, L.P., Clare, M.A., Rosenberger, K.J., Cartigny, M.J.B., Talling, P.J., Paull, C.K., Gwiazda, R., Parsons, D.R., Simmons, S.M., Xu, J., Haigh, I.D., Maier, K.L., McGann, M., and Lundsten, E. 2021. Preconditioning by sediment accumulation can produce powerful turbidity currents without major external triggers. Earth and Planetary Science Letters. 562, 116845. https://doi.org/10.1016/j.epsl.2021.116845

Basham, P.W., Forsyth, D.A. and Wetmiller, R.J. 1977. The seismicity of northern Canada. Canadian Journal of Earth Sciences. 14, 7, 1647–1667. https://doi.org/10.1139/e77-140

Barrie, J. V, Lewis, C. F. M., Parrott, D. R. & Collins, W. T. 1992. Submersible observations of an iceberg pit and scour on the Grand Banks of Newfoundland. Geo-Marine Letters. 12, 1–6. https://doi.org/10.1007/BF02092101

Bea, R., Wright, S., Sircar, P. and Niedoroda, A.W., 1983. Wave induced slides in South Pass Block 70, Mississippi Delta. ASCE Journal of Geotechnical Engineering. 109, 4, 619–644. https://doi.org/10.1061/(ASCE)0733-9410(1983)109

Bellwald, B., Hjelstuen, B.O., Sejrup, H.P., and Haflidason, H. 2016. Postglacial mass movements and depositional environments in a high-latitude fjord system – Hardangerfjorden, Western Norway. Marine Geology. 379, 157–175. https://doi.org/10.1016/j.margeo.2016.06.002

Bennett, R., Normandeau, A. and Campbell, D.C. 2021. Preliminary assessment of the distribution of submarine slope failures in Baffin Island fiords, Nunavut; in Summary of Activities 2020, Canada-Nunavut Geoscience Office. 73–80. https://cngo.ca/summary-of-activities/2020 [October 2021]

Bennett, M.R., Doyle, P., and Mather, A.E. 1996. Dropstones: Their origin and significance. Palaeogeography, Palaeoclimatology, Palaeoecology. 121, 331–339. https://doi.org/10.1016/0031-0182(95)00071-2

Bent, A.L. 2002. The 1933 Ms = 7.3 Baffin Bay earthquake: Strike-slip faulting along the northeastern Canadian passive margin. Geophysical Journal International. 150, 724–736. doi:10.1046/j.1365-246X.2002.01722.x

Bierman, P., Marsella, K., Patterson, C., Davis, P., Caffee, M., 1999. Mid-Pleistocene cosmogenic minimum-age limits for pre-Wisconsinan glacial surfaces in southwestern Minnesota and southern Baffin Island: a multiple nuclide approach. Geomorphology. 27, 25-39. https://doi.org/10.1016/S0169-555X(98)00088-9

Bornhold, B.D., Ren, P. and Prior, D.B. 1994. High-frequency turbidity currents in British Columbia fjords. Geo-Marine Letters. 14, 238–243, https://doi.org/10.1007/BF01274059

Bronk Ramsey, C. 2008. Radiocarbon dating: revolutions in understanding. Archaeometry. 50, 249–275, https://doi.org/10.1111/j.1475-4754.2008.00394.x

Brooks, G.R. 2016. Evidence of late glacial paleoseismicity from submarine landslide deposits within Lac Dasserat, northwestern Quebec, Canada. Quaternary Research (United States). 86, 184–199, https://doi.org/10.1016/j.yqres.2016.06.005

Broom, L.M., Campbell, D.C. and Gosse, J.C. 2017. Investigation of a Holocene marine sedimentary record from Pond Inlet, northern Baffin Island, Nunavut; in Summary of Activities 2017, Canada-Nunavut Geoscience Office. 93–104, http://cngo.ca/summary-of-activities/2017/ [October 2021]

Brothers, D.S., Haeussler, P.J., Liberty, L., Finlayson, D., Geist, E., Labay, K. and Byerly, M. 2016. A submarine landslide source for the devastating 1964 Chenega tsunami, southern Alaska. Earth and Planetary Letters. 438, 112–121, https://doi.org/10.1016/j.epsl.2016.01.008

Brouard, E. and Lajeunesse, P. 2019. Submarine geomorphology of the northeastern Baffin Island fiords and cross-shelf troughs. Journal of Maps. 15, 2, 662–676, https://doi.org/10.1080/17445647.2019.1647302

Bruel, R. and Sabatier, P. 2020. serac: An R package for ShortlivEd RAdionuclide chronology of recent sediment cores. Journal of Environmental Radioactivity. 225, 106449. https://doi.org/10.1016/j.jenvrad.2020.106449

Bryn, P., Berg, K., Forsberg, C.F., Solheim, A., and Kvalstad, T.J. 2005. Explaining the Storegga Slide. Marine and Petroleum Geology. 22, 11–19. https://doi.org/10.1016/j.marpetgeo.2004.12.003

Canals, M., Lastras, G., Urgeles, R., Casamor, J.L., Mienert, J., Cattaneo, A., de Batist, M., Haflidason, H., Imbo, Y., Laberg, J.S., Locat, J., Long, D., Longva, O., Masson, D.G., Sultan, N., Trincardi, F., and Bryn, P. 2004. Slope failure dynamics and impacts from seafloor and shallow sub-seafloor geophysical data: Case studies from the COSTA project. Marine Geology. 213, 9–72. https://doi.org/10.1016/j.margeo.2004.10.001

Chillarige, A.R.V., Morgenstern, N.B., Robertson, P.K. and Christian, H.A. 1997. Seabed instability due to flow liquefaction in the Fraser River delta. Canadian Geotechnical Journal. 34, 520–533, https://doi.org/10.1139/T97-019

Clare, M.A., Hughes Clarke, J.E., Talling, P.J., Cartigny, M.J.B., and Pratomo, D.G. 2016. Preconditioning and triggering of offshore slope failures and turbidity currents revealed by most detailed monitoring yet at a fjord-head delta. Earth and Planetary Science Letters. 450, 208–220. https://doi.org/10.1016/j.epsl.2016.06.021

Clare, M., Chaytor, J., Dabson, O., Gamboa, D., Georgiopoulou, A., Eady, H., Hunt, J., Jackson, C., Katz, O., Krastel, S., León, R., Micallef, A., Moernaut, J., Moriconi, R., Moscardelli, L., Mueller, C., Normandeau, A., Patacci, M., Steventon, M., Urlaub, M. et al. 2019. A consistent global approach for the morphometric characterization of subaqueous landslides; Subaqueous Mass Movements. Geological Society of London, Special Publications. 477, 455–477. https://doi.org/10.1144/SP477.15

Clare, M., Lintern, D., Pope, E., Baker, M., Ruffell, S., Zulkifli, M., Simmons, S., Urlaub, M., Belal, M., Talling, P. 2021. Seismic and Acoustic Monitoring of Submarine Landslides: Ongoing Challenges, Recent Successes and Future Opportunities. Special publication of the American Geophysical Union: Noisy Oceans: Monitoring Seismic and Acoustic Signals in the Marine Environment. https://doi.org/10.31223/X5703Q

Comiso, J.C., Meier, W.N., and Gersten, R. 2017. Variability and trends in the Arctic Sea ice cover: Results from different techniques. Journal of Geophysical Research: Oceans. 122, 6883–6900. https://doi.org/10.1002/2017JC012768

Corbett, L.B., Bierman, P.R., and Davis, P.T. 2016. Glacial history and landscape evolution of southern Cumberland Peninsula, Baffin Island, Canada, constrained by cosmogenic ^{10}Be and ^{26}Al. Bulletin of the Geological Society of America. 128, 1173–1192. https://doi.org/10.1130/B31402.1

Coulthard, R., Furze, M.F.A., Pieńkowski, A.J., Nixon, F.C. and England, J.H. 2010. New marine ΔR values for Arctic Canada. Quaternary Geochronology. 5, 4, 419–434. https://doi.org/10.1016/j.quageo.2010.03.002

Courtney, B. 2009. SegyJp2 Viewer Version 1.0 software; Geological Survey of Canada, Natural Resources Canada, available at <https://ge0mlib.com/software.htm> [February 2022]

Cowan, B., Carter, J., Forbes, D.L., and Bell, T. 2021. Postglacial Sea-Level Lowstand on Cumberland Peninsula, Baffin Island, Eastern Arctic Canada. Canadian Journal of Earth Sciences. 1–46. https://doi.org/10.1139/cjes-2021-0026

Cruden, D.M. and Varnes, D.J. 1996. Landslide types and processes, National Academy of Sciences. Transportation Research Board, Special Report. 247, 36–75.

Dahl-Jensen, T., Larsen, L.M., Pedersen, S.A.S., Jepsen, H.F., Nielsen, T., Von Platen-Hallermund, F. and Weng, W. 2004. Landslide and tsunami, 21 November 2000 in Paatuut, West Greenland. Natural Hazards. 31, 277–287. https://doi.org/10.1023/B:NHAZ.0000020264.70048.95

Davis, P., Bierman, P., Marsella, K., Caffee, M., Southon, J. 1999. Cosmogenic analysis of glacial terrains in the eastern Canadian Arctic: a test for inherited nuclides and the effectiveness of glacial erosion. Annals of Glaciology. 28, 181-188. http://doi.org/10.3189/172756499781821805

Deering, R., Bell, T., Forbes, D.L., Campbell, C., and Edinger, E. 2019. Morphological characterization of submarine slope failures in a semi-enclosed fjord, Frobisher Bay, eastern Canadian Arctic. Geological Society Special Publication. 477, 367–376. http://dx.doi.org/10.1144/SP477.35

Demarco, L.F.W., Klein, A.H.F., De Souza., J.A.G. 2017. Marine substrate response from the analysis of seismic attributes in CHIRP sub-bottom profiles. Brazilian Journal of Oceanography. 65, 3, 332-345. https://doi.org/10.1590/S1679-87592017124306503

Dionne, J-C. 2002. The boulder barricade at Cap à La Baleine, North Shore of Gaspé Peninsula (Québec): Nature of boulders, origin and significance. Journal of Coastal Research. 16, 4, 652-661. https://doi.org/10.1080/04353676.2020.1711665

Dyke, A. 1979. Glacial and sea-level history of southwestern Cumberland Peninsula, Baffin Island, NWT, Canada. Arctic Alpine Research. 11, 179-202. https://doi.org/10.1016/j.gloplacha.2006.06.023

Dyke, A.S., Andrews, J.T., and Miller, G.H. 1982. Quaternary Geology of Cumberland Peninsula, Baffin Island, District of Franklin. Geological Survey of Canada. 403, 2 sheets. https://doi.org/10.4095/116169

Dyke, A.S., Andrews, J.T., Clark, P.U., England, J.H., Miller, G.H., Shaw, J., and Veillette, J.J. 2002. The Laurentide and Innuitian ice sheets during the Last Glacial Maximum. Quaternary Science Reviews. 21, 9–31. https://doi.org/10.1016/S0277-3791(01)00095-6

Dyke, A.S., 2011. Surficial geology, Clearwater Fiord–Pangnirtung south, Baffin Island, Nunavut; Geological Survey of Canada, Canadian Geoscience Map 18 (preliminary version), scale 1:100 000. https://doi.org/10.4095/288963

Eckel, E.B. 1958. Introduction, Landslides and Engineering Practice, Special Report. Eckel E.B. (Ed). National Research Council, Highway Res. Board. 29, 1-5. https://onlinepubs.trb.org/Onlinepubs/sr/sr29.pdf [October 2021]

Environment Canada. 2009. The climate normals of Canada. http://www.climate.weatheroffice.gc.ca/climate_normals/stnselect_e.html [May 2020]

Evans, J., and Dowdeswell, J.A. 2016. Submarine gullies and an axial channel in glacier-influenced Courtauld Fjord, East Greenland. Geological Society Memoir. 46, 103–104. https://doi.org/10.1144/M46.22

Eyles, N., and Lazorek, M. 2014. Glacigenic Lithofacies Sediments in Glaciated Landscapes. In Reference Module in Earth Systems and Environmental Sciences. doi:10.1016/b978-0-12-409548-9.09427-6

Fisheries and Oceans Canada. 2019. Pangnirtung – Site 04029, https://www.waterlevels.gc.ca/en/stations/4029. [November 2019]

Forbes D.L., and Taylor R.B. 1994. Ice in the shore zone and the geomorphology of cold coasts. Progress in Physical Geography. 18, 1, 59–89. https://doi.org/10.1177/030913339401800104

Galappaththi, E.K., Ford, J.D., Bennett, E.M., and Berkes, F. 2019. Climate change and community fisheries in the arctic: A case study from Pangnirtung, Canada. Journal of Environmental Management. 250, 109534. https://doi.org/10.1016/j.jenvman.2019.109534

Gauthier, D., Anderson, S.A., Fritz, H.M. and Giachetti, T. 2017. Karat Fjord (Greenland) tsunamigenic landslide of 17 June 2017: initial 3D observations. Landslides. 15, 327–332. https://doi.org/10.1007/s10346-017-0926-4

Gatter, R., Clare, M.A., Kuhlmann, J., and Huhn, K. 2021. Characterisation of weak layers, physical controls on their global distribution and their role in submarine landslide formation. Earth-Science Reviews. 223, 103845. https://doi.org/10.1016/j.earscirev.2021.103845

Gilbert, R. 1978. Observations on oceanography and sedimentation at Pangnirtung Fiord, Baffin Island. Atlantic Geoscience. 14, 1, 1–9. https://doi.org/10.4138/1952

Gilbert, R. 1982. Contemporary Sedimentary Environments on Baffin Island, N.W.T. Canada: Glaciomarine Processes in Fiords of Eastern Cumberland Peninsula. Arctic and Alpine Research. 14, 1–12. https://doi.org/10.2307/1550809

Gilbert, R. and Church, M. 1983. Contemporary Sedimentary Environments on Baffin Island, N.W.T., Canada: Reconnaissance of Lakes on Cumberland Peninsula. Arctic and Alpine Research. 15, 3, 321-332. https://doi.org/10.2307/1550828

Gilbert, R. 1983. Sedimentary processes of Canadian Arctic fjords. Sedimentary Geology. 36, 147–175. https://doi.org/10.1016/0037-0738(83)90007-6

Gilbert, R., and McKenna Neuman, C. 1988. Occurrence and potential significance of warm weather during winter in the eastern Canadian Arctic. Arctic & Alpine Research. 20, 395–403. https://doi.org/10.2307/1551337

Girardclos, S., Schmidt, O.T., Sturm, M., Ariztegui, D., Pugin, A., and Anselmetti, F.S. 2007. The 1996 AD delta collapse and large turbidite in Lake Brienz. Marine Geology. 241, 137–154. https://doi.org/10.1016/j.margeo.2007.03.011

Goldberg, E. D. 1963. Geochronology with ^{210}Pb. In Radioactive Dating. Proceedings of the Symposium on Radioactive Dating Held by the International Atomic Energy Agency in Co-operation with the Joint Commission on Applied Radioactivity, Athens, November 19–23, 1962. 121–131.

Gosse, J.C., Tremblay, T., Broom, L.A., Campbell, D.C., Wenzel, G., Nedimovic, M.R., Forget Brisson, L. 2020. Initial results from the ULINNIQ seismicity and tsunami hazard project, northeastern Baffin Island, Nunavut; in Summary of Activities 2019, Canada-Nunavut Geoscience Office. 101–124.

Hampton, M.A., Lee, H.J. and Locat, J. 1996. Submarine landslides. Springer Geology. 34, 33–59. https://doi.org/10.1007/978-3-319-57852-1_13

Heaton, T., Köhler, P., Butzin, M., Bard, E., Reimer, R., Austin, W.E.N., Ramsey, C.B., Grootes, P.M., Hughen, K.A., Kromer, B., Reimer, P.J., Adkins, J., Burke, A., Cook, M.S., Olsen, J. and Skinner, L. 2020. Marine20 – the marine radiocarbon age calibration curve (0–55,000 cal. BP). Radiocarbon. 62, 4, 779–820. https://doi.org/10.1017/RDC.2020.68

Higman, B., Shugar, D.H., Stark, C.P., Ekström, G., Koppes, M.N., Lynett, P., Dufresne, A., Haeussler, P.J., Geertsema, M., Gulick, S., Mattox, A., Venditti, J.G., Walton, M.A.L., McCall, N., Mckittrick, E., MacInnes, B., Bilderback, E.L., Tang, H., Willis, M.J., Richmond, B. et al. 2018. The 2015 landslide and tsunami in Taan Fiord, Alaska. Nature: Scientific Reports. 8, 12993. https://doi.org/10.1038/s41598-018-30475-w

Horton, P., Jaboyedoff, M., Rudaz, B., and Zimmermann, M. 2013. Flow-R, a model for susceptibility mapping of debris flows and other gravitational hazards at a regional scale. Natural Hazards and Earth System Sciences. 13, 869–885. https://doi.org/10.5194/nhess-13-869-2013

Hughes Clarke, J.E., Muggah, J., Renoud, W., Bell, T., Forbes, D.L., Cowan, B. and Kennedy, J. 2015. Reconnaissance seabed mapping around Hall and Cumberland peninsulas, Nunavut: opening up southeastern Baffin Island to nearshore geological investigations; in Summary of Activities 2014, Canada-Nunavut Geoscience Office. 133–144. https://cngo.ca/summary-of-activities/2014/ [January 2022]

Hungr, O., Evans, S.G., Bovis, M.J. and Hutchinson, J.N. 2001. A review of the classification of landslides of the flow type. Environmental and Engineering Geoscience. 7, 221–238. https://doi.org/10.2113/gseegeosci.7.3.221

Jackson, G.D. and Sanborn-Barrie, M. 2014. Geology, Pangnirtung Fiord, Nunavut; Geological Survey of Canada, Canadian Geoscience Map 4, 1:100 000 scale. https://doi.org/10.4095/288928

Johns, M.W., Prior, D.B., Bornhold, D.B., Coleman, J.M. and Bryant, W.R. 1985. Geotechnical aspects of a submarine slope failure, Kitimat Fjord, British Columbia. Marine Geotechnology. 6, 243–279. https://doi.org/10.1080/10641198609388190

Kaplan, M., Pfeffer, W., Sassolas, C., and Miller, G. 1999. Numerical modelling of the Laurentide Ice Sheet in the Baffin Island region: the role of a Cumberland Sound ice stream. Canadian Journal of Earth Sciences. 36, 1315-1326. https://doi.org/10.1139/cjes-36-8-1315

Knapp, R.W. 1990. Vertical resolution of thick beds, thin beds and thin-bed cyclotherms. Geophysics. 55, 1183-1190. https://doi.org/10.1190/1.1442934

Krishnaswamy, S., Lal, D., Martin, J.M., and Meybeck, M. 1971. Geochronology of lake sediments. Earth and Planetary Science Letters, 11, 407–414, https://doi.org/10.1016/0012-821X(71)90202-0

Kuenen, P.H. 1952. Estimated size of the Grand Banks turbidity current. American Journal of Science. 250, 874–884. https://doi.org/10.2475/ajs.250.12.874

Laugrand, F., Oosten, J., Trudel, F. 2006. Apostle to the Inuit: The Journals and Ethnographic Notes of Edmund James Peck - The Baffin Years, 1894-1905. University of Toronto Press, pp. 420.

Le Bouteiller, P., Lafuerza, S., Charléty, J., Reis, A.T., Granjeon, D., Delprat-Jannaud, F., and Gorini, C. 2019. A new conceptual methodology for interpretation of mass transport processes from seismic data. Marine and Petroleum Geology. 103, 438–455. http://doi.org/10.1016/j.marpetgeo.2018.12.027

L'Heureux, J.S., Hansen, L., Longva, O., Emdal, A., and Grande, L.O. 2010. A multidisciplinary study of submarine landslides at the Nidelva fjord delta, Central Norway - Implications for geohazard assessment. Norwegian Journal of Geology. 90, 1–20. https://njg.geologi.no/images/NJG_articles/NJG_1_2010_LHeureux_pr1.pdf [October 2021]

Lundblad, E.R., Wright, D.J., Miller, J., Larkin, E.M., Rinehart, R., Naar, D.F., Donahue, B.T., Anderson, S.M., Battista, T. 2006. A benthic terrain classification scheme for American Samoa. Marine Geodesy. 29, 89–111. https://doi.org/10.1080/01490410600738021

Margreth, A., Gosse, J.C., and Dyke, A.S. 2016. Quantification of subaerial and episodic subglacial erosion rates on high latitude upland plateaus: Cumberland Peninsula, Baffin Island, Arctic Canada. Quaternary Science Reviews. 133, 108-129. https://doi.org/10.1016/j.quascirev.2015.12.017

Margreth, A., Gosse, J.C., and Dyke, A.S. 2017. Wisconsinan and early Holocene glacial dynamics of Cumberland Peninsula, Baffin Island, Arctic Canada. Quaternary Science Reviews. 168, 79–100. https://doi.org/10.1016/j.quascirev.2017.04.033

Marsella, K.A. 1998. Timing and extent of glaciation in the Pangnirtung Fjord region, southern Cumberland Peninsula: Determined using in situ produced cosmogenic ^{10}Be and ^{26}Al. Master's Thesis. Burlington, University of Vermont, 135 pp.

Marsella, K.A., Bierman, P.R., Thompson Davis, P., and Caffee, M.W. 2000. Cosmogenic ^{10}Be and ^{26}Al ages of the Last Glacial Maximum, Eastern Baffin Island, Arctic Canada. Bulletin of the Geological Society of America. 112, 1296–1312. https://doi.org /10.1130/0016-7606(2000)112<1296:CBAAAF>2.0.CO;2

Maslin, M., Owen, M., Day, S., and Long, D. 2004. Linking continental-slope failures and climate change: Testing the clathrate gun hypothesis. Geology. 32, 53–56, https://doi.org /10.1130/G20114.1

Masson, D.G., Harbitz, C.B., Wynn, R.B., Pedersen, G. and Løvholt, F. 2006. Submarine landslides: processes, triggers and hazard prediction. Philosophical Transactions of the Royal Society, A: Mathematical, Physical and Engineering Sciences. 364, 2009–2039. https://doi.org/10.1098/rsta.2006.1810

Mattson, L.E., Gardner, J.S. 1991. Mass Wasting on Valley-Side Ice-Cored Moraines, Boundary Glacier, Alberta, Canada. Geografiska Annaler. Series A, Physical Geography. 73, 3-4, 123–128. https://doi.org/10.2307/521017

Maxwell, J. B. 1981. Climatic regions of the Canadian Arctic Islands. Arctic. 34, 225–240. https://doi.org/10.14430/arctic2525

McCann, S.B., Dale, J.E., and Hale, P.B. 1981. Subarctic tidal flats in areas of large tidal range, southern Baffin Island, eastern Canada. Geographie Physique et Quaternaire, 35, 183–204. https://doi.org/10.7202/1000436ar

McCrystall, M.R., Stroeve, J., Serreze, M., Forbes, B.C., and Screen, J.A. 2021. New climate models reveal faster and larger increases in Arctic precipitation than previously projected. Nature Communications. 12, 6765. https://doi.org/10.1038/s41467-021-27031-y

McGuire, B., and Maslin, M.A. 2013. Climate Forcing of Geological Hazards. John Wiley & Sons, 328 pp.

Miller, D.J. 1960. Giant waves in Lituya Bay, Alaska. U.S. Geological Survey, Professional Paper 354-C. http://pubs.er.usgs.gov/publication/pp354C [January 2022]

Miller, G., Dyke, A. 1974. Proposed extent of late Wisconsin Laurentide ice on eastern Baffin Island. Geology. 2, 125-130.

Miller, G.H. 1975. Glacial and climatic history of northern Cumberland Peninsula, Baffin Island, Canada, during the last 10,000 years. Ph.D. thesis. Department of Geological Sciences, University of Colorado, Boulder Colorado

Mountjoy, J., and Micallef, A. 2018. Submarine Landslides. Springer Geology. 235–250, https://doi.org/10.1007/978-3-319-57852-1_13

Mudie, P.J., Piper, D.J.W., Rideout, K., Robertson, K.R., Schafer, C.T., Vilks, G., and Hardy, I.A. 1984. Standard methods for collecting, describing and sampling Quaternary sediments at the Atlantic Geoscience Center. Open file 1044, 47 pp.

Noël, B., van de Berg, W.J., Lhermitte, S., Wouters, B., Schaffer, N., and van den Broeke, M.R. 2018. Six decades of glacial mass loss in the Canadian Arctic Archipelago. Journal of Geophysical Research: Earth Surface, 123, 1430–1449, https://doi.org/10.1029/2017JF004304

Normandeau, A., Dietrich, P., Hughes Clarke, J., Van Wychen, W., Lajeunesse, P., Burgess, D. and Ghienne, J.F. 2019a. Retreat pattern of glaciers controls the occurrence of turbidity currents on high-latitude fjord deltas (eastern Baffin Island). Journal of Geophysical Research: Earth Surface. 124, 1559–1571. https://doi.org/doi:10.1029/2018JF004970

Normandeau, A., Robertson, A.G., Philibert, G., Regular, K., and Sedore, P., 2019b. R/V Nuliajuk expedition 2019Nuliajuk: marine geohazards near Qikiqtarjuaq, Padle Fjord, Southwind Fjord and Pangnirtung, Southeast Baffin Island, Nunavut. Geological Survey of Canada. Open File 8641, 63. https://doi.org/10.4095/315676

Normandeau, A., Brown, O., Jarrett, K., Francus, P., and De Coninck, A. 2019c. Epoxy impregnation of unconsolidated marine sediment core subsamples for the preparation of thin sections at the Geological Survey of Canada (Atlantic); Geological Survey of Canada, Technical Note. 10, 10 pp. https://doi.org/10.4095/313055

Normandeau, A., MacKillop, K., Macquarrie, M., Richards, C., Bourgault, D., Campbell, D.C., Maselli, V., Philibert, G. and Hughes Clarke, J. 2021a. Submarine landslides triggered by iceberg collision with the seafloor. Nature Geoscience. 14, 599–605, https://doi.org/10.1038/s41561-021-00767-4

Normandeau, A., Blais-Stevens, A., Horton, T., Oppikofer, T., Sedore, P. and Maselli, V. 2022a. Landslide susceptibility in Pangnirtung Fiord, Nunavut; Geological Survey of Canada, Open File 8843, 1 poster

Normandeau, A., Carson, T., Sharpe, H., Edinger, E., Neves, B., and Belko, A., 2022b. CCGS Amundsen 2021805-806: marine geohazards, late Quaternary paleoenvironments, and seabed habitats in offshore Newfoundland and Labrador, and Nunavut, Canada. Geological Survey of Canada, Open File 8842, 51 pp. https://doi.org/10.4095/329213

Oppikofer, T., Jaboyedoff, M., Derron, M.H. and Bilkra, L.H. 2009. Geometric back-analysis of ancient rockslides in Tafjord (Norway). Geophysical Research Abstracts, EGU General Assembly 2009. 11, EGU 2009-7647, https://ui.adsabs.harvard.edu/abs/2009EGUGA.11.7647O/abstract [October 2021]

Paris, A., Okal, E.A., Guérin, C., Heinrich, P., Schindelé, F., and Hébert, H. 2019. Numerical Modeling of the June 17, 2017 Landslide and Tsunami Events in Karrat Fjord, West Greenland. Pure and Applied Geophysics. 176, 3035–3057. https://doi.org/10.1007/s00024-019-02123-5

Peterson, B.J., Holmes, R.M., McClelland, J.W., Vörösmarty, C.J., Lammers, R.B., Shiklomanov, A.I., Shiklomanov, I.A., and Rahmstorf, S. 2002. Increasing river discharge to the Arctic Ocean. Science, 298, 2171–2173. https://doi.org/10.1126/science.1077445

Pope, E.L., Talling, P.J., Urlaub, M., Hunt, J.E., Clare, M.A., and Challenor, P. 2015. Are large submarine landslides temporally random or do uncertainties in available age constraints make it impossible to tell? Marine Geology. 369, 19–33. https://doi.org/10.1016/j.margeo.2015.07.002.

Pourchet, M., Pinglot, J.F. and Marie, A.M. 1989: Cesium-137 and lead-210 in alpine lake sediments: measurements and modeling of mixing process. Journal of Geophysical Research. 94, C9, 12761–12770. https://doi.org/10.1029/JC094iC09p12761

Previdi, M., Smith, K.L., and Polvani, L.M. 2021. Arctic amplification of climate change: A review of underlying mechanisms. Environmental Research Letters. 16. https://doi.org/10.1088/1748-9326/ac1c29.

Prior, D.B. and Bornhold, B.D. 1989. Submarine sedimentation on a developing Holocene fan delta. Sedimentology. 36, 1053–1076. https://doi.org/10.1002/9781444304473.ch34

Rosen, P.S. 1979. Boulder Barricades in central Labrador. Journal of Sedimentary Petrology. 49, 4, 1113–1124. https://www.jstor.org/stable/4299117?seq=1#metadata_info_tab_contents [October 2021]

Sangree, J.B. and Widmier, J.M. 1979. Interpretation of depositional facies from seismic data. Geophysics. 44, 2. 131–160. https://doi.org/10.1190/1.1440957

Scarselli, N. 2020. Chapter 16 - Submarine landslides – architecture, controlling factors and environments. A summary. Regional Geology and Tectonics (Second Edition). 417-439. https://doi.org/10.1016/B978-0-444-64134-2.00015-8

Schaffer, N., Copland, L., Zdanowicz, C., Burgess, D., and Nilsson, J. 2020. Revised Estimates of Recent Mass Loss Rates for Penny Ice Cap, Baffin Island, Based on 2005–2014 Elevation Changes Modified for Firn Densification. Journal of Geophysical Research: Earth Surface. 125, 0–3. https://doi.org/10.1029/2019JF005440

Schuster, R. L. 1978. Introduction, in Landslides-Analysis and Control, Schuster, R.L. and Krizek, R.J. (Eds), Special Report. Transportation Research Board, National Research Council, Washington, D.C. 176, 1-10.

Spinney, J.A., and Pennesi, K.E. 2013. When the river started underneath the land: Social constructions of a "severe" weather event in Pangnirtung, Nunavut, Canada. Polar Record. 49, 362–372. https://doi.org/10.1017/S0032247412000320

Stacey, C.D., Lintern, D.G., Shaw, J., and Conway, K.W. 2020. Slope stability hazard in a fjord environment: Douglas channel, Canada. Geological Society Special Publication. 500, 427–451. https://doi.org/10.1144/SP500-2019-191

Stein, S., Sleep, N.H., Geller, R.J., Wang, S. and Kroeger, G.C. 1979. Earthquakes along the passive margin of eastern Canada. Geophysical Research Letters. 6, 537–540, https://doi.org/10.1029/GL006i007p00537

St-Onge, G., Mulder, T., Francus, P., and Long, B. 2007. Chapter Two Continuous Physical Properties of Cored Marine Sediments. Developments in Marine Geology. 1, 63–98. https://doi.org/10.1016/S1572-5480(07)01007-X

Strupler, M., Anselmetti, F.S., Hilbe, M. and Strasser, M. 2019. Quantitative characterization of subaqueous landslides in Lake Zurich (Switzerland) based on a high-resolution bathymetric dataset. Geological Society of London, Special Publications. 477, 399–412. https://doi.org/:://doi.org/10.1144/SP477.7

Syvitski, J., Burrell, D.C. and Skei, J.M. 1987: Fjords: processes and products. Arctic and Alpine Research, 20, 3, https://doi.org/10.1007/978-1-4612-4632-9

Syvitski, J.P.M., and Shaw, J. 1995. Chapter 5: Sedimentology and Geomorphology of Fjords. Developments in Sedimentology. 53, 113–178. https://doi.org/10.1016/S0070-4571(05)80025-1

Syvitski, J., Ángel, J.R., Saito, Y., Overeem, I., Vörösmarty, C.J., Wang, H., and Olago, D. 2022. Earth's sediment cycle during the Anthropocene. Nature Reviews Earth and Environment. https://doi.org/10.1038/s43017-021-00253-w

Talling, P.J., Clare, M., Urlaub, M., Pope, E., Hunt, J.E., and Watt, S.F.L. 2014. Large submarine landslides on continental slopes: Geohazards, methane release, and climate change. Oceanography. 27, 32–45. https://doi.org/10.5670/oceanog.2014.38

Talling, P.J., Allin, J., Armitage, D.A., Arnott, R.W.C., Cartigny, M.J.B., Clare, M.A., Felletti, F., Covault, J.A., Girardclos, S., Hansen, E., Hill, P.R., Hiscott, R.N., Hogg, A.J., Hughes Clarke, J., Jobe, Z.J., Malgesini, G., Mozzato, A., Naruse, H., Parkinson, S., Peel, F.J., Piper, D.J.W., et al. 2015. Key Future Directions for Research On Turbidity Currents and Their Deposits. Journal of Sedimentary Research. 85, 2, 153–169. https://doi.org/10.2110/jsr.2015.03

Tappin. D.R. 2010. Submarine mass failures as tsunami sources – their climate control; Philosophical Transactions of the Royal Society A: Mathematical, Physical and Engineering Sciences. 368, 1919, 2417–2434. https://doi.org/10.1098/rsta.2010.0079

Urlaub, M., Talling, P.J. and Masson, D.G. 2013. Timing and frequency of large submarine landslides: implications for understanding triggers and future geohazard. Quaternary Science Reviews. 72, 63–82, https://doi.org/10.1016/j.quascirev.2013.04.020

Varnes, D.J. 1978. Slope movement types and processes. Schuster, R.L. and Krizek, R.J. (Eds), Landslides, Analysis and Control, Special Report 176: Transportation Research Board, National Academy of Sciences, Washington, D.C. 11-33.

Waldmann, N., Vasskog, K., Simpson, G., Chapron, E., Støren, E.W.N., Hansen, L., Loizeau, J., Nesje, A. and Ariztegui, D. 2021. Anatomy of a catastrophe: reconstructing the 1936 rock fall and tsunami event in Lake Lovatnet, western Norway. Frontiers in Earth Science. 9, 1–18. https://doi.org/10.3389/feart.2021.671378

Water Survey of Canada. 1983. Daily discharge graph for Duval River near Pangnirtung (10UF001) [NU]. Water Survey of Canada. https://wateroffice.ec.gc.ca/report/historical_e.html?stn=10UF001 [October 2021]

Whitmarsh R. B. 1971. Precise sediment density determination by gamma-ray attenuation alone. Journal of Sedimentary Research. 41, 3, 882–883. https://doi.org/10.1306/74D72397-2B21-11D7-8648000102C1865D

Williams, L. D. 1972. Some factors influencing cirque glacierization on eastern Cumberland Peninsula, Baffin Island, Canada. M.S thesis. University of Colorado. 131 pp.

Zdanowicz, C., Smetny-Sowa, A., Fisher, D., Schaffer, N., Copland, L., Eley, J., and Dupont, F. 2012. Summer melt rates on Penny Ice Cap, Baffin Island: Past and recent trends and implications for regional climate. Journal of Geophysical Research: Earth Surface. 117, 1–21. https://doi.org/10.1029/2011JF002248

Zhang, Y., Chen, W., and Riseborough, D.W. 2006. Temporal and spatial changes of permafrost in Canada since the end of the Little Ice Age. Journal of Geophysical Research Atmospheres. 111, 1–14. https://doi.org/10.1029/2006JD007284

APPENDICES

Appendix A: Core location maps

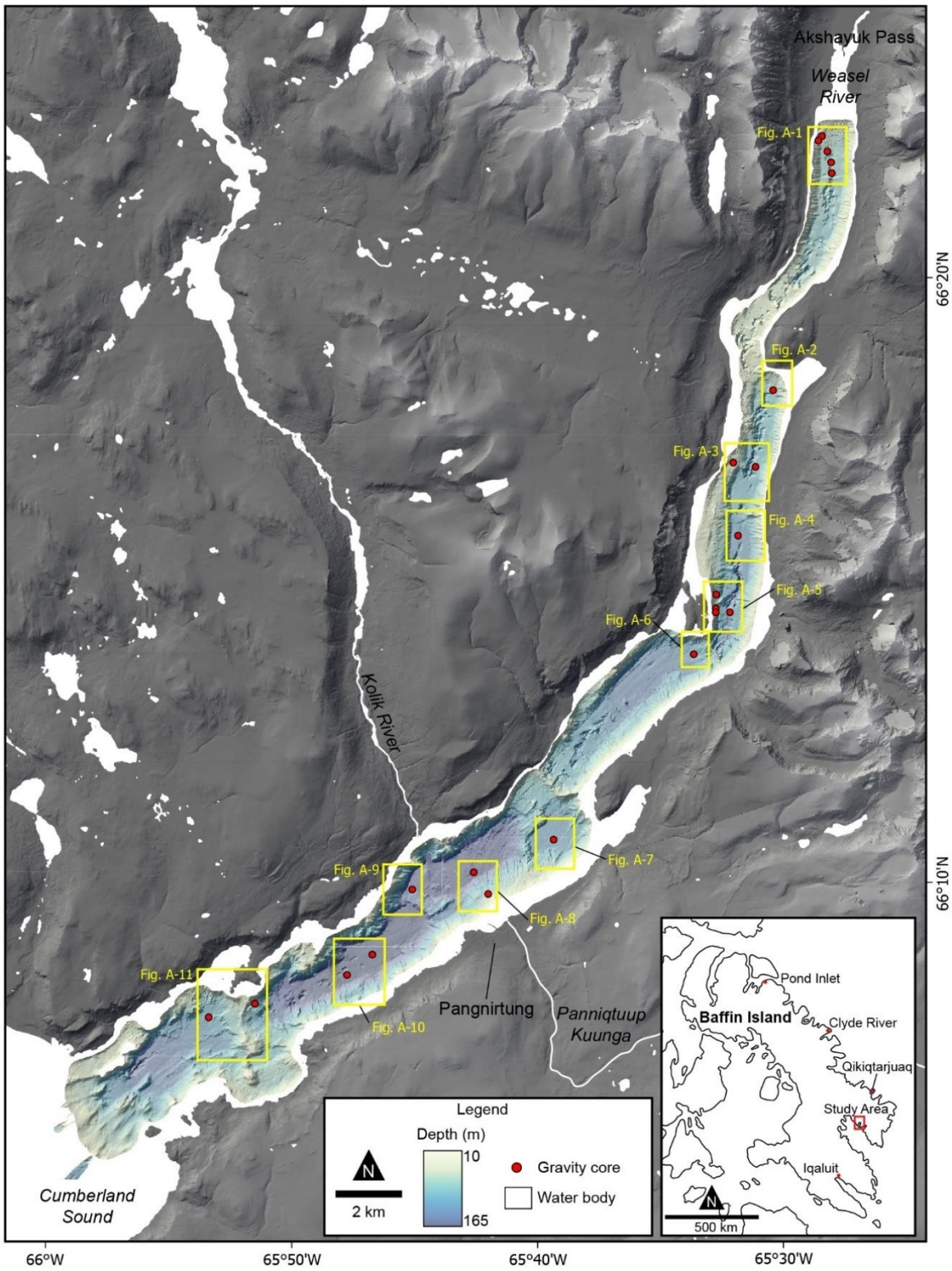

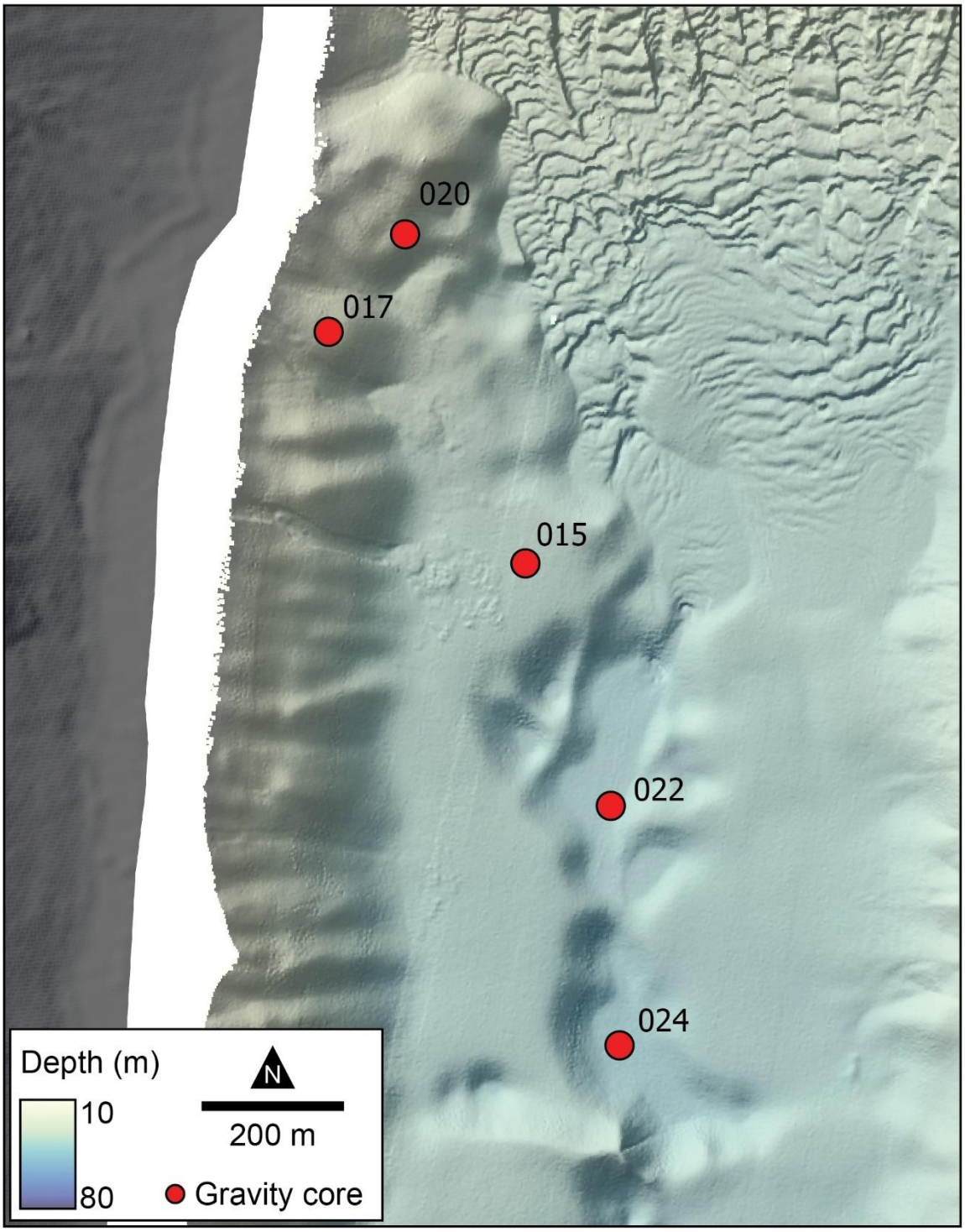

Figure A-1. Coring locations for cores 015, 017, 020, 022, and 024.

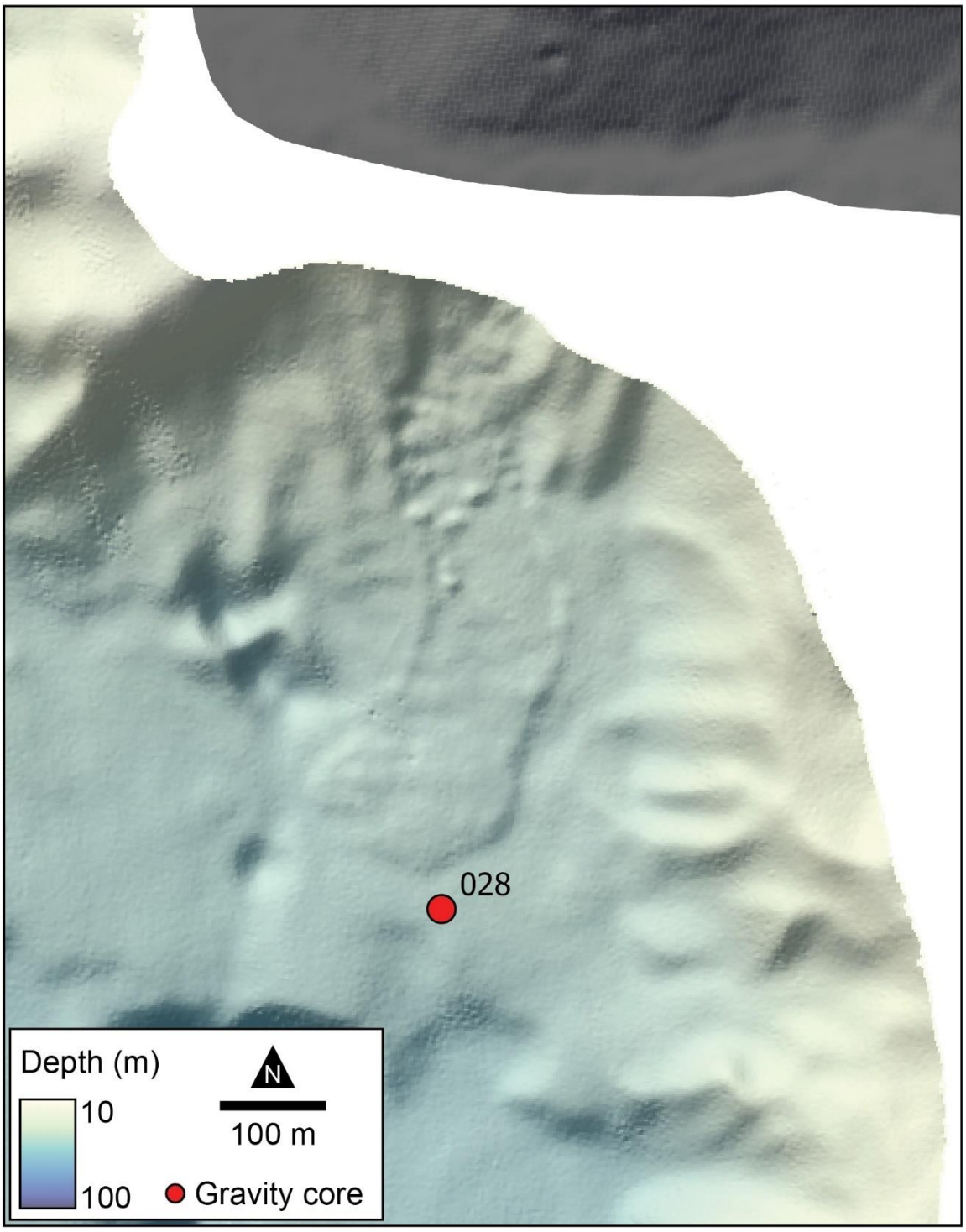

Figure A-2. Coring location for core 028.

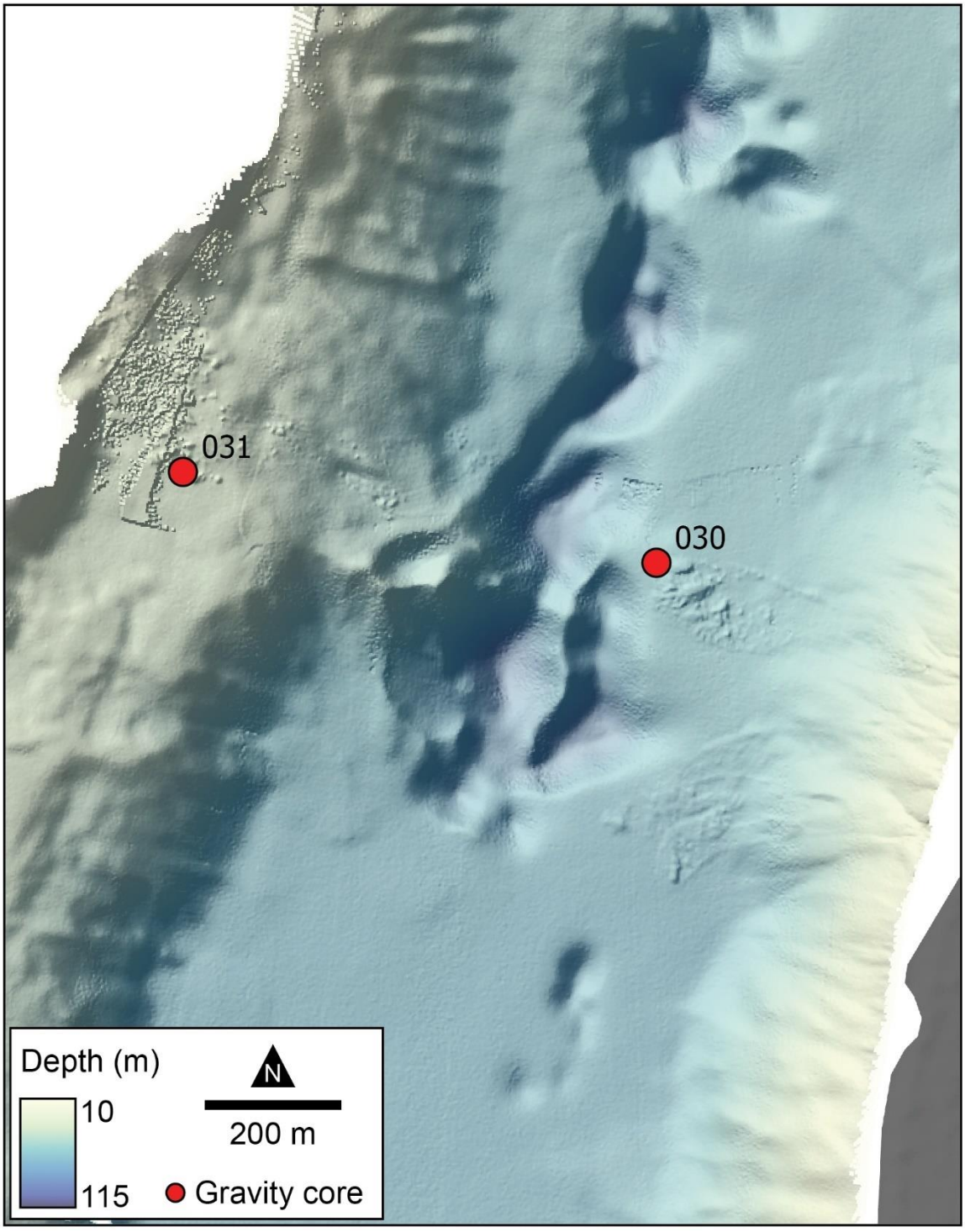

Figure A-3. Coring locations for cores 030, and 031.

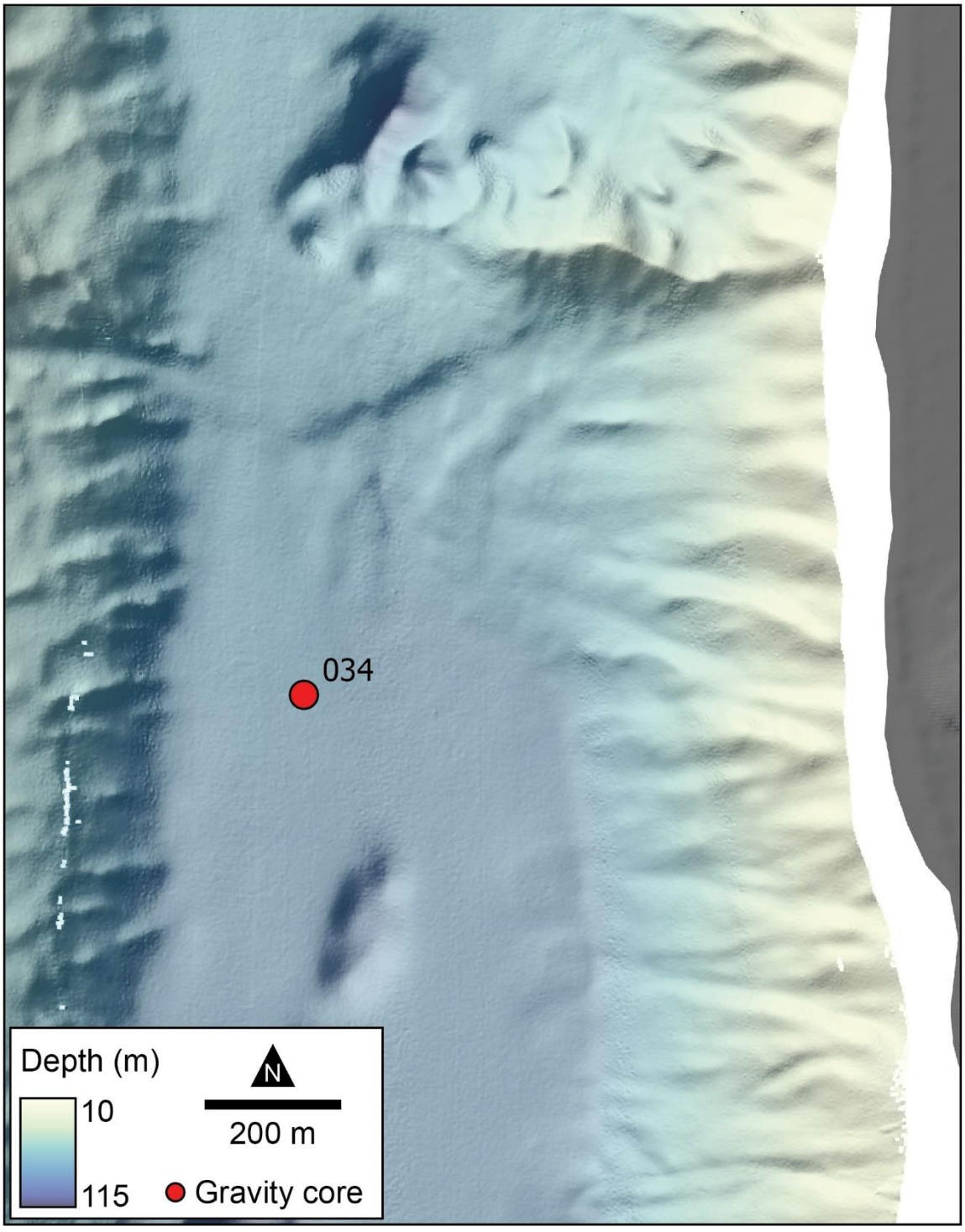

Figure A-4. Coring location for core 034.

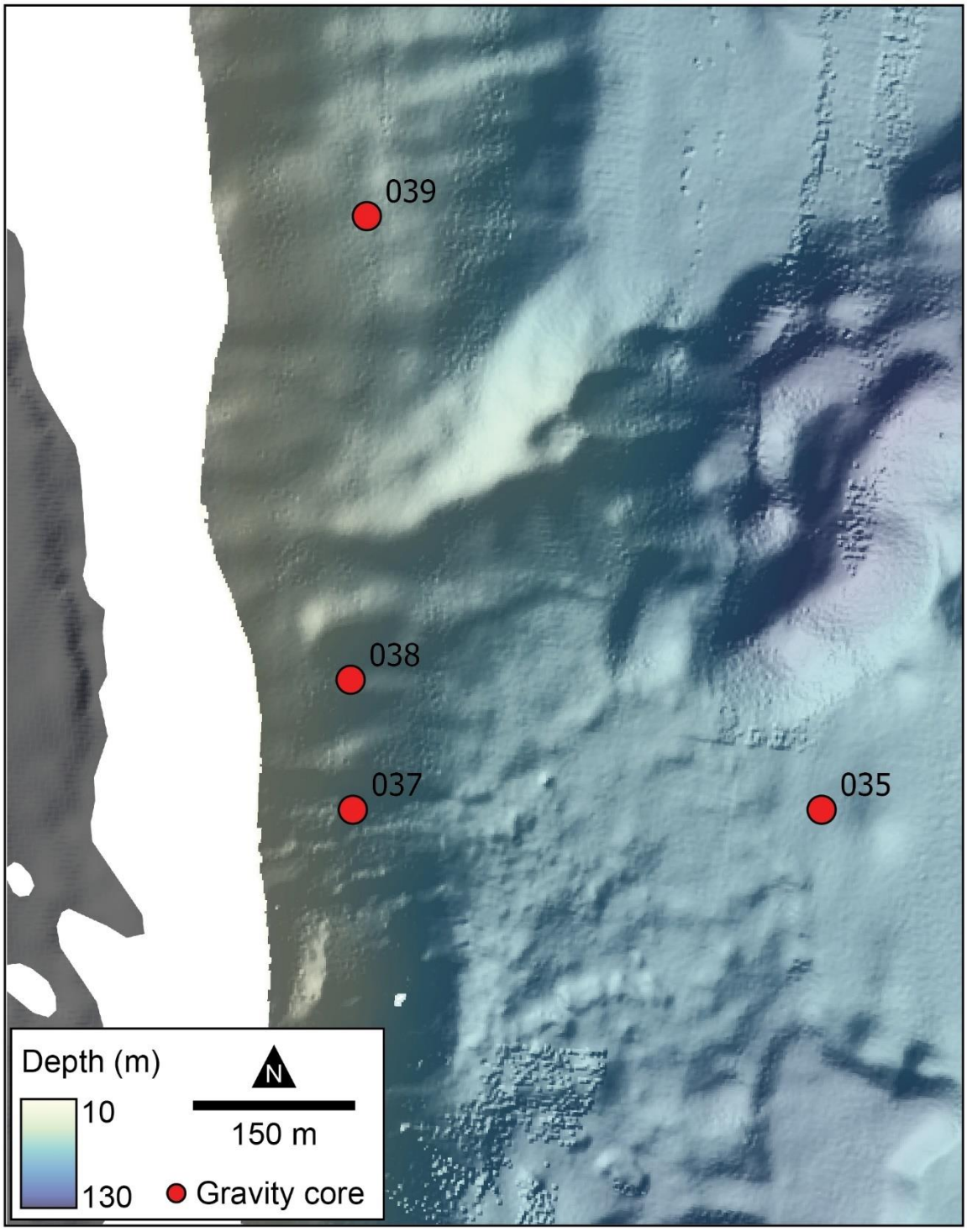

Figure A-5. Coring locations for cores 035, 037, 038, and 039.

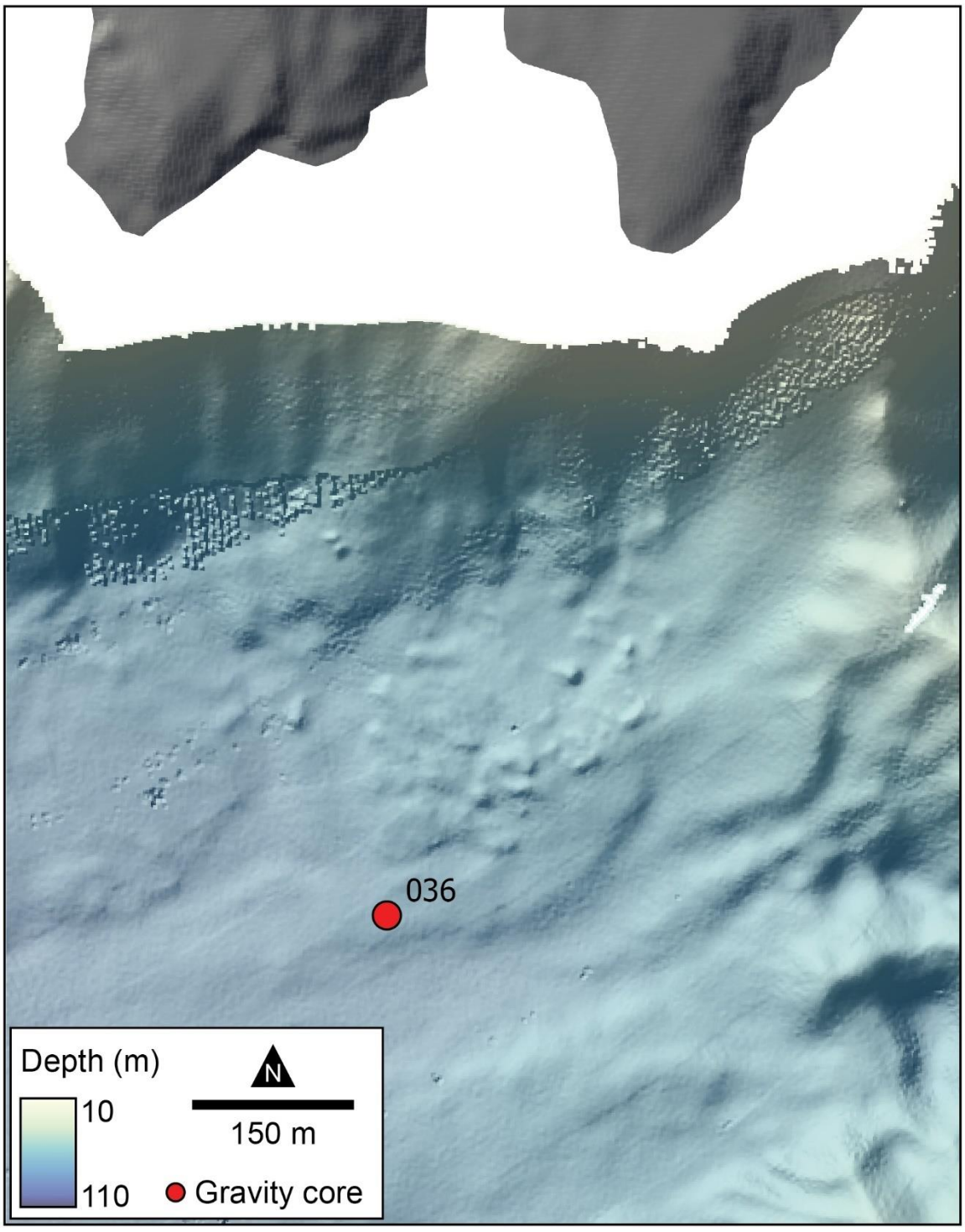

Figure A-6. Coring location for core 036.

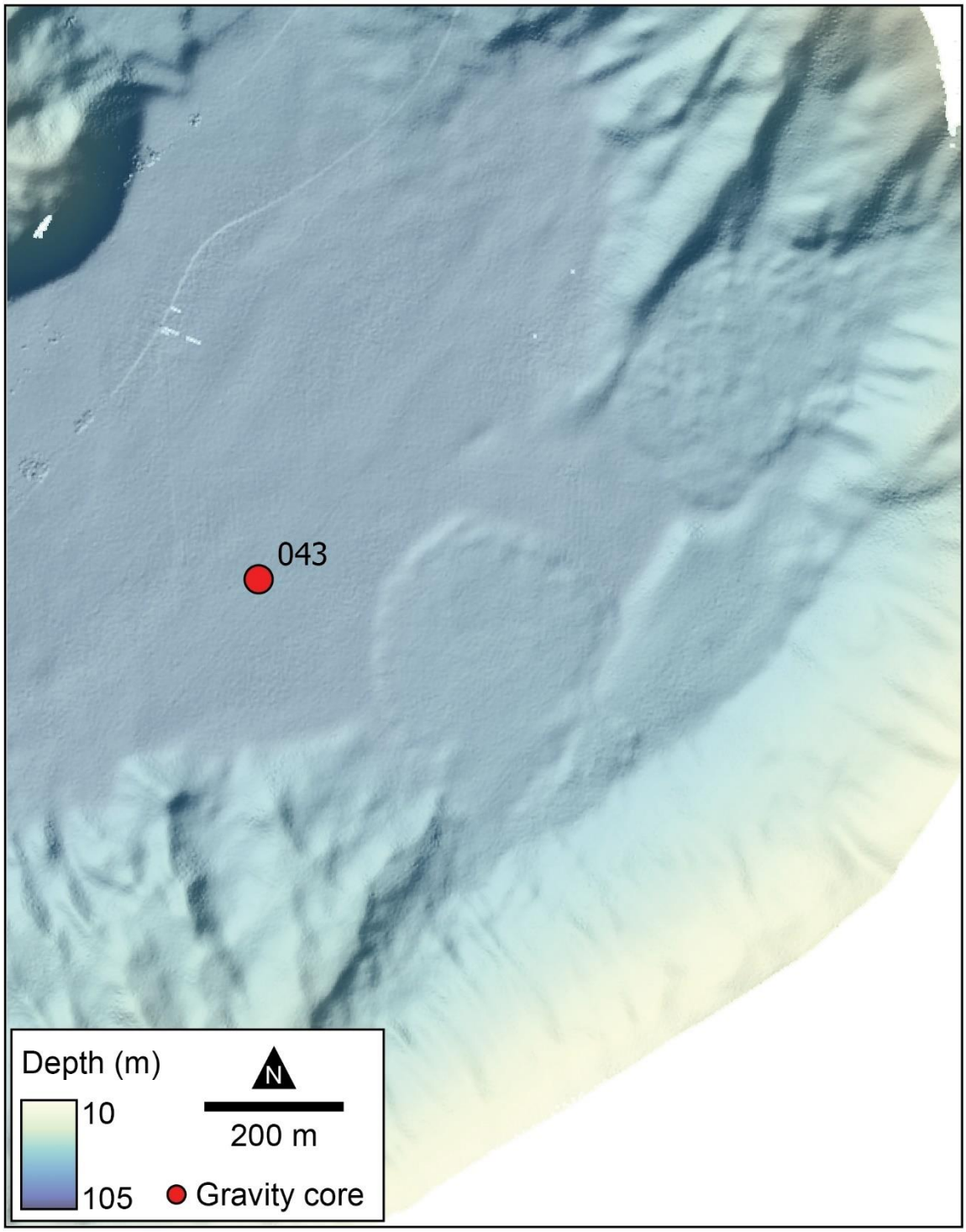

Figure A-7. Coring location for core 043.

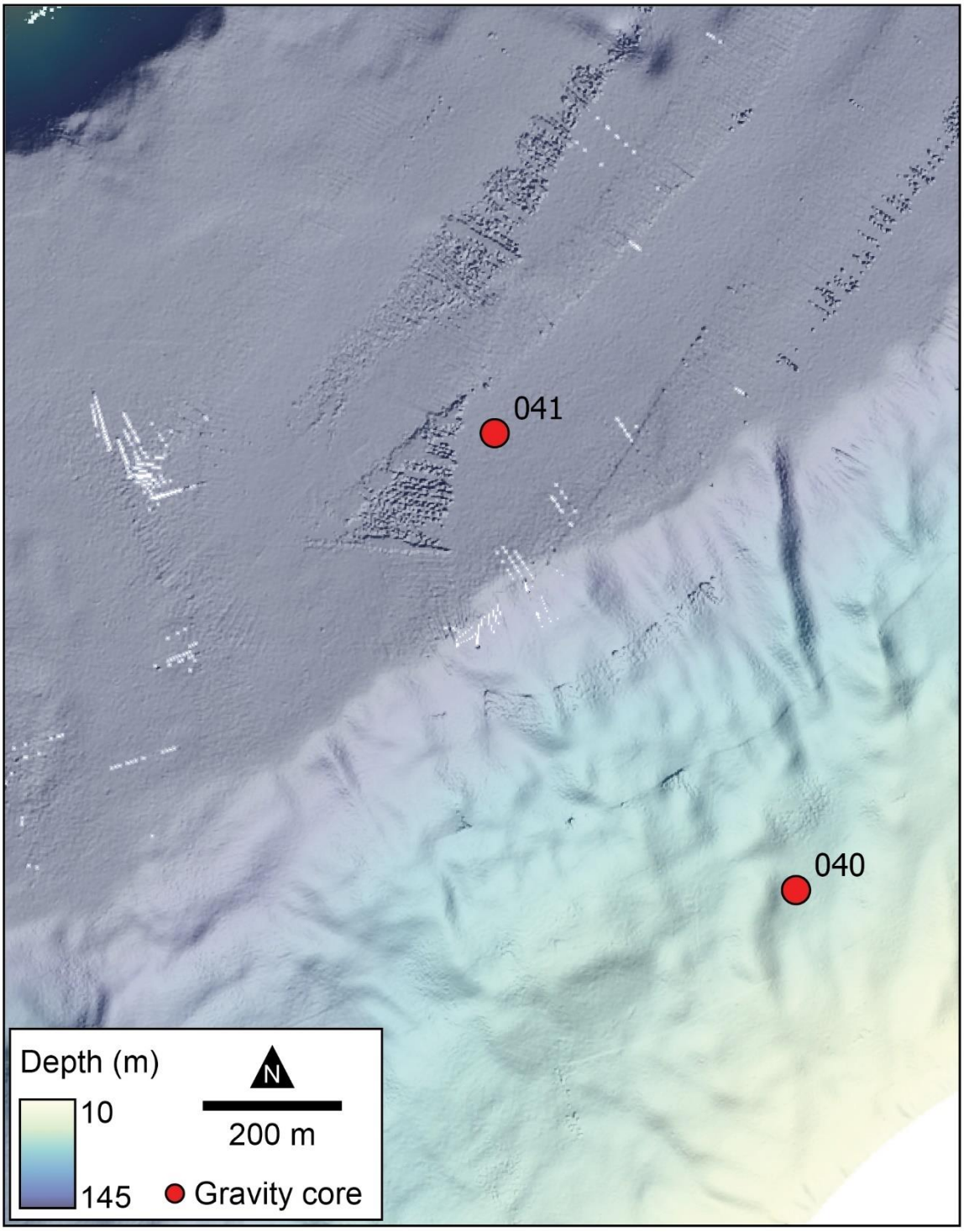

Figure A-8. Coring locations for cores 040, and 041.

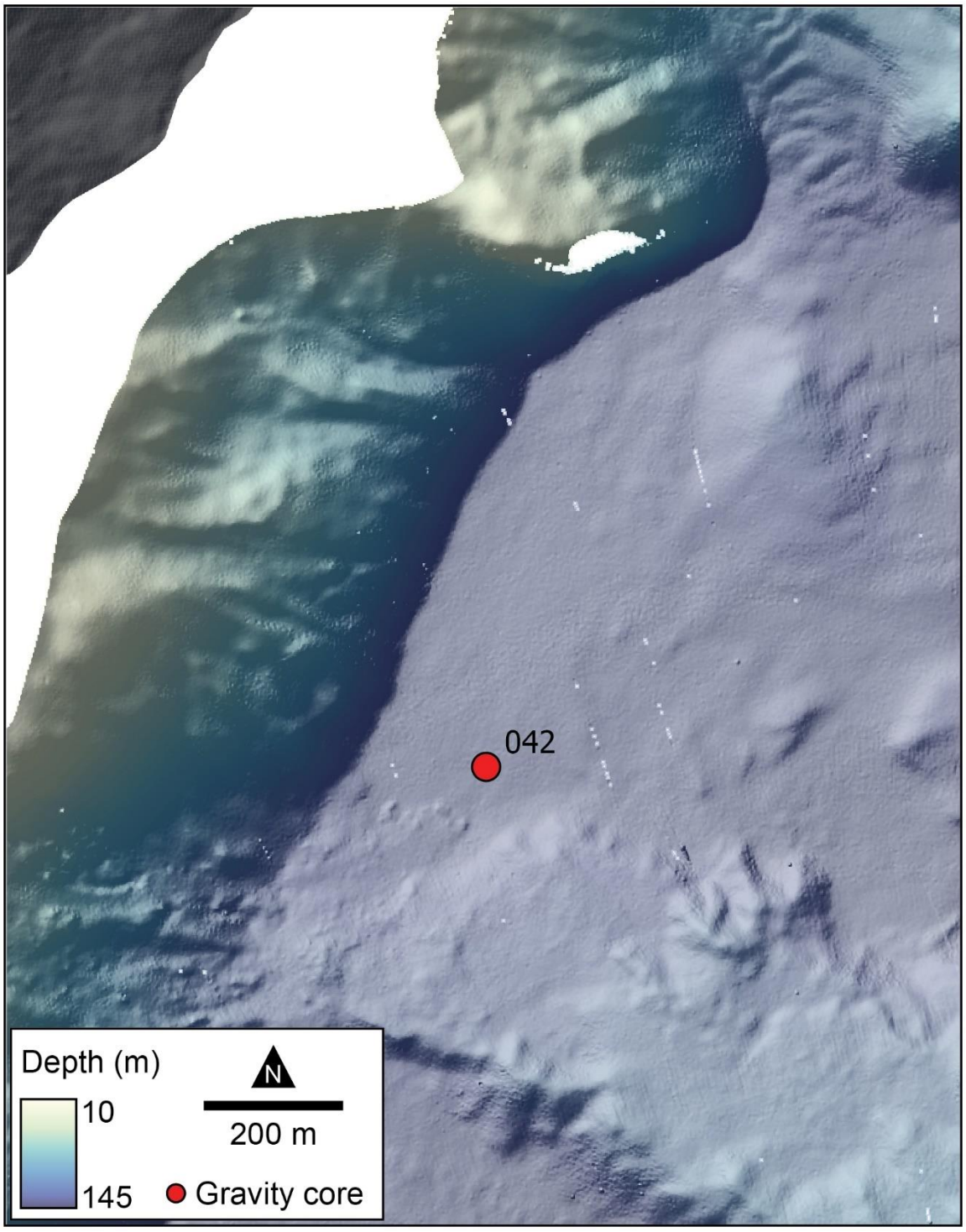

Figure A-9. Coring location for core 042.

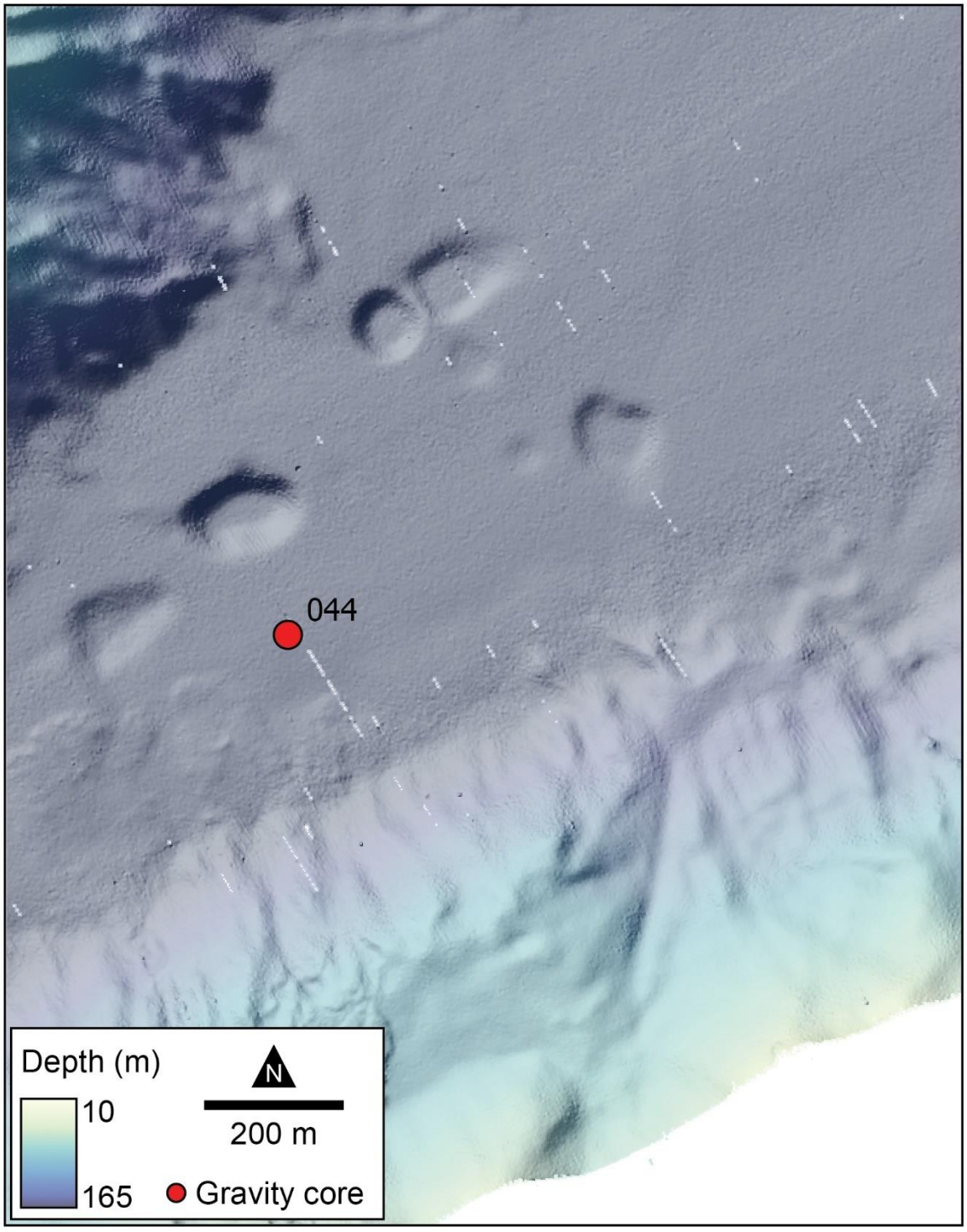

Figure A-10. Coring location for core 044.

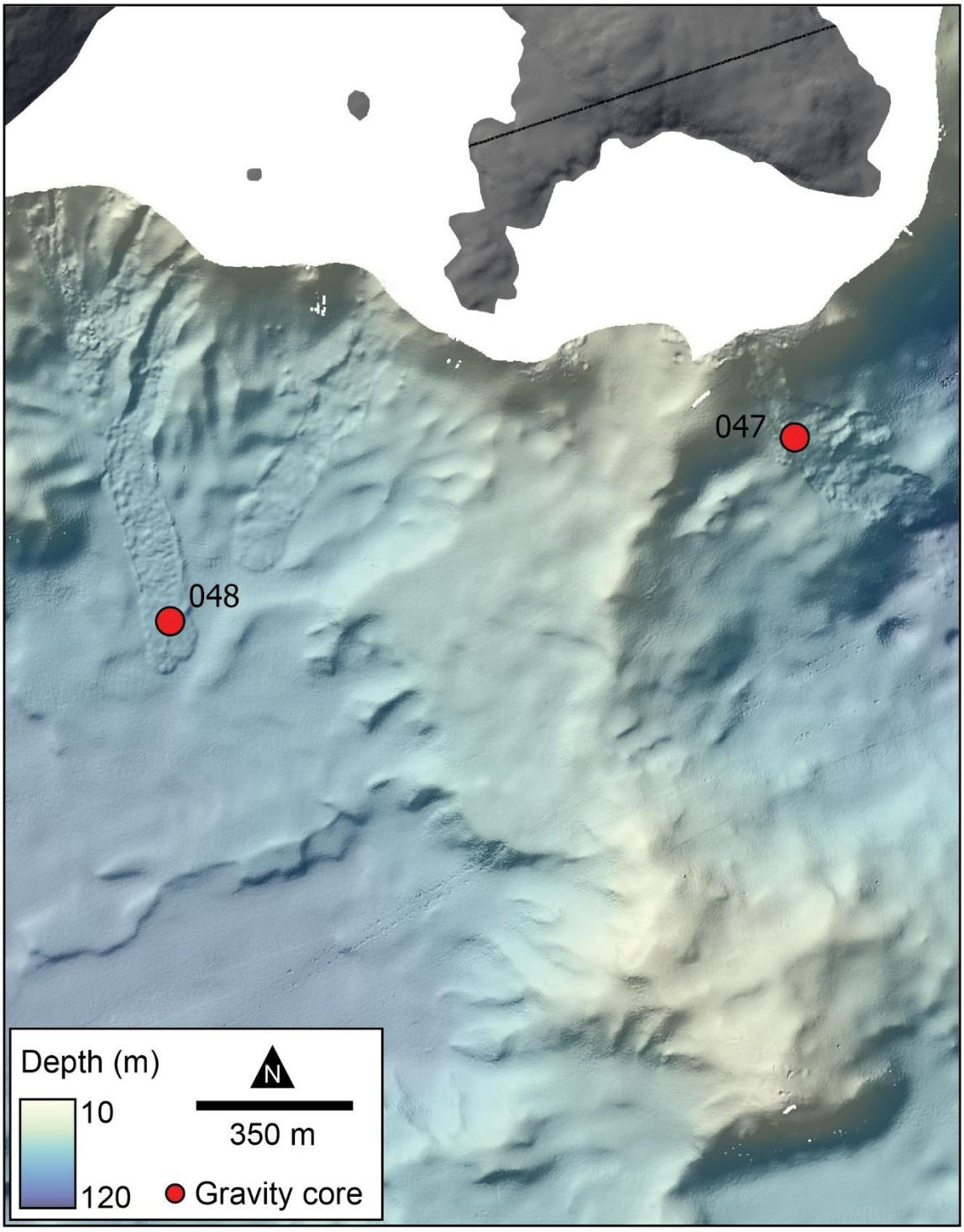

Figure A-11. Coring locations for cores 047, and 048.

Appendix B: Core physical properties

2019Nuliajuk Gravity Core Legend

Lithofacies

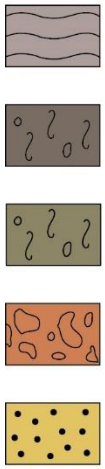

Lithofacies 1

Lithofacies 2

Lithofacies 3

Lithofacies 4

Lithofacies 5

Symbols legend

Magnetic susceptibility (MS)

- MSCL loop sensor
- MSCL point sensor

P-wave velocity

- MSCL velocity
- Discrete longitudinal velocity
- Discrete transverse velocity

Bulk density

- MSCL bulk density
- Discrete bulk density - split core

Shear strength

- Peak shear strength
- Remoulded shear strength

Colour spectrophotometer

- MSCL spectrophotometer

2019Nuliajuk Gravity Core 015

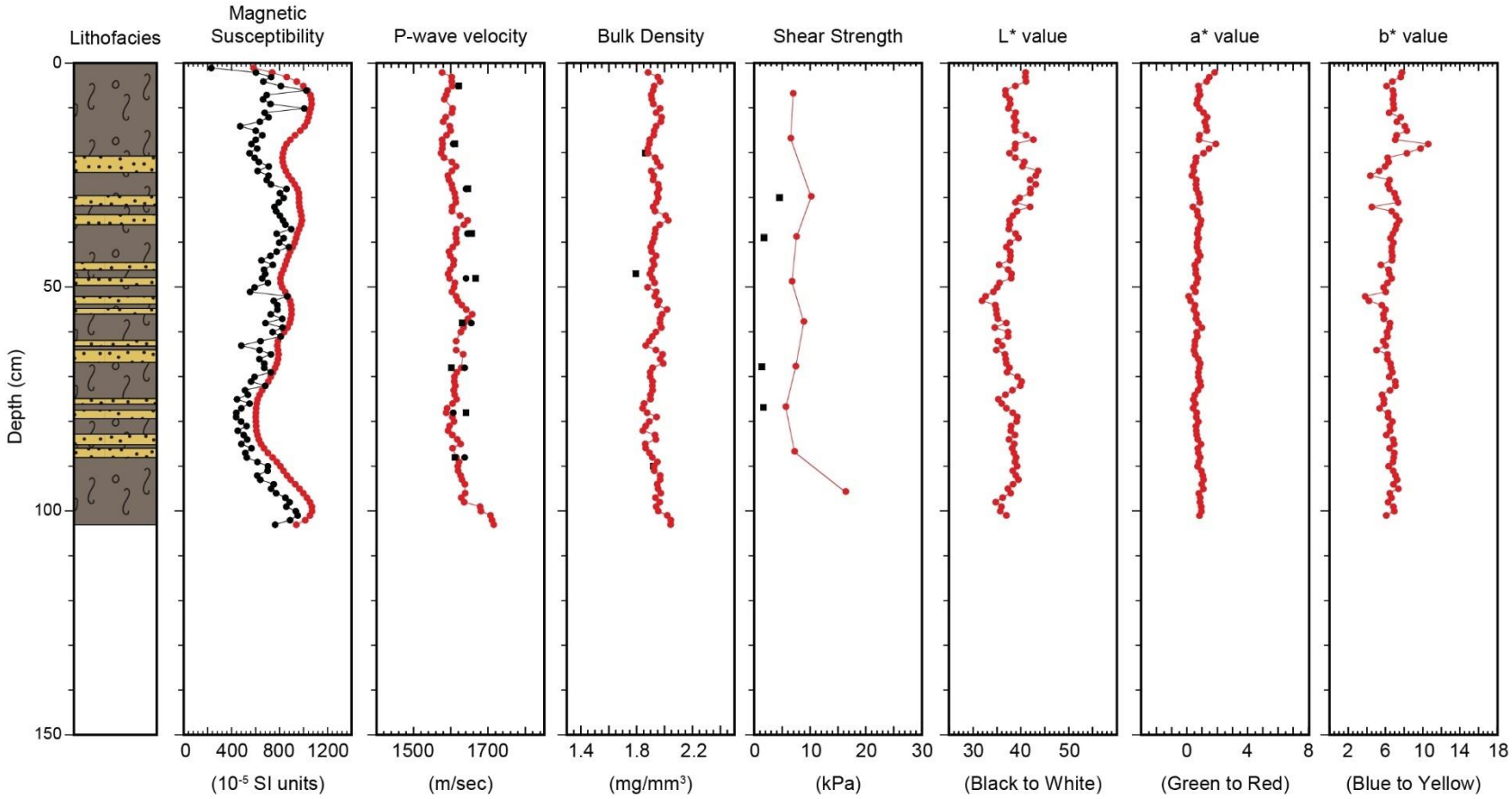

(66°36989' N, -65°503538' W; 27 m water depth)

2019Nuliajuk Gravity Core 017

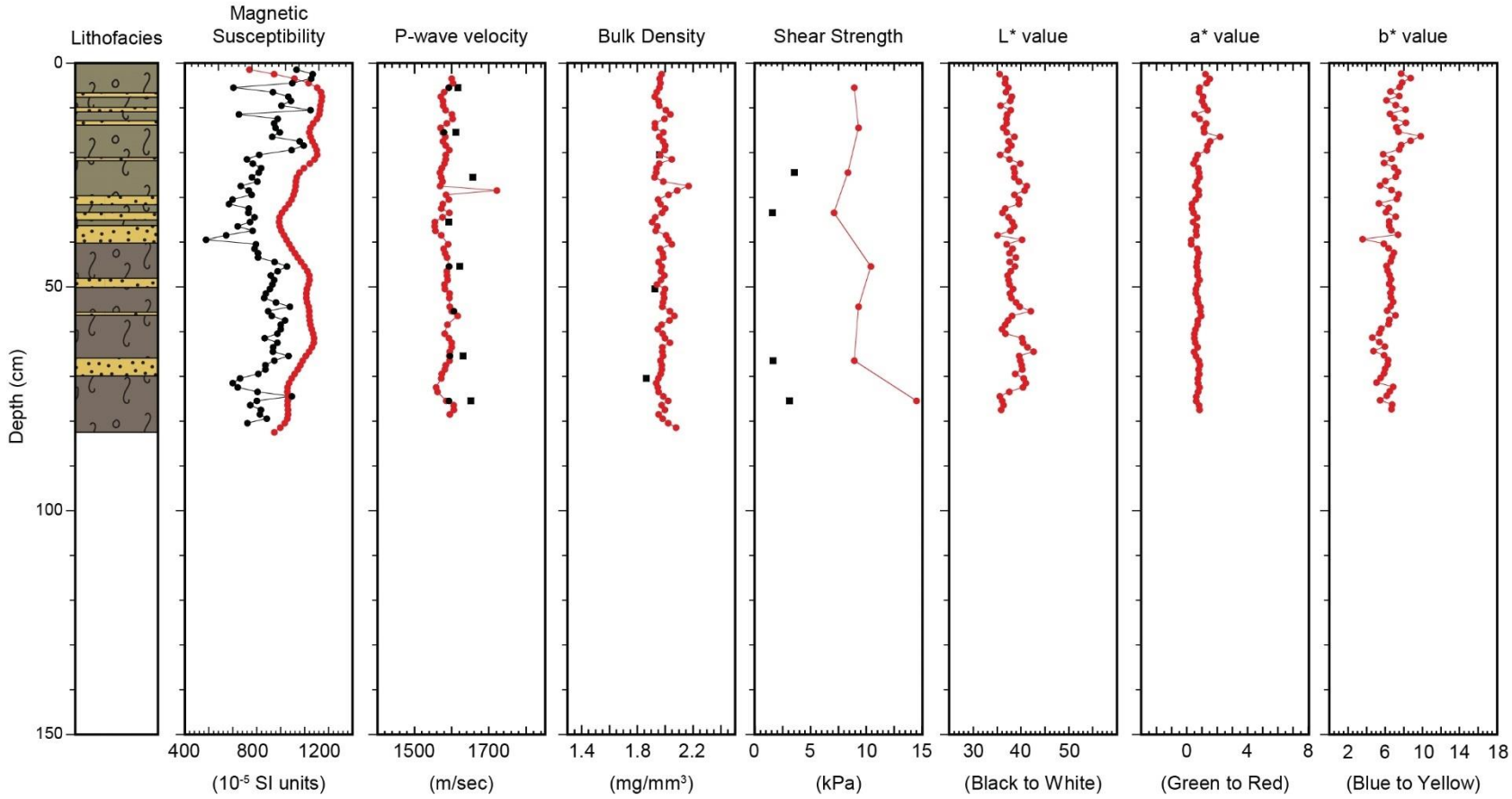

(66°36989' N, -65°503538' W; 27 m water depth)

2019Nuliajuk Gravity Core 020

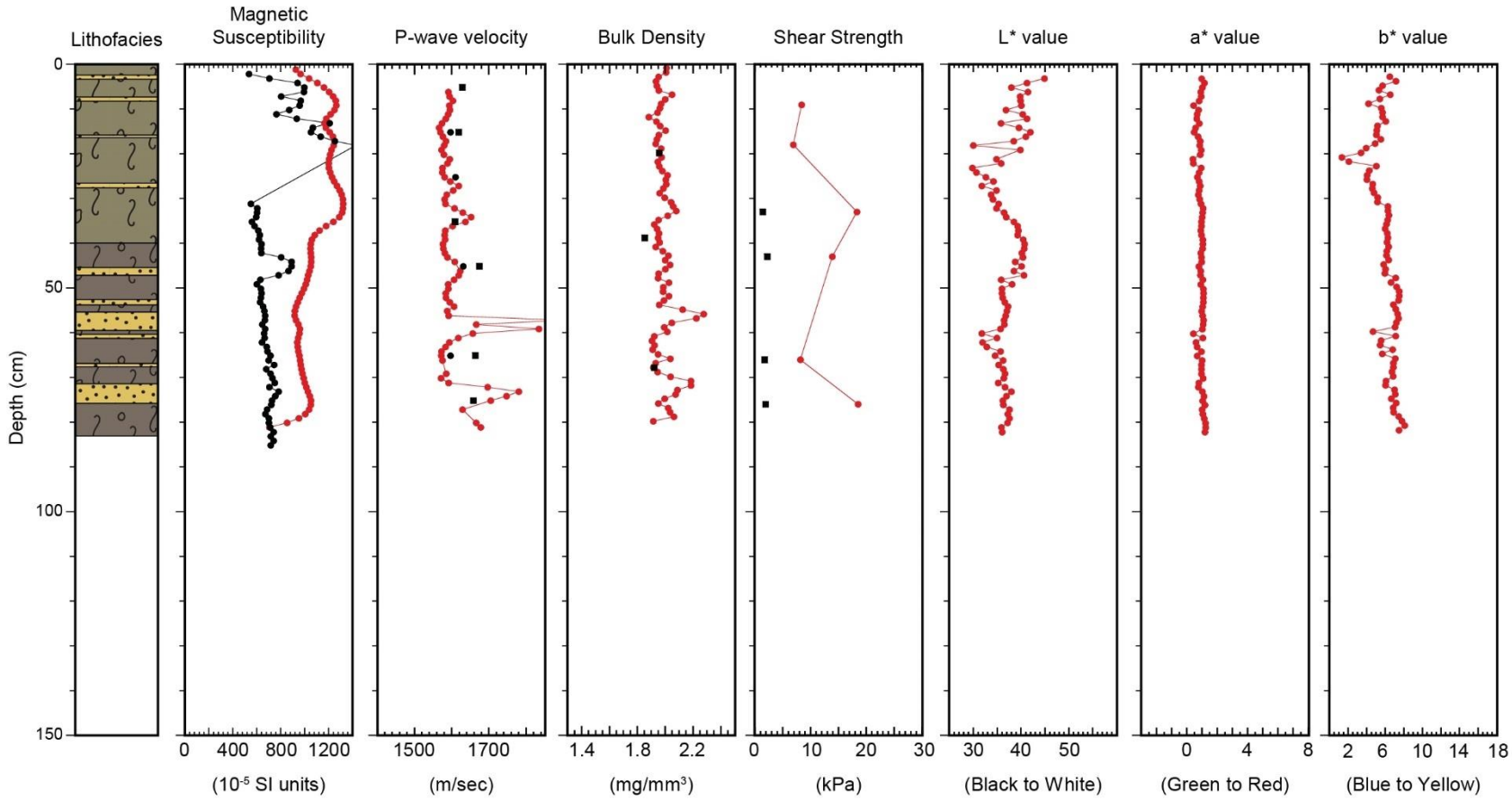

(66°371148' N, -65°50126' W; 36.5 m water depth)

2019Nuliajuk Gravity Core 022

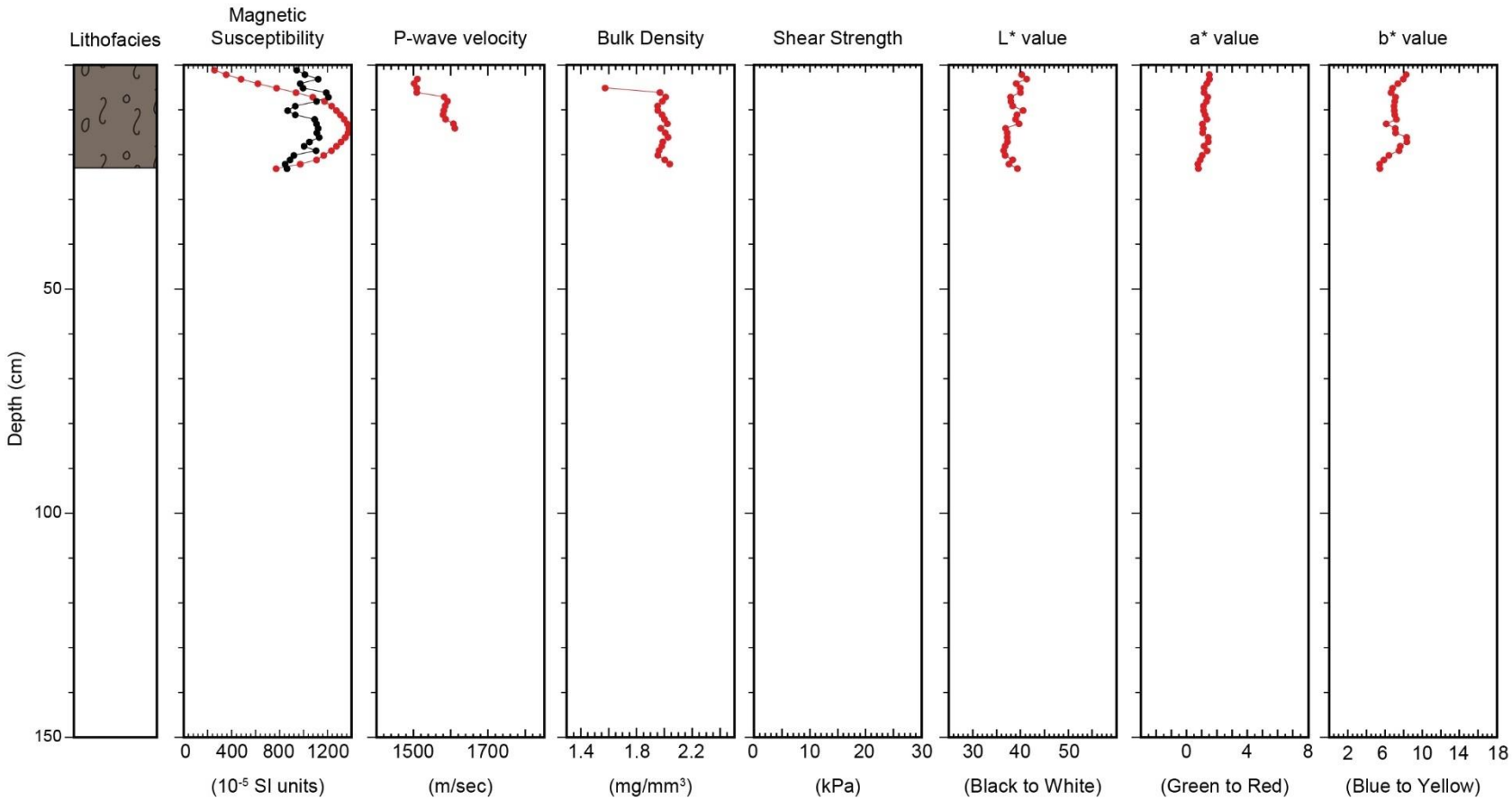

(66°364073' N, -65°494122' W; 80 m water depth)

2019Nuliajuk Gravity Core 024

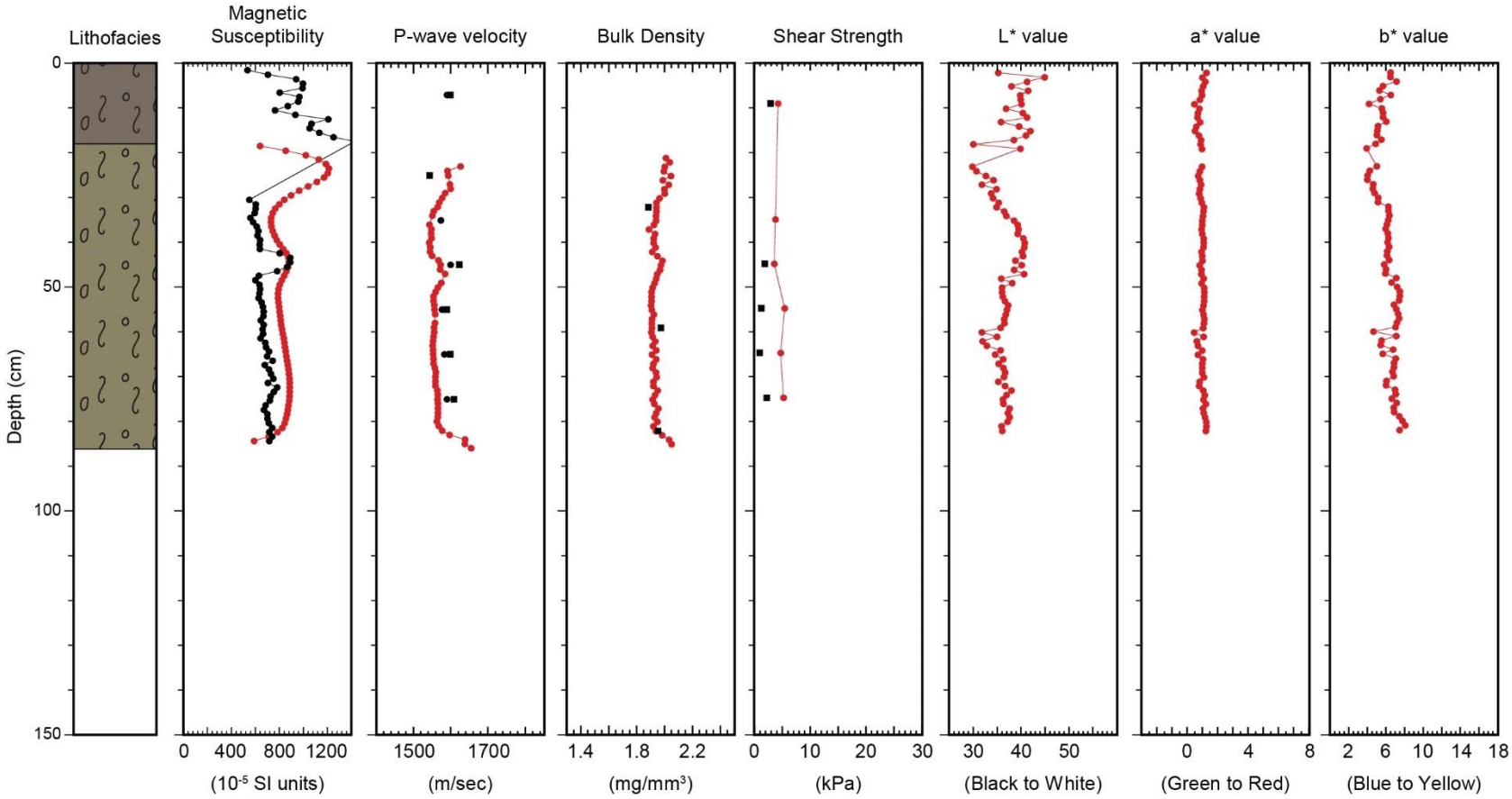

(66°3641083' N, -65°493517' W; 87 m water depth)

2019Nuliajuk Gravity Core 028

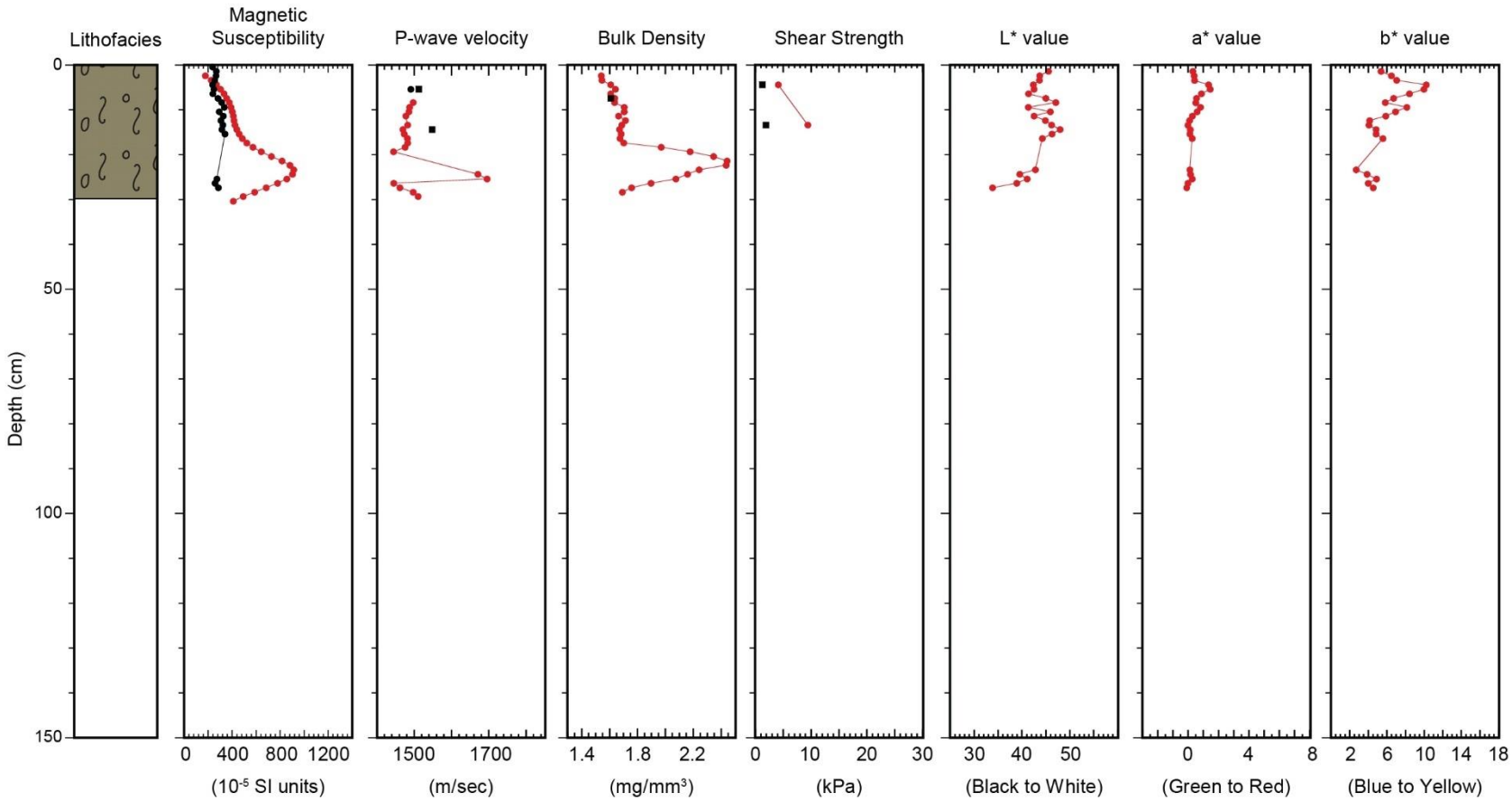

(66°00633' N, -65°527517' W; 67 m water depth)

2019Nuliajuk Gravity Core 030

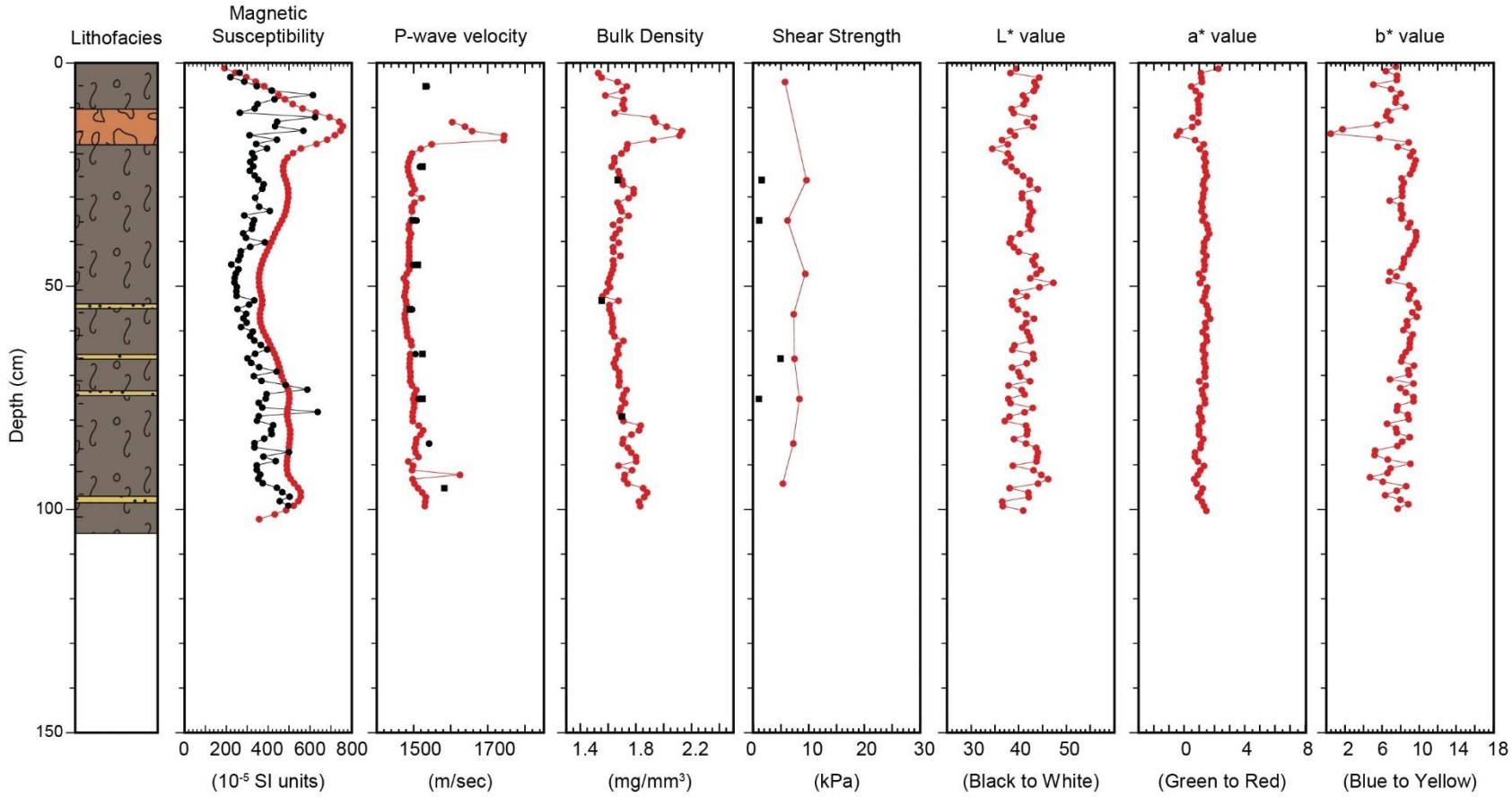

(66°279327' N, -65°537513' W; 87 m water depth)

2019Nuliajuk Gravity Core 031

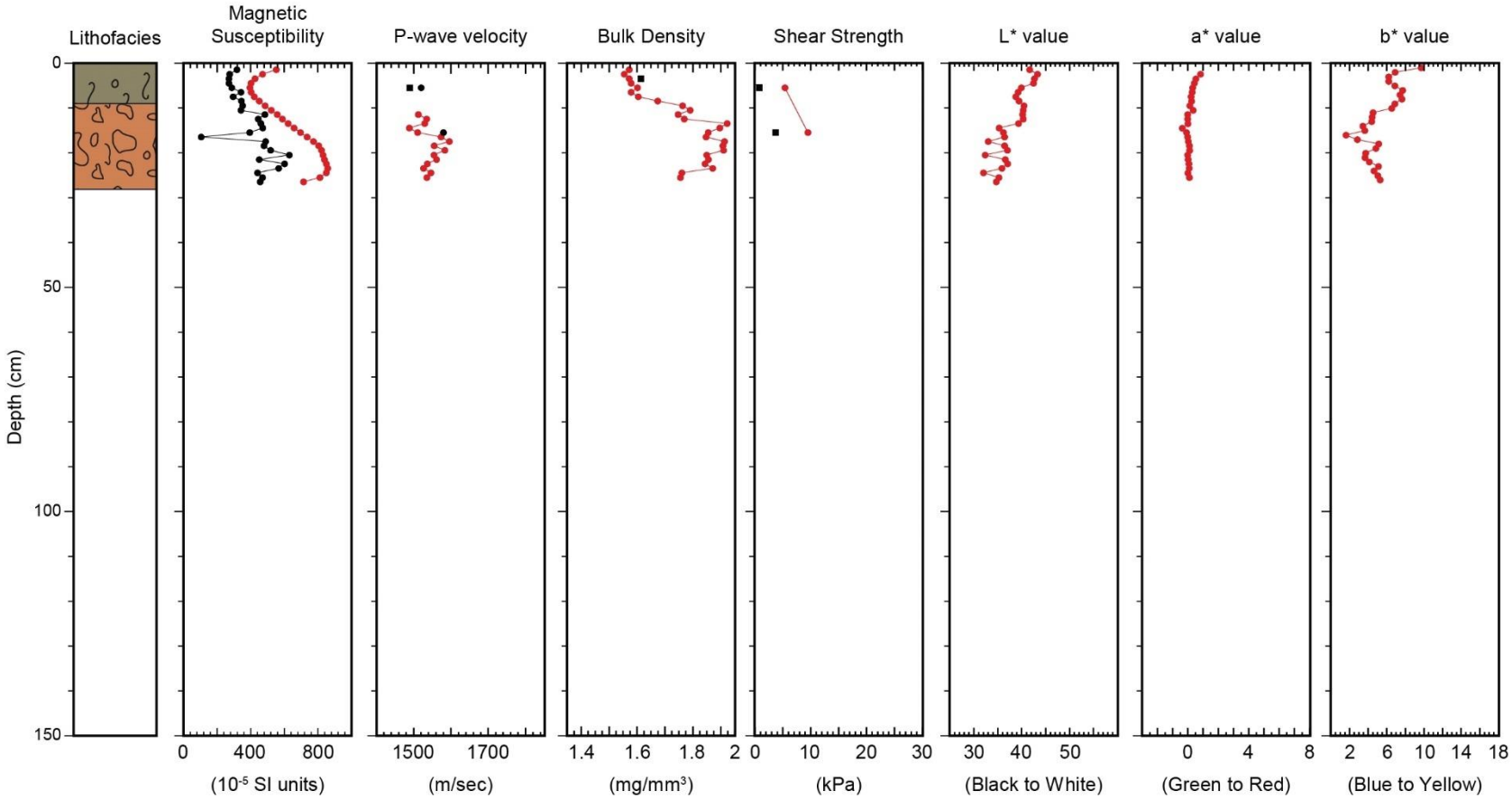

(66°280232' N, -65°552828' W; 44 m water depth)

2019Nuliajuk Gravity Core 034

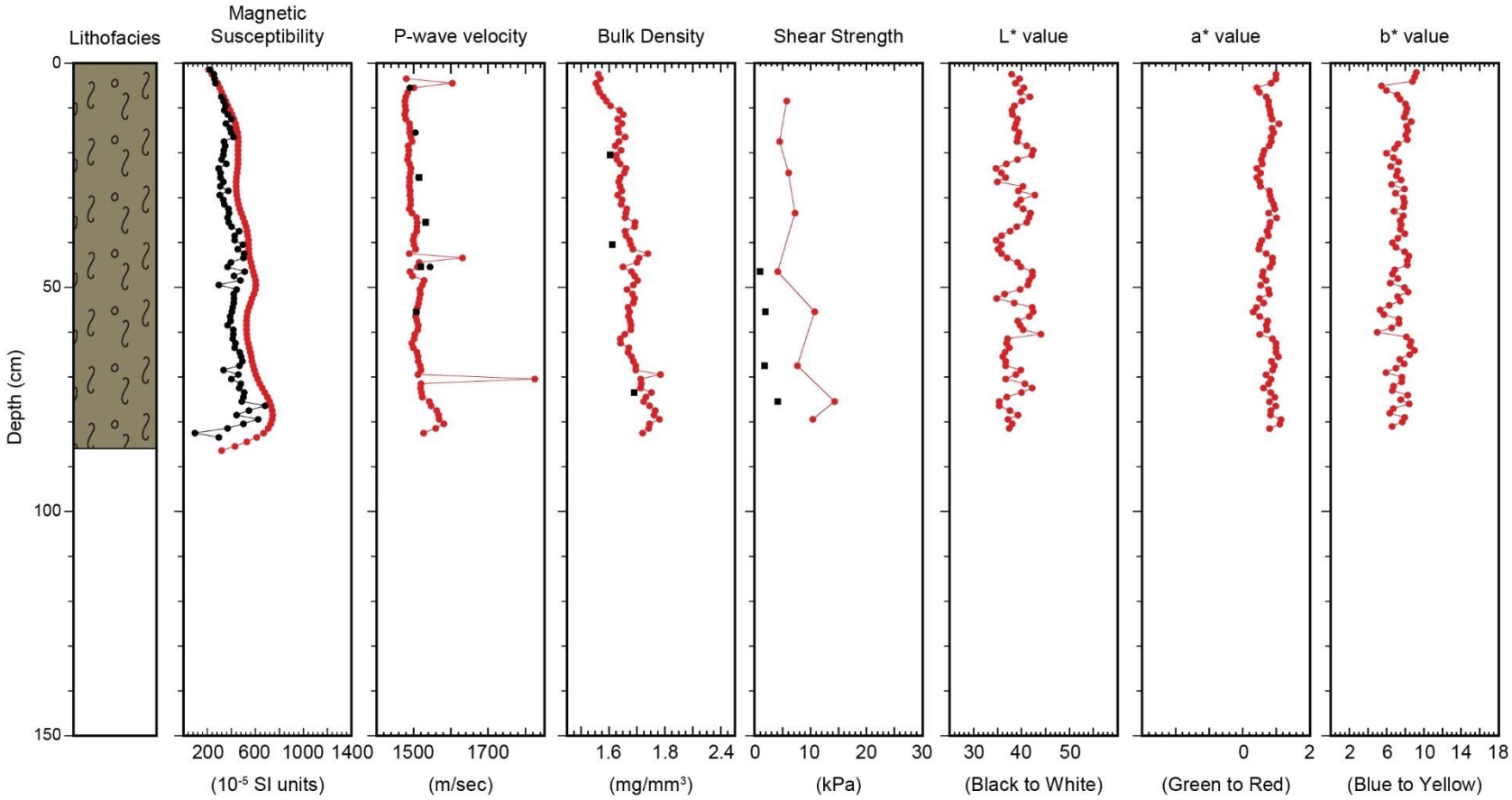

(66°260178' N, -65°547673' W; 110 m water depth)

2019Nuliajuk Gravity Core 035

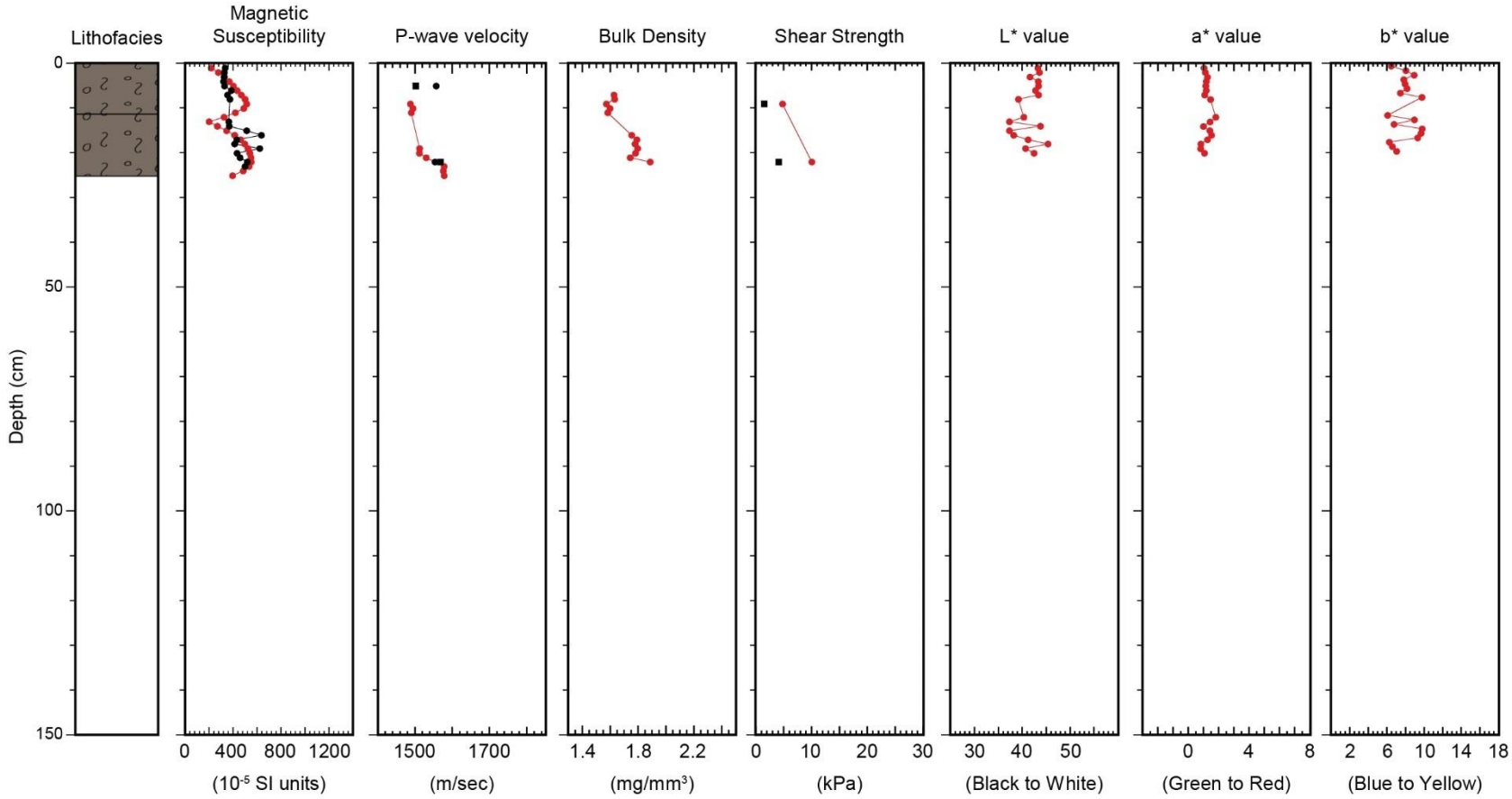

(66°239003' N, -65°550998' W; 101 m water depth)

2019Nuliajuk Gravity Core 037

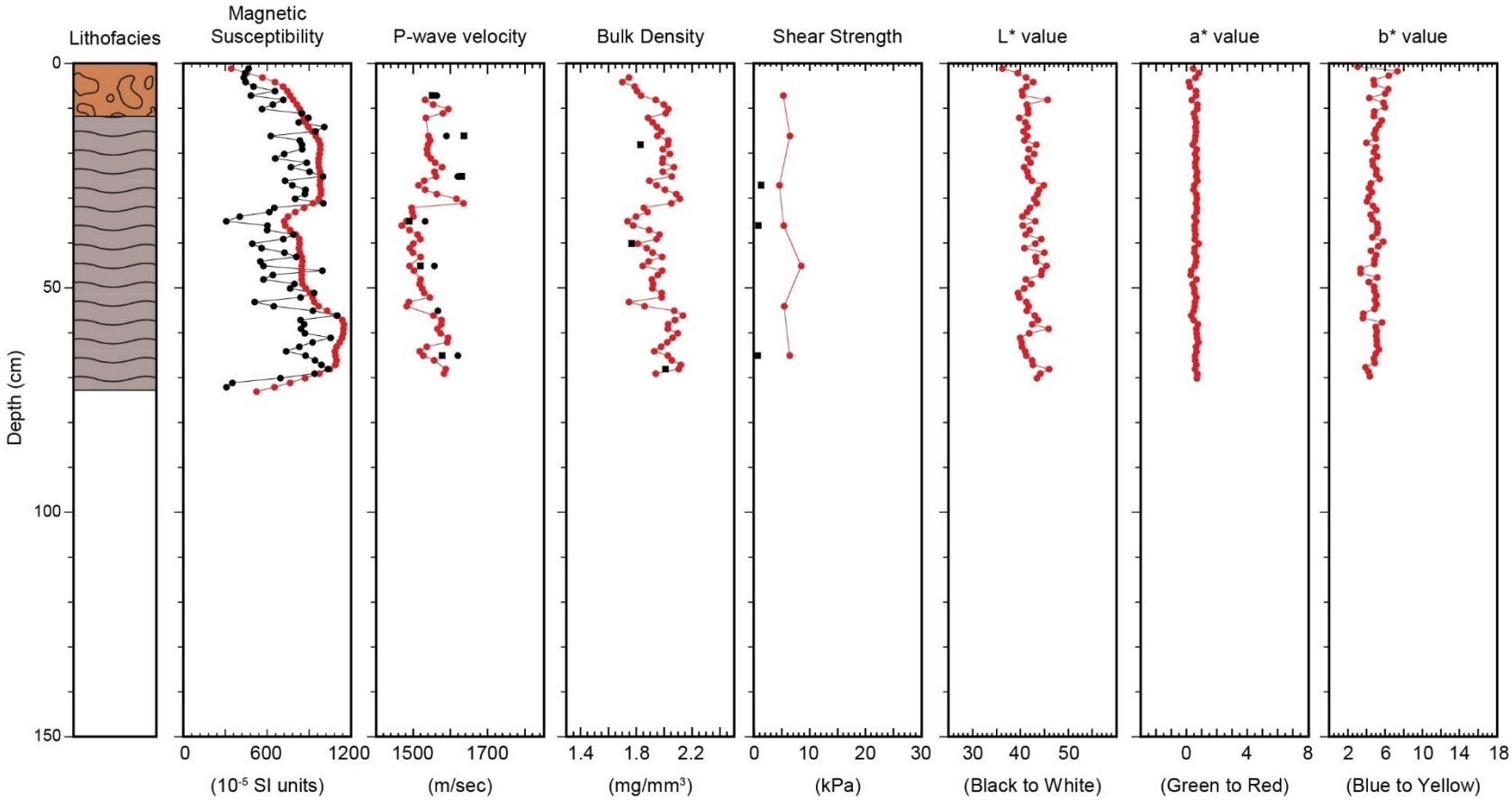

(66°238832' N, -65°560567' W; 65 m water depth)

2019Nuliajuk Gravity Core 038

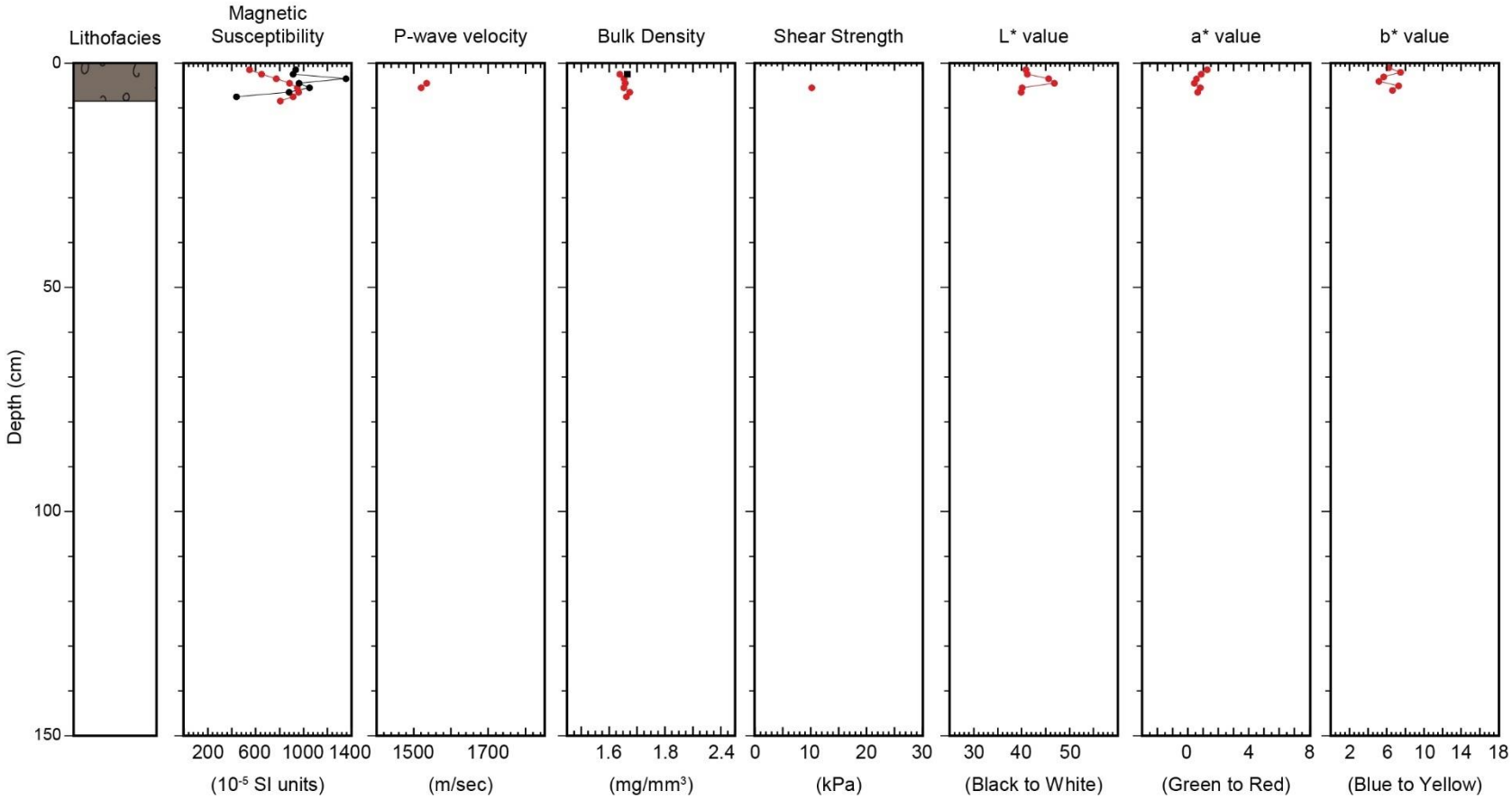

(66°239893' N, -65°560745' W; 57 m water depth)

2019Nuliajuk Gravity Core 039

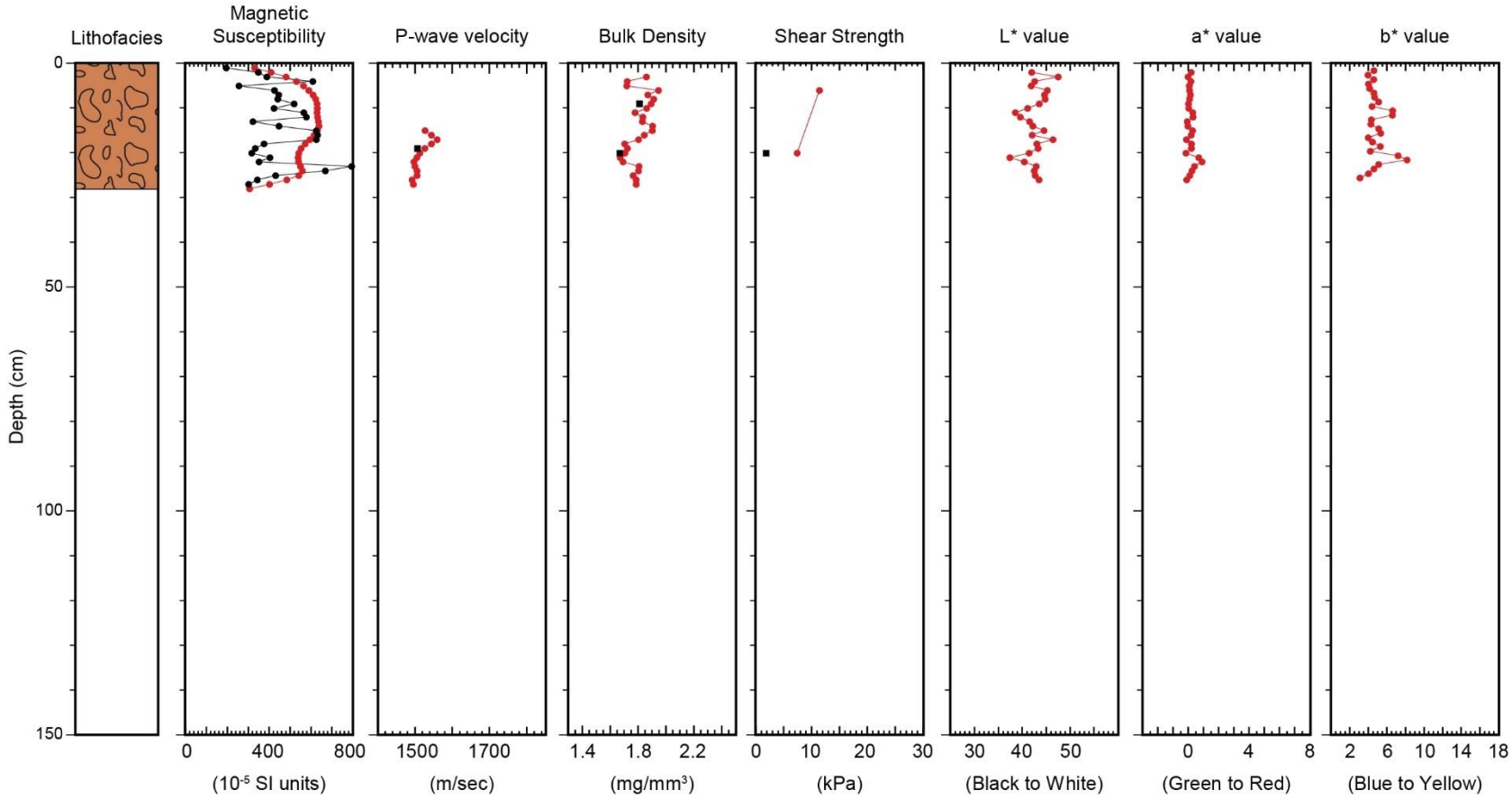

(66°24374' N, -65°560828' W; 61 m water depth)

2019Nuliajuk Gravity Core 040

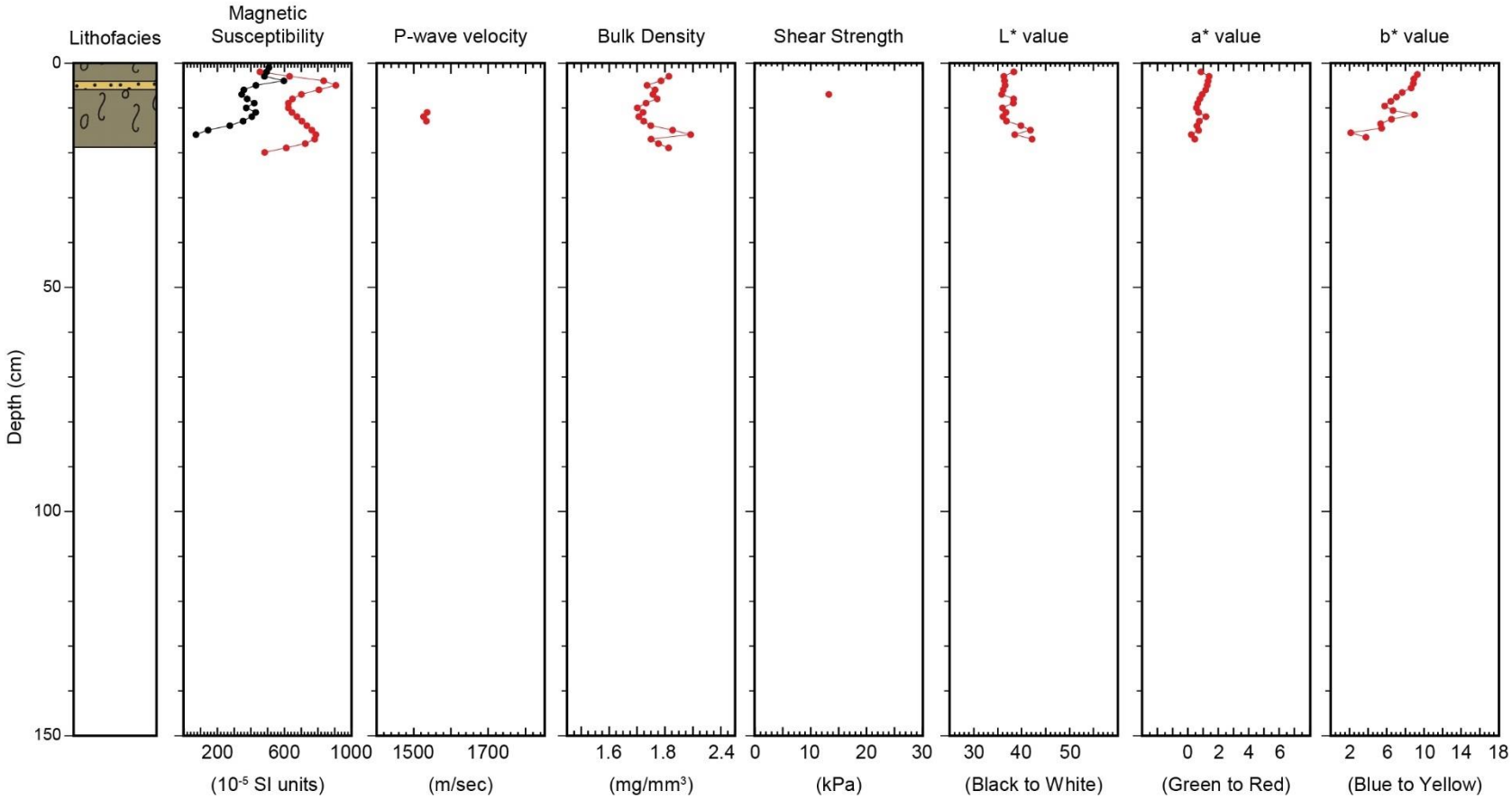

(66°158628' N, -65°707868' W; 70 m water depth)

2019Nuliajuk Gravity Core 041

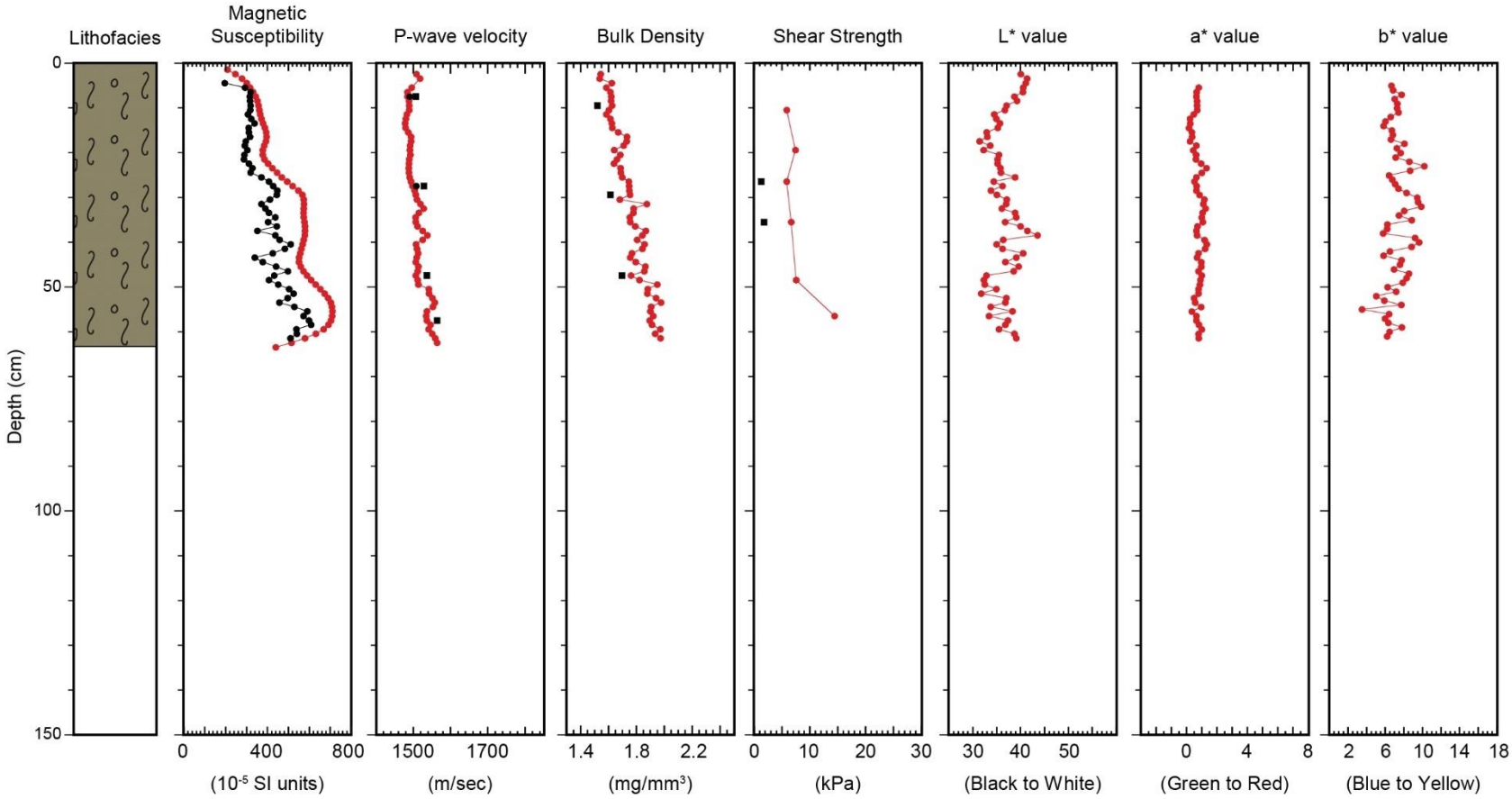

(66°164393' N, -65°718175' W; 145 m water depth)

2019Nuliajuk Gravity Core 042

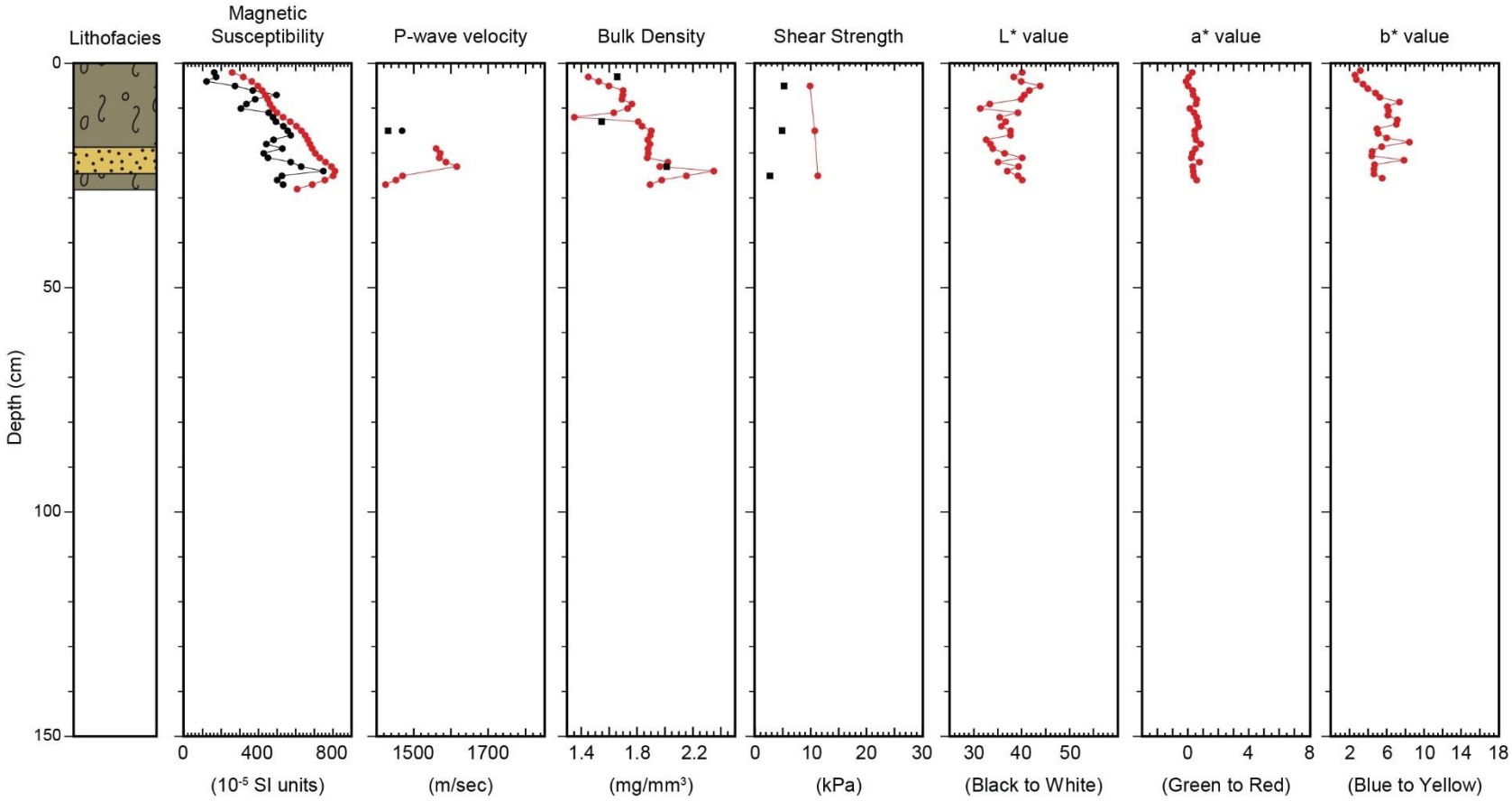

(66°158917' N, -65°75927' W; 140 m water depth)

2019Nuliajuk Gravity Core 043

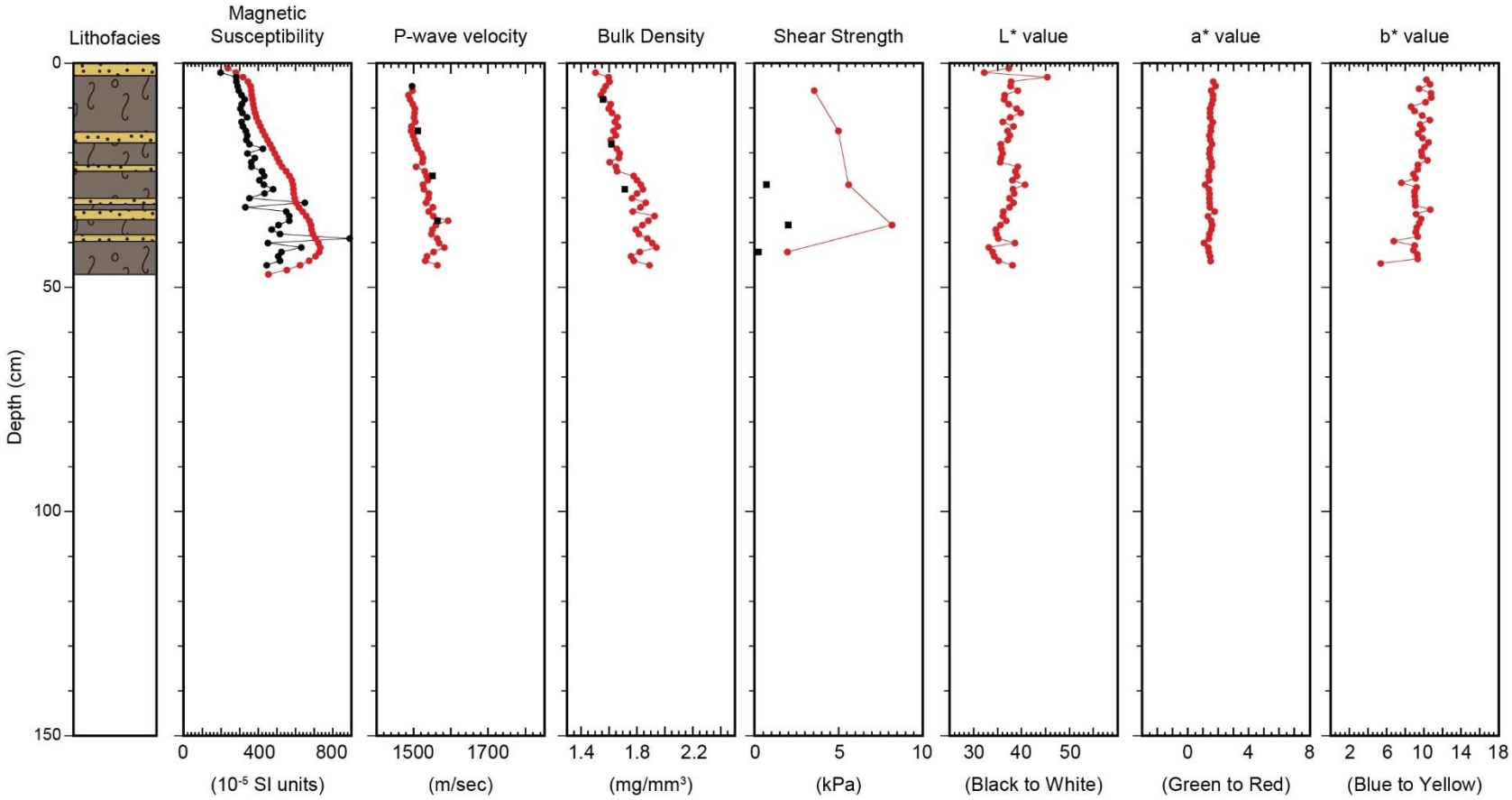

(66°174225' N, -65°664755' W; 108 m water depth)

2019Nuliajuk Gravity Core 044

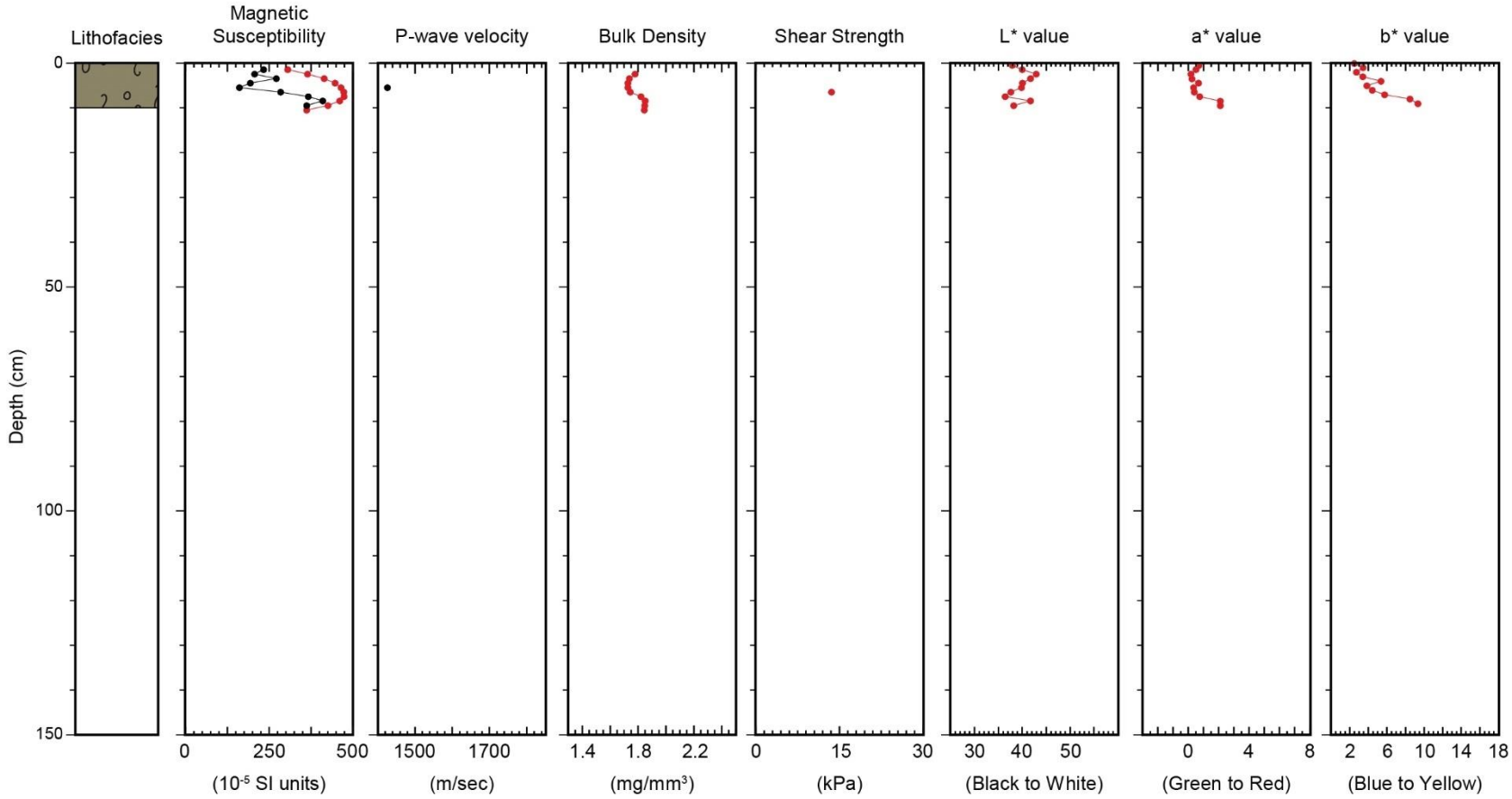

(66°134585' N, -65°80121' W; 156 m water depth)

2019Nuliajuk Gravity Core 047

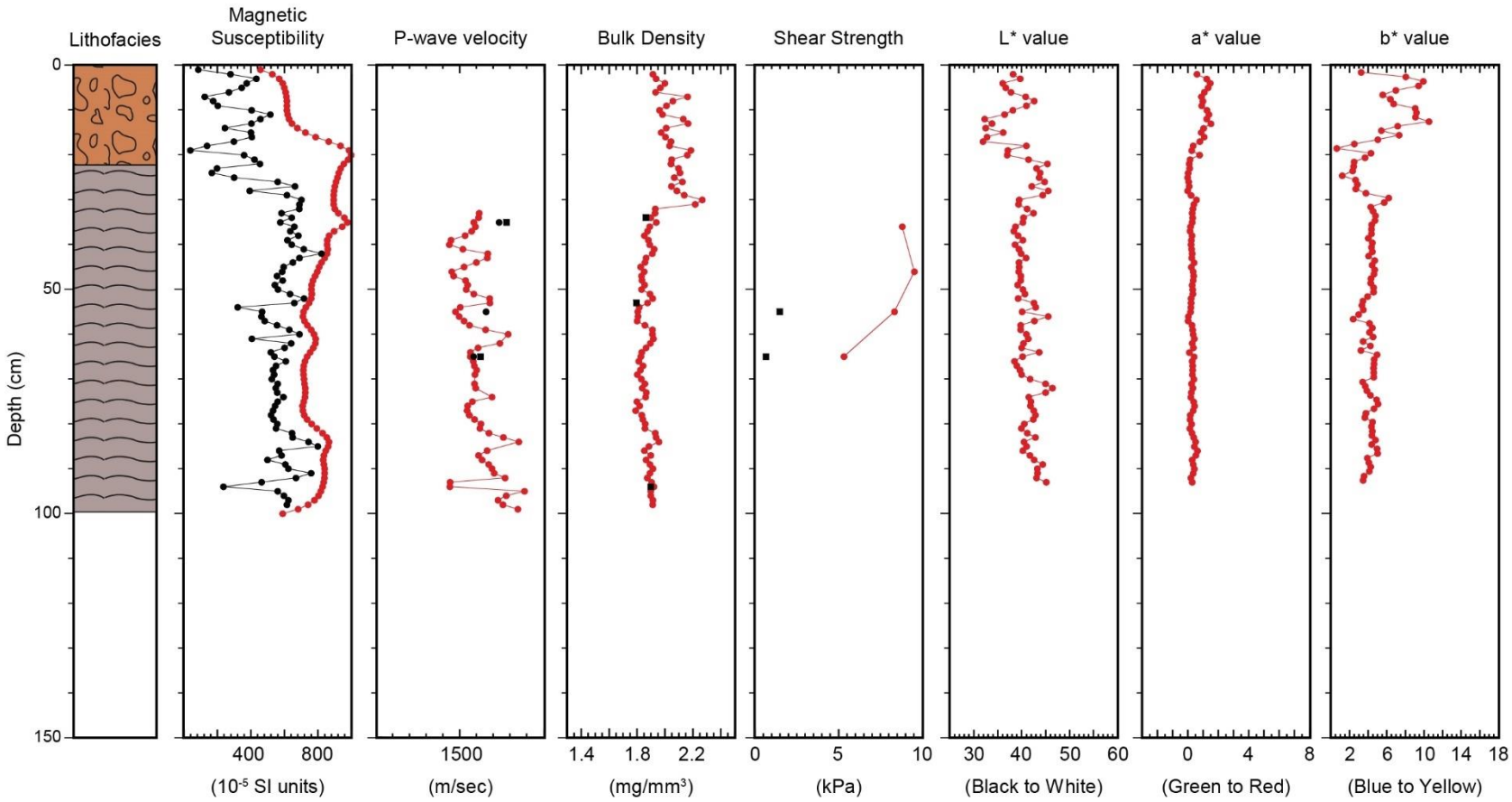

(66°125497' N, -65°863072' W; 66 m water depth)

2019Nuliajuk Gravity Core 048

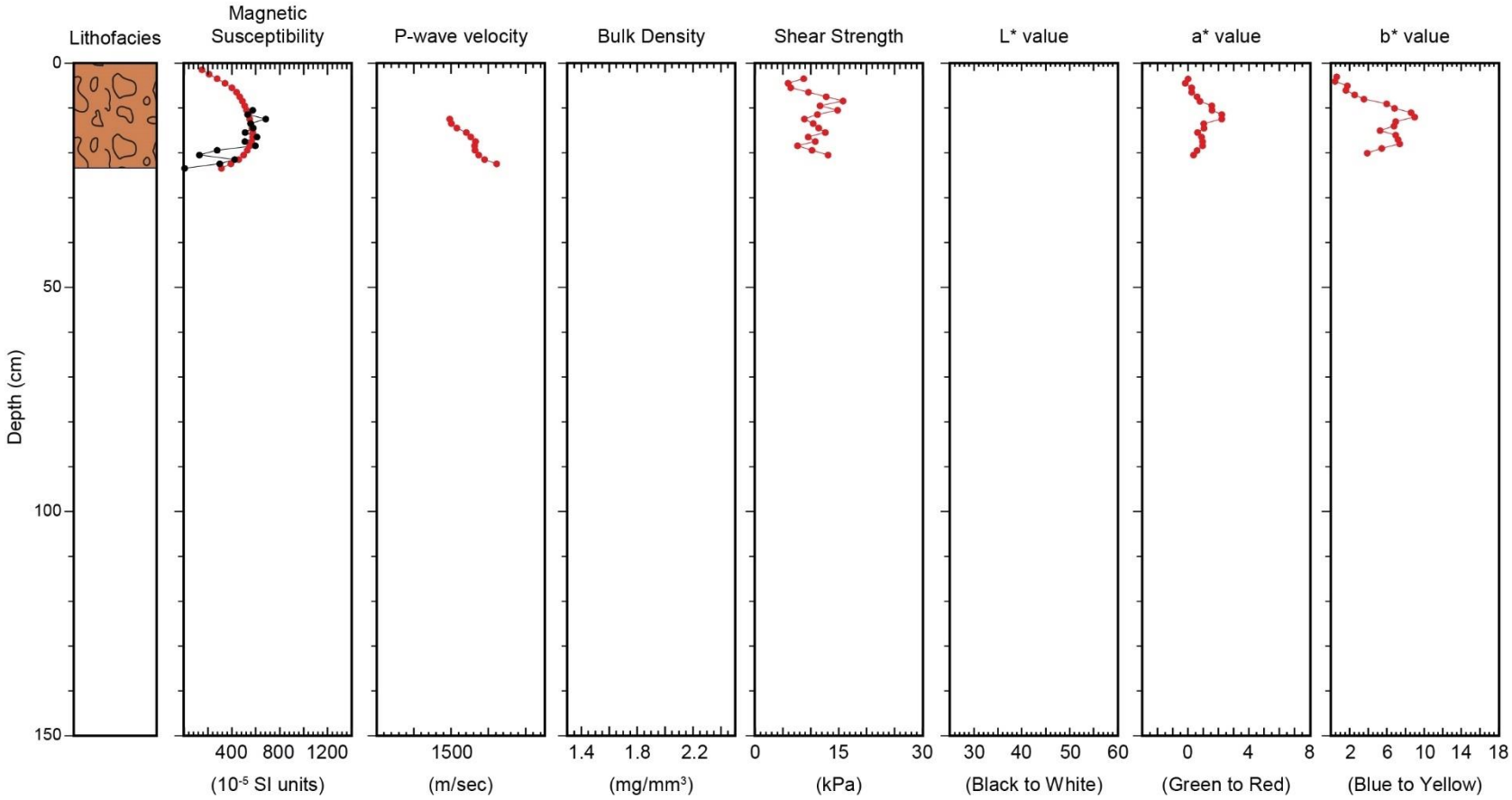

(66°121208' N, -65°893797' W; 98 m water depth)

Appendix C: Core photos, X-radiographs, and grain size plots

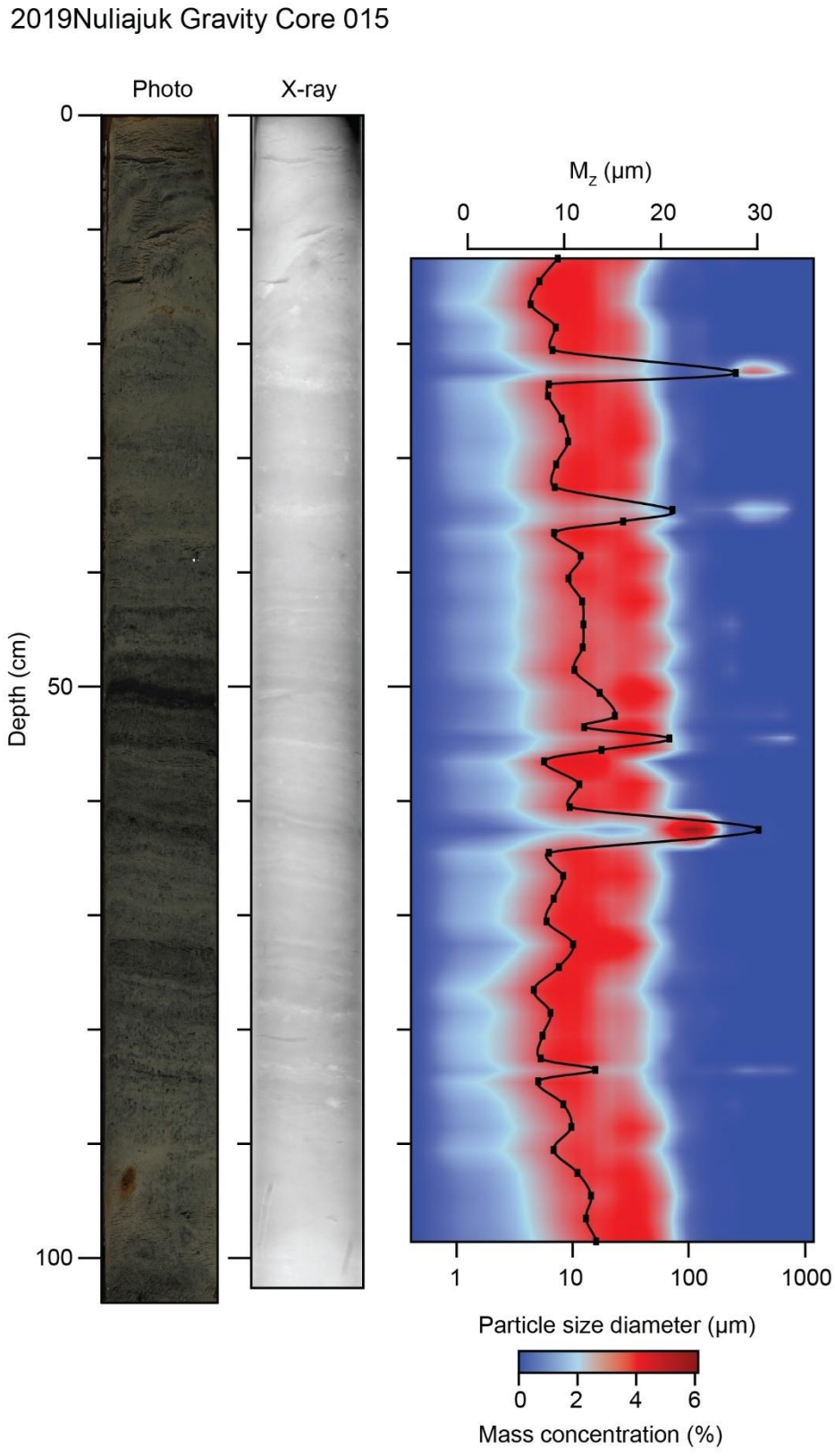

2019Nuliajuk Gravity Core 017

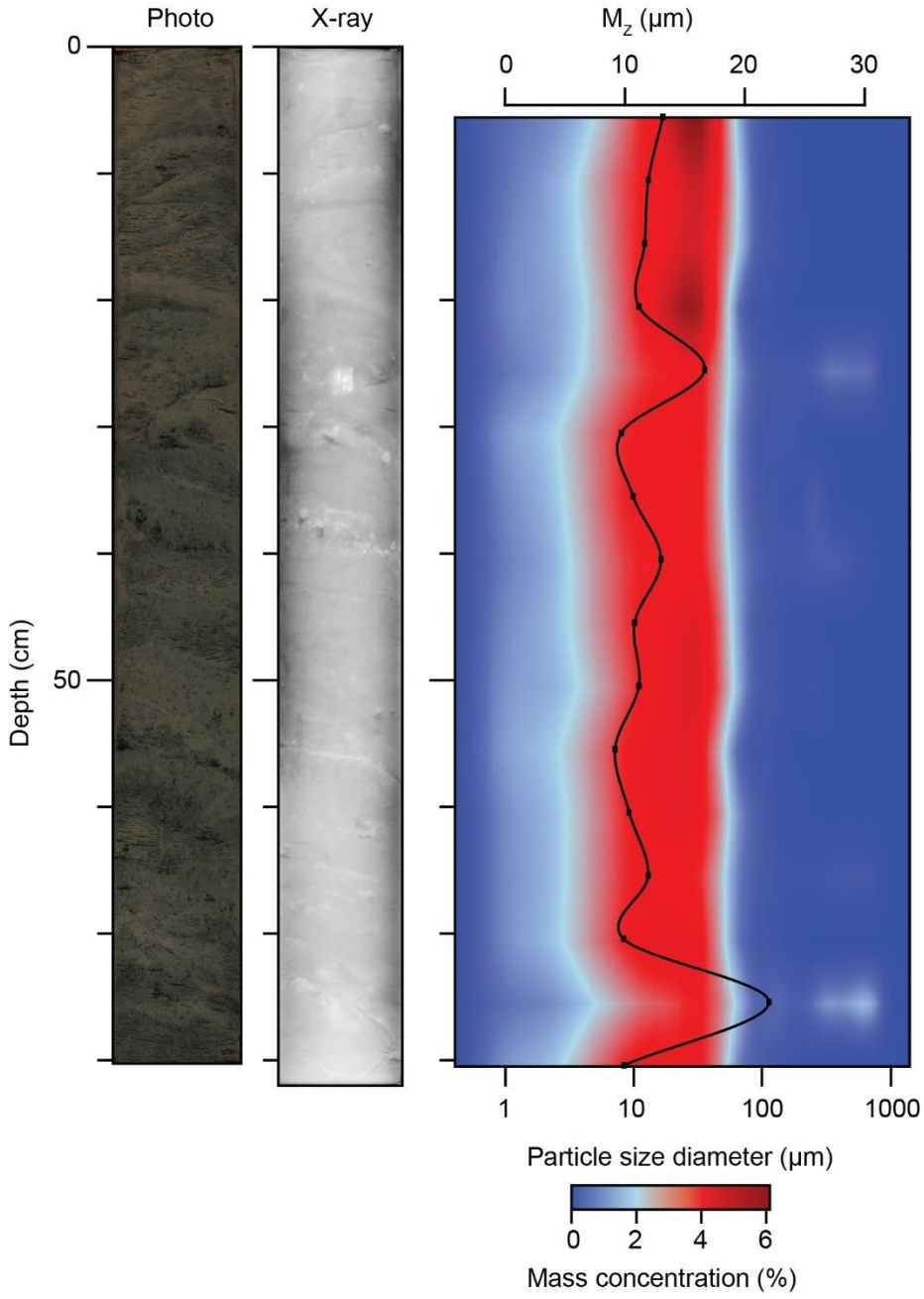

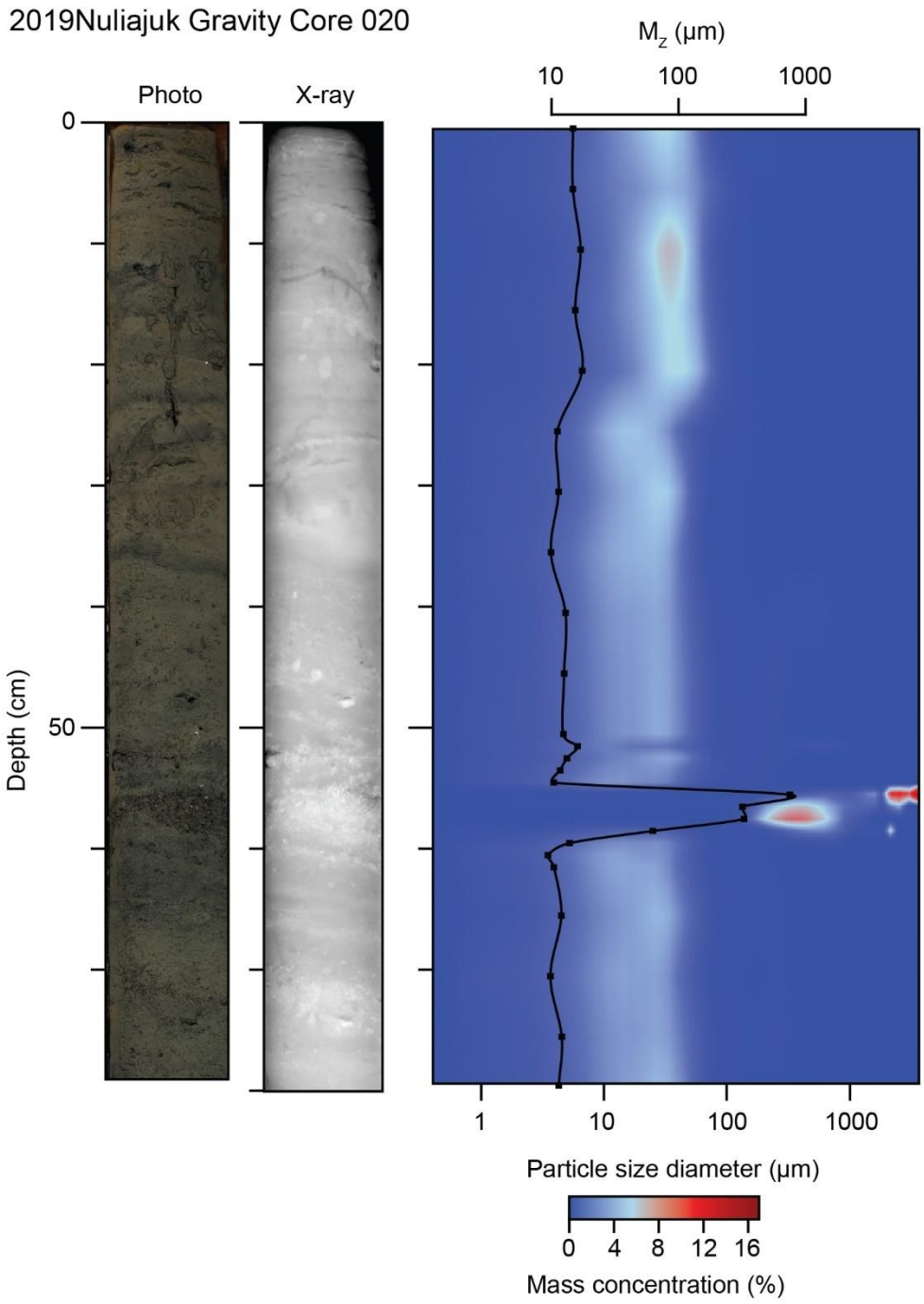
2019Nuliajuk Gravity Core 020
Photo
X-ray
M_z (µm)
10
100
1000
0
50
Depth (cm)
1
10
100
1000
Particle size diameter (µm)
0
4
8
12
16
Mass concentration (%)

2019Nuliajuk Gravity Core 024

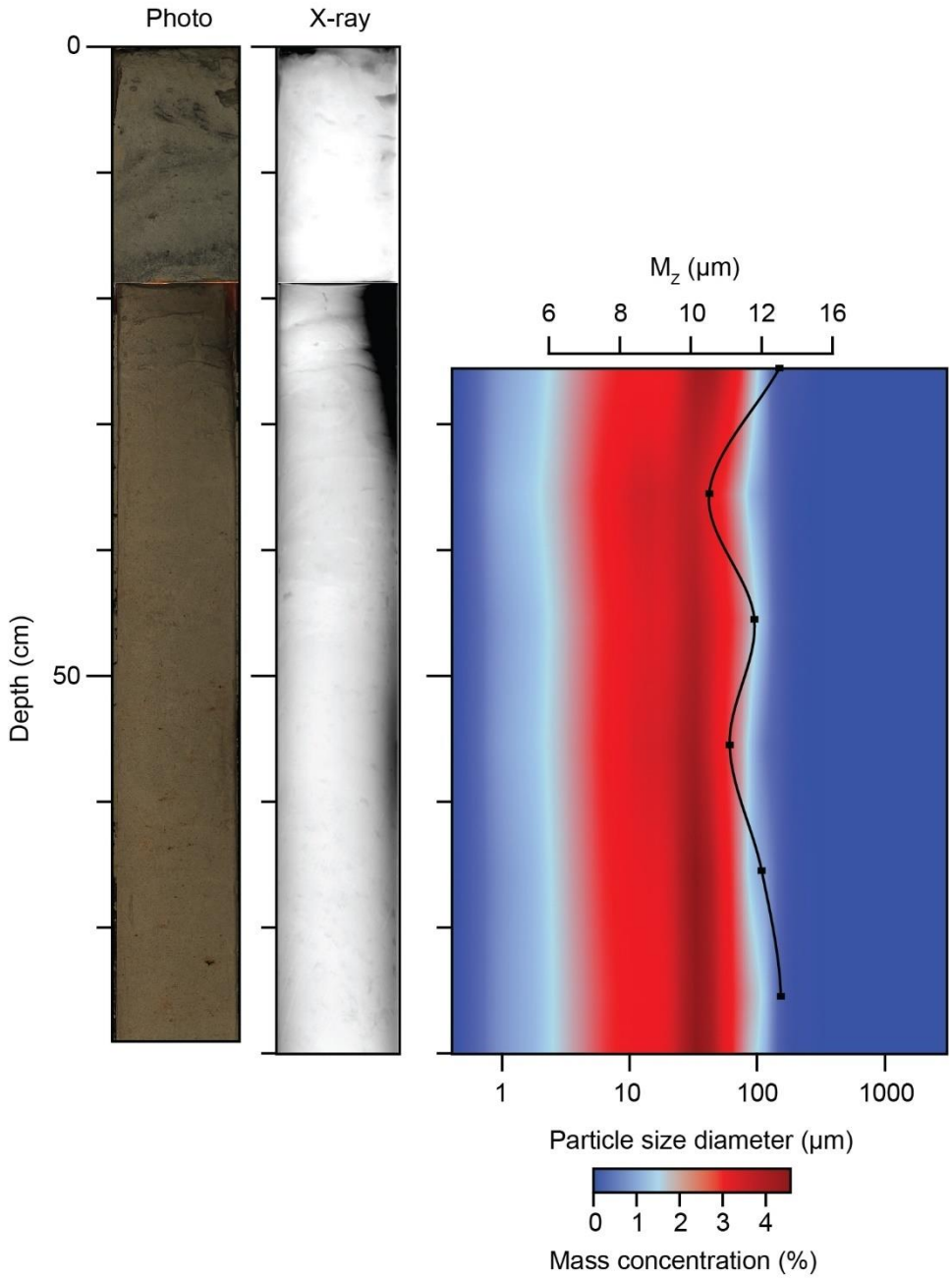

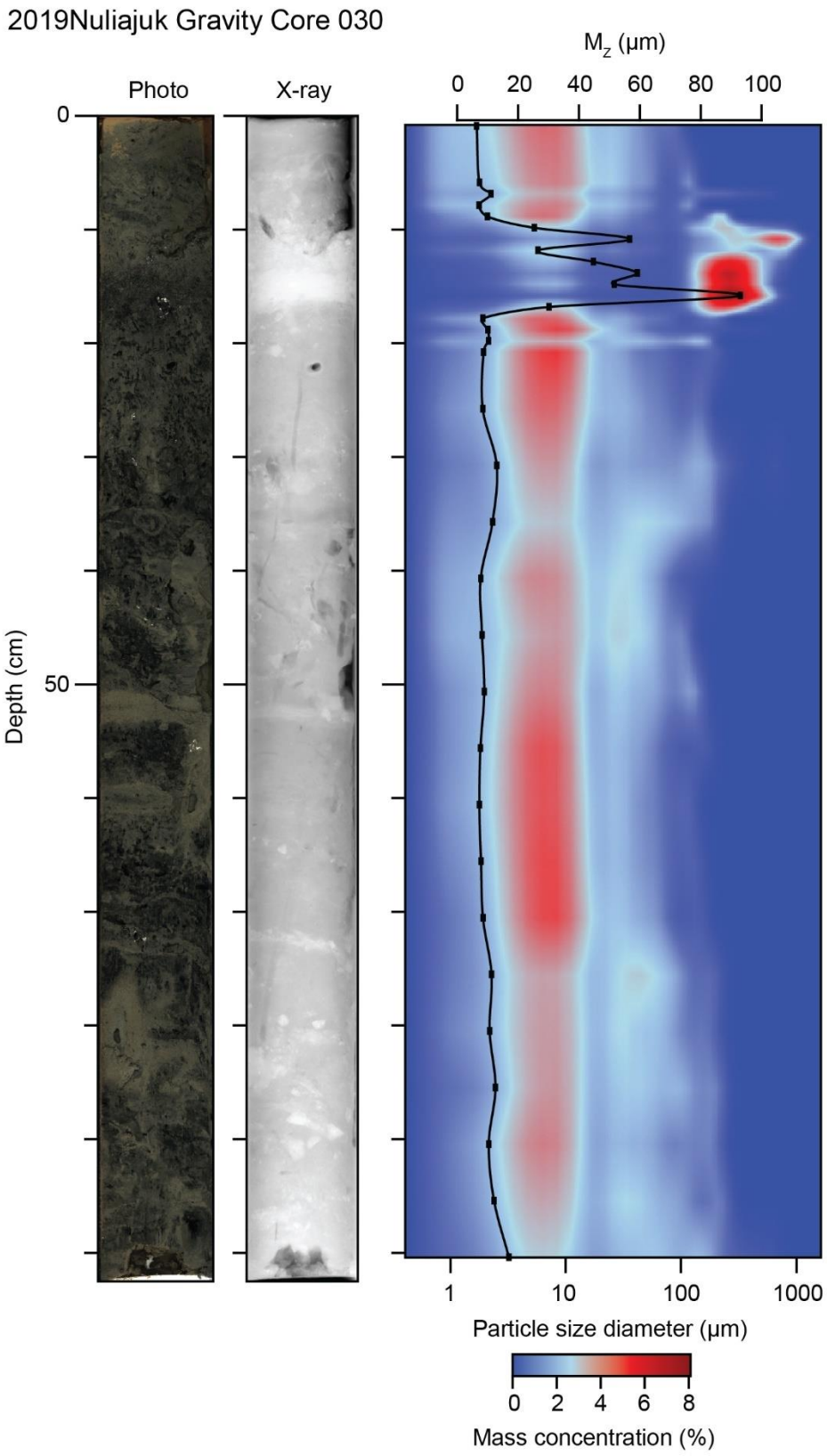
2019Nuliajuk Gravity Core 030
Photo
X-ray
M_z (μm)
0
20
40
60
80
100
Depth (cm)
0
50
1
10
100
1000
Particle size diameter (μm)
0
2
4
6
8
Mass concentration (%)

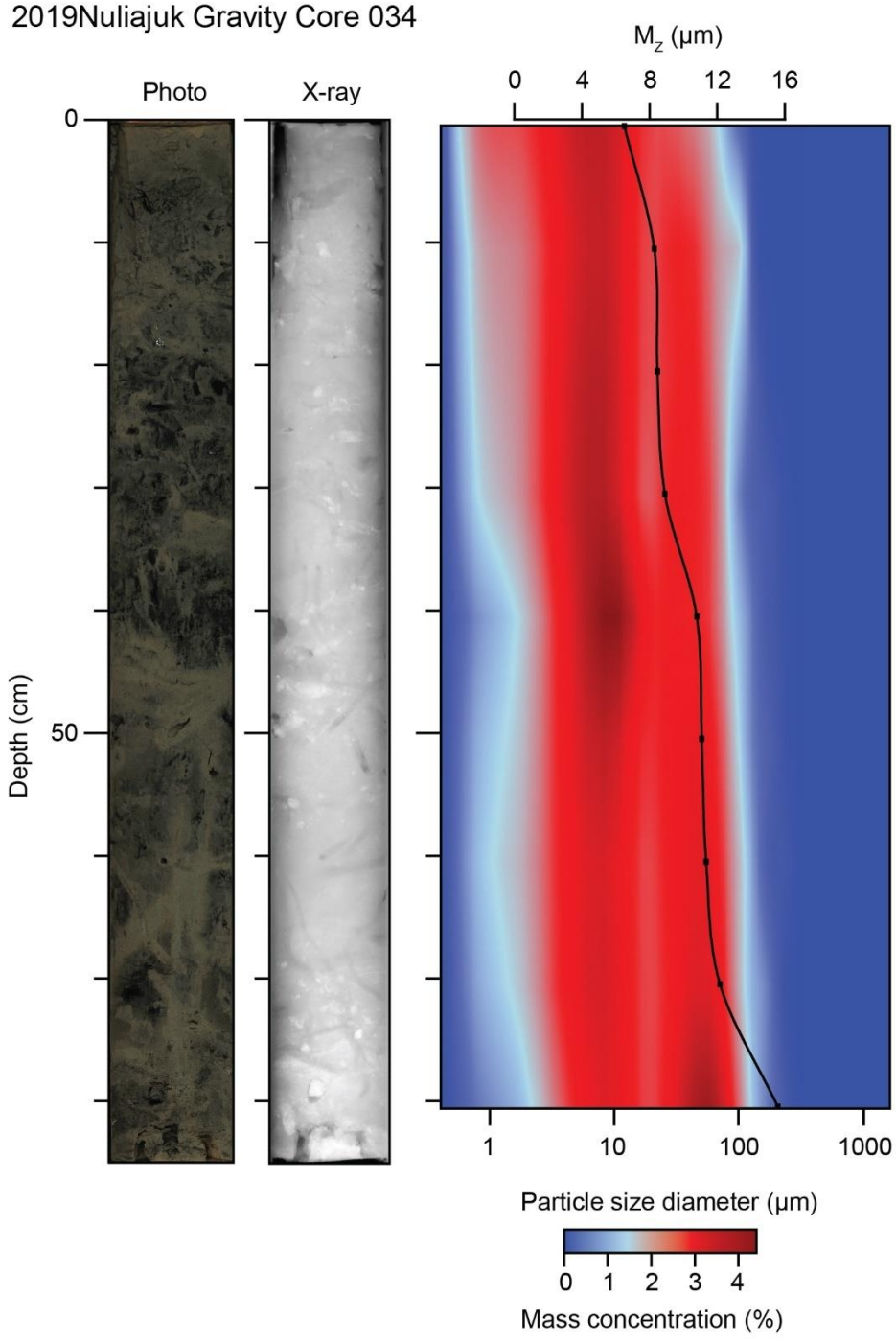
2019Nuliajuk Gravity Core 034
Photo
X-ray
M_z (μm)
0
4
8
12
16
0
50
Depth (cm)
1
10
100
1000
Particle size diameter (μm)
0
1
2
3
4
Mass concentration (%)

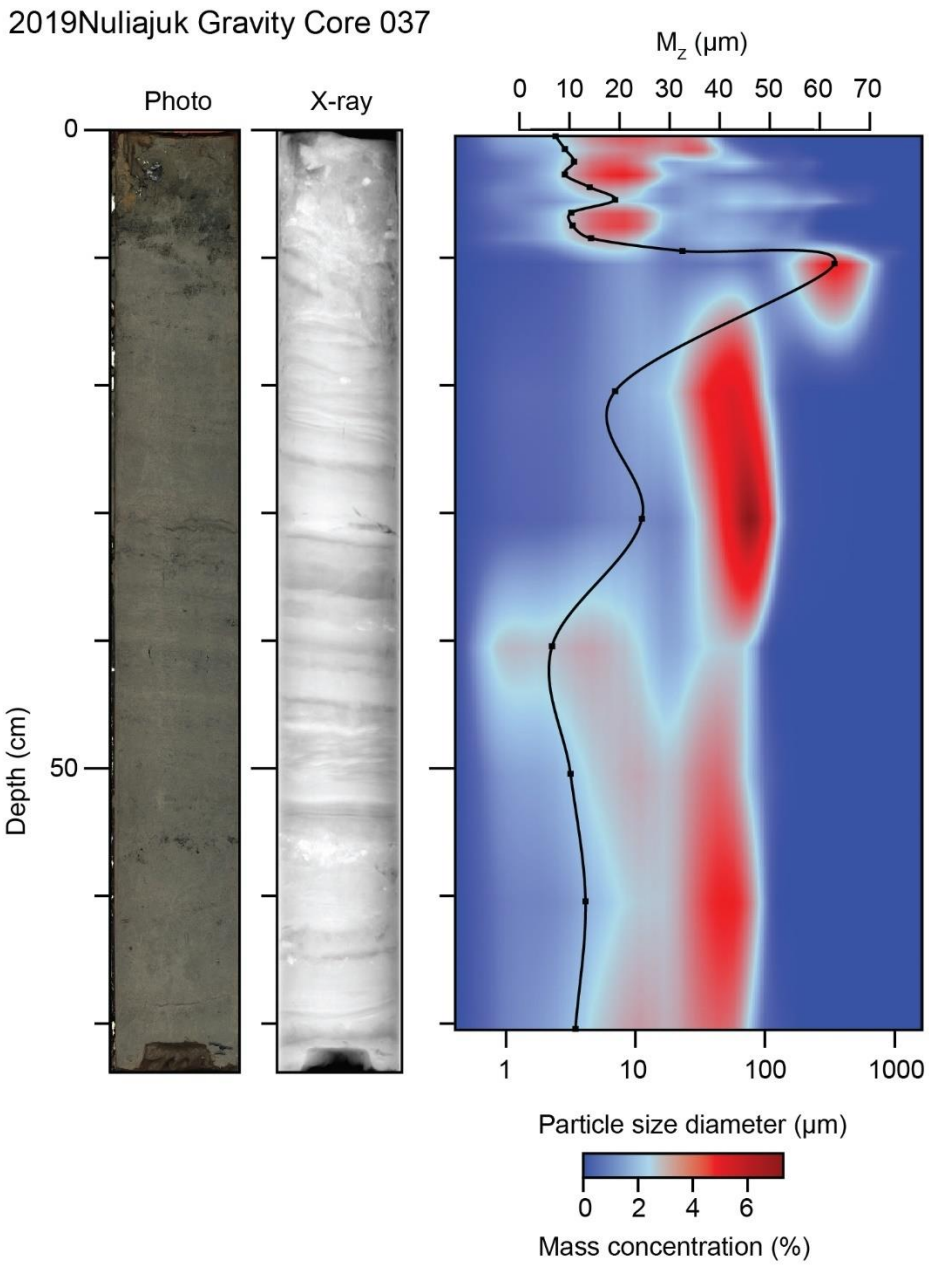
2019Nuliajuk Gravity Core 037
Photo
X-ray
M_z (μm)
0 10 20 30 40 50 60 70
0
50
Depth (cm)
1 10 100 1000
Particle size diameter (μm)
0 2 4 6
Mass concentration (%)

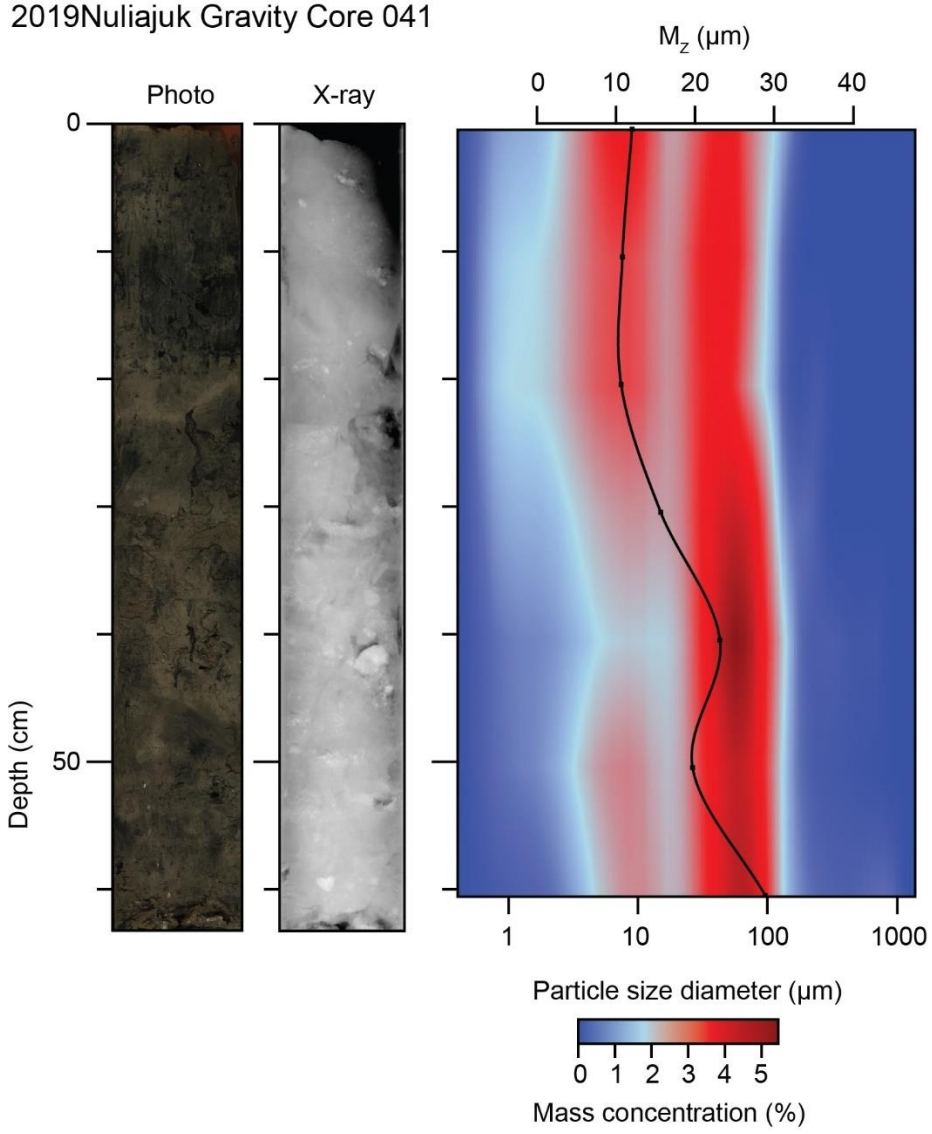
2019Nuliajuk Gravity Core 041
Photo
X-ray
M_z (µm)
0
10
20
30
40
0
50
Depth (cm)
1
10
100
1000
Particle size diameter (µm)
0 1 2 3 4 5
Mass concentration (%)

2019Nuliajuk Gravity Core 042

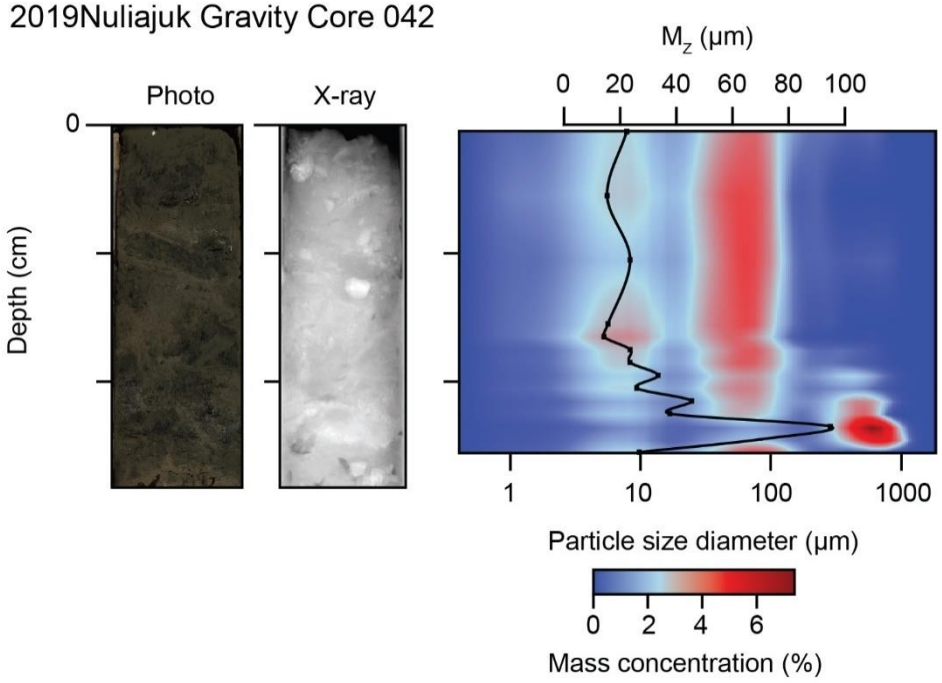

2019Nuliajuk Gravity Core 043

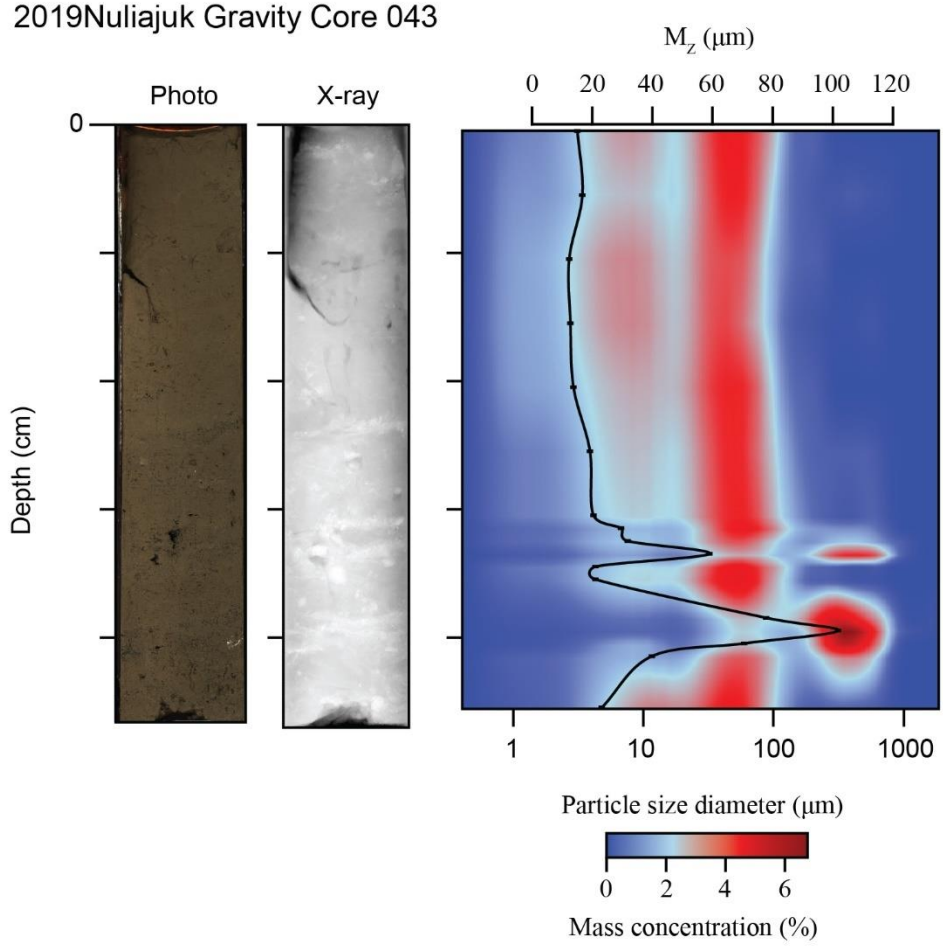

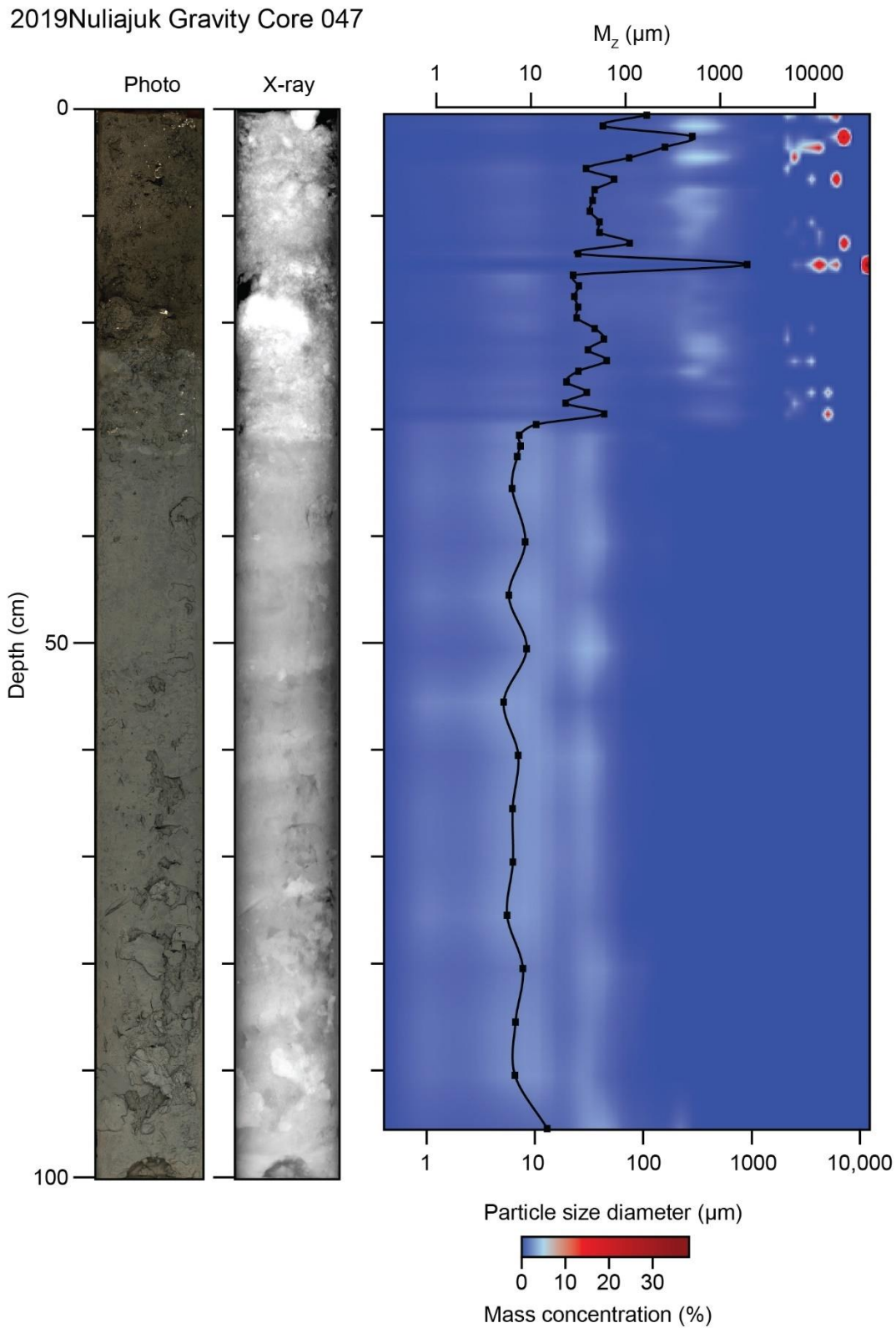
2019Nuliajuk Gravity Core 047
Photo
X-ray
M_z (µm)
1
10
100
1000
10000
0
50
100
Depth (cm)
1
10
100
1000
10,000
Particle size diameter (µm)
0
10
20
30
Mass concentration (%)

2019Nuliajuk Gravity Core 048

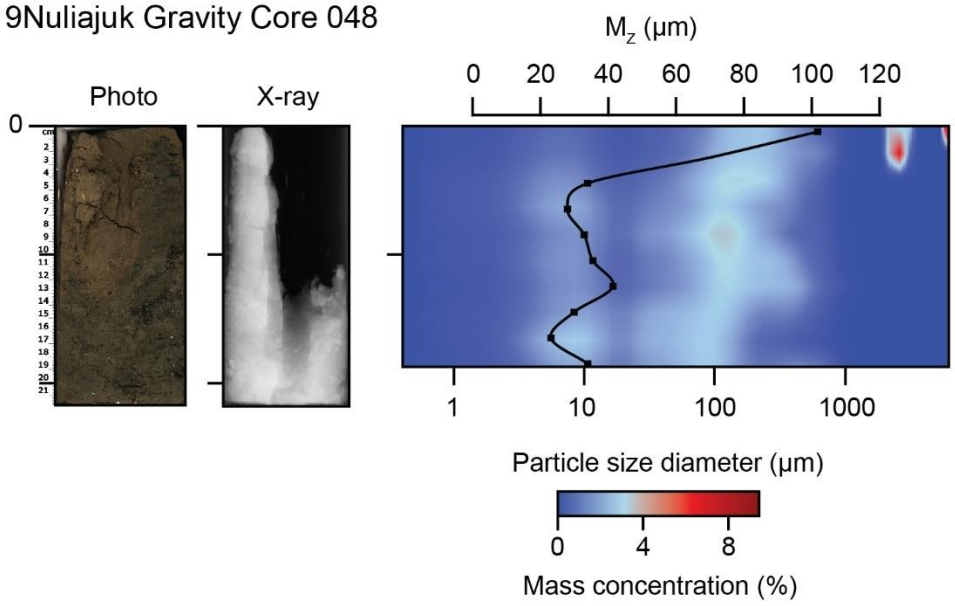

Appendix D: Grain size data table

							% of major sediment type			
Sample ID	Station Number	Latitude	Longitude	Water depth (m)	Subsample top (cm)	Subsample base (cm)	Gravel (>2 mm)	Sand (63 um - 2 mm)	Silt (63 - 4 um)	Clay (< 4 um)
0015-1-4	15	66.367	-65.497	61	12	13	0.00	6.93	66.30	26.77
0015-2-4	15	66.367	-65.497	61	14	15	0.00	3.42	66.91	29.67
0015-3-4	15	66.367	-65.497	61	16	17	0.00	1.71	65.29	33.00
0015-4-4	15	66.367	-65.497	61	18	19	0.00	6.31	67.72	25.97
0015-5-4	15	66.367	-65.497	61	20	21	0.00	5.87	66.86	27.27
0015-6-4	15	66.367	-65.497	61	22	23	0.00	34.39	47.09	18.53
0015-7-4	15	66.367	-65.497	61	23	24	0.00	5.25	66.30	28.45
0015-8-4	15	66.367	-65.497	61	24	25	0.00	4.14	67.61	28.25
0015-9-4	15	66.367	-65.497	61	26	27	0.00	6.21	68.31	25.48
0015-10-4	15	66.367	-65.497	61	28	29	0.00	7.23	68.47	24.30
0015-11-4	15	66.367	-65.497	61	30	31	0.00	5.79	67.99	26.21
0015-12-4	15	66.367	-65.497	61	32	33	0.00	4.36	69.90	25.74
0015-13-4	15	66.367	-65.497	61	34	35	0.00	28.24	51.35	20.40
0015-14-4	15	66.367	-65.497	61	35	36	0.00	19.96	58.45	21.59
0015-15-4	15	66.367	-65.497	61	36	37	0.00	5.04	68.74	26.22
0015-16-4	15	66.367	-65.497	61	38	39	0.00	9.76	67.98	22.26
0015-17-4	15	66.367	-65.497	61	40	41	0.00	7.81	68.44	23.75
0015-18-4	15	66.367	-65.497	61	42	43	0.00	9.30	68.87	21.84
0015-19-4	15	66.367	-65.497	61	44	45	0.00	12.99	63.13	23.88
0015-20-4	15	66.367	-65.497	61	46	47	0.00	12.14	65.16	22.70
0015-21-4	15	66.367	-65.497	61	48	49	0.00	10.54	65.53	23.93
0015-22-4	15	66.367	-65.497	61	50	51	0.00	11.33	69.55	19.12
0015-23-4	15	66.367	-65.497	61	52	53	0.00	17.16	62.42	20.42
0015-24-4	15	66.367	-65.497	61	53	54	0.00	8.78	69.94	21.28
0015-25-4	15	66.367	-65.497	61	54	55	0.00	22.45	60.49	17.07
0015-26-4	15	66.367	-65.497	61	55	56	0.00	13.18	67.04	19.79
0015-27-4	15	66.367	-65.497	61	56	57	0.00	2.83	70.53	26.64
0015-28-4	15	66.367	-65.497	61	58	59	0.00	9.16	68.35	22.49
0015-29-4	15	66.367	-65.497	61	60	61	0.00	7.63	68.96	23.41
0015-30-4	15	66.367	-65.497	61	62	63	0.00	46.41	39.64	13.95
0015-31-4	15	66.367	-65.497	61	64	65	0.00	4.66	67.04	28.30
0015-32-4	15	66.367	-65.497	61	66	67	0.00	5.83	69.64	24.53
0015-33-4	15	66.367	-65.497	61	68	69	0.00	5.80	67.09	27.11
0015-34-4	15	66.367	-65.497	61	70	71	0.00	4.47	67.36	28.17

							% of major sediment type			
Sample ID	Station Number	Latitude	Longitude	Water depth (m)	Subsample top (cm)	Subsample base (cm)	Gravel (>2 mm)	Sand (63 um - 2 mm)	Silt (63 - 4 um)	Clay (< 4 um)
0015-35-4	15	66.367	-65.497	61	72	73	0.00	5.91	72.97	21.13
0015-36-4	15	66.367	-65.497	61	74	75	0.00	8.01	65.98	26.01
0015-37-4	15	66.367	-65.497	61	76	77	0.00	3.74	63.12	33.13
0015-38-4	15	66.367	-65.497	61	78	79	0.00	6.75	64.93	28.32
0015-39-4	15	66.367	-65.497	61	80	81	0.00	5.53	63.39	31.08
0015-40-4	15	66.367	-65.497	61	82	83	0.00	4.11	65.69	30.20
0015-41-4	15	66.367	-65.497	61	83	84	0.00	18.43	54.85	26.71
0015-42-4	15	66.367	-65.497	61	84	85	0.00	4.09	63.94	31.97
0015-43-4	15	66.367	-65.497	61	86	87	0.00	9.19	64.40	26.41
0015-44-4	15	66.367	-65.497	61	88	89	0.00	8.54	67.20	24.27
0015-45-4	15	66.367	-65.497	61	90	91	0.00	6.45	65.48	28.07
0015-46-4	15	66.367	-65.497	61	92	93	0.00	8.54	69.32	22.14
0015-47-4	15	66.367	-65.497	61	94	95	0.00	11.28	68.01	20.71
0015-48-4	15	66.367	-65.497	61	96	97	0.00	9.22	69.98	20.80
0015-49-4	15	66.367	-65.497	61	98	99	0.00	10.52	69.78	19.70
0015-50-4	15	66.367	-65.497	61	100	101	0.00	12.45	66.49	21.07
0015-51-4	15	66.367	-65.497	61	102	103	0.00	11.86	66.63	21.51
0017-54-4	17	66.370	-65.504	27	5	6	0.00	5.29	77.54	17.17
0017-55-4	17	66.370	-65.504	27	10	11	0.00	6.02	74.34	19.65
0017-56-4	17	66.370	-65.504	27	15	16	0.00	6.49	72.95	20.56
0017-57-4	17	66.370	-65.504	27	20	21	0.00	3.07	76.66	20.27
0017-58-4	17	66.370	-65.504	27	25	26	0.00	16.90	63.76	19.34
0017-59-4	17	66.370	-65.504	27	30	31	0.00	5.50	69.85	24.65
0017-60-4	17	66.370	-65.504	27	35	36	0.00	7.33	69.96	22.71
0017-61-4	17	66.370	-65.504	27	40	41	0.00	12.07	66.84	21.09
0017-62-4	17	66.370	-65.504	27	45	46	0.00	5.83	71.94	22.23
0017-63-4	17	66.370	-65.504	27	50	51	0.00	6.65	71.02	22.33
0017-64-4	17	66.370	-65.504	27	55	56	0.00	3.21	72.03	24.76
0017-65-4	17	66.370	-65.504	27	60	61	0.00	5.51	71.83	22.66
0017-66-4	17	66.370	-65.504	27	65	66	0.00	10.54	66.82	22.64
0017-67-4	17	66.370	-65.504	27	70	71	0.00	4.48	72.48	23.04
0017-68-4	17	66.370	-65.504	27	75	76	0.00	24.28	58.02	17.70
0017-69-4	17	66.370	-65.504	27	80	81	0.00	5.68	70.57	23.74
0020-71-4	20	66.371	-65.501	36.5	0	1	0.00	7.93	76.05	16.02
0020-72-4	20	66.371	-65.501	36.5	5	6	0.00	12.33	69.76	17.91
0020-73-4	20	66.371	-65.501	36.5	10	11	0.00	8.53	77.95	13.52

							% of major sediment type			
Sample ID	Station Number	Latitude	Longitude	Water depth (m)	Subsample top (cm)	Subsample base (cm)	Gravel (>2 mm)	Sand (63 um - 2 mm)	Silt (63 - 4 um)	Clay (< 4 um)
0020-74-4	20	66.371	-65.501	36.5	15	16	0.00	9.17	74.61	16.21
0020-75-4	20	66.371	-65.501	36.5	20	21	0.00	12.61	72.58	14.81
0020-76-4	20	66.371	-65.501	36.5	25	26	0.00	6.14	73.96	19.90
0020-77-4	20	66.371	-65.501	36.5	30	31	0.00	3.81	75.95	20.24
0020-78-4	20	66.371	-65.501	36.5	35	36	0.00	2.93	74.55	22.52
0020-79-4	20	66.371	-65.501	36.5	40	41	0.00	10.02	69.75	20.23
0020-80-4	20	66.371	-65.501	36.5	45	46	0.00	9.68	69.79	20.53
0020-81-4	20	66.371	-65.501	36.5	50	51	0.00	9.84	68.99	21.17
0020-82-4	20	66.371	-65.501	36.5	51	52	0.00	19.05	59.22	21.72
0020-83-4	20	66.371	-65.501	36.5	52	53	0.00	11.27	68.08	20.65
0020-84-4	20	66.371	-65.501	36.5	53	54	0.00	10.47	66.74	22.79
0020-85-4	20	66.371	-65.501	36.5	54	55	0.00	8.81	66.83	24.36
0020-86-4	20	66.371	-65.501	36.5	55	56	48.15	38.66	9.74	3.45
0020-87-4	20	66.371	-65.501	36.5	56	57	7.95	80.17	8.99	2.89
0020-88-4	20	66.371	-65.501	36.5	57	58	0.00	96.44	2.58	0.98
0020-89-4	20	66.371	-65.501	36.5	58	59	5.99	41.91	39.16	12.94
0020-90-4	20	66.371	-65.501	36.5	59	60	0.00	13.39	64.69	21.92
0020-91-4	20	66.371	-65.501	36.5	60	61	0.00	5.18	69.59	25.23
0020-92-4	20	66.371	-65.501	36.5	61	62	0.00	6.47	70.91	22.62
0020-93-4	20	66.371	-65.501	36.5	65	66	0.00	7.16	72.54	20.29
0020-94-4	20	66.371	-65.501	36.5	70	71	0.00	5.35	70.10	24.55
0020-95-4	20	66.371	-65.501	36.5	75	76	0.00	9.08	69.76	21.16
0020-96-4	20	66.371	-65.501	36.5	79	80	0.00	6.12	72.53	21.35
0024-100-4	24	66.361	-65.494	87	25	26	0.00	13.55	66.62	19.84
0024-101-4	24	66.361	-65.494	87	35	36	0.00	9.36	68.98	21.66
0024-102-4	24	66.361	-65.494	87	45	46	0.00	12.02	68.21	19.77
0024-103-4	24	66.361	-65.494	87	55	56	0.00	9.53	70.10	20.37
0024-104-4	24	66.361	-65.494	87	65	66	0.00	10.83	70.00	19.17
0024-105-4	24	66.361	-65.494	87	75	76	0.00	12.89	68.07	19.04
0024-106-4	24	66.361	-65.494	87	85	86	0.00	11.20	69.78	19.02
0030-108-4	30	66.279	-65.538	87	0	1	0.00	5.60	57.59	36.81
0030-109-4	30	66.279	-65.538	87	5	6	0.00	8.56	56.88	34.56
0030-110-4	30	66.279	-65.538	87	6	7	0.00	19.33	49.51	31.16
0030-111-4	30	66.279	-65.538	87	7	8	0.00	8.81	55.85	35.34
0030-112-4	30	66.279	-65.538	87	8	9	0.00	17.05	52.23	30.72
0030-113-4	30	66.279	-65.538	87	9	10	0.00	38.95	38.05	23.00
0030-114-4	30	66.279	-65.538	87	10	11	0.00	53.83	29.40	16.77

							% of major sediment type			
Sample ID	Station Number	Latitude	Longitude	Water depth (m)	Subsample top (cm)	Subsample base (cm)	Gravel (>2 mm)	Sand (63 um - 2 mm)	Silt (63 - 4 um)	Clay (< 4 um)
0030-115-4	30	66.279	-65.538	87	11	12	0.00	38.63	38.44	22.93
0030-116-4	30	66.279	-65.538	87	12	13	0.00	52.63	31.26	16.11
0030-117-4	30	66.279	-65.538	87	13	14	0.00	60.98	25.05	13.97
0030-118-4	30	66.279	-65.538	87	14	15	0.00	57.00	28.92	14.08
0030-119-4	30	66.279	-65.538	87	15	16	0.00	71.67	18.70	9.63
0030-120-4	30	66.279	-65.538	87	16	17	0.00	43.18	38.80	18.02
0030-121-4	30	66.279	-65.538	87	17	18	0.00	11.91	56.08	32.01
0030-122-4	30	66.279	-65.538	87	18	19	0.00	12.37	61.88	25.75
0030-123-4	30	66.279	-65.538	87	19	20	0.00	16.93	52.95	30.12
0030-124-4	30	66.279	-65.538	87	20	21	0.00	10.76	60.56	28.68
0030-125-4	30	66.279	-65.538	87	25	26	0.00	10.97	57.96	31.07
0030-126-4	30	66.279	-65.538	87	30	31	0.00	22.49	50.87	26.64
0030-127-4	30	66.279	-65.538	87	35	36	0.00	19.50	52.19	28.30
0030-128-4	30	66.279	-65.538	87	40	41	0.00	8.07	58.47	33.46
0030-129-4	30	66.279	-65.538	87	45	46	0.00	9.42	57.76	32.81
0030-130-4	30	66.279	-65.538	87	50	51	0.00	12.49	56.49	31.02
0030-131-4	30	66.279	-65.538	87	55	56	0.00	8.38	59.13	32.49
0030-132-4	30	66.279	-65.538	87	60	61	0.00	7.50	59.24	33.26
0030-133-4	30	66.279	-65.538	87	65	66	0.00	8.27	60.69	31.04
0030-134-4	30	66.279	-65.538	87	70	71	0.00	8.50	62.92	28.58
0030-135-4	30	66.279	-65.538	87	75	76	0.00	16.31	56.75	26.94
0030-136-4	30	66.279	-65.538	87	80	81	0.00	15.75	56.14	28.10
0030-137-4	30	66.279	-65.538	87	85	86	0.00	19.71	55.35	24.94
0030-138-4	30	66.279	-65.538	87	90	91	0.00	16.09	55.23	28.68
0030-139-4	30	66.279	-65.538	87	95	96	0.00	19.01	54.16	26.83
0030-140-4	30	66.279	-65.538	87	100	101	0.00	27.77	48.49	23.74
0034-175-4	34	66.260	-65.548	110	0	1	0.00	5.27	57.83	36.90
0034-176-4	34	66.260	-65.548	110	10	11	0.00	8.97	59.56	31.47
0034-177-4	34	66.260	-65.548	110	20	21	0.00	8.70	60.79	30.51
0034-178-4	34	66.260	-65.548	110	30	31	0.00	9.14	61.54	29.32
0034-179-4	34	66.260	-65.548	110	40	41	0.00	10.56	67.08	22.36
0034-180-4	34	66.260	-65.548	110	50	51	0.00	12.35	63.34	24.31
0034-181-4	34	66.260	-65.548	110	60	61	0.00	14.10	60.50	25.40
0034-182-4	34	66.260	-65.548	110	70	71	0.00	15.29	61.11	23.60
0034-183-4	34	66.260	-65.548	110	80	81	0.00	19.01	62.71	18.28
0037-204-4	37	66.239	-65.561	65	0	1	0.00	3.15	65.06	31.79
0037-205-4	37	66.239	-65.561	65	1	2	0.00	6.99	64.75	28.27

							% of major sediment type			
Sample ID	Station Number	Latitude	Longitude	Water depth (m)	Subsample top (cm)	Subsample base (cm)	Gravel (>2 mm)	Sand (63 um - 2 mm)	Silt (63 - 4 um)	Clay (< 4 um)
0037-206-4	37	66.239	-65.561	65	2	3	0.00	16.38	56.97	26.66
0037-207-4	37	66.239	-65.561	65	3	4	0.00	12.18	60.09	27.73
0037-208-4	37	66.239	-65.561	65	4	5	0.00	25.04	47.61	27.36
0037-209-4	37	66.239	-65.561	65	5	6	0.00	32.40	43.16	24.43
0037-210-4	37	66.239	-65.561	65	6	7	0.00	15.59	57.32	27.09
0037-211-4	37	66.239	-65.561	65	7	8	0.00	16.00	57.71	26.29
0037-212-4	37	66.239	-65.561	65	8	9	0.00	24.71	48.77	26.52
0037-213-4	37	66.239	-65.561	65	9	10	0.00	41.89	40.11	18.00
0037-214-4	37	66.239	-65.561	65	10	11	0.00	57.12	31.30	11.59
0037-215-4	37	66.239	-65.561	65	20	21	0.00	22.53	59.55	17.92
0037-216-4	37	66.239	-65.561	65	30	31	0.00	36.99	46.76	16.25
0037-217-4	37	66.239	-65.561	65	40	41	0.00	8.09	50.92	40.99
0037-218-4	37	66.239	-65.561	65	50	51	0.00	10.25	61.92	27.83
0037-219-4	37	66.239	-65.561	65	60	61	0.00	13.82	63.42	22.76
0037-220-4	37	66.239	-65.561	65	70	71	0.00	10.68	64.37	24.95
0041-222-4	41	66.164	-65.718	145	0	1	0.00	15.10	61.36	23.55
0041-223-4	41	66.164	-65.718	145	10	11	0.00	12.66	60.16	27.18
0041-224-4	41	66.164	-65.718	145	20	21	0.00	13.05	58.88	28.08
0041-225-4	41	66.164	-65.718	145	30	31	0.00	21.50	56.61	21.89
0041-226-4	41	66.164	-65.718	145	40	41	0.00	29.97	53.23	16.80
0041-227-4	41	66.164	-65.718	145	50	51	0.00	26.48	55.67	17.85
0041-228-4	41	66.164	-65.718	145	60	61	0.00	33.83	53.91	12.26
0042-251-4	42	66.159	-65.759	140	0	1	0.00	33.00	47.32	19.68
0042-252-4	42	66.159	-65.759	140	5	6	0.00	23.46	53.70	22.84
0042-253-4	42	66.159	-65.759	140	10	11	0.00	33.06	48.03	18.91
0042-254-4	42	66.159	-65.759	140	15	16	0.00	22.80	55.84	21.36
0042-255-4	42	66.159	-65.759	140	16	17	0.00	19.87	57.80	22.33
0042-256-4	42	66.159	-65.759	140	17	18	0.00	33.39	49.56	17.05
0042-257-4	42	66.159	-65.759	140	18	19	0.00	33.07	49.64	17.29
0042-258-4	42	66.159	-65.759	140	19	20	0.00	41.44	42.67	15.90
0042-259-4	42	66.159	-65.759	140	20	21	0.00	35.25	46.96	17.78
0042-260-4	42	66.159	-65.759	140	21	22	0.00	47.86	38.56	13.58
0042-261-4	42	66.159	-65.759	140	22	23	0.00	43.54	41.25	15.21
0042-262-4	42	66.159	-65.759	140	23	24	0.00	62.79	27.02	10.19
0042-263-4	42	66.159	-65.759	140	24	25	0.00	56.06	31.78	12.16
0042-264-4	42	66.159	-65.759	140	25	26	0.00	37.31	47.38	15.31
0043-265-4	43	66.174	-65.665	108	0	1	0.00	19.94	58.72	21.34

							% of major sediment type			
Sample ID	Station Number	Latitude	Longitude	Water depth (m)	Subsample top (cm)	Subsample base (cm)	Gravel (>2 mm)	Sand (63 um - 2 mm)	Silt (63 - 4 um)	Clay (< 4 um)
0043-266-4	43	66.174	-65.665	108	5	6	0.00	22.79	54.59	22.62
0043-267-4	43	66.174	-65.665	108	10	11	0.00	16.44	58.03	25.53
0043-268-4	43	66.174	-65.665	108	15	16	0.00	16.44	58.23	25.33
0043-269-4	43	66.174	-65.665	108	20	21	0.00	18.18	58.06	23.76
0043-270-4	43	66.174	-65.665	108	25	26	0.00	25.78	54.28	19.94
0043-271-4	43	66.174	-65.665	108	30	31	0.00	27.96	52.41	19.64
0043-272-4	43	66.174	-65.665	108	31	32	0.00	37.47	46.44	16.09
0043-273-4	43	66.174	-65.665	108	32	33	0.00	38.36	44.94	16.70
0043-274-4	43	66.174	-65.665	108	33	34	0.00	53.87	34.12	12.01
0043-275-4	43	66.174	-65.665	108	34	35	0.00	28.01	53.61	18.38
0043-276-4	43	66.174	-65.665	108	35	36	0.00	26.78	55.72	17.50
0043-277-4	43	66.174	-65.665	108	38	39	0.00	62.50	27.44	10.06
0043-278-4	43	66.174	-65.665	108	39	40	0.00	67.36	24.59	8.06
0043-279-4	43	66.174	-65.665	108	40	41	0.00	58.46	32.42	9.12
0043-280-4	43	66.174	-65.665	108	41	42	0.00	44.22	41.79	13.99
0043-281-4	43	66.174	-65.665	108	45	46	0.00	25.38	61.59	13.03
0047-283-4	47	66.125	-65.863	126	0	1	28.38	37.10	21.88	12.63
0047-284-4	47	66.125	-65.863	126	1	2	0.00	57.74	27.22	15.04
0047-285-4	47	66.125	-65.863	126	2	3	42.79	35.38	14.31	7.52
0047-286-4	47	66.125	-65.863	126	3	4	30.62	44.75	16.22	8.41
0047-287-4	47	66.125	-65.863	126	4	5	9.53	57.68	21.80	10.99
0047-288-4	47	66.125	-65.863	126	5	6	5.16	39.80	36.32	18.73
0047-289-4	47	66.125	-65.863	126	6	7	21.48	28.55	32.52	17.45
0047-290-4	47	66.125	-65.863	126	7	8	0.00	51.39	32.01	16.61
0047-291-4	47	66.125	-65.863	126	8	9	0.00	51.06	32.71	16.23
0047-292-4	47	66.125	-65.863	126	9	10	0.00	48.68	34.79	16.54
0047-293-4	47	66.125	-65.863	126	10	11	6.50	44.43	32.85	16.22
0047-294-4	47	66.125	-65.863	126	11	12	6.43	44.83	33.10	15.65
0047-295-4	47	66.125	-65.863	126	12	13	18.90	39.93	28.51	12.65
0047-296-4	47	66.125	-65.863	126	13	14	0.00	41.59	40.07	18.34
0047-297-4	47	66.125	-65.863	126	14	15	75.78	9.16	10.41	4.65
0047-298-4	47	66.125	-65.863	126	15	16	0.00	38.31	42.88	18.81
0047-299-4	47	66.125	-65.863	126	16	17	0.00	40.99	41.32	17.69
0047-300-4	47	66.125	-65.863	126	17	18	0.00	39.43	41.43	19.13
0047-301-4	47	66.125	-65.863	126	18	19	0.00	41.27	40.57	18.16
0047-302-4	47	66.125	-65.863	126	19	20	0.00	40.47	41.35	18.18
0047-303-4	47	66.125	-65.863	126	20	21	5.08	42.29	37.79	14.84

							% of major sediment type			
Sample ID	Station Number	Latitude	Longitude	Water depth (m)	Subsample top (cm)	Subsample base (cm)	Gravel (>2 mm)	Sand (63 um - 2 mm)	Silt (63 - 4 um)	Clay (< 4 um)
0047-304-4	47	66.125	-65.863	126	21	22	3.92	49.30	31.91	14.87
0047-305-4	47	66.125	-65.863	126	22	23	0.00	46.16	35.44	18.41
0047-306-4	47	66.125	-65.863	126	23	24	12.81	37.90	32.13	17.16
0047-307-4	47	66.125	-65.863	126	24	25	0.00	41.75	37.76	20.49
0047-308-4	47	66.125	-65.863	126	25	26	0.00	34.04	41.01	24.95
0047-309-4	47	66.125	-65.863	126	26	27	16.77	20.41	37.82	25.00
0047-310-4	47	66.125	-65.863	126	27	28	6.36	24.82	42.35	26.47
0047-311-4	47	66.125	-65.863	126	28	29	14.84	32.33	33.25	19.57
0047-312-4	47	66.125	-65.863	126	29	30	0.00	18.33	48.29	33.38
0047-313-4	47	66.125	-65.863	126	30	31	0.00	6.77	58.02	35.21
0047-314-4	47	66.125	-65.863	126	31	32	0.00	7.45	57.64	34.91
0047-315-4	47	66.125	-65.863	126	32	33	0.00	5.08	58.98	35.95
0047-316-4	47	66.125	-65.863	126	35	36	0.00	2.96	58.77	38.27
0047-317-4	47	66.125	-65.863	126	40	41	0.00	8.36	59.21	32.43
0047-318-4	47	66.125	-65.863	126	45	46	0.00	2.12	57.89	39.99
0047-319-4	47	66.125	-65.863	126	50	51	0.00	6.42	63.41	30.17
0047-320-4	47	66.125	-65.863	126	55	56	0.00	1.05	55.29	43.66
0047-321-4	47	66.125	-65.863	126	60	61	0.00	3.58	62.30	34.12
0047-322-4	47	66.125	-65.863	126	65	66	0.00	2.99	58.97	38.03
0047-323-4	47	66.125	-65.863	126	70	71	0.00	2.76	59.51	37.73
0047-324-4	47	66.125	-65.863	126	75	76	0.00	0.91	57.86	41.23
0047-325-4	47	66.125	-65.863	126	80	81	0.00	8.50	57.44	34.05
0047-326-4	47	66.125	-65.863	126	85	86	0.00	5.65	56.76	37.59
0047-327-4	47	66.125	-65.863	126	90	91	0.00	4.41	58.55	37.04
0047-328-4	47	66.125	-65.863	126	95	98	0.00	21.53	52.63	25.84
0048-331-4	48	66.121	-65.894	98	0	1	18.68	42.59	26.29	12.44
0048-332-4	48	66.121	-65.894	98	2	3	11.44	46.12	28.81	13.64
0048-333-4	48	66.121	-65.894	98	4	5	0.00	46.77	36.00	17.24
0048-334-4	48	66.121	-65.894	98	6	7	0.00	40.82	41.11	18.07
0048-335-4	48	66.121	-65.894	98	8	9	0.00	43.98	40.51	15.51
0048-336-4	48	66.121	-65.894	98	10	11	0.00	46.27	38.06	15.67
0048-337-4	48	66.121	-65.894	98	12	13	0.00	48.59	37.71	13.70
0048-338-4	48	66.121	-65.894	98	14	15	0.00	39.72	44.62	15.67
0048-339-4	48	66.121	-65.894	98	16	17	0.00	32.77	50.79	16.44
0048-340-4	48	66.121	-65.894	98	18	19	0.00	41.78	43.77	14.45
0048-341-4	48	66.121	-65.894	98	20	21	0.00	37.66	46.50	15.84

Appendix E: Thin sections

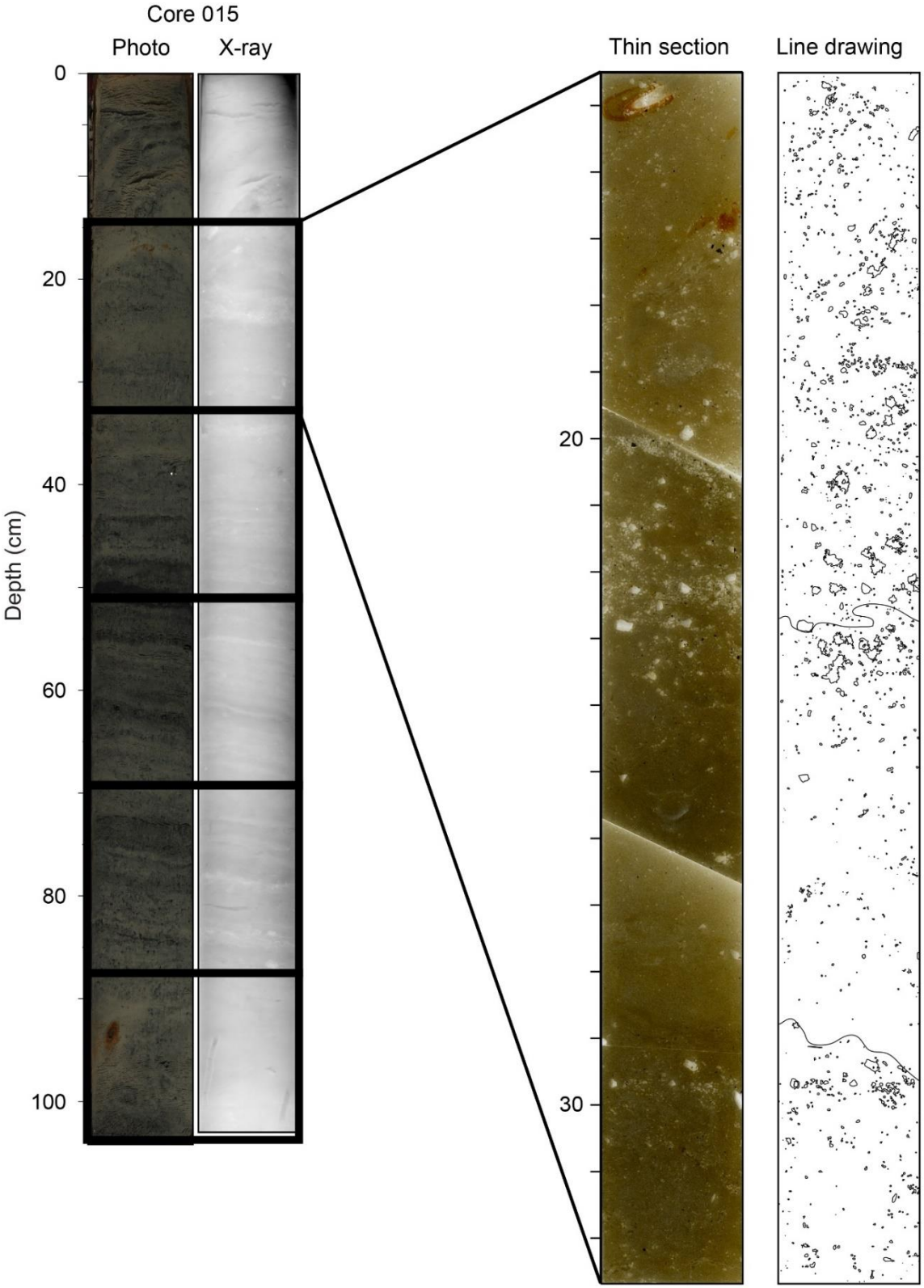

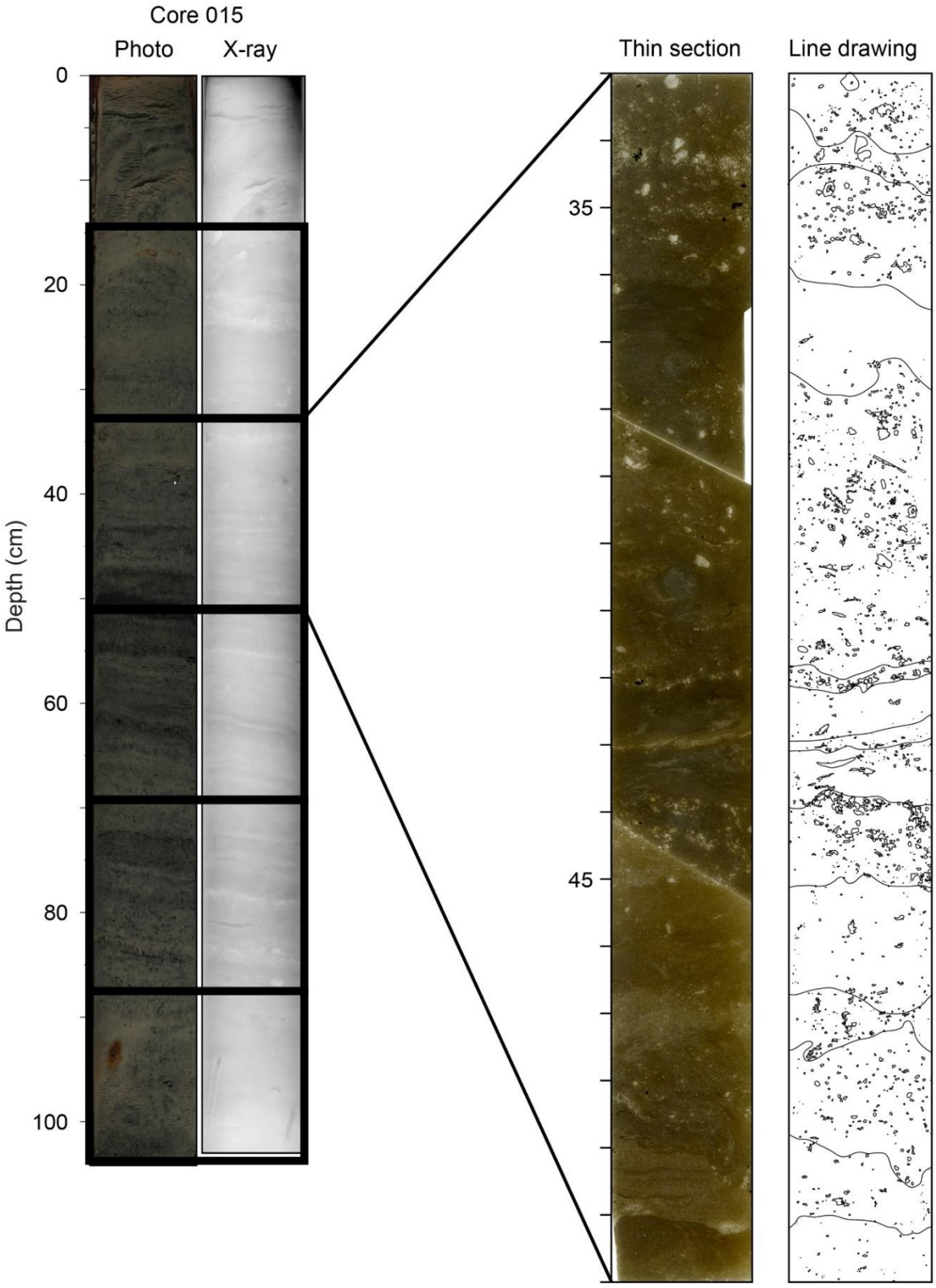
Core 015
Photo
X-ray
Thin section
Line drawing
Depth (cm)
0
20
40
60
80
100
35
45

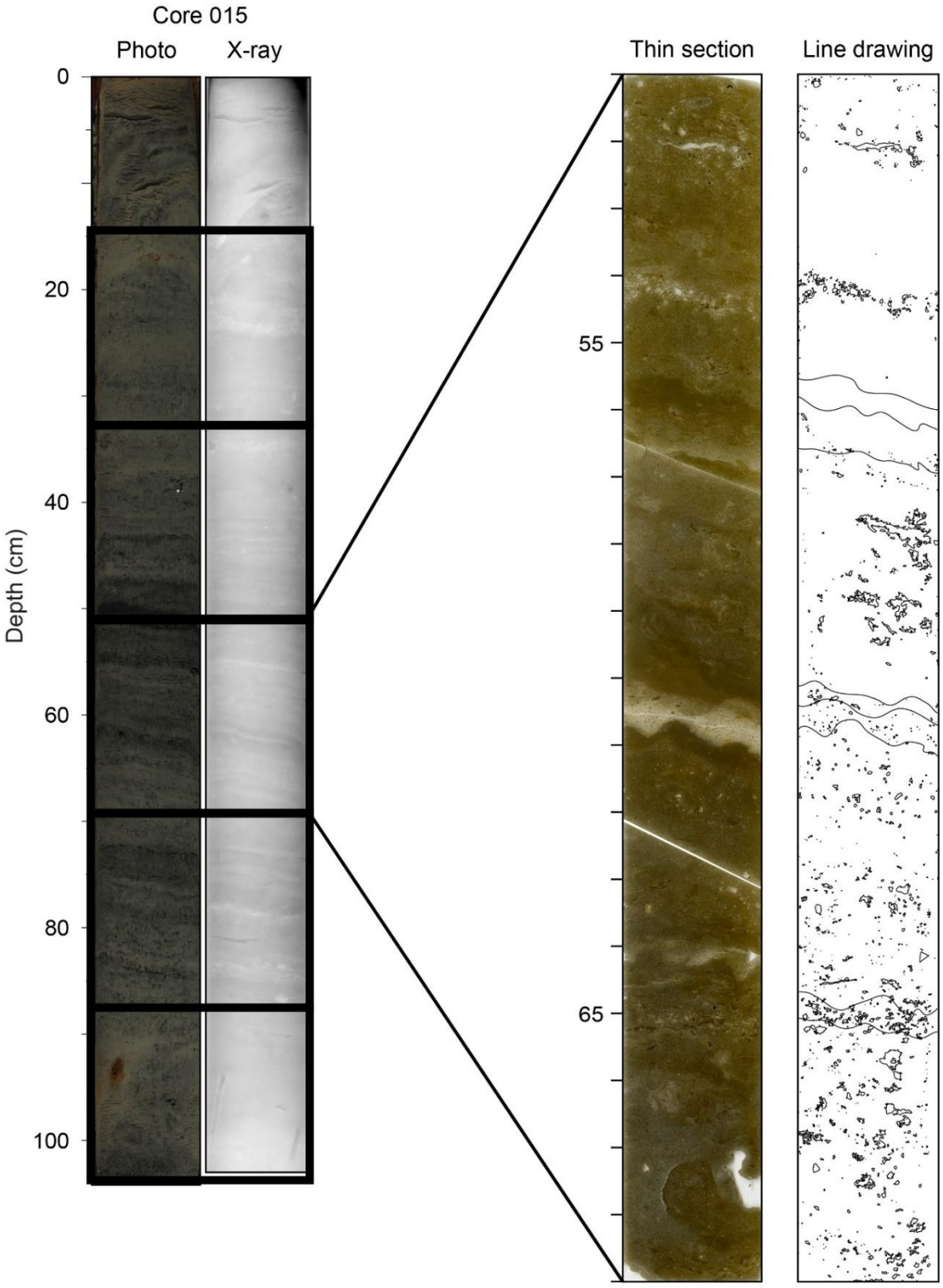
Core 015
Photo
X-ray
Thin section
Line drawing
Depth (cm)
0
20
40
60
80
100
55
65

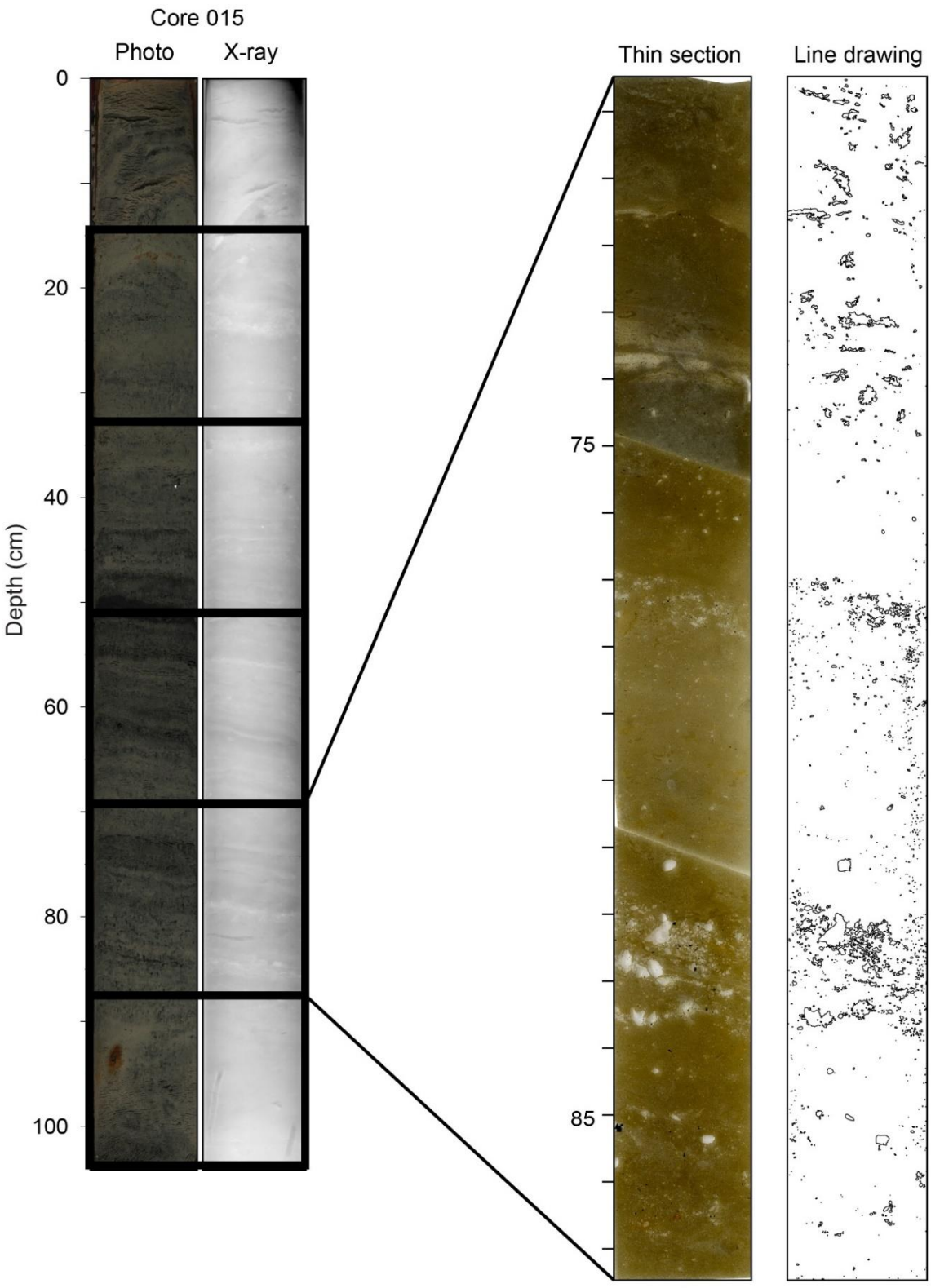
Core 015
Photo
X-ray
Thin section
Line drawing
Depth (cm)
0
20
40
60
80
100
75
85

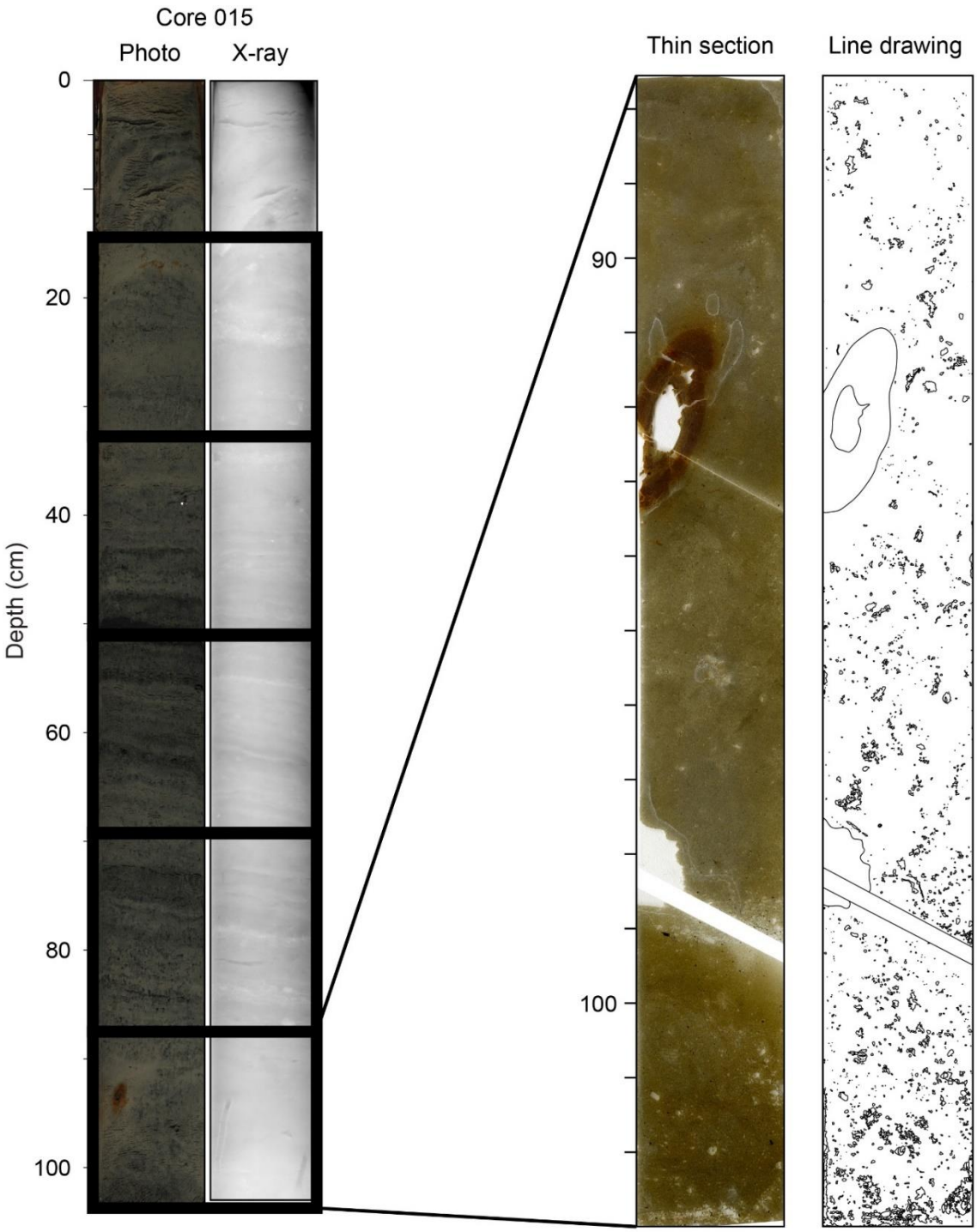
Core 015
Photo
X-ray
Thin section
Line drawing
Depth (cm)
0
20
40
60
80
100
90
100

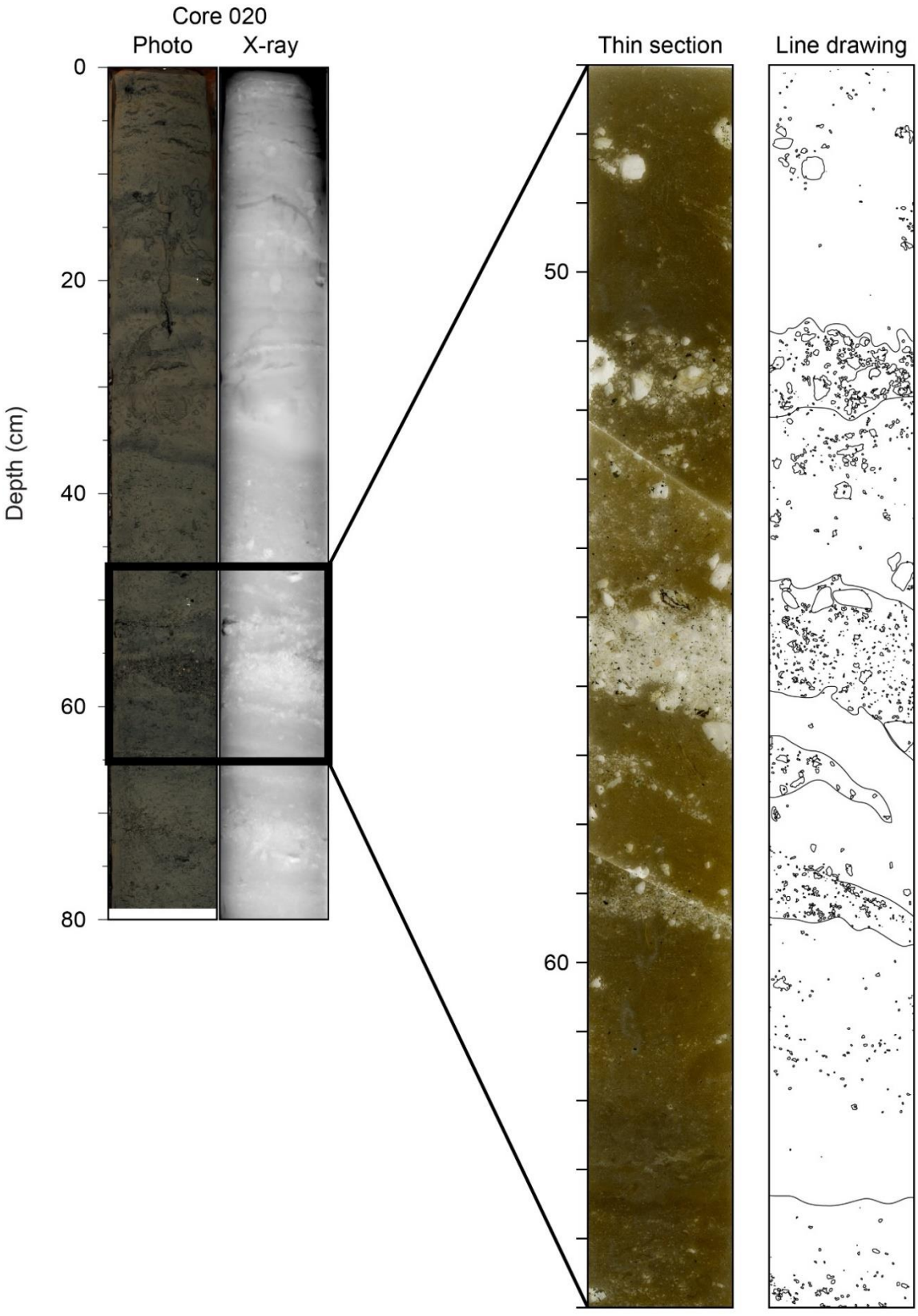
Core 020
Photo
X-ray
Thin section
Line drawing
Depth (cm)
0
20
40
60
80
50
60

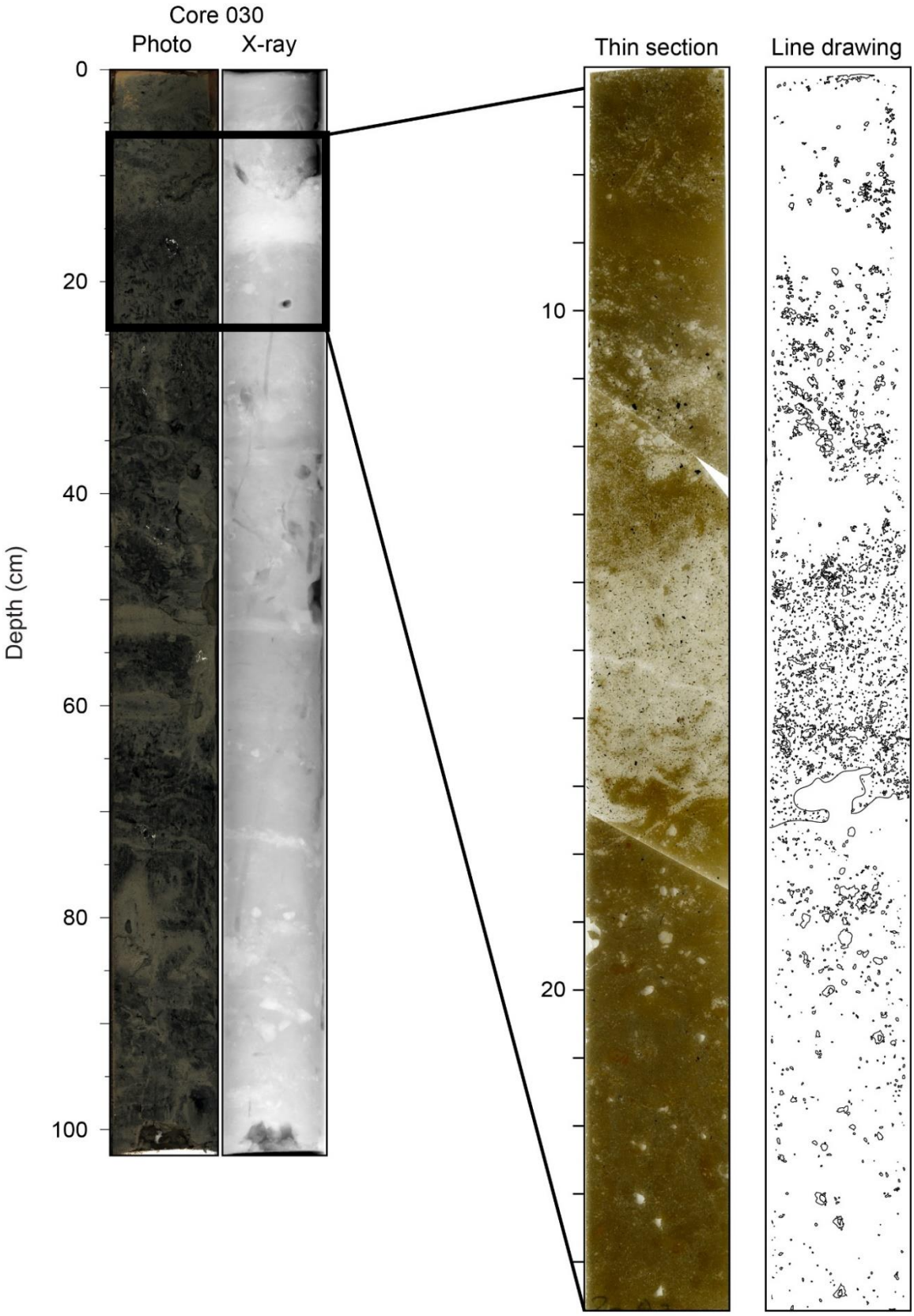
Core 030
Photo
X-ray
Thin section
Line drawing
Depth (cm)
0
20
40
60
80
100
10
20

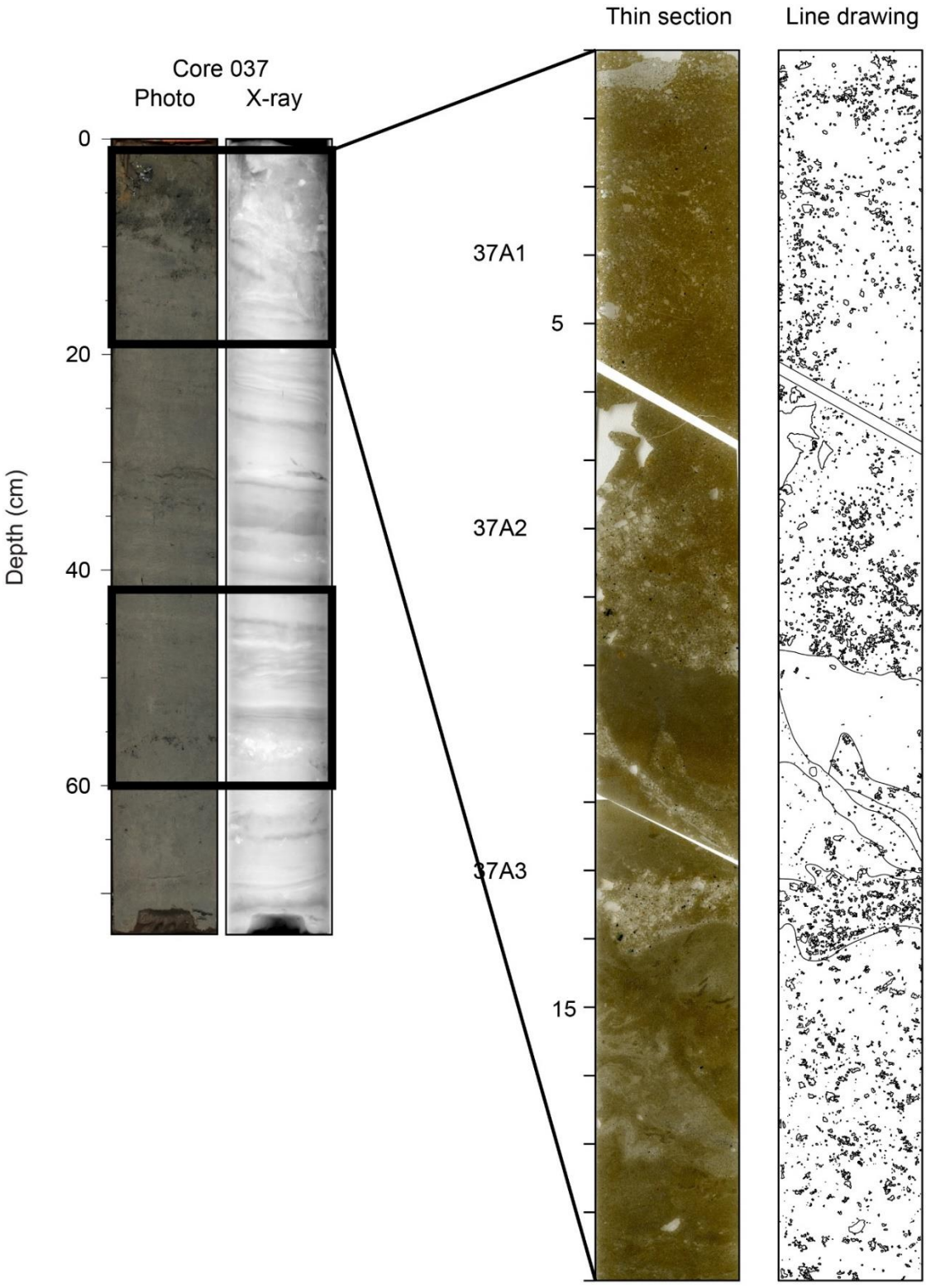
Thin section
Line drawing
Core 037
Photo
X-ray
0
20
40
60
Depth (cm)
37A1
5
37A2
37A3
15

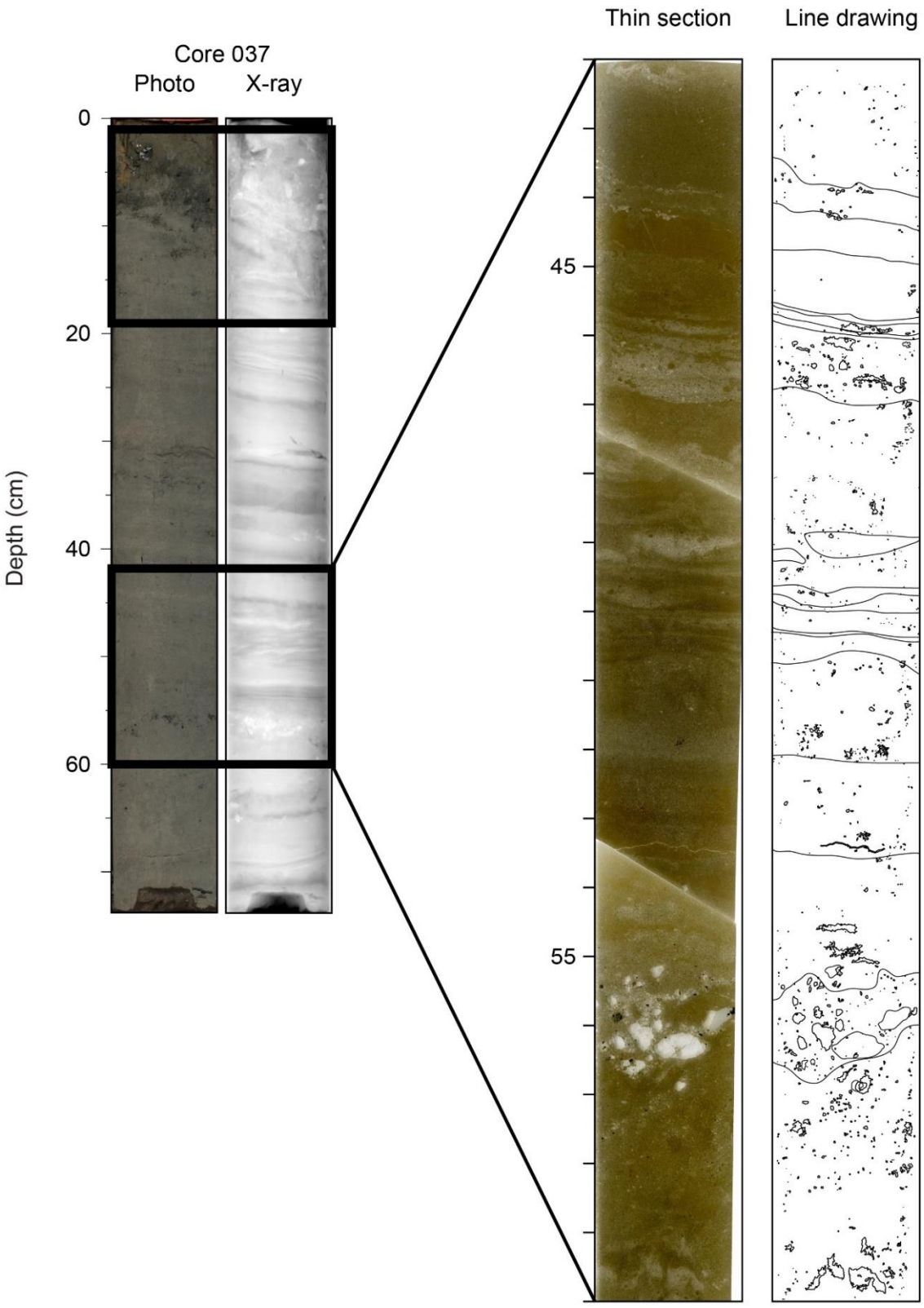
Thin section
Line drawing
Core 037
Photo
X-ray
0
20
40
60
Depth (cm)
45
55

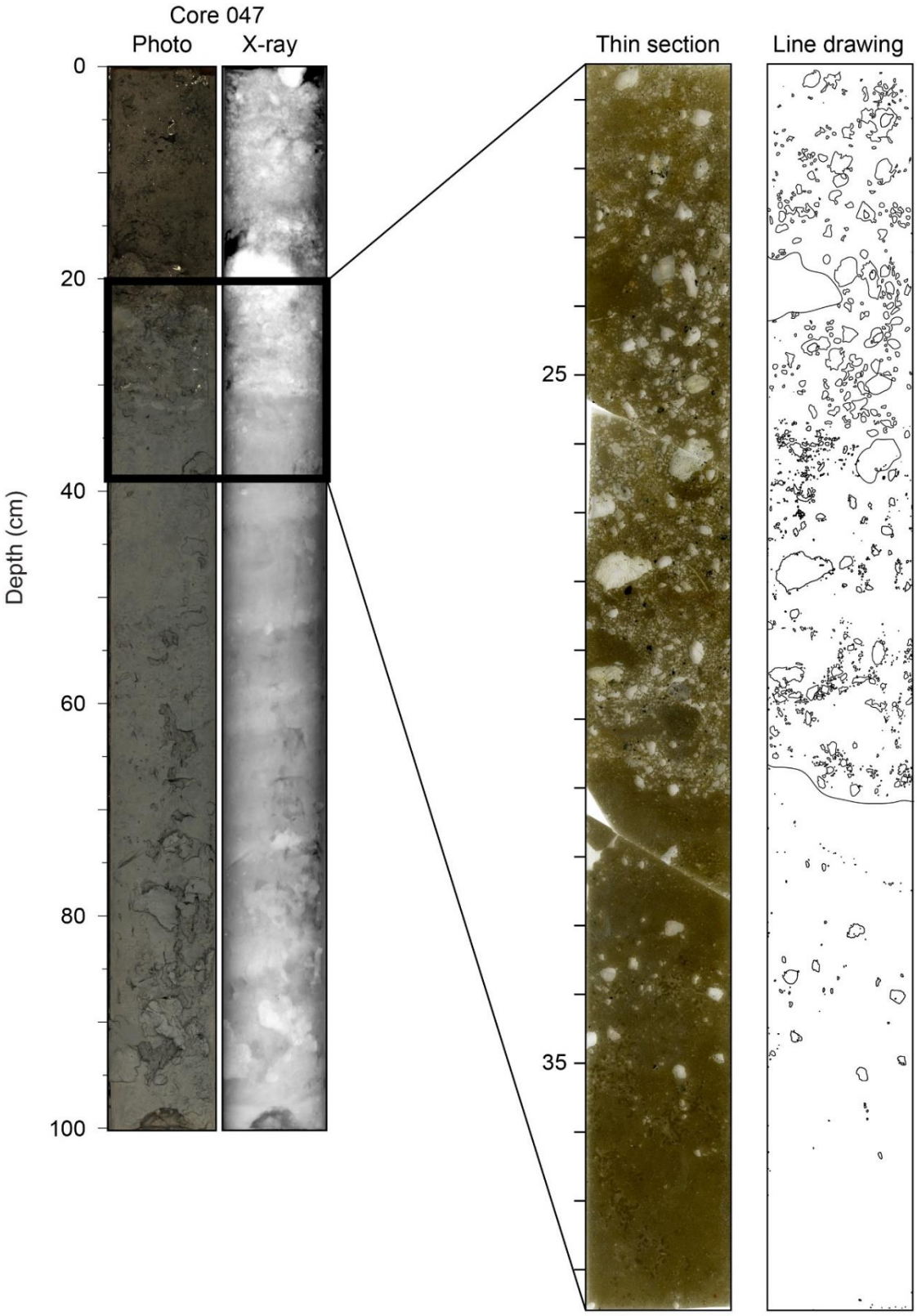
Core 047
Photo
X-ray
Thin section
Line drawing
Depth (cm)
0
20
40
60
80
100
25
35

Appendix F: Delta-R data locations

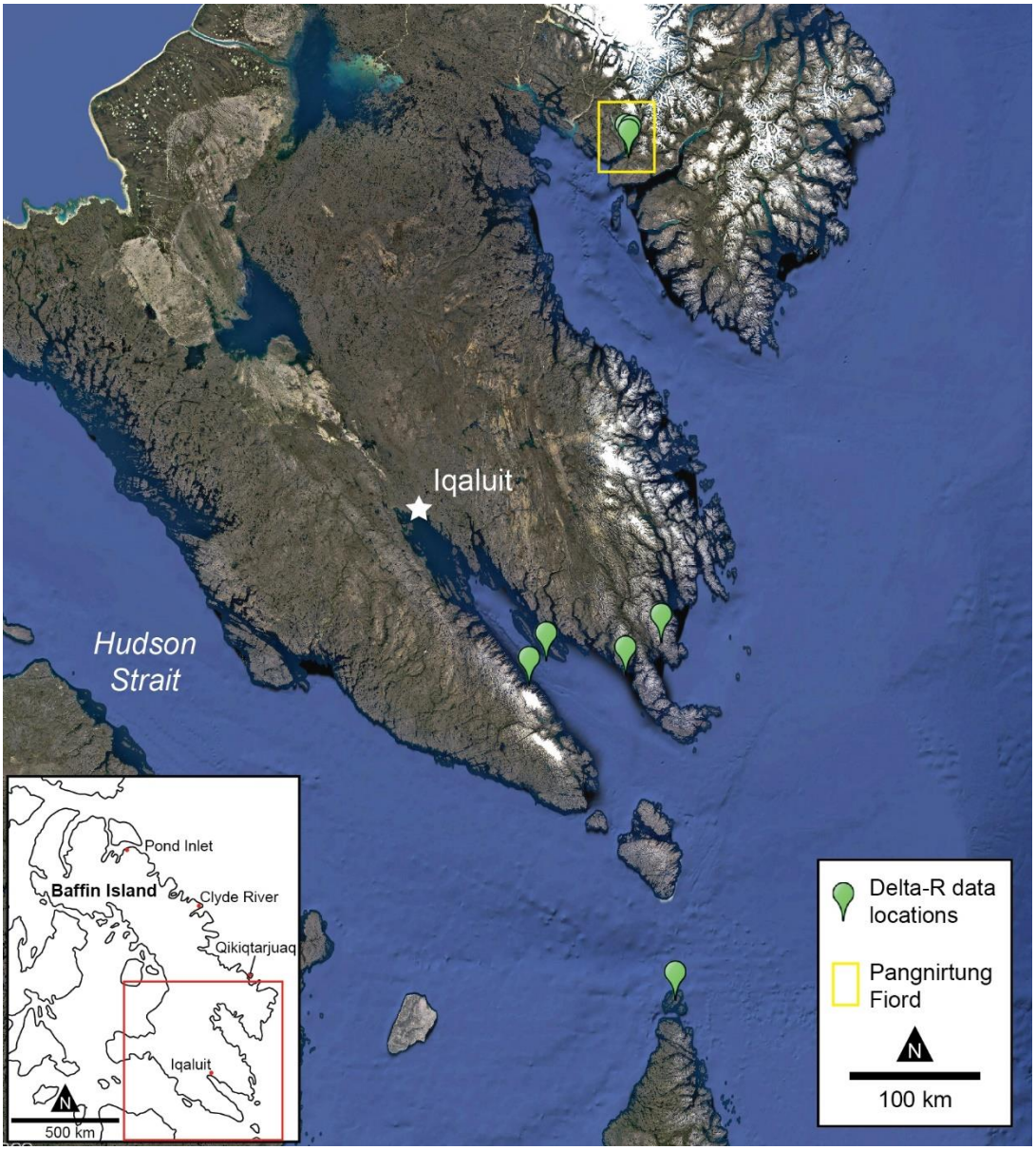

Appendix F: Delta-R data locations from the Marine20 database. Data are sourced from Coulthard et al. (2010).

Appendix G: Bathymetry of Pangnirtung Fiord, Cumberland Sound, Nunavut - Open File 8863

Sedore, P., Normandeau, A., Maselli, V., and Regular, K., 2022. Bathymetry of Pangnirtung Fiord, Cumberland Sound, Nunavut; Geological Survey of Canada, Open File 8863, 1 poster. https://doi.org/10.4095/329614

Geological Survey of Canada
Open File 8863

BATHYMETRY OF PANGNIRTUNG FIORD, CUMBERLAND SOUND, NUNAVUT
ᐃᑎᓐᖓ ᐃᒪᑉ ᐸᖕᓂᖅᑐᑉ ᐃᒪᖓᓂ, ᐸᖕᓂᖅᑐᖅ ᑲᖏᖅᑐᐊᓗᐊᓂ, ᓄᓇᕗᑦ

P. Sedore[1], A. Normandeau[2], V. Maselli[1], and K. Regular[3]

ABSTRACT

This map depicts the multibeam bathymetry data acquired in September 2019 onboard the R/V Nuliajuk in Pangnirtung Fiord, Cumberland Sound. The mapped area extends from the head of the fiord, where the Weasel River drains the surrounding highlands, to Cumberland Sound. The Hamlet of Pangnirtung rests on the SE shore of Pangnirtung Fiord. Glacial landforms and modern sediment processes are identified throughout the fiord using sub-bottom profiles and multibeam bathymetry.

STUDY AREA

Pangnirtung Fiord (Figure 1) is a ~43 km long, 1-3 km wide U shaped valley draining a ~1700 km² area of Cumberland Peninsula into Cumberland Sound and is underlain by Paleoproterozoic crystalline rock (Jackson and Sanborn Barrie 2014). The Hamlet of Pangnirtung, Nunavut, lies along the SE shore of the fiord. The northern extent of the fiord is surrounded by steep sidewalls and highlands reaching ~1500 m above mean sea level (amsl). Rivers drain the highlands through narrow valleys, transporting sediment into the fiord.

Pangnirtung Fiord was mapped in September 2019 during a Geological Survey of Canada research cruise onboard the Government of Nunavut's R/V Nuliajuk. A high-resolution bathymetric survey was conducted using a hull-mounted Kongsberg EM2040C multibeam echosounder and sub-bottom profiles were acquired using a hull-mounted Knudsen 3260 3.5 kHz echosounder.

RECENT GEOLOGICAL HISTORY

Cumberland Sound and surrounding fiords were carved by glacial ice advance and retreat throughout the Late Pleistocene. The Penny Ice Cap, currently located to the NW of the fiord, extended into Pangnirtung Fiord during the Pleistocene, merging with the Laurentide Ice Sheet. Around 10,000 years ago, Cumberland Sound and Pangnirtung Fiord were largely ice-free, except for the cirque glaciers of the surrounding highlands and a diminished Penny Ice Cap (Margreth et al. 2017). The seafloor morphology of Pangnirtung Fiord consists of glacial landforms that reflect the glacial history of the region. For example, sills, recessional moraines, and kettles are all identified in the bathymetry (Figures 2, 3, 4, 5, and 7). These glacial landforms were created through a combination of erosion, transportation, and deposition of sediment by glacial ice and proglacial rivers. Sills (Figure 4) are formed of resistant bedrock which create four distinct basins throughout the fiord. Recessional moraines are linear features on the seabed (Figure 3) formed as sediment was deposited along the retreating glacial front. Kettles (Figure 2, 3, 5) are depressions on the seabed resulting from sediment accumulating around glacial ice that has been separated from the main glacier, creating a depression upon melting (Powell and Domack 2002).

MODERN PROCESSES
Submarine Landslides

Submarine landslide deposits are identified on the seafloor throughout the fiord using multibeam bathymetric mapping (Figures 1, 4, 5, 6, 7). Submarine landslide deposits are identified in the bathymetric map by their lobate shape and irregular surface expression. This distinct morphology is the result of the sudden mass movement of sediment and rock debris downslope (Hampton et al. 1996). As a submarine landslide travels farther away from the failure scarp, a dense sediment flow can develop from the entrainment of water, potentially generating a sediment avalanche, known as a turbidity current (Masson et al. 2006). Trigger mechanisms of submarine landslides are varied and often more than one trigger mechanism causes a slope to fail. In Pangnirtung Fiord, the most likely triggers of submarine landslides are earthquakes, the oversteepening of slopes and subaerial debris flows extended under water (Figure 7). The rapid displacement of sediment in a submarine landslide can produce tsunami waves that propagate through the fiord and present a natural hazard for low-lying coastal communities (Gauthier et al. 2017). It is currently unknown if the submarine landslides observed in Pangnirtung Fiord have produced a tsunami in the past.

Deltas and Floods

River systems transport sediment from the surrounding highlands and valleys into the fiord. A large river system, like the Weasel River (Figure 7) transports significant quantities of sediment into the fiord. As the river enters the fiord, the flow velocity decreases, and the sediment is deposited, producing an accumulation of sediment called a delta. The multibeam bathymetry is used to identify channels and sediment waves (Figure 7). These sediment waves are active, meaning that turbidity currents are likely triggered every year during spring snowmelt. Seasonal variations in river flow control the quantity of sediment entering the fiord. During higher flows, flooding can occur, producing a sudden outwash of sediment laden freshwater into the fiord. This sudden influx of sediment can trigger submarine landslides near the mouth of the river. In 2008, the Duval River flooded and potentially deposited a large quantity of sediment directly in front of the hamlet. This recent flooding broke the bridge and separated the community in half for several days (Spinney and Pennesi 2013). Similar flooding events may have occurred in the past and within other rivers draining into the fiord. The bathymetry and sub bottom profiles can be used to analyze these past flooding events.

ACKNOWLEDGMENTS

This mapping project was funded by Crown-Indigenous Relations and Northern Affairs Canada (CIRNAC), the Government of Nunavut Fisheries and Sealing Division, the Public Safety Geoscience program of NRCan, and the Ocean Frontier Institute (OFI) through an award from the Canada First Research Excellence Fund. A special thanks to the crew of the R/V Nuliajuk and the Hamlet of Pangnirtung.

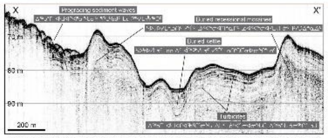

Figure 2. Prograding sediment waves, buried recessional moraines, buried kettles, and turbidites are identified in a sub bottom profile taken near the head of the fiord.

Figure 3. Discontinuous recessional moraines, kettles, and post glacial gullies are identified in the bathymetry.

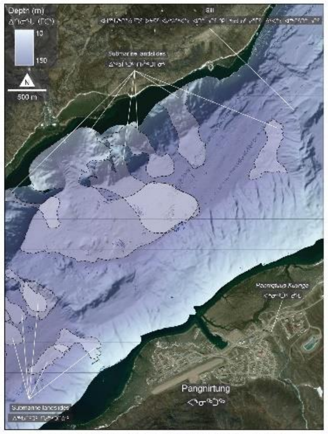

Figure 4. Submarine landslide deposits, and sills are identified near the Hamlet of Pangnirtung, NU.

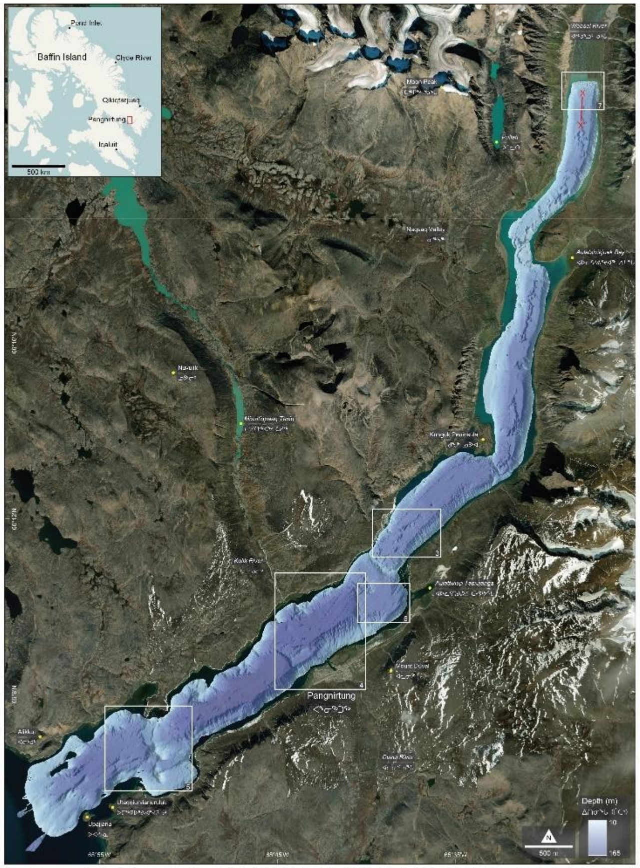

Figure 1. A bathymetric image of Pangnirtung Fiord. Place names and locations are sourced from the First Nation Profiles Interactive Map (2018) NRCan CanVec data (2017). Figure location reference boxes and the location of the sub-bottom profile (Figure 2) is provided.

Figure 5. Submarine landslide deposits and kettles are identified near the mouth of Pangnirtung Fiord.

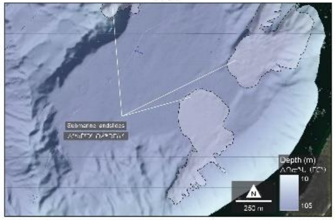

Figure 6. A bathymetric image of an area NE of the Hamlet of Pangnirtung, NU. The outlines of two submarine landslide deposits are identified by the dashed lines indicating their limits.

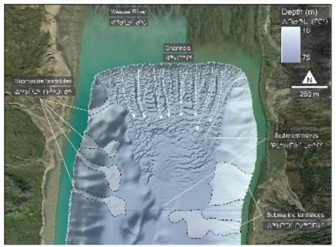

Figure 7. A bathymetric shaded-relief image of the fiord-head delta with identified channels, submarine landslides, and sediment waves.

REFERENCES
ᑖᒃᑯᐊ ᐊᑐᖅᑕᐅᔪᑦ

Corbett, L.B., Bierman, P.R., and Davis, P.T. 2016. Glacial history and landscape evolution of southern Cumberland Peninsula, Baffin Island, Canada, constrained by cosmogenic 10Be and 26Al. Bulletin of the Geological Society of America, 128, 1173–1192. doi:10.1130/B31402.1.
Dalton, A.S., Margold, M., Stokes, C.R., Tarasov, L. et al. 2020. An updated radiocarbon-based ice margin chronology for the last deglaciation of the North American Ice Sheet Complex. Quaternary Science Reviews, 234. doi:10.1016/j.quascirev.2020.106223.
Hampton, M.A., Lee, H.J., and Locat, J. 1996. Submarine Landslides. Springer Geology, 33–58. doi:10.1007/978-3-319-57852-1_13
Jackson, G.D., and Sanborn-Barrie, M. 2014. Jackson and Sanborn-Barrie. 2014. Bedrock of Pangnirtung. GSC Map.pdf
Margreth, A., Gosse, J.C., and Dyke, A.S. 2017. Wisconsinan and early Holocene glacial dynamics of Cumberland Peninsula, Baffin Island, Arctic Canada. Quaternary Science Reviews, 168: 79–100. Elsevier Ltd. doi:10.1016/j.quascirev.2017.04.033.
Masson, D.G., Harbitz, C.B., Wynn, R.B., Pedersen, G., and Løvholt, F. 2006. Submarine landslides: Processes, triggers and hazard prediction. Philosophical Transactions of the Royal Society A: Mathematical, Physical and Engineering Sciences, 364: 2009–2039. doi:10.1098/rsta.2006.1810.
Powell, R., and Domack, G.W. 2002. Modern glaciomarine environments. Modern and Past Glacial Environments: 361–389. doi:10.1016/b978-075064226-2/50015-5.
Spinney, J.A., and Pennesi, K.E. 2013. When the river started underneath the land: Social constructions of a 'severe' weather event in Pangnirtung, Nunavut, Canada. Polar Record, 49: 362–372. doi:10.1017/S0032247412000320.

---

[1] Department of Earth and Environmental Sciences, Dalhousie University, 1459 Oxford Street, Halifax, Nova Scotia
[2] Geological Survey of Canada, 1 Challenger Drive, P.O. Box 1006, Dartmouth, Nova Scotia
[3] Fisheries and Marine Institute, Memorial University of Newfoundland, 155 Ridge Road, St. John's, Newfoundland and Labrador

For more information, please contact A. Normandeau at (alexandre.normandeau@nrcan-rncan.gc.ca)

Permanent link: https://doi.org/10.4095/329814

This publication is available for free download through GEOSCAN (https://geoscan.nrcan.gc.ca/).

OPEN FILE
DOSSIER PUBLIC
8863
2022

Recommended citation
Sedore, P., Normandeau, A., Maselli, V., and Regular, K., 2022.
Bathymetry of Pangnirtung Fiord, Cumberland Sound, Nunavut;
Geological Survey of Canada, Open File 8863, 1 poster.
https://doi.org/10.4095/329814

Natural Resources Canada
Ressources naturelles Canada
Canada

Appendix H: Submarine landslides in Pangnirtung Fiord, eastern Baffin Island, Nunavut

Sedore, P., Normandeau, A. and Maselli, V. 2022: Submarine landslides in Pangnirtung Fiord, eastern Baffin Island, Nunavut; in Summary of Activities 2021, Canada-Nunavut Geoscience Office, *in press.*

Submarine landslides in Pangnirtung Fiord, Baffin Island, Nunavut

Philip Sedore[1], Alexandre Normandeau[2] and Vittorio Maselli[3]

[1]*Department of Earth and Environmental Sciences, Dalhousie University, Halifax, Nova Scotia <sedore.p@dal.ca>*

[2]*Natural Resources Canada, Geological Survey of Canada–Atlantic, Dartmouth, Nova Scotia*

[3]*Department of Earth and Environmental Sciences, Dalhousie University, Halifax, Nova Scotia*

This work is part of the Baffin Bay Geohazards Activity of the Landslides and Marine Geohazards Project of Natural Resources Canada's Public Safety Geoscience Program. This program undertakes research across Canada to support risk reduction from the effects of hazardous natural conditions (i.e., space weather, earthquakes, tsunamis, volcanoes and landslides). The program develops authoritative scientific knowledge and tools to reduce future economic, social and environmental losses from these hazards. Additional funding for this research was provided by Crown-Indigenous Relations and Northern Affairs Canada and the Ocean Frontier Institute through an award from the Canada First Research Excellence Fund.

Sedore, P., Normandeau, A. and Maselli, V. 2022: Submarine landslides in Pangnirtung Fiord, Baffin Island, Nunavut; *in* Summary of Activities 2021, Canada-Nunavut Geoscience Office, p. 31–46.

Abstract

As part of the Geological Survey of Canada's continuing aim to identify the potential marine geohazards in Baffin Bay, this study sought to generate a comprehensive understanding of the distribution, timing and potential triggers of submarine landslides in Pangnirtung Fiord. The high-relief topography of Pangnirtung Fiord is comparable to fiords in Greenland and Alaska, where recent studies have investigated landslide-generated tsunamis. Since the low-lying community of Pangnirtung is situated along the coast of Pangnirtung Fiord, it is ever more critical to understand the submarine-landslide hazard of the area.

The study identified 180 near-surface submarine landslides in Pangnirtung Fiord using multibeam bathymetric and sub-bottom profiler data, along with gravity cores collected in 2019. Morphometric analysis shows that most submarine landslides are relatively small (~0.13 km^2), with elongated failure zones and wide deposits dispersed along the basin floor. Radiometric dating reveals that eight of the eleven dated landslides are younger than 500 years. Landslide-surface roughness was tested as a proxy for age, but the relationship was found to be weak, thus limiting the ability to accurately date all identified landslides. Four broad categories of submarine-landslide triggers were identified and it was shown that at least 53% (96 of 180) of landslides are associated with subaerial sources and, at most, 31% (56 of 180) are shallow-water, non-subaerially influenced. This suggests that triggers of most submarine landslides within Pangnirtung Fiord include rapid flood-water input, subaerial debris flows and sea-ice loading during low tide.

Introduction

Fiords are narrow, submerged, glacially carved valleys flanked by steep, high-relief sidewalls, which are susceptible to subaerial and submarine geological hazards such as landslides and rock avalanches (Syvitski et al., 1987). Landslides may occur as slow or sudden, and potentially catastrophic, downslope movement of rock and sediment (Cruden and Varnes, 1996; Hampton et al., 1996). They have the potential to damage land-based and seabed infrastructure and threaten coastal communities through the generation of displacement waves (i.e., tsunamis) in high-latitude fiords (e.g., Brothers et al., 2016; Gauthier et al., 2017; Higman et al., 2018). In fact, over the last century, eight of the fourteen largest tsunamis recorded worldwide were caused by landslides in fiords (Miller, 1960; Dahl-Jensen et al., 2004; Oppikofer et al., 2009; Gauthier et al., 2017; Higman et al., 2018; Waldmann et al., 2021). Although no landslide-generated tsunami has been documented within the fiords of Baffin Island, the high-relief topography and dynamic sedimentation present similarities to the high-latitude fiords of Alaska, Greenland and Norway, all of which have a history of tsunami generation.

Landslides can be caused by internal stresses; however, seabed sediments need to be preconditioned for failure and an external trigger is often needed to generate downslope movement (Masson et al., 2006). Dynamic fiord sedimen-

This publication is available, free of charge, as colour digital files in Adobe Acrobat® PDF format from the Canada-Nunavut Geoscience Office website: https://cngo.ca/. Il est aussi disponible en français sur https://cngo.ca/fr/.

tation, which often includes high sedimentation rates and coarse-grained layers, can create weak preconditioned surfaces. An increase in shear stress or the development of overpressure in the pore fluid between sediment grains can then provide the necessary triggering mechanism for slope failure (Tappin, 2010; Urlaub et al., 2013; Clare et al., 2016). Numerous processes can trigger submarine landslides, including earthquakes caused by tectonic-plate movement (Kuenen, 1952) and isostatic adjustment (Brooks et al., 2016), wave action (Bea et al., 1983; Prior et al., 1989), sea-ice or iceberg groundings (Normandeau et al., 2021), tides (Johns et al., 1985; Chillarige et al., 1997) and increased river discharge that may promote rapid sediment accumulation and oversteepening of river-delta fronts (Prior and Bornhold, 1989; Bornhold et al., 1994; Girardclos et al., 2007; Clare et al., 2016). Submarine landslides can also be triggered when a subaerial landslide or rock avalanche extends to the water, destabilizing the seabed in shallow water. Subaerial landslides can be triggered by multiple processes, including permafrost thawing, increased precipitation and frost wedging (Gauthier et al., 2017; Higman et al., 2018).

Since 2018, the Geological Survey of Canada (GSC) has sought to identify potential marine geohazards in Baffin Island fiords, including submarine landslides. Seafloor-mapping initiatives reveal that submarine landslides occur within 86% (Bennett et al., 2021) of the mapped fiords (e.g., Broom et al., 2017; Brouard and Lajeunesse 2019; Normandeau et al., 2019; Deering et al., 2019; Bennett et al., 2021); however, their timing and causes are generally poorly understood. To better constrain these critical aspects of submarine landslides within a Baffin Island fiord, multibeam echosounder and sub-bottom profiler data, along with short (<115 cm) gravity cores, and unmanned aerial vehicle (UAV) images were collected in Pangnirtung Fiord in September 2019 aboard the Government of Nunavut Research Vessel (RV) *Nuliajuk* (Figure 1). This paper presents an assessment of submarine-landslide distribution, morphology and timing in Pangnirtung Fiord, and provides insights into possible trigger mechanisms.

A better understanding of submarine geohazards in Baffin Island fiords can help increase public safety for low-lying Arctic communities such as Pangnirtung (population 1481), located along the southeast coast of Pangnirtung Fiord on Baffin Island (Figure 1). All 467 dwellings within the hamlet lie below 60 m asl (metres above sea level), and the airport, fuel-storage tanks, health centre and schools are all below 30 m asl. An assessment of the submarine-landslide hazard in this dynamic fiord environment may help inform the community and protect this low-lying essential infrastructure. Similar assessments throughout the fiords of Baffin Island will be imperative with future development and expansion of essential infrastructure in a rapidly changing Arctic climate.

Regional setting

Pangnirtung Fiord is oriented northeast-southwest, with a length of 43 km, a width of 1–3 km and a maximum water depth of 165 m (Figure 1). In the southwest, the surrounding subaerial landscape features low-relief terrain of glacial till overlying bedrock. The northeastern section of the fiord is surrounded by high-relief terrain rising to 1500 m asl and divided by glacial valleys and cirques. Erosion of the steep fiord side walls that surround the coast has produced talus slopes and debris cones that extend to the shallow intertidal zone. The remaining cirque and alpine glaciers make up ~25% of Pangnirtung Fiord's catchment area (Gilbert, 1978). The bedrock surrounding Pangnirtung Fiord comprises three rock types of the Paleoproterozoic Qikiqtarjuaq dominantly felsic plutonic suite, dated at ca. 1.9–1.88 Ga (Jackson and Sanborn-Barrie, 2014).

Sediment supply to the fiord is sourced from numerous rivers and alluvial fans that drain the 1700 km^2 partially glaciated catchment area (Gilbert, 1978). Two main rivers, the Weasel River at the head of the fiord and the Kolik River across from the Hamlet of Pangnirtung, drain 67% of the catchment area (Figure 1; Gilbert, 1978). Other smaller rivers include Panniqtuup Kuunga (commonly referred to as the Duval River in the literature), which flows through the Hamlet of Pangnirtung, and the Puurusiq River, located to the northeast of the fiord. Although flow-rate measurements are sparse, the winter months see little to no flow, and snowmelt and precipitation in the summer months lead to high and sporadic discharge levels (e.g., average peak discharge of Panniqtuup Kuunga (Duval River) in 1973–1983 was 17.6 m^3/s; Water Survey of Canada, 1983).

Seismic activity surrounding Pangnirtung is concentrated in the northern Labrador Sea, Davis Strait and Baffin Bay, all of which are basins formed through seafloor spreading associated with the rifting of Canada and Greenland in the Late Cretaceous (Basham et al., 1977). Intraplate seismic events in Baffin Bay are caused by postglacial rebound that reactivates faults formed from the original Cretaceous rifting (Stein et al., 1979).

Methods

Hydroacoustic analysis and morphometrics

High-resolution multibeam bathymetric data were collected using a Kongsberg EM2040C. The data were then gridded to 5 m horizontal resolution and exported to Esri® ArcGIS Pro 2.5 to create shaded-relief maps intended for seafloor morphological interpretation (Figure 1). Sub-bottom profiles were acquired using a hull-mounted Knudsen 3260 3.5 kHz sub-bottom profiler (Figure 1). The sub-bottom data were visualized and interpreted using the SegyJp2Viewer developed at the Geological Survey of Canada (Courtney, 2009). Submarine-landslide deposits were

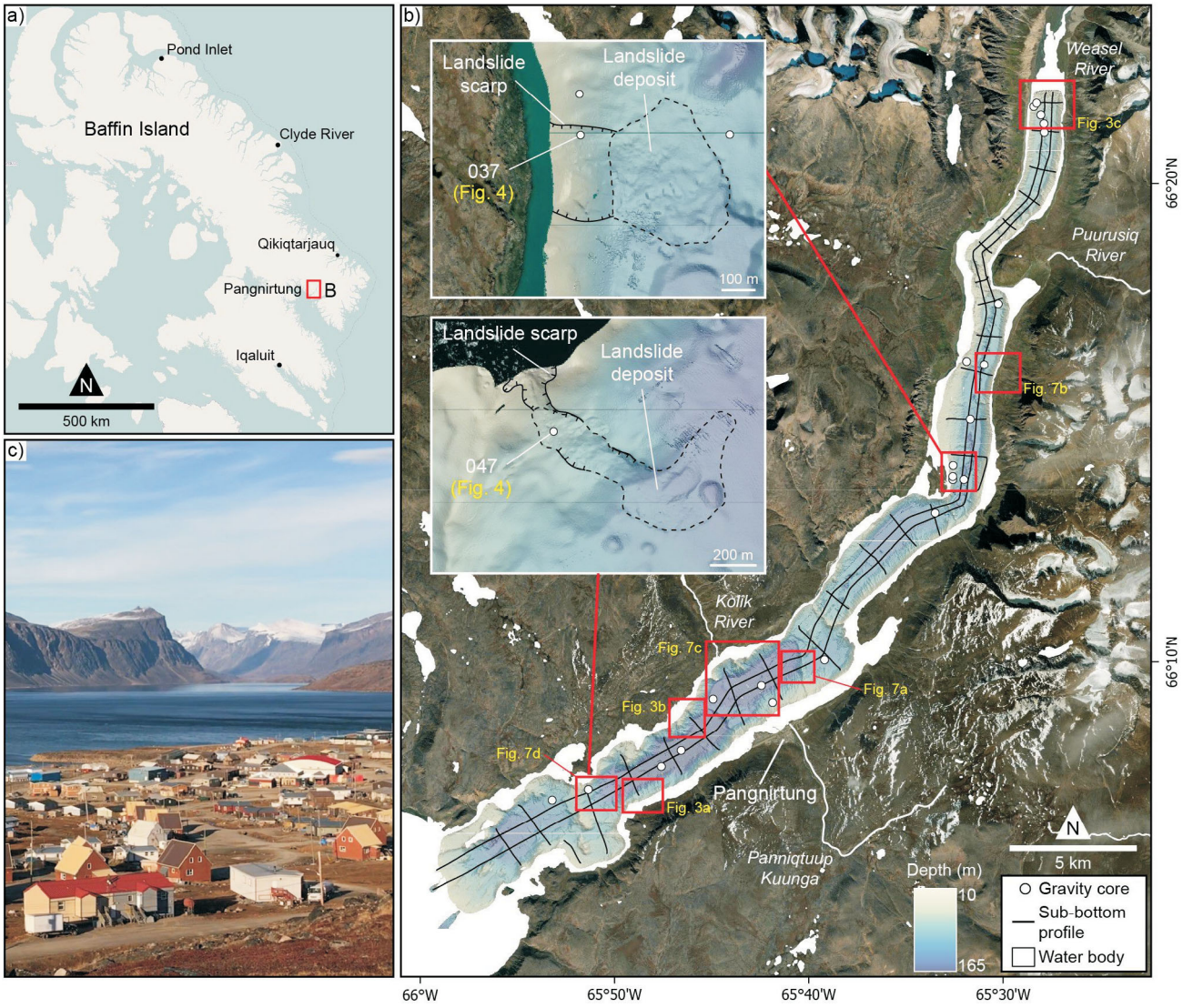

Figure 1: a) Location of Pangnirtung Fiord on eastern Baffin Island, Nunavut. **b)** Multibeam bathymetry of Pangnirtung Fiord, with the locations of gravity-core samples and sub-bottom profiles. Inset is a detailed view of the locations of cores 037 and 047, within mapped landslides. **c)** Photograph of Pangnirtung, facing north. Base map from Maxar Technologies.

identified by integrating bathymetry and sub-bottom data; a fully delineated submarine-landslide features a zone of slope failure including a head scarp, a flow path or transition zone, and a deposit. The relevant morphometric parameters for this study (Table 1) were measured following the standardized procedure outlined in Clare et al. (2019).

Core analysis

Twenty-one sediment gravity cores (Figure 1), ranging in length from 8 to 111 cm, were collected from the RV *Nuliajuk* and processed at the Geological Survey of Canada–Atlantic (GSC-A) facility located at the Bedford Institute of Oceanography (BIO) in Dartmouth, Nova Scotia. Physical and sedimentological properties were measured as an initial interpretation of the depositional processes and to identify landslide deposits. Using a Geotek Multi-Sensor Core Logger (MSCL), whole cores were analyzed for 1) magnetic susceptibility via a Barrington loop sensor (MS2B); 2) bulk density based on the gamma-ray attenuation of the sediment; 3) P-wave velocity based on the travel time of a compressional wave between transducers; and 4) colour reflectance via a Konica Minolta colour spectrophotometer to measure L* (lightness), a* (green to red) and b* (blue to yellow) values.

The cores were then split into a working half and an archive half, and then X-rayed and photographed. Grain-size measurements were completed using a Beckman Coulter LS230 Laser Diffraction Analyzer for grain sizes of 4–2000 µm, and manually sieved and weighed for particles above 1000 µm. Thin sections were also created to aid in characterizing the lithofacies.

Table 1: Descriptions of morphometric parameters used in this study of submarine landslides in Pangnirtung Fiord, eastern Baffin Island.

Parameter	Description
Area (km^2)	Total extent of the landslides and associated scar and flow path
Deposit length (m)	Maximum length of the landslide deposit
Maximum deposit width (m)	Maximum width of the deposit measured perpendicular to the maximum deposit length
Minimum water depth (m)	Water depth measured at the shallowest point of the delineated landslide
Total length (m)	Total length of the landslide from the upper limit of the head scarp to the downslope extent of the landslide
Scar width (m)	Maximum width of the scar
Slope gradient (º)	Measured slope of an adjacent slope outside of the slope failure scar and deposit
Slope gradient at toe (º)	Slope measured directly in front of the toe of the deposit
Elongation	Ratio of the total length to the maximum width of the deposit; a value less than 1 represents a longer width than length, and a value greater than 1 represents a longer length than width

Geochronology

Radiocarbon dates were obtained from shell fragments collected within 10 of the sediment cores (Sedore, M.Sc. in progress [Distribution, timing and potential trigger mechanisms of submarine landslides in Pangnirtung Fiord, eastern Baffin Island, Nunavut]) and analyzed at the A.E. Lalonde Accelerator Mass Spectrometry (AMS) Laboratory at the University of Ottawa (Table 2). The ^{14}C ages were corrected using a local marine reservoir correction (ΔR) of –6 ±58 years, calculated as the average of the 10 nearest shell measurements (Coulthard et al., 2010) and calibrated using the Marine20 calibration curve in Calib 8.2 (Heaton et al., 2020). Heaton et al. (2020) do not recommend this model for high latitudes (higher than 40–50°N), but presently there is not a better model. The ^{210}Pb and ^{137}Cs radioisotope activities for four sediment gravity cores were used to calculate sedimentation rates within the fiord. Subsamples were taken within the top 30 cm of the cores at 1–2 cm intervals (Pourchet and Pinglot, 1989; Bronk Ramsey, 2008) and analyzed at the Laboratory for the Analysis of Natural and Synthetic Environmental Toxins (LANSET) at the University of Ottawa. Sedimentation rates were calculated using the 'serac' R package developed by Bruel and Sabatier (2020) and the Constant Flux Constant Sedimentation (CFCS) model (Krishnaswamy et al., 1971). This model assumes that the ^{210}Pb activity in the

Table 2: Radiocarbon dating information, including core number, lab number, sample depth, radiocarbon age and uncertainty, and calibrated age and total uncertainty for cores 015, 017, 020, 030, 034, 037, 041, 043, 047 and 048 from Pangnirtung Fiord, eastern Baffin Island.

Core	Lab number	Sample depth (cm)	Radiocarbon age (yr BP)	Uncertainty (yr BP)	Calibrated age (cal. yr BP; ΔR = –6±58)	Uncertainty (yr BP)
015	UOC-13995	38–39	722	26	165	165
017	UOC-13996	68	697	24	145	145
020	UOC-13997	20	>Modern		>Modern	
020	UOC-13998	41–43	183	24	>Modern	
020	UOC-13999	49–51	>Modern		>Modern	
030	UOC-14000	72	1129	25	540	150
034	UOC-14001	2–3	>Modern		>Modern	
037	UOC-14002	3-5	>Modern		>Modern	
041	UOC-14003	49–51	899	25	325	175
043	UOC-14004	40–41	1733	25	1110	170
047	UOC-14005	0-1	>Modern		>Modern	
047	UOC-14006	22–25	4181	25	4060	230
048	UOC-14007	2-3	1362	25	745	165

newly deposited sediment has been constant throughout time; however, bioturbation, which is a prevalent process occurring throughout the hemipelagic sediments within the fiord, will affect the measured ^{210}Pb and ^{137}Cs activities. The CFCS model is the simplest model, with other models requiring porosity measurements that were not recorded during sampling.

The morphological and sedimentological characterizations of the submarine landslides were used to determine the intervals of interest. The ages of the submarine-landslide deposits were constrained through a combination of radiocarbon ages and the ^{210}Pb/^{137}Cs activity–derived sedimentation rates. In cores with only radiocarbon dates available, the sedimentation rates in the sediment cores were calculated through manual age-depth modelling. For these calculations, the instantaneous landslide deposits were excluded. Using these sedimentation rates (Sedore, M.Sc. in progress), the absolute ages of the instantaneous landslide deposits were calculated based on their depth in the cores and subbottom profiles using linear interpolation.

Surface roughness

The standard deviation (SD) of the bathymetric position index (BPI) was used to calculate the surface roughness for the delineated landslide deposits using ArcGIS Pro 2.5. The BPI is a measurement of the relative position of a pixel (2 m resolution) compared to the surrounding neighbourhood of pixels (Lundblad et al., 2006). The BPISD expresses the surface roughness for each landslide deposit, as a highly variable topographic surface will have a larger standard deviation than a smoother topographic surface. Under the assumption that older, buried landslides will have a smoother surface than recently deposited landslides, this measurement can be used as a proxy for the landslide's relative age when compared to other landslides. The surface roughness of the landslide deposits is also influenced by the type of landslide, the run-out distance, the slope and the sediment type. A linear regression was used to test the validity of this method for Pangnirtung Fiord submarine landslides, comparing the BPISD value to the absolute ages of landslides determined from radiometric dating. From this, an age for each landslide was calculated based on the BPISD and then compared to the absolute age of the landslide (Sedore, M.Sc. in progress).

Results and discussion

Distribution, morphology and sedimentology of submarine landslides

The high-resolution bathymetric data reveal 180 partially or fully delineated submarine landslides throughout Pangnirtung Fiord. Failure zones are identified in areas of high seafloor gradients (>4º), demonstrating an association between slope failure and high-relief sections of the fiord, such as the subaqueous fiord sidewalls and glacial sills (Figure 2). Conversely, no distinct slope failures are observed in areas with a low gradient (0–4º). Most landslide deposits are mapped along the relatively flat basin floor and, in some instances, crosscut other landslide deposits. Not every landslide deposit can be linked to its head scarp due to mapping limitations that prevent imaging the seafloor in shallow water. Due to this, the minimum water-depth measurement is a truncated distribution that should normally extend to 0 m but instead is restricted at about 10–30 m to 0 m (Figure 2). Considering this mapping limitation, at least 62% of mapped landslides have their head scarps at a water depth of less than 40 m.

Morphometric parameters were measured for the submarine landslides, and descriptive statistics can be summarized to provide the morphometrics of a typical submarine landslide in Pangnirtung Fiord (Figure 2). Most submarine-landslide deposits have an area less than 0.13 km^2 (lower quartile (Q1) = 0.03 km^2 and upper quartile (Q3) = 0.13 km^2), while the minimum water depth of the landslides varies from 3 to 132 m (mean = 38 m). The maximum scar width (Q1 = 98 m, Q3 = 260 m) and total length of deposit (Q1 = 310 m, Q3 = 637 m) can be used to calculate the elongation parameter for each landslide deposit. The elongation value of most deposits is above 1 (Q1 = 1.4, Q3 = 3.4), indicating a long and narrow feature oriented toward the downslope gradient. The slope gradient measured adjacent to the slope failure zone (Q1 = 9.5º, Q3 = 5º) is meant to provide insight into the unfailed slope angle; however, slope measurements within the failure zones show little deviation from the slope-gradient parameter. The mean slope of <1º at the toe of the landslides demonstrates the flow of the landslides to the flat basin floor.

The various morphologies and surface expressions of mapped submarine landslides in the geophysical datasets represent distinct landslide processes, including debris avalanches and debris flows (Figure 3). Debris avalanches are made up of unsorted sediment and rock that move rapidly downslope and do not appear to have distinct lateral bathymetric constraints (i.e., into an underwater channel; Hungr et al., 2001). Within Pangnirtung Fiord, the debris avalanches have a wide failure zone with distinct side scarps. The associated deposits are blocky and rough, with transverse compressional ridges. Debris flows are distinguished from debris avalanches by flowing through confined channels developed along the submarine slope from repeated failures. Generally, debris-flow deposits are lobe shaped and have a smoother appearance. Multiple debris-flow deposits can be identified at the base of these channels or gullies. Side scarps are not as distinct and the failure zones are narrower, creating an elongated landslide. Turbidity currents are inferred from the distinct sediment waves at the head of the fiord (Normandeau et al., 2019), as well as from potential turbidites in both sediment cores and

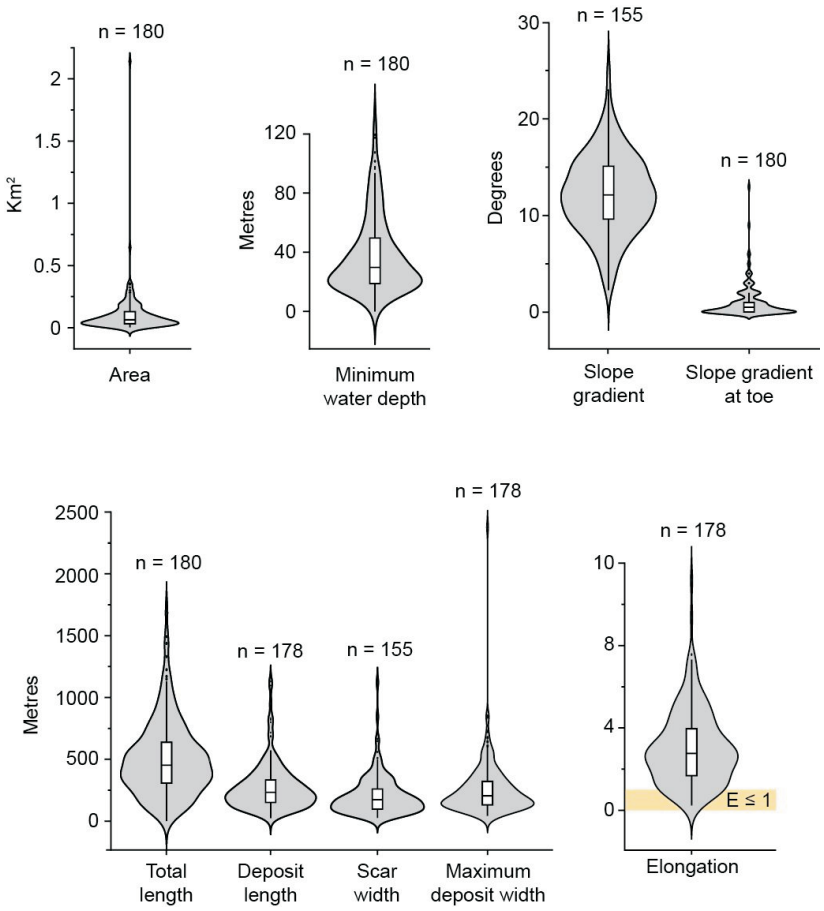

Figure 2: Violin plots of the morphometric parameters for the submarine landslides identified within Pangnirtung Fiord, eastern Baffin Island, including area, minimum water depth, slope gradient, slope gradient at toe, total length, deposit length, scar width, maximum deposit width, and elongation (parameters are defined in Table 1).

the sub-bottom profiles downslope of the fiord-head delta (Figure 3).

Photographs, X-radiographs and physical properties of 14 gravity cores (Sedore, M.Sc. in progress) were used to describe the landslide deposits, as well as discern the dominant lithological facies found in the fiord. The main lithofacies of interest to this study is identified at the top of cores 037 and 047 that were collected within the failure zones of two landslides along the steeply sloped (~20º and ~7º, respectively) submarine fiord sidewalls (Figure 4). These intervals, consisting of coarse-grained sand and a minor proportion of gravel, are interpreted as landslide deposits. These deposits have a lower magnetic susceptibility, and generally a higher but variable bulk density, than the hemipelagic sedimentation found in most cores. The landslide deposits are assumed to be thicker downslope from the coring position; however, these intervals capture remnant sediments associated with the mapped landslides. In core 037, the fining-upward sequence within the top 10 cm was caused by slow sediment settling at the sediment-water interface during the core extraction process; however, coarse-grained sand, gravel and shell fragments are still interpreted as a part of the landslide deposit. These upper intervals of cores 037 and 047 have erosive contacts with the underlying sediment that makes up the rest of the cores (Figure 4).

The underlying facies features wavy-parallel–laminated, dark grey clayey silt with intervals of very fine grained sand and granules identified in the X-radiograph images. These intervals, distinguished by their colour from the rest of the cored sediment, are interpreted as older postglacial sediments. To capture these older sediments in the short sediment cores, there must have been high erosion rates from submarine landslides along the fiord sidewall that removed thick sequences of postglacial hemipelagic sedimentary cover. Additionally, landslide deposits are also identified by fine- to coarse-grained sandy-silt laminations interpreted as turbidites associated with the respective landslide. The coarser grain size of these laminations distinguishes them from the surrounding dark grey or olive grey, highly bioturbated clay and silt with minor occurrences of very fine grained sand and granules. This surrounding lithofacies is interpreted to represent the background hemi-

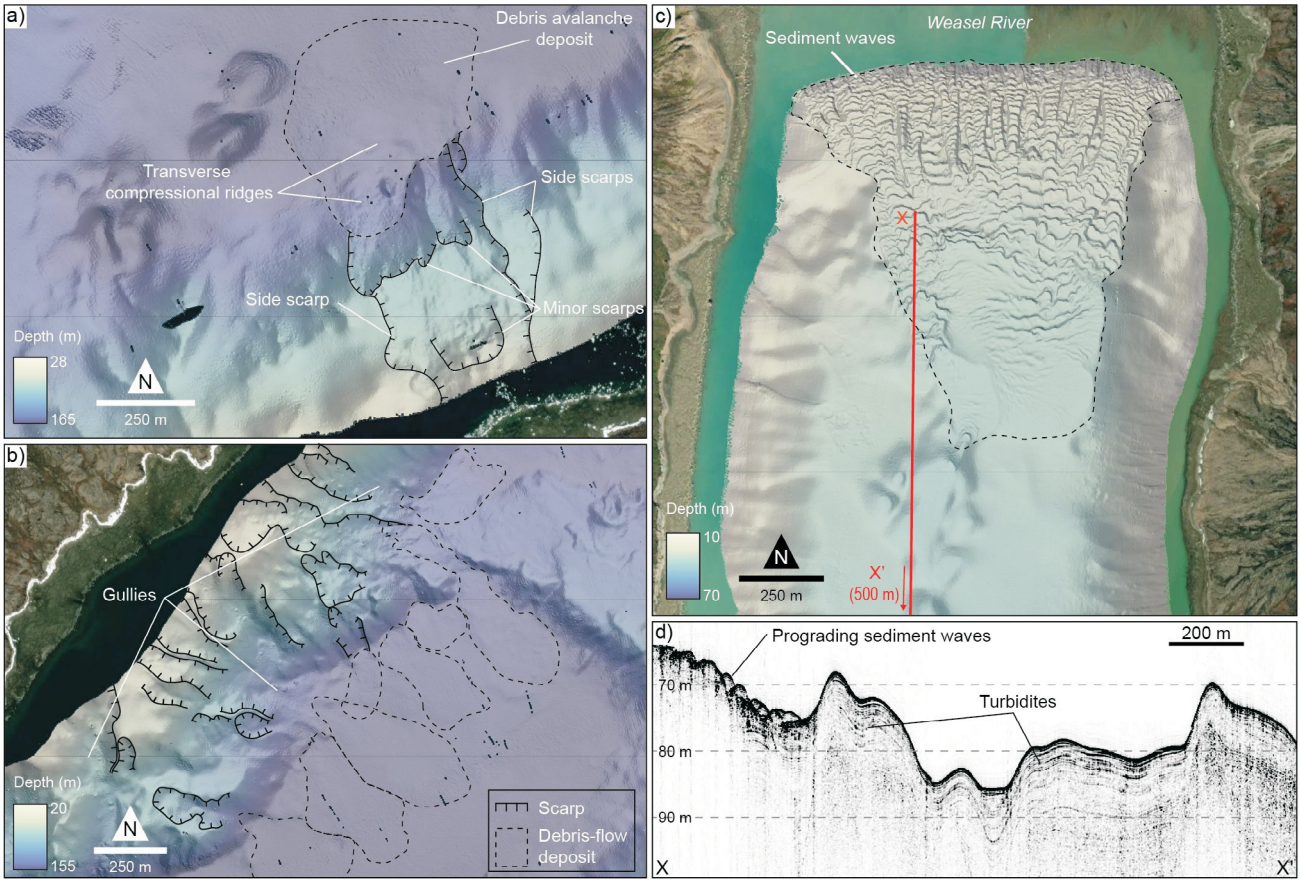

Figure 3: Example of **a)** debris avalanche; **b)** debris flow; **c)** sediment waves identified at the fiord-head delta; and **d)** turbidites and sediment waves identified in a sub-bottom profile acquired near the fiord-head delta. See Figure 1 for locations in Pangnirtung Fiord, eastern Baffin Island. Base map from Maxar Technologies.

pelagic sedimentation within the fiord that also incorporates ice-rafted debris.

Timing of submarine landslides

Using sedimentation rates derived from ^{14}C dating and ^{210}Pb and ^{137}Cs activities (Table 3), the ages of 11 landslides were calculated: eight occurred within the last 500 years with four of these found to be modern events (post-1950). Two examples of these modern landslides are captured in cores 037 and 047 (Figure 4). In core 047, an additional radiocarbon date of 4060 ±230 cal. yr BP (Table 2) at 22 cm depth from within a landslide deposit demonstrates the erosive nature of these landslides to incorporate this older material. The oldest landslide deposit is dated to approximately 4000 yr BP using the sedimentation rates determined from an overlying sediment core and an overburden height of 3 m estimated from sub-bottom data. The largest landslide, which the authors have tentatively named the Kolik River landslide, has an overburden height of approximately 1 m, and is tentatively dated to 1500–2000 yr BP. Future analysis of a sediment core collected in 2021 will precisely date this event. The modern ages of most landslides indicate that there has been recent landslide activity in the fiord, suggesting that these processes are still active and being caused by modern triggering mechanisms. There is a bias toward modern landslides in this study because only short sediment cores were collected; therefore, many buried landslide deposits identified in the multibeam echosounder data are excluded from this analysis. The exclusion of these buried landslide deposits and insufficient sub-bottom profile resolution to differentiate multiple landslides prevent accurate estimates of landslide recurrence in the fiord.

Strupler et al. (2019) found that, in a study of submarine landslides in Lake Zurich, Switzerland, dating based on BPISD can produce a first-order assessment of landslide ages, distinguishing between recent landslides that occurred within the last 150 years and sub-recent landslides. In Pangnirtung Fiord, there is an insufficient number of absolute landslide ages to validate the BPISD as a similar proxy for first-order landslide age. Of the landslide deposits dated in this study (Figure 5), recent landslides (cores 030, 037, 047 and 048 in Table 3) have a wider range of BPISD values than older deposits (cores 034, 041 and 043 in Table 3). The intervals tentatively interpreted as landslides in cores 015, 017 and 020 are not included in this BPISD analysis due to low confidence in the correct interpretation of the landslide

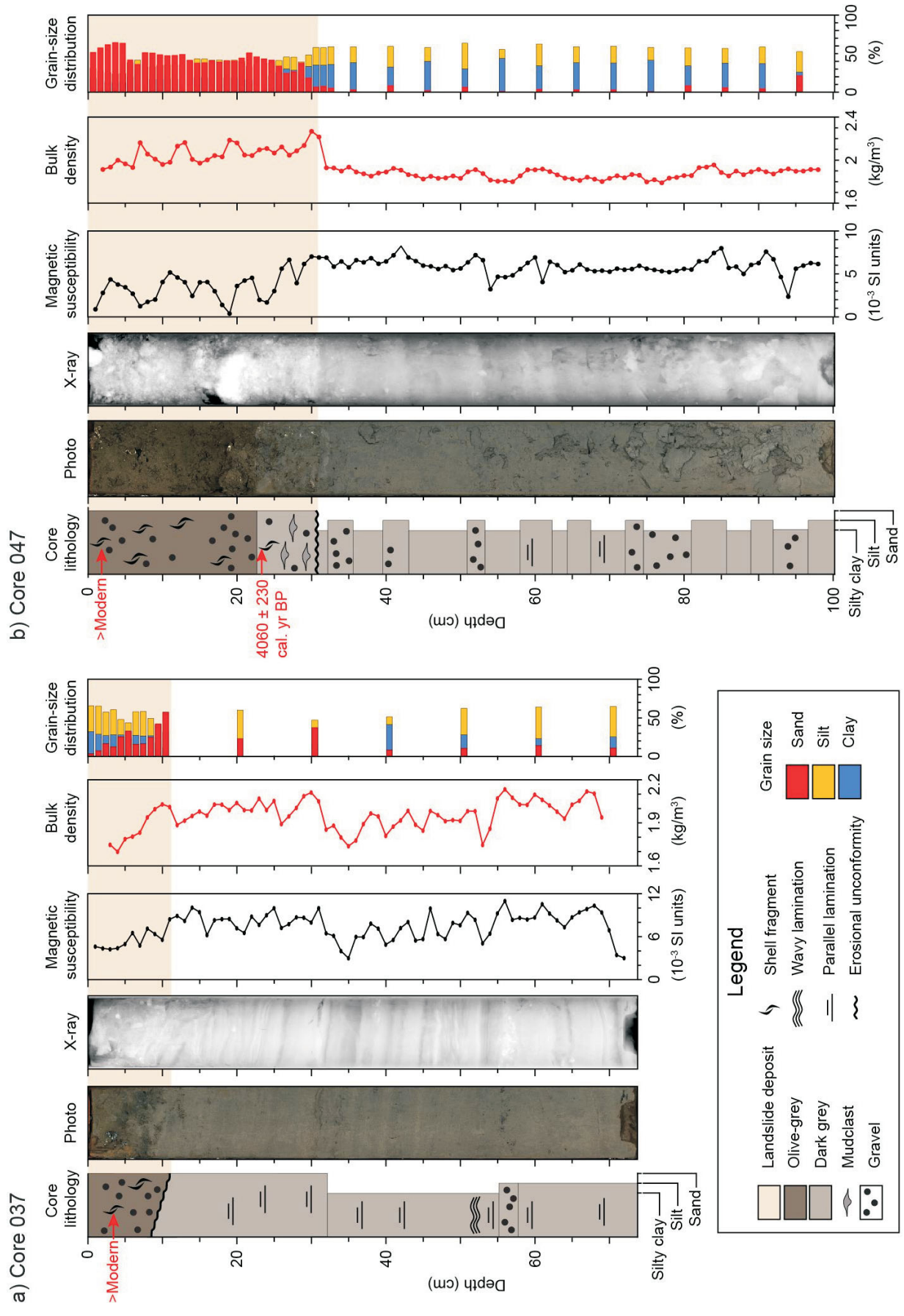

Figure 4: Lithological interpretations, photographs, X-radiographs, physical properties (magnetic susceptibility, bulk density), radiocarbon-dating results (see Table 2) and grain-size data of cores **a)** 037, and **b)** 047. See Figure 1 for core locations in Pangnirtung Fiord, eastern Baffin Island.

interval, as they are located near the fiord-head delta. The landslide interval identified in core 031 is also not included, as artifacts in the bathymetric data prevent accurate surface-roughness analysis. The wide range of BPISD values in recent landslides is reflected by large differences between the absolute and calculated ages of the deposits. In older deposits, their calculated age is a more accurate representation of their absolute age. However, this does not result in a sufficient differentiation of BPISD values to enable the use of surface roughness of the landslides as a proxy for landslide age.

The large range of landslide surface-roughness values is most likely caused by the different types of landslides identified in the fiord, along with variations in slope and landslide run-out (total length). Additionally, possible variations in overburden sedimentation rates, not captured in the dating results from this study, may cause less accurate age predictions of submarine landslides. Despite this conclusion, the surface-roughness analysis suggests that landslide deposits near each other with different relative surface-roughness values may be asynchronous, allowing for a semiquantitative interpretation of the sequence of events (Sedore, M.Sc. in progress).

Trigger mechanisms of submarine landslides

Based on the morphometric parameters, the spatial distribution and the relationship with the subaerial environment (Figure 6), the submarine landslides in Pangnirtung Fiord were grouped into four categories that reflect their possible trigger mechanisms. As an initial discerning factor, the 'minimum water depth' measured parameter, referring to the initiation depth of a submarine landslide, differentiates the mapped landslides into deep-water and shallow-water triggers. The shallow-water triggers are then subdivided based on the submarine landslide's relationship to the subaerial environment. From this, four categories of trigger mechanisms emerge: 1) deep water; 2) shallow water, subaerial debris-flow influenced; 3) shallow water, fluvially influenced; and 4) shallow water, non-subaerially influenced (Figure 7).

Table 3: Landslide interval ages calculated from ^{14}C dating and $^{210}Pb/^{137}Cs$ activities, Pangnirtung Fiord, eastern Baffin Island. Abbreviation: SAR, sediment accumulation rate.

Core	Dating method	Sample interval	Landslide interval depth (cm)	Calibrated age (cal. yr BP)	SAR (cm^2/yr)	Landslide age (cal. yr BP)
015	^{14}C	38–39	20–24	165	0.1834	109
017	^{14}C	68	36–39	145	0.4324	83
020	^{14}C	49–51	51–60	>Modern	-	0
030	$^{210}Pb/^{137}Cs$	-	10–18	-	0.09723	43
031	$^{210}Pb/^{137}Cs$	-	9–28	-	0.07946	58
034	$^{210}Pb/^{137}Cs$	-	300†	-	0.07946	3775
037	^{14}C	3–5	0–9	>Modern	-	0
041	$^{210}Pb/^{137}Cs$	-	100†	-	0.06161	1625
043	^{14}C	40–41	100†	1110	0.0358	2795
047	^{14}C	22–25	0–31	4060	-	0
048	^{14}C	2–3	0–22	745	-	0‡

†Landslide interval depth calculated from sub-bottom profiles.

‡Radiocarbon age is likely older material incorporated into a modern landslide interval.

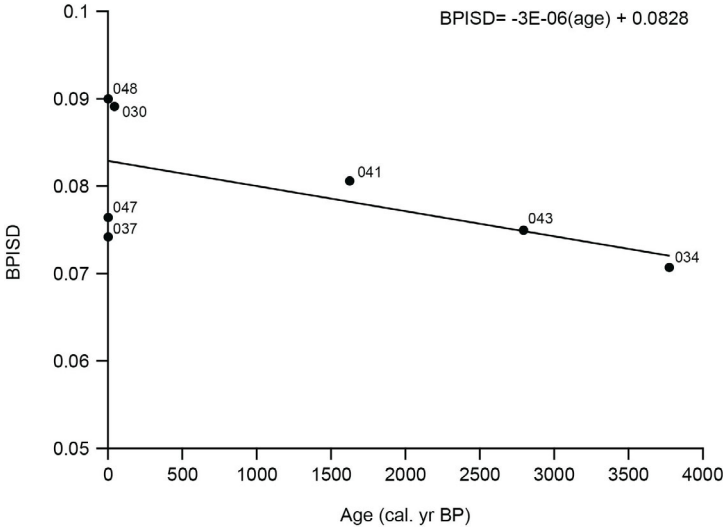

Figure 5: Standard deviation of the bathymetric position index (BPISD) plotted against the ages of the landslide deposits in Pangnirtung Fiord, eastern Baffin Island. Landslides are identified based on their respective core number (see Table 3). The trendline represents the calculated ages of the landslides (R^2 = 0.364).

Deep-water trigger mechanisms

Submarine landslides initiated in deep water (e.g., Figure 7a) constitute 15% of the mapped landslides and are not likely to have a shallow-water or subaerial trigger (Figure 6). The failure zones are identified along the middle of sills where the shallowest possible head scarp is far deeper than wave or tidal influence and far enough away from the fiord sidewalls and major sediment inputs that subaerial and fluvial triggers likely have no influence. Many of these landslides appear to be the result of slope failures in recessional moraine sediments and have numerous scarps over a wide failure area. The most probable triggers for these deeper water landslides are most likely a combination of seismicity induced by isostatic rebound during the retreat of the glaciers in Pangnirtung Fiord and the oversteepening of slopes. Oversteepening of slopes can act as a preconditioning factor, leaving sediment susceptible to seismic triggers (Clare et al., 2016).

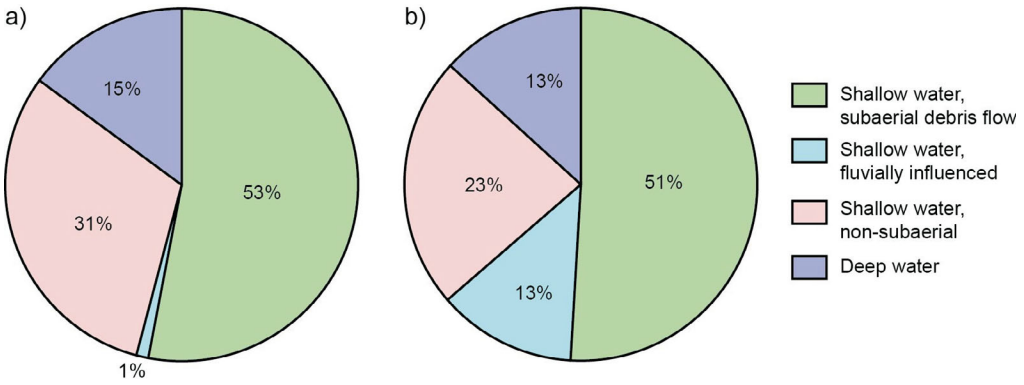

Figure 6: Proportion of interpreted triggering mechanisms of submarine landslides in Pangnirtung Fiord, eastern Baffin Island based on **a)** number of landslides, and **b)** total area of landslides in each trigger classification.

Shallow-water, subaerial debris-flow trigger mechanisms

Subaerial debris flows have been suggested as a potential trigger mechanism of shallow submarine landslides (Bellwald et al., 2016; Deering et al., 2019). Sudden rapid colluvial and alluvial outwash into the shallow water would increase the pore pressure and potentially increase shear stress in the shallow-water sediments. Deering et al. (2019) suggested that subaerial slope failures are a contributing triggering mechanism for most submarine landslides identified in Frobisher Bay, Baffin Island. In Pangnirtung Fiord, the shallow minimum water depth of most landslide failure zones also suggests a possible subaerial influence. Conclusive evidence of a connection between the subaerial environment and submarine landslides in the fiord is shown in satellite imagery from 2019 overlain by the multibeam bathymetry (Figure 7b). A subaerial debris fan clearly extends to the intertidal zone and three submarine landslides are visible downslope; however, no head scarp is mapped in the bathymetry, only side scarps and a transition zone. Three likely head scarps are distinguished in the satellite imagery downslope from the debris fan by their concave shape created at the cusp of the intertidal zone. The proximity of the submarine-landslide head scarps to the subaerial debris fan demonstrates a clear connection between subaerial debris flows and submarine-landslide occurrence. Based on ^{210}Pb geochronological data, the middle landslide, with the highest surface-roughness value, occurred in the early 20th century.

Building on these initial findings, subaerial susceptibility modelling of Pangnirtung Fiord (Normandeau et al., 2022) can be used to understand which of the other submarine landslides were potentially triggered by subaerial debris flows. Normandeau et al. (2022) employed subaerial-landslide susceptibility modelling at the scale of the fiord to identify potential source and propagation areas for subaerial debris-flow hazards following the steps of Horton et al. (2013). The Figure 8 inset shows the results of subaerial susceptibility debris-flow modelling for the subaerial debris-flow example shown in Figure 7b. The area classified as a potential zone for 'large torrents', shaded black, is upslope of the submarine landslides with a clear subaerial connection. This example demonstrates that this subaerial debris-flow susceptibility modelling can be used to determine the number of submarine landslides potentially triggered by subaerial processes. Examining the entire fiord, Figure 8 presents the relative probability of the modelled subaerial landslides entering the fiord, as well as the location of the submarine-landslide deposits identified in the bathymetry. Those landslides located directly downslope of the modelled subaerial debris flows make up 53% of submarine landslides (Figure 6). Overall, this classification of submarine landslides presents a definitive relationship between submarine landslides and the subaerial environment, and illustrates the impact subaerial debris flows have as a major triggering mechanism of submarine landslides in Pangnirtung Fiord.

Shallow-water, fluvial trigger mechanisms

Landslides located downslope of fluvial sources account for 1% of the mapped landslides in the fiord; however, they represent 13% of the total area of all submarine landslides in Pangnirtung Fiord (Figure 6). The largest landslide (2.1 km^2), the Kolik River landslide, was identified downslope from the Kolik River (Figure 7c). Failure scarps are mapped within the bathymetric coverage, but the head scarp is likely in shallower waters, outside the mapping area. A potential head scarp or portion of a head scarp is identified in satellite imagery (Figure 7c). The associated landslide deposit features large blocks that create an undulating surface texture. Delta collapse was the likely cause of the Kolik River landslide, similar to that of a submarine landslide in Lake Brienz, Switzerland (Girardclos et al., 2007). Elevated discharge rates in the Kolik River or an earthquake may be responsible for the delta collapse. There are ongoing efforts to determine the tsunamigenic potential of this landslide.

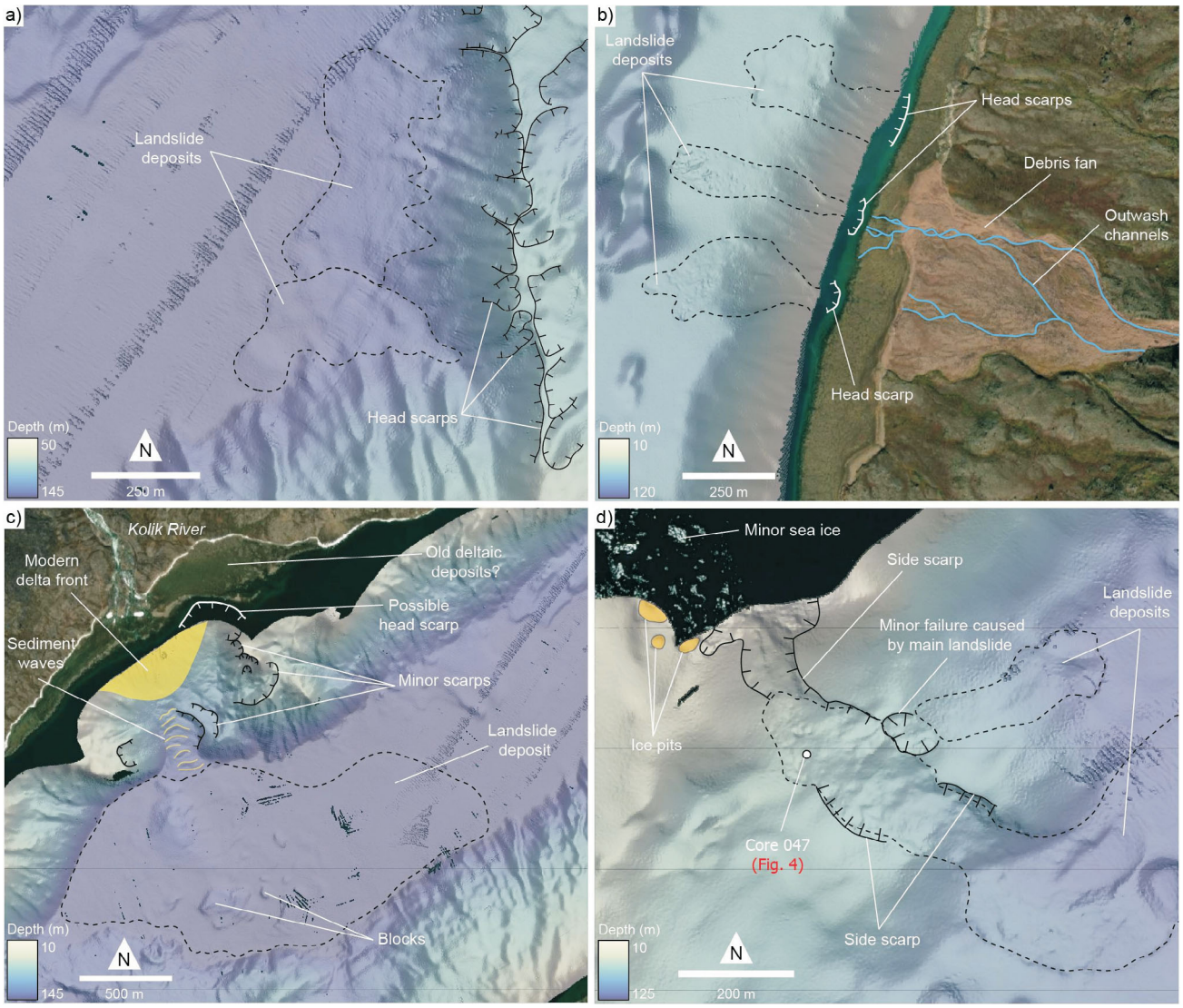

Figure 7: Examples of detailed landslide mapping in Pangnirtung Fiord, eastern Baffin Island: **a)** landslide triggered by deep water; **b)** submarine landslide influenced by shallow-water debris flow; **c)** shallow-water, fluvially influenced submarine landslide at the mouth of the Kolik River; **d)** shallow-water, non-subaerially influenced submarine landslide. See Figure 1 for locations. Base map from Maxar Technologies.

Shallow-water, non-subaerial trigger mechanisms

Thirty-one percent of landslides (Figure 6) are initiated in shallow water but do not have an obvious relationship to a subaerial trigger (Figure 7d). Like the previous classification, the head scarps are identified in shallow water or the assumed head scarps are too shallow to map; however, these landslides do not occur downslope of an area modelled to be susceptible to subaerial landslides. In addition, these landslides are also generally elongated, suggesting a point-source trigger. Likely point-source triggers for these slides include sea-ice and iceberg groundings, wave action and tides. Earthquakes are a possible trigger mechanism, although they would likely cause a wider area of sediment to fail, thus presenting lower elongation values, which is not supported by the morphometric measurements (Figure 2). These mechanisms may also trigger the previously described submarine landslides with perceived connections to fluvial output and subaerial debris flows. These subaerial debris flows and rivers transport sediment to the marine environment, preconditioning the slopes for failure, with these shallow-water, non-subaerially influenced mechanisms ultimately triggering a landslide.

Economic considerations

Both submarine and subaerial landslides are known natural hazards in fiords that can affect coastal communities. Landslide-generated displacement waves of sufficient height can inundate coastal areas and damage low-lying infrastructure. The existence of high-relief fiord sidewalls and mapped subaerial and submarine landslides in Pangnirtung Fiord provide the necessary elements seen in previous Arctic displacement-wave locations (e.g., Brothers et al., 2016;

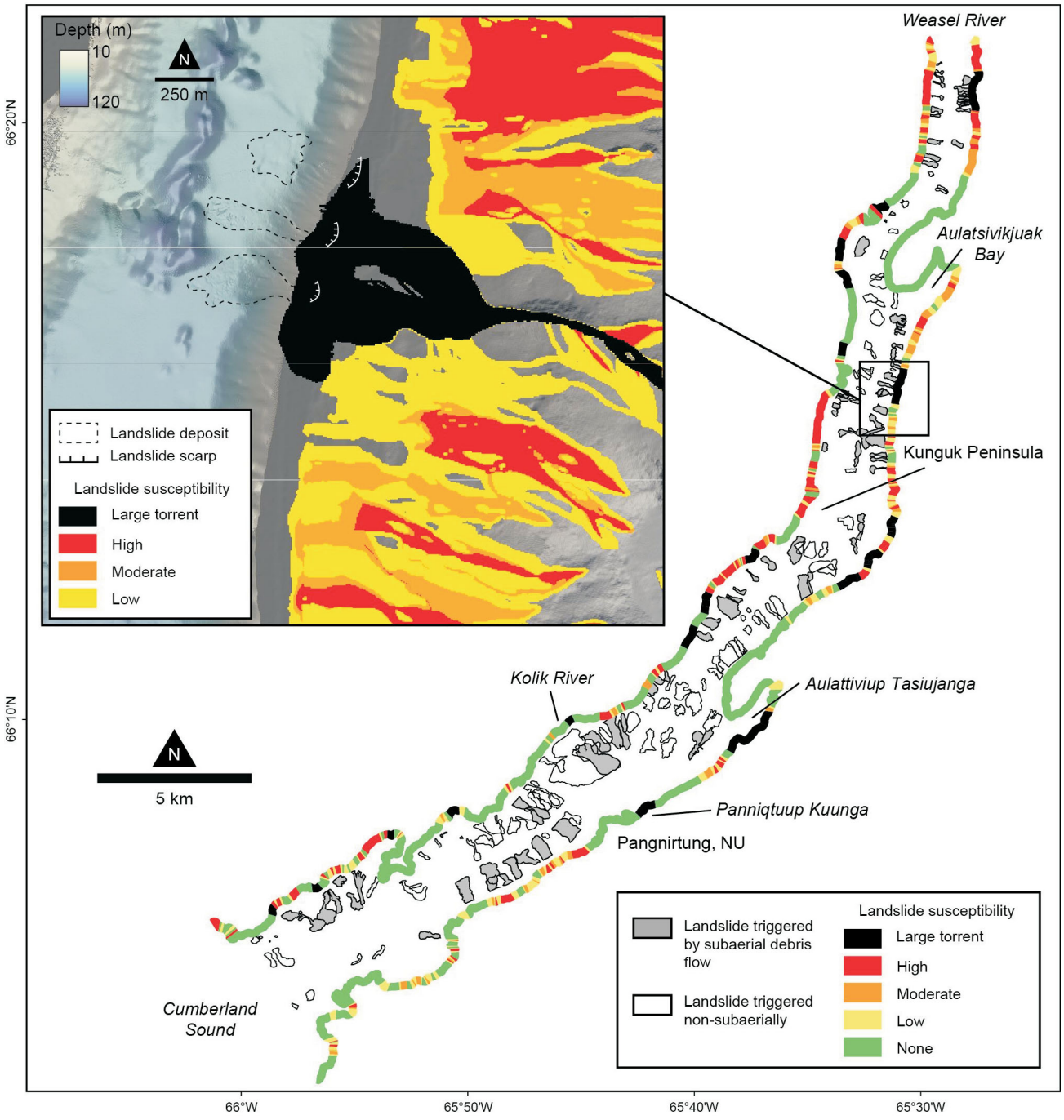

Figure 8: Relative probability of modelled subaerial debris flows (Normandeau et al., 2022) extending to the coast, superimposed on mapping of submarine landslides in Pangnirtung Fiord, eastern Baffin Island. Inset: shallow-water submarine landslides influenced by subaerial debris flows shown in Figure 7b, overlain by results of subaerial debris-flow susceptibility modelling. Digital elevation model created from DigitalGlobe imagery and funded under National Science Foundation awards 1043681, 1559691 and 1542736.

Gauthier et al., 2017; Higman et al., 2018). Without consideration of seafloor-sediment dynamics, submarine landslides can also damage seafloor infrastructure. Proposed seafloor fibre-optic Internet cables may connect the community of Pangnirtung to high-speed Internet, which will help with economic growth. However, submarine landslides remain a possible threat to damage seafloor cables, which would involve costly and lengthy repairs. Mapping the seafloor and understanding the landslide hazards that may affect this infrastructure is a crucial step when planning routes and depths at which cables are buried.

Conclusions

Landslides are proven geological hazards in high-latitude fiords, potentially causing tsunamis and damaging essen-

tial infrastructure. This study sought to provide an evaluation of the distribution, timing, and trigger mechanisms of submarine landslides and associated geohazards for Pangnirtung Fiord. Results of radiometric dating, combined with an analysis of the surface roughness of the landslide deposits, indicate that most landslides occurred within the last 500 years and at least five have occurred since 1900.

This attempt to discern the cause of these submarine landslides produced four categories of triggers. The most abundant trigger mechanism is interpreted as subaerial debris flows entering the sea, causing a rapid influx of sediment and water, and triggering submarine landslides. An examination of subaerial debris flows shows that there is a clear relationship between the distribution of submarine landslides and the surrounding subaerial environment. This relationship demonstrates the need to integrate an evaluation of the subaerial environment when addressing geohazards in the high-relief fiords of Baffin Island. Although most submarine landslides do not appear to have the capacity to initiate a tsunami, ongoing work is focusing on determining the tsunamigenic potential of the largest submarine landslide, the Kolik River landslide (Figure 7c).

Acknowledgments

The authors thank the Captain, officers, crew and scientific staff onboard the RV *Nuliajuk*, and the Hamlet of Pangnirtung. Thanks also go to T. Tremblay of the Canada-Nunavut Geoscience Office for the insightful and detailed review. Financial support for this study was provided by Crown-Indigenous Relations and Northern Affairs Canada, the Government of Nunavut Fisheries and Sealing Division, the Public Safety Geoscience Program of Natural Resources Canada and the Ocean Frontier Institute through an award from the Canada First Research Excellence Fund. Finally, thank you to K. Regular of the Marine Institute and L. Broom, O. Brown, J. Higgins, K. Jarrett, K. Jenner and G. Philibert of the Geological Survey of Canada–Atlantic.

Natural Resources Canada, Lands and Minerals Sector contribution 20210542

References

Basham, P.W., Forsyth, D.A. and Wetmiller, R.J. 1977: The seismicity of northern Canada; Canadian Journal of Earth Sciences, v. 14, no. 7, p. 1647–1667, URL <https://doi.org/10.1139/e77-140>.

Bea, R., Wright, S., Sircar, P. and Niedoroda, A.W. 1983: Wave induced slides in South Pass Block 70, Mississippi Delta; ASCE Journal of Geotechnical Engineering, v. 109, no. 4, p. 619–644, URL <https://doi.org/10.1061/(ASCE)0733-9410(1983)109>.

Bellwald, B., Hjelstuen, B.O., Sejrup, H.P. and Haflidason, H. 2016: Postglacial mass movements and depositional environments in a high-latitude fjord system – Hardangerfjorden, western Norway; Marine Geology, v. 379, p. 157–175, URL <http://dx.doi.org/10.1016/j.margeo.2016.06.002>.

Bennett, R., Normandeau, A. and Campbell, D.C. 2021: Preliminary assessment of the distribution of submarine slope failures in Baffin Island fiords, Nunavut; *in* Summary of Activities 2020, Canada-Nunavut Geoscience Office, p. 73–80, URL <https://cngo.ca/summary-of-activities/2020> [October 2021].

Bornhold, B.D., Ren, P. and Prior, D.B. 1994: High-frequency turbidity currents in British Columbia fjords; Geo-Marine Letters, v. 14, p. 238–243, URL <https://doi.org/10.1007/BF01274059>.

Bronk Ramsey, C. 2008: Radiocarbon dating: revolutions in understanding; Archaeometry, v. 50, p. 249–275, URL <https://doi.org/10.1111/j.1475-4754.2008.00394.x>.

Brooks, G.R. 2016: Evidence of late glacial paleoseismicity from submarine landslide deposits within Lac Dasserat, northwestern Quebec, Canada; Quaternary Research (United States), v. 86, p. 184–199, URL <https://doi.org/10.1016/j.yqres.2016.06.005>.

Broom, L.M., Campbell, D.C. and Gosse, J.C. 2017: Investigation of a Holocene marine sedimentary record from Pond Inlet, northern Baffin Island, Nunavut; *in* Summary of Activities 2017, Canada-Nunavut Geoscience Office, p. 93–104, URL <https://cngo.ca/summary-of-activities/2017/> [October 2021].

Brothers, D.S., Haeussler, P.J., Liberty, L., Finlayson, D., Geist, E., Labay, K. and Byerly, M. 2016: A submarine landslide source for the devastating 1964 Chenega tsunami, southern Alaska; Earth and Planetary Letters, v. 438, p. 112–121, URL <https://doi.org/10.1016/j.epsl.2016.01.008>.

Brouard, E. and Lajeunesse, P. 2019: Submarine geomorphology of the northeastern Baffin Island fiords and cross-shelf troughs; Journal of Maps, v. 15, no. 2, p. 662–676, URL <https://doi.org/10.1080/17445647.2019.1647302>.

Bruel, R. and Sabatier, P. 2020: *serac*: An R package for ShortlivEd RAdionuclide chronology of recent sediment cores; Journal of Environmental Radioactivity, v. 225, p. 106449, URL <https://doi.org/10.1016/j.jenvrad.2020.106449>.

Chillarige, A.R.V., Morgenstern, N.B., Robertson, P.K. and Christian, H.A. 1997: Seabed instability due to flow liquefaction in the Fraser River delta; Canadian Geotechnical Journal, v. 34, p. 520–533, URL <https://doi.org/10.1139/T97-019>.

Clare, M.A., Hughes Clarke, J.E., Talling P.J., Cartigny, M.J.B. and Pratomo, D.G. 2016: Preconditioning and triggering of offshore slope failures and turbidity currents revealed by most detailed monitoring yet at a fjord-head delta; Earth and Planetary Science Letters, v. 450, p. 208–220, URL <https://doi.org/10.1016/j.epsl.2016.06.021>.

Clare, M., Chaytor, J., Dabson, O., Gamboa, D., Georgiopoulou, A., Eady, H., Hunt, J., Jackson, C., Katz, O., Krastel, S., León, R., Micallef, A., Moernaut, J., Moriconi, R., Moscardelli, L., Mueller, C., Normandeau, A., Patacci, M., Steventon, M., Urlaub, M. et al. 2019: A consistent global approach for the morphometric characterization of subaqueous landslides; Subaqueous Mass Movements, Geological Society of London, Special Publications, v. 477, p. 455–477, URL <https://doi.org/10.1144/SP477.15>.

Coulthard, R., Furze, M.F.A., Pieńkowski, A.J., Nixon, F.C. and England, J.H. 2010: New marine ΔR values for Arctic Canada; Quaternary Geochronology, v. 5, no. 4, p. 419–434, URL <https://doi.org/10.1016/j.quageo.2010.03.002>.

Courtney, B. 2009: SegyJp2 Viewer Version 1.0 software; Geological Survey of Canada, Natural Resources Canada, available

at URL <https://ge0mlib.com/software.htm> [January 2022].

Cruden, D.M. and Varnes, D.J. 1996: Landslide types and processes, National Academy of Sciences, Transportation Research Board, Special Report, v. 247, p. 36–75.

Dahl-Jensen, T., Larsen, L.M., Pedersen, S.A.S., Jepsen, H.F., Nielsen, T., Von Platen-Hallermund, F. and Weng, W. 2004: Landslide and tsunami, 21 November 2000 in Paatuut, West Greenland; Natural Hazards, v. 31, p. 277–287, URL <https://doi.org/10.1023/B:NHAZ.0000020264.70048.95>.

Deering, R., Bell, T., Forbes, D.L., Campbell, C. and Edinger, E. 2019: Morphological characterization of submarine slope failures in a semi-enclosed fjord, Frobisher Bay, eastern Canadian Arctic; Subaqueous Mass Movements, v. 477, p. 367–376, URL <https://doi.org/10.1144/SP477.35>.

Gauthier, D., Anderson, S.A., Fritz, H.M. and Giachetti, T. 2017: Karat Fjord (Greenland) tsunamigenic landslide of 17 June 2017: initial 3D observations; Landslides, v. 15, p. 327–332, URL <https://doi.org/10.1007/s10346-017-0926-4>.

Gilbert, R. 1978: Observations on oceanography and sedimentation at Pangnirtung Fiord, Baffin Island; Maritime Sediments, v. 14, no. 1, p. 1–9, URL <https://doi.org/10.4138/1952>.

Girardclos, S., Schmidt, O.T., Sturm, M., Ariztegui, D., Pugin, A., and Anselmetti, F.S. 2007: The 1996 AD delta collapse and large turbidite in Lake Brienz; Marine Geology, v. 241, p. 137–154, URL <https://doi.org/10.1016/j.margeo.2007.03.011>.

Hampton, M.A., Lee, H.J. and Locat, J. 1996: Submarine landslides; Springer Geology, v. 34, p. 33–59, URL <https://doi.org/10.1007/978-3-319-57852-1_13>.

Heaton, T., Köhler, P., Butzin, M., Bard, E., Reimer, R., Austin, W.E.N., Ramsey, C.B., Grootes, P.M., Hughen, K.A., Kromer, B., Reimer, P.J., Adkins, J., Burke, A., Cook, M.S., Olsen, J. and Skinner, L. 2020: Marine20 – the marine radiocarbon age calibration curve (0–55,000 cal. BP); Radiocarbon, v. 62, no. 4, p. 779–820, <https://doi.org/10.1017/RDC.2020.68>.

Higman, B., Shugar, D.H., Stark, C.P., Ekström, G., Koppes, M.N., Lynett, P., Dufresne, A., Haeussler, P.J., Geertsema, M., Gulick, S., Mattox, A., Venditti, J.G., Walton, M.A.L., McCall, N., Mckittrick, E., MacInnes, B., Bilderback, E.L., Tang, H., Willis, M.J., Richmond, B. et al. 2018: The 2015 landslide and tsunami in Taan Fiord, Alaska; Nature: Scientific Reports, v. 8, art. 12993, URL <https://doi.org/10.1038/s41598-018-30475-w>.

Horton, P., Jaboyedoff, M., Rudaz, B., and Zimmermann, M. 2013: Flow-R, a model for susceptibility mapping of debris flows and other gravitational hazards at a regional scale; Natural Hazards and Earth System Sciences, v. 13, p. 869–885, URL <https://doi.org/10.5194/nhess-13-869-2013>.

Hungr, O., Evans, S.G., Bovis, M.J. and Hutchinson, J.N. 2001: A review of the classification of landslides of the flow type; Environmental and Engineering Geoscience, v. 7, p. 221–238, URL <https://doi.org/10.2113/gseegeosci.7.3.221>.

Jackson, G.D. and Sanborn-Barrie, M. 2014: Geology, Pangnirtung Fiord, Nunavut; Geological Survey of Canada, Canadian Geoscience Map 4, 1:100 000 scale, URL <https://doi.org/10.4095/288928>.

Johns, M.W., Prior, D.B., Bornhold, D.B., Coleman, J.M. and Bryant, W.R. 1985: Geotechnical aspects of a submarine slope failure, Kitimat Fjord, British Columbia. Marine Geotechnology, v. 6, p. 243–279, URL <https://doi.org/10.1080/10641198609388190>.

Krishnaswamy, S., Lal, D., Martin, J.M. and Meybeck, M. 1971: Geochronology of lake sediments; Earth and Planetary Science Letters, v. 11, p. 407–414, URL <https://doi.org/10.1016/0012-821X(71)90202-0>.

Kuenen, P.H. 1952: Estimated size of the Grand Banks turbidity current; American Journal of Science, v. 250, p. 874–884, URL <https://doi.org/10.2475/ajs.250.12.874>.

Lundblad, E.R., Wright, D.J., Miller, J., Larkin, E.M., Rinehart, R., Naar, D.F., Donahue, B.T., Anderson, S.M. and Battista, T. 2006: A benthic terrain classification scheme for American Samoa; Marine Geodesy, v. 29, p. 89–111, URL <https://doi.org/10.1080/01490410600738021>.

Masson, D.G., Harbitz, C.B., Wynn, R.B., Pedersen, G. and Løvholt, F. 2006: Submarine landslides: processes, triggers and hazard prediction; Philosophical Transactions of the Royal Society, A: Mathematical, Physical and Engineering Sciences, v. 364, p. 2009–2039, URL <https://doi.org/10.1098/rsta.2006.1810>.

Miller, D.J. 1960: Giant waves in Lituya Bay, Alaska; U.S. Geological Survey, Professional Paper 354-C, URL <http://pubs.er.usgs.gov/publication/pp354C> [January 2022].

Normandeau, A., Blais-Stevens, A., Horton, T., Oppikofer, T., Sedore, P. and Maselli, V. 2022: Landslide susceptibility in Pangnirtung Fiord, Nunavut; Geological Survey of Canada, Open File 8843, 1 poster.

Normandeau, A., Dietrich, P., Hughes Clarke, J., Van Wychen, W., Lajeunesse, P., Burgess, D. and Ghienne, J.F. 2019: Retreat pattern of glaciers controls the occurrence of turbidity currents on high-latitude fjord deltas (eastern Baffin Island); Journal of Geophysical Research: Earth Surface, v. 124, p. 1559–1571, URL <https://doi.org/doi:10.1029/2018JF004970>.

Normandeau, A., MacKillop, K., Macquarrie, M., Richards, C., Bourgault, D., Campbell, D.C., Maselli, V., Philibert, G. and Hughes Clarke, J. 2021: Submarine landslides triggered by iceberg collision with the seafloor; Nature Geoscience, v. 14, p. 599–605, URL <https://doi.org/10.1038/s41561-021-00767-4>.

Oppikofer, T., Jaboyedoff, M., Derron, M.H. and Bilkra, L.H. 2009: Geometric back-analysis of ancient rockslides in Tafjord (Norway); Geophysical Research Abstracts, EGU General Assembly 2009, v. 11, EGU 2009-7647, URL <https://ui.adsabs.harvard.edu/abs/2009EGUGA.11.7647O/abstract>.

Pourchet, M., Pinglot, J.F. and Marie, A.M. 1989: Cesium-137 and lead-210 in alpine lake sediments: measurements and modeling of mixing process; Journal of Geophysical Research, v. 94, no. C9, p. 12761–12770. URL <https://doi.org/10.1029/JC094iC09p12761>.

Prior, D.B. and Bornhold, B.D. 1989. Submarine sedimentation on a developing Holocene fan delta; Sedimentology, v. 36, p. 1053–1076, URL <https://doi.org/10.1002/9781444304473.ch34>.

Strupler, M., Anselmetti, F.S., Hilbe, M. and Strasser, M. 2019: Quantitative characterization of subaqueous landslides in Lake Zurich (Switzerland) based on a high-resolution bathymetric dataset; Geological Society of London, Special Publications, v. 477, p. 399–412, URL <https://doi.org/10.1144/SP477.7>.

Stein, S., Sleep, N.H., Geller, R.J., Wang, S. and Kroeger, G.C. 1979: Earthquakes along the passive margin of eastern Canada; v. 6, p. 537–540, URL <https://doi.org/10.1029/GL006i007p00537>.

Syvitski, J., Burrell, D.C. and Skei, J.M. 1987: Fjords: processes and products; Arctic and Alpine Research, v. 20, no. 3, URL <https://doi.org/10.1007/978-1-4612-4632-9>.

Tappin. D.R. 2010: Submarine mass failures as tsunami sources – their climate control; Philosophical Transactions of the Royal Society A: Mathematical, Physical and Engineering Sciences, v. 368, no. 1919, p. 2417–2434. URL <https://doi.org/10.1098/rsta.2010.0079>.

Urlaub, M., Talling, P.J. and Masson, D.G. 2013: Timing and frequency of large submarine landslides: implications for understanding triggers and future geohazard; Quaternary Science Reviews, v. 72, p. 63–82, URL <https://doi.org/10.1016/j.quascirev.2013.04.020>.

Waldmann, N., Vasskog, K., Simpson, G., Chapron, E., Støren, E.W.N., Hansen, L., Loizeau, J., Nesje, A. and Ariztegui, D. 2021: Anatomy of a catastrophe: reconstructing the 1936 rock fall and tsunami event in Lake Lovatnet, western Norway; Frontiers in Earth Science, v. 9, p. 1–18, URL <https://doi.org/10.3389/feart.2021.671378>.

Water Survey of Canada 1983: Daily discharge graph for Duval River near Pangnirtung (10UF001) [NU]; Water Survey of Canada, URL <https://wateroffice.ec.gc.ca/report/historical_e.html?stn=10UF001> [October 2021].